Chemical Sensing as a Utility using Swept-Source Raman Spectroscopy

by

Nili Persits

B.S., Tel-Aviv University (2008)

M.S., Tel-Aviv University (2016)

Submitted to the Department of Electrical Engineering and Computer Science in partial fulfillment of the requirements for the degree of

DOCTOR OF PHILOSOPHY

at the

MASSACHUSETTS INSTITUTE OF TECHNOLOGY

MAY 2024

Authored by: Nili Persits
Department of Electrical Engineering and Computer Science
April 8, 2024

Certified by: Rajeev J. Ram
Professor of Electrical Engineering and Computer Science
Thesis Supervisor

Accepted by: Leslie A. Kolodziejski
Professor of Electrical Engineering and Computer Science
Chair, Department Committee on Graduate Students

Chemical Sensing as a Utility using Swept-Source Raman Spectroscopy

by

Nili Persits

Submitted to the Department of Electrical Engineering and Computer Science on April 8th 2024, in partial fulfillment of the requirements for the degree of Doctor of Philosophy in Electrical Engineering and Computer Science

Abstract

The integration of chemical sensing into everyday life is a decades-old dream that has so far failed to come to fruition. Many sensor technologies have been proposed and developed, but few can claim to be non-destructive, reagent-free, and suitable for multiple applications while also enabling significant scale-up and remaining cost-effective.

This thesis proposes a utility service model for chemical sensing using Swept Source-Raman Spectroscopy (SSRS) that addresses these challenges. First, we introduce the SSRS fiber-probe that allows to measure Raman spectra with a single-point detector and only a few milliwatts of tunable laser excitation. We validate the probe design by monitoring nitrate fertilizer in a hydroponic setup, in environmental water samples, and in growing plants with sensitivity and resolution which are equivalent to benchtop systems. We further demonstrate the scaling up of SSRS into a sensor network by leveraging readily-available data communication optical fiber infrastructure. We showcase a 16-sensor network that uses the laser as a shared resource and develop an engineering-based cost model that supports the scaling up of this network to dozens of sensors deployed over kilometers. Lastly, we monitor metabolites in a therapeutic-producing cell culture, and use linear regression models and a-priori information of our samples to reduce the spectral acquisition time, making this sensor architecture competitive in both performance and cost to existing solutions. These findings represent significant progress towards achieving ubiquitous chemical sensing and facilitating the integration of chemical sensors into everyday life.

Thesis Supervisor: Rajeev J. Ram

Title: Professor of Electrical Engineering and Computer Science

This doctoral thesis has been examined by a Committee of the
Department of Electrical Engineering and Computer Science as follows

Professor Rajeev J. Ram . . . . . .

Chairman, Thesis Committee
Professor of Electrical Engineering and Computer Science

Professor Sixian You . . . . . .

Member, Thesis Committee
Professor of Electrical Engineering and Computer Science

Professor Anthony J. Sinskey. . . . . .

Member, Thesis Committee
Professor of Biology

Acknowledgments

This thesis was by no means an accomplishment of a single person. Despite the fact that most of the technical work was indeed done by me, I had the most wonderful group of people supporting me profesionally and personally troughtout this rocky road and I'd like to take this opportunity and thank them.

First of all my family: Lev, you are a force to be recokned with. Not always (ever) subtle, but I would not have applied to MIT or made it through without you. Words cannot describe how much you have given me and how much I appreciate your love, unfailing belief in me, and continued support. I love you.

Maya and Libby, my wonderful duaghters – it is a priviliage to be your mother. You are a constant reminder of the things that really matter in life. I hope I have inspired you to work hard and pursue your dreams. I love you so much.

My twin, Yael, who would always know immidiately that I needed to talk. If there is one think I hate to have sacrificed is being close to you. I missed you so much.

My parents, for giving me the best eduaction, for all the help along the way, for showing up and giving Lev and I much needed breaks, and for being the best grnadparents! I love you (and I got the brains from both of you!)

To my friends who have kept me sane (ok, mostly sane): Ayalla, Nitsan, Aner, Revital, Dan, Sarah, Rachel – you gave me more energy and motivation than you know. Hanging with you and having your love and support were many times what gave me energy to go through the long weeks (months, years…) of classes and lab work. I appreciate you all so very much.

Valentin, my raft in troubled water, thank you for the coffee. And the shoulder to cry on, and the coffee. Did I mention coffee? Seriously, thank you sunshine. It was great having someone to go through this monstrous obstacle course with. You made

everything butter.

My lab mates, thank you for letting me vent (a lot) and letting me make you really strong coffee. Dodd - the best frickin' optics teacher, Gavin – the brutal honesty and laser tutorials, Marc – morning therapy sessions, Jaehwan – the nicest guy ever to walk the earth, Dahlia - for all the code and for being the best UROP a grad student could ever ask for, and Elise – for making me laugh and the for the cookies (!) you guys made lab worth coming to.

Lastly Rajeev, who was an extremely patient mentor and PI, and who gave me the opportunity to make a lot of mistakes and learn slowly from them and who continues to support me while I embrak on an etrepreneurial journey.

Table of Contents

List of Figures

List of Tables

CHAPTER 1

Introduction and Overview

1.1 Chemical Sensing as a Utility

For decades, the idea of ubiquitous chemical sensors that provide instantaneous molecular composition information, has captivated our imagination. Visors that analyze the composition of any material in the field of view, planetary and environmental monitoring, and prompt medical diagnosis have become a staple in the portrayal of futuristic technology[1]. Increased demand for bio-chemical sensors for medical, environmental, food production, and security applications, emphasizing point-of-sample operation and decentralization of chemical analytics labs[2], have propelled research and ingenuity in this domain[3].

The multiple uses of such ubiquitous chemical sensing have many similarities with utility services. A utility is a service provided on a continuous basis by virtue of a physical infrastructure network - examples include water, sewage, electricity, and more recently, the internet. The infrastructure can be public or private but the service provided should be essential (necessary), scalable, sharable, generic, easy-to-use, and metered[4,5].We see how these criteria can be applied to electricity, water, sewage, and internet but are also relevant for novel utility models such as edge or cloud computing[5,6].

One way to accomplish distributed chemical sensing is through a wireless network that connects various single-point sensors. Numerous miniaturized chemical

sensors have been designed and deployed[3,7], often aided by mobile phones[8], leveraging existing communication protocols to create the network. The chemical detection itself is based on traditional transductions mechanisms, predominantly electrochemical, electrical, optical, or mass-based. Despite significant advances, there are still many challenges with the operation of such sensors, that have so far prevented them from being acceptable replacements for lab-based analysis. In many cases the physical transduction interface has limited selectivity and would respond to several analytes simultaneously, without the ability to differentiate between them. Additionally, sensitivity could be low, meaning low analyte concentrations cannot be reliably detected. This has been reported to be the key problem with these conventional sensors, followed by repeatability and longevity issues[3,9].

Another significant hurdle is centered around power consumption. While a wireless sensor network architecture is considered advantageous due to the ability to deploy sensors over large areas and perform in-situ measurements, or just mobilize deployment on demand, wireless sensors suffer from strict power consumption limitations. The power constraints dictate the selection of materials, mechanical components, electronics, light sources, and optical amplifiers, effectively limiting the applicable sensing modalities.

Wired sensor networks, both in regards to power and connectivity, provide significant advantages for reliable, persistent, and high-performance measurements and enable more extensive sensing methods that demand higher power consumption[10]. Optical fiber networks that monitor strain and temperature by Brillouin scattering or Bragg gratings are notable examples of such wired networks[10,11]. These sensors persistently monitor kilometers of optical fibers embedded into structures like damns, bridges, tunnels, using laser sources with laser powers exceeding 300mW[12]. Another common example is Closed Circuit TV (CCTV) where the

reliability and security of the network demand a wired architecture. However, many traditional and useful chemical sensing modalities, particularly optical spectroscopic methods cannot be easily adapted to perform in a network. A key example of this is Raman spectroscopy.

Raman Spectroscopy is based on inelastic light scattering[13], which is a weak non-linear scattering effect that occurs due to the vibrational motion of a molecule[14]. Raman spectroscopy is a purely optical sensing method, that is reagent-free, non-destructive that can be implemented in-line[14]. It further stands out over other optical methods since it can detect multiple chemical compounds simultaneously, even in complex mixtures. These advantages have made Raman Spectroscopy a useful chemical analysis tool[14–16].

Over the last decade Raman has been adopted as a Process Analytical Tool (PAT) in pharmaceutical production and other chemical manufacturing processes[17–19]. It is a valuable tool for chemical characterization and monitoring since sensors can be integrated into a specific production step and provide real-time data on dynamic processes. A notable example is the monitoring of cells that have been genetically modified to produce therapeutic proteins[20], where Raman is used to continuously monitor metabolites such as glucose and lactate in the cell culture vessel. Raman is also gaining attention for environmental and in-line water monitoring[21–24], for clinical applications[25,26], chemical and material science[27,28], geology and archeology[29,30], ocean exploration[31,32], forensics[33], food, agriculture[34,35], and many more[27].

Raman spectroscopy, however, is challenged by the inherently weak signal from Raman scattering (discusses in more detail in Section 1.3) demanding powerful lasers for excitation, multiple optical components for optimized signal collection, and cooled spectrometers for detection.

Figure 1.1 shows a schematic illustration of a conventional Raman system

including a fixed laser wavelength, and a spectrometer (the collection optics are left out for simplicity). Benchtop spectrometers are often expensive and delicate because of micron-scale alignment required between components for optimal throughput and resolution. They cannot feasibly be deployed in many sensing points. Additionally, the use of a shared spectrometer for several sensors is significantly limited by the need to guide the weak Raman signal to the entrance slit of the spectrometer. Portable and hand-held versions offer limited sensitivity and lower spectral resolution, as is further discussed in Section 1.4.3. Raman spectroscopy has, therefore, been confined primarily to laboratories due to fundamentally weak interactions, equipment complexity and cost, hindering its widespread adoption.

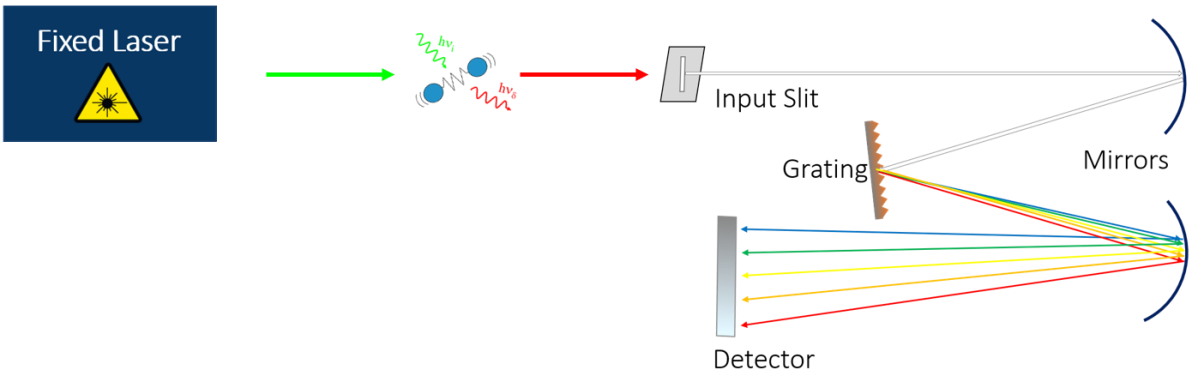

Figure 1.1: An illustration of a standard Raman system. A fixed wavelength laser is used to excite a sample. The scattered signal is collected and guided into a dispersive spectrometer.

This thesis proposes to leverage a recent novel Raman spectroscopy architecture, Swept Source Raman Spectroscopy[36] (SSRS), to overcome the traditional Raman instrumentation obstacles and create a Raman optical fiber sensor network. SSRS uses a tunable laser source and replaces the spectrometer with a single-point optically narrow-band photodetector. Instead of acquiring the spectrum in a single "one-shot", the spectrum is sampled sequentially as the laser wavelength is tuned. A schematic illustration of SSRS is given in Figure 1.2.

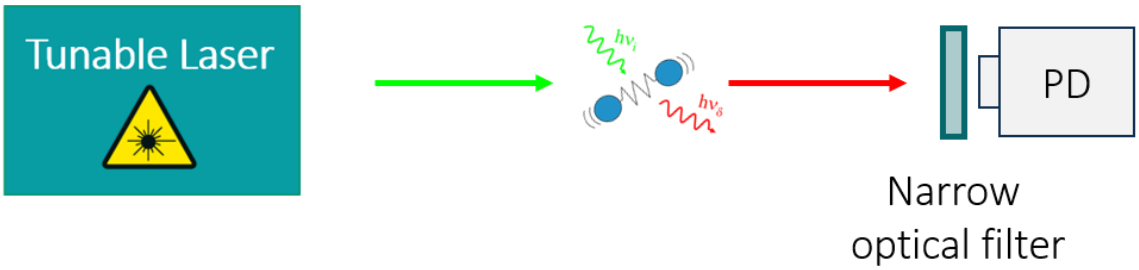

Figure 1.2: A schematic illustration of an SSRS system with a tunable laser and a narrow line width filter in front of a photodetector. The spectra is acquired sequentially as the laser tunes.

The benefit of removing the spectrometer from the system is two-fold: First, the optical throughput of the system is no longer limited by the spectrometer, but rather by other optical components such as the acceptance angle of the narrow line width filter or the area of the detector, effectively increasing the optical signal collection by up to a thousand-fold. Additionally, this collection improvement does not entail sacrificing the spectral resolution, which is typical in traditional dispersive spectrometers (see Section 1.4.2). Fourier Transform (FT) spectroscopy system that do offer enhanced light collection (discussed in Section 0) are significantly more complex than SSRS.

Secondly and paramount to this work, the SSRS architecture allows one to implement a star-shaped optical fiber sensor network using a single tunable laser as a shared source and deploy multiple sensors[37], as shown in Figure 1.3.

The use of established and readily available optical fiber infrastructure combined with SSRS unlocks the potential for ubiquitous large-scale deployment of Raman spectroscopy sensors.

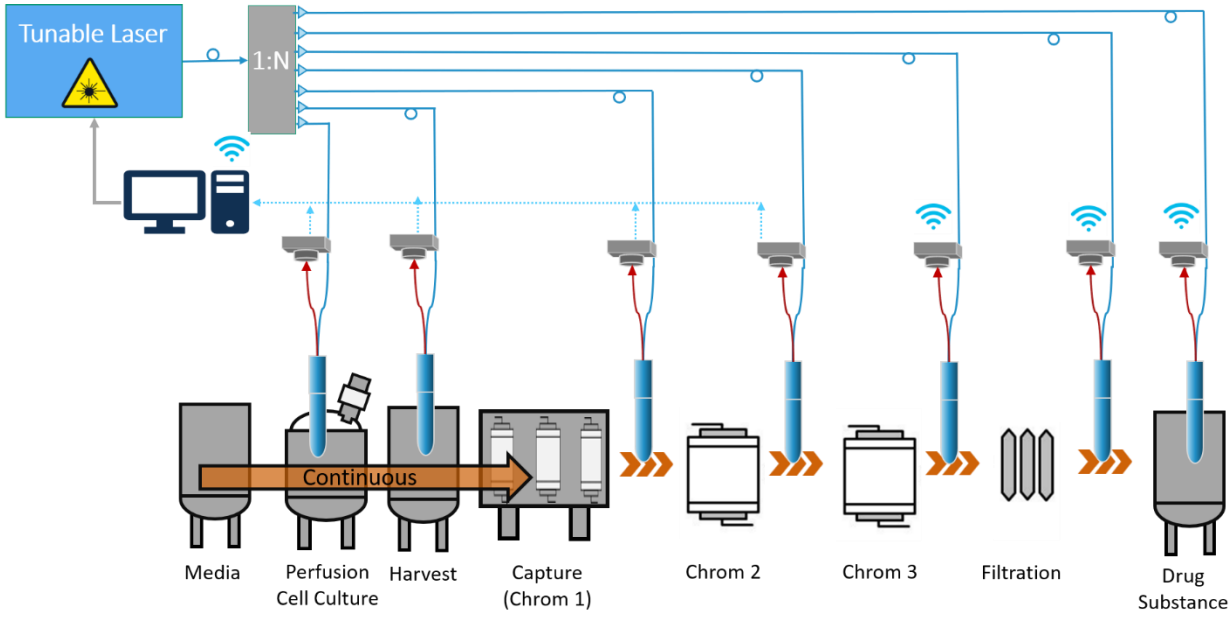

Figure 1.3: An illustration of an SSRSS sensor network integrated for process monitoring into a continuous pharmaceutical production line. Sensors are integrated in multiple steps prividing real-time data.

The next sections in this chapter will include a brief review of optical chemical sensing methods (Section 1.2) followed by a more detailed review of Raman spectroscopy (Section1.3). Étendue or light gathering (Section 1.4.1) and spectral resolution (Section 1.4.2) are introduced as key metrics for performance comparison of different spectral acquisition methods, namely dispersive (Section 1.4.3), and SSRS (Section 1.4.4). A review of Raman probes, their design considerations and applications is provided in Section 1.5. Section 1.6 will review common spectral decomposition algorithm and feature-selection methods that allow for the analysis of complex Raman spectra. Lastly Section 1.7 will review various use-cases of Raman spectroscopy.

1.2 Chemical Sensing with Optical Spectroscopy

Optical chemical sensing encompasses the detection, quantification, and

analysis of chemical compounds in diverse substances and environments. It plays a pivotal role in numerous fields, such as earth sciences, environmental monitoring, healthcare, food manufacturing, consumer safety, and material sciences, offering critical insights and enabling important advancements[38,39].

There are many spectroscopy techniques, each leveraging a different type of interaction of the electromagnetic field, such as nuclear and electronic transitions, molecular rotation and vibration, or spin of electrons and nuclei in a magnetic field. Each method offers unique advantages and limitations, driving their application in various fields[19,40–43]. Figure 1.44 shows a diagram depicting the energy level transitions and their respective wavelength range for spectroscopic methods[43].

From the wide array of spectroscopy methods those which use Ultraviolet (UV) or Infrared (IR) wavelengths, are a powerful tools for chemical sensing of the molecular structure since these wavelength correspond to energetic transitions that can be detected and identified[40,41,43,44]. The spectra can be generated from emission, reflection, absorption, transmission, or scattering processes. Optical spectroscopic methods are often non-destructive, preserving the integrity of valuable or limited samples during analysis. They can also be used for real-time or near real-time analysis. With the comprehensive information they provide, optical spectroscopic methods facilitate the detection and quantification of trace amounts of compounds, even in complex matrices.

Some of the more common methods, namely Ultraviolet-Visible (UV-Vis) absorption, IR absorption, Fluorescence spectroscopy, and Raman Spectroscopy, described in more detail below, stand out for their relative simplicity and wide array of applications. Over the last few decades, they have been used as PATs in many forms of manufacturing, and particularly for bioprocessing[19]. Bioprocessing refers to the use of living cells or their components to produce desired products such as therapeutics,

cosmetics, or food and beverage. Figure 1.65 (reproduced from reference[20]) shows the application of optical spectral methods along with their wavelength ranges in monitoring of bioprocess manufacturing.

While this thesis focuses on Raman spectroscopy, which will be discussed in detail in the following sections, it is useful to briefly review the other key optical spectroscopy methods to provide context and benchmark against Raman spectroscopy.

UV-Vis spectroscopy measures the absorption, transmission, diffraction, and refraction of light in the wavelength region of 200-780nm. The absorption of UV-Vis light is due to bonding electron transitions in certain molecular functional groups[20,40]. These functional groups are shared among many materials and so this method has limited specificity. UV absorption is widely used in bioprocessing to measure the concentration of a variety of substances such as proteins (240-280nm, 340, 410-450, 550-600nm)[20,41,45,46], amino acids (240-280nm)[41], nucleic acids and DNA (350-410nm)[41]. It is also used as a tool in the food and beverage industry, mostly for Optical Density (OD) or turbidity detection[47], and is also gaining traction for water measurements of nitrates and nitrites and other water quality indicators[48].

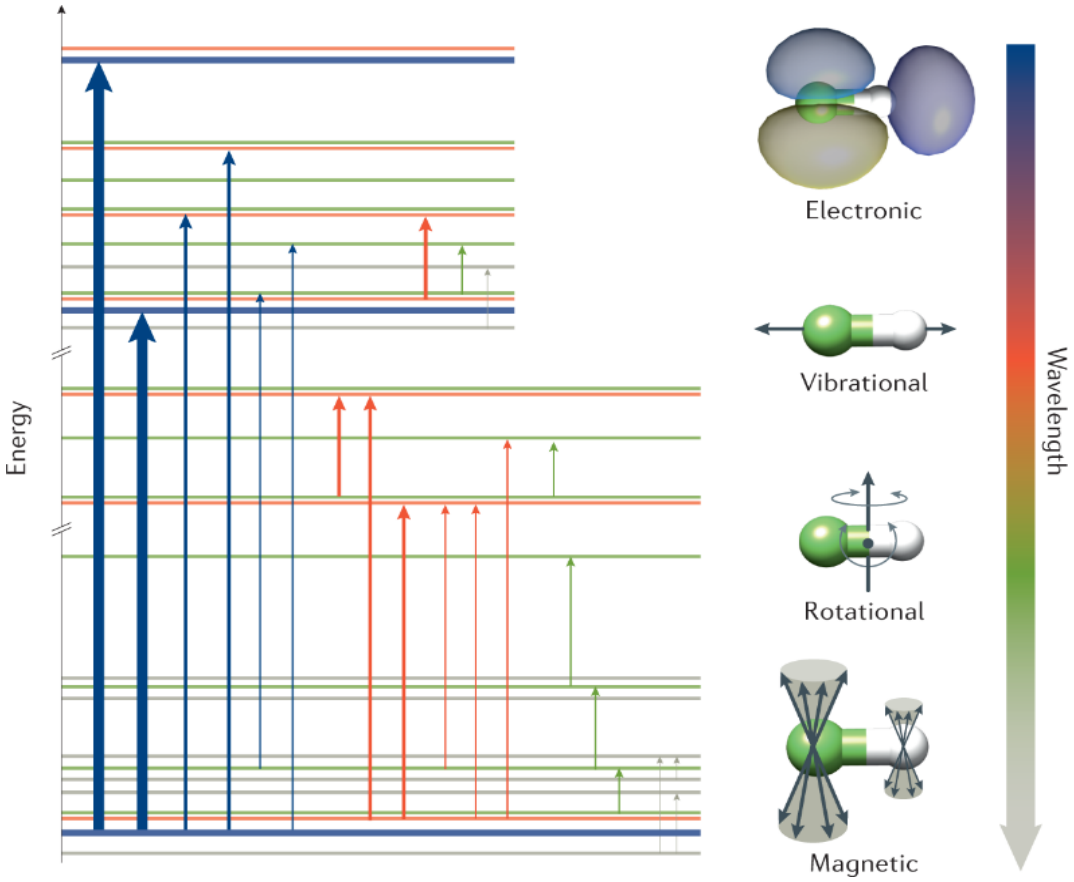

Figure 1.4: Schematic representation of molecular energy levels and types of possible transitions. Blue arrows denote the transitions involving a change in the electronic state (from left to right, thicker to thinner: electronic, vibronic and rovibronic transitions). Red arrows denote the transitions involving different vibrational states (from left to right: vibrational and ro-vibrational transitions). Green arrows denote the transitions only involving rotational energy levels. Dark grey arrows denote the transitions between energy levels obtained from magnetic field (reproduced from[43])

Many useful and intense absorbance spectral regions are in the UV range, as seen above, with a few weaker absorption bands in the visible range. The use of UV radiation is, nonetheless, detrimental due to mutagenesis, covalent bond breaking and the creation of reactive oxygen species[49,50], making it destructive and unsafe for cell monitoring or in-vivo applications. Additionally, the instrumentation required for UV-Vis spectroscopy must be precisely calibrated and is particularly sensitive to fouling, which is very common in biological and environmental samples[48,51,52].

A different type of absorption spectra is measured with IR wavelengths which are subdivided into Near Infra-Red (NIR), in the 800-2500nm wavelength range, Mid Infra-Red (MIR) in the 2500-25000 nm range, and Far Infra-Red (FIR) in the 25-1000 μm wavelength range. The IR absorption bands corresponds to molecular rotations and vibrations frequencies, making IR spectroscopy a widely used technique for molecular structure characterization, concentration and purity measurements[14,19,20,40,41]. IR is mostly detected using Fourier Transform Infra-Red (FTIR) which allows us the use of a single point detector instead of an array which is expensive in the IR range[40,41] (see Section 0). IR spectroscopy is extensively used as a PAT in production processes such as oil refinement, chemical production of polymers and plastics, food and beverage, semiconductors, pharmaceuticals, and many more[19,20]. IR absorption, however, has reduced performance in aqueous environments due to the water's high absorption of IR energy in wavelengths larger than 1μm (see Figure1.5), limiting the usefulness of the method for certain environments and samples.

Figure1.5: Absorption coefficient of water as a function of radiation wavelength.

Fluorescence spectroscopy has become one of the dominant techniques in the life sciences. It leverages fluorophores, which are chemical compounds that re-emit light when excited with light in the UV-Vis wavelength range[20,53]. Fluorescence occurs when light, matching certain electron transitions, is absorbed by the fluorophore and then relaxes back into the ground state by radiative recombination. The intensity of the emission is proportional to the concentration of fluorophores[19,20,41,53]. Many biological molecules naturally include fluorophores and are autofluorescent, e.g. flavins, vitamins, certain amino acids (tyrosine, tryptophan, phenylalanine), adenosine triphosphate, and more[53]. Fluorescent dyes are used extensively to selectively bind to target molecules which are then detected at the appropriate fluorescent excitation and emission wavelengths. Fluorescence is a relatively intense emission process with long radiative lifetimes (on the order of nanoseconds), making it a prime candidate for imaging and quantitative measurements[20,53].

Fluorescence spectroscopy, however, requires extensive sample preparation and manipulation. Often, selective fluorescent dyes need to be mixed into the samples in order to bind to target molecules. If several molecules are sought, then multiple dyes need to be used, each selectively targeting a unique molecule. Genetic editing of cells to express fluorescent proteins such as Green Fluorescent Protein (GFP) is also quite common, requiring sample perturbation. Last and not least, fluorescent tagging is a useful technique for in-vivo applications, particularly for large molecules. However, the tagging of small molecules such as glucose, while possible, prevents their normal function and so has limited usefulness[54].

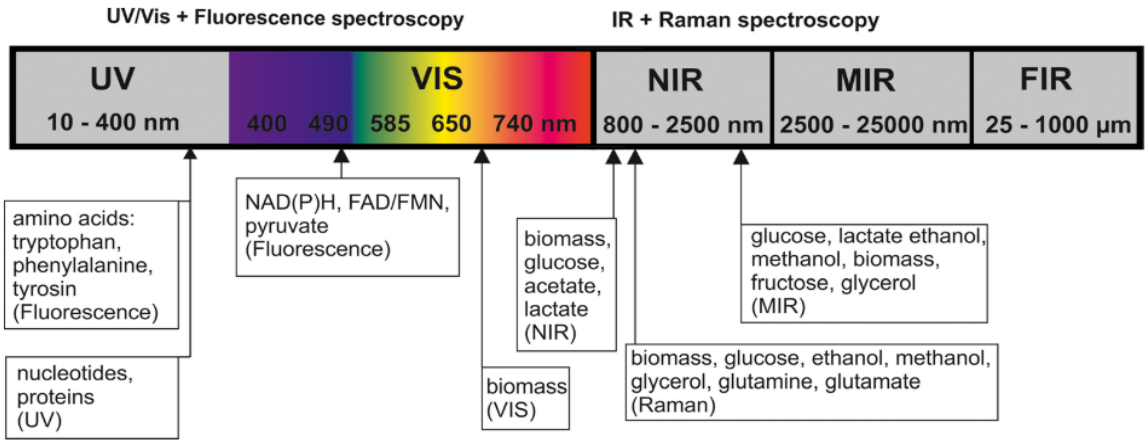

Figure 1.6: Spectral ranges and the corresponding methods for bioprocess monitoring using spectroscopy (reproduced from[20]).

Many materials such as proteins, collagen, and flavins naturally include fluorophores and are autofluorescent in the UV-Vis range, where absorption is high. Autofluorescence can be useful since it removes the need for sample tagging, however, it is quite challenging for Raman spectroscopy. Autofluorescence is much more intense than Raman scattering and it creates an emission background which interferes with the measurement of the weak Raman signal. This phenomenon has driven Raman excitation wavelengths to the NIR range, where autofluorescence is significantly weaker due to lower absorption of the exciting wavelengths[14,19,41,42,55,56].

In many cases optical spectroscopic methods require powerful light sources and extensive sample preparation such as tagging, filtering, dissolving, mounting, etc. These procedures are rarely automated and require significant work, making most spectroscopy methods laboratory-based, meaning samples have to be removed from their process or natural environment and transported to be analyzed[19,40,41].

The need to extract samples is in itself challenging. First, extraction of samples from a process might compromise their integrity as sampling can introduce contamination or alter the sample composition. Second, manual sampling further increases the variability due to operator error and is costly and time consuming. Third,

any analysis that is done off-line or at-line (near the process but separate from it) reduces the speed of the analysis, making real-time feedback for control challenging[19]. Furthermore, in some applications such as monitoring of waste water streams, water from mining facilities, or other remote locations, removing and transporting samples is simply not feasible or extremely cost-prohibitive.

In-line spectroscopic methods are advantageous since they do not require sample removal or transportation. UV-Vis, IR and Raman spectroscopy can be integrated as in-line sensors[19,20,57]. Raman spectroscopy, described in detail in the following section, has the added advantage of providing specific chemical fingerprints based on a unique molecular structure, even in aqueous environments.

1.3 Spontaneous Raman Spectroscopy

1.3.1 Theory

Raman spectroscopy, like IR absorption spectroscopy, probes the vibrational states of a molecule[14,26]. However, their physical mechanism and operation is significantly different. IR absorption directly probes the molecule with excitation corresponding to the vibrational oscillations frequencies, and depends on a molecule's dipole moment, $P\ [C \cdot m]$, which is the measure of the separation of positive and negative electrical charges[14,41]. Raman, on the other hand, uses visible to NIR wavelengths and depends on the polarizability, $\alpha\ [C \cdot \frac{m^2}{V}]$, of the material, which is the tendency of a charge distribution (or electron cloud) to be distorted by an oscillating electrical field. As an example, we consider the symmetric stretch of CO_2. A symmetric stretch mode is not IR active because there is no change in the molecular dipole, however, there is a change in the molecule polarizability as both oxygen atoms are

farther away from the carbon atom. The opposite occurs for the asymmetric stretch mode which is IR active but Raman inactive[14].

α is defined by the ratio of the dipole moment to an electric field, $E\ [\frac{V}{m}]$, and while P is a tensor, Equation 1.1 is written for an isotropic medium for simplicity[15,16]:

$$P = \alpha E \tag{1.1}$$

Let Q_j be the j[th] vibrational mode of a molecule, oscillating at frequency υ_j where the oscillation amplitude (spatial displacement) is given as $Q_0\ [m]$:

$$Q_j = Q_0 cos(2\pi \upsilon_j t) \tag{1.2}$$

The polarizability of the electrons is modulated due to the molecular vibrations and can be expanded to a series:

$$\alpha = \alpha_0 + \frac{\delta \alpha}{\delta Q_j} Q_j + \cdots \tag{1.3}$$

We can write the laser induced electrical field oscillating at frequency υ_0(the laser frequency) as:

$$E = E_0 cos(2\pi \upsilon_0 t) \tag{1.4}$$

Combining Equations 1.3 and 1.4 we get the effective dipole moment:

$$\mathrm{P} = \alpha_0 E_0 cos(2\pi \upsilon_0 t) + E_0 Q_0 \left(\frac{\delta \alpha}{\delta Q}\right) \frac{cos\, 2\pi(\upsilon_j + \upsilon_0)t + cos\, 2\pi(\upsilon_j - \upsilon_0)t}{2} \tag{1.5}$$

While Equation 1.5 does not provide a complete description of the Raman scattering, at a first glance we can see the elastic (Rayleigh) scattering as the first term, at the same frequency as the electric field, υ_0 and the terms relating to the beat frequencies of the electric field and molecular vibrations, corresponding to the Raman scattering, in the second term.

Raman scattering occurs both for molecules in their ground state and in their excited state. When the interaction occurs at the ground state, exciting the molecular vibration and leaving the photon with lower energy (corresponding to a longer wavelength) the returning energy is Stokes-shifted. An Anti-Stokes shift occurs when

the photon interaction occurs at an excited vibrational state and the photon is scattered with more energy, corresponding to shorter wavelengths. Figure 1.7 shows a schematic energy diagram illustrating the energetic shift for Stokes and Anti-Stokes shifted Raman scattering along with Rayleigh scattering and IR and UV-Vis absorption.

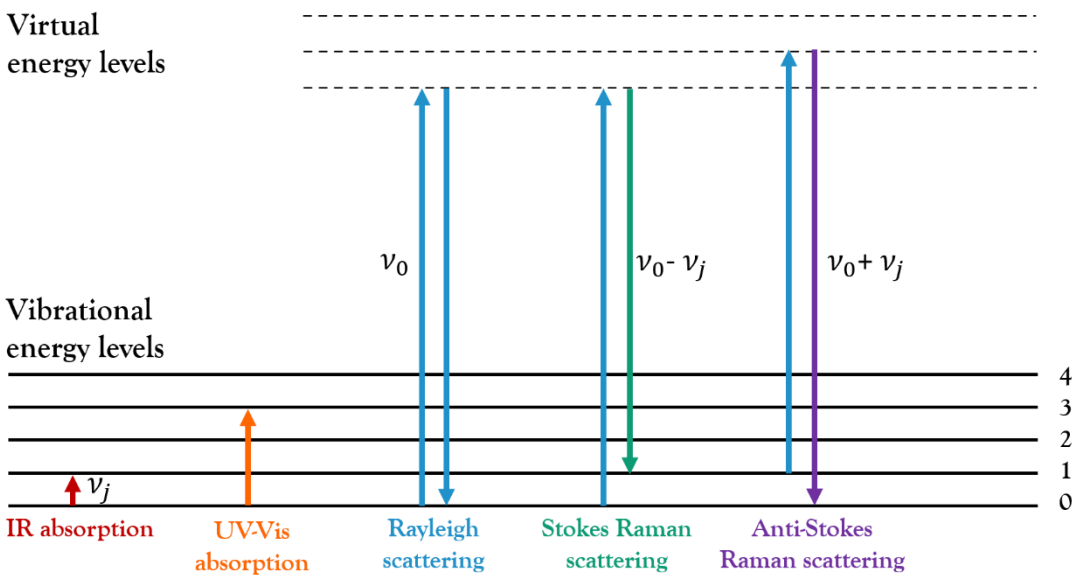

Figure 1.7: A schematic energy band diagram showing the energetic shifts for Rayleigh scattering along with Raman scattering for both Stokes and Anti-Stokes shift as well as IR and UV-Vis absorption transitions.

Equation 1.5, however, is incomplete since it does not include the frequency dependence of the scattered intensity for the Rayleigh and Raman scattering. First, we conveniently replace the frequency υ with the wavenumber $\nu = \upsilon/c = 1/\lambda$ (c being the speed of light). The use of wavenumbers is the convention for Raman spectroscopy, allowing to describe the Raman spectrum as a function of energetic shift relative to the excitation, independent of the excitation wavelength. Now we can describe the intensity of a specific Raman line, related to $\frac{\delta\alpha}{\delta Q}$, in Equation 1.6, where K is a constant[14-16]:

$$I_R = K(\nu_j \pm \nu_0)^4 \alpha^2 Q_j^2 \tag{1.6}$$

The factor $(\nu_j \pm \nu_0)^4$ in Equation 1.6, derived from the classical treatment of scattering from an oscillating induced dipole[14,16], bears great significance for the selection of excitation wavelength. With longer wavelength excitation, there is a fourth-power rapid reduction of the Raman scattering intensity.

In addition to the strong wavelength dependence evident from Equation 1.6, there is an additional difference in intensity between the Stokes and Anti-stokes scattering. Due to the higher occupancy of lower energetic states, the ratio of Stokes to Anti-Stokes scattering is given in Equation 1.7, as described by the Boltzmann distribution[14], where $\mathbf{k_B}$ is the Boltzmann constant:

$$\frac{I_R(\nu_j + \nu_0)}{I_R(\nu_j - \nu_0)} = \frac{(\nu_j + \nu_0)^4}{(\nu_j - \nu_0)^4} exp\left(-\frac{h\nu_j}{k_B T}\right) \tag{1.7}$$

From Equation 1.5 it is also evident that the Rayleigh scattering is dependent on α_0 and that Raman scattering is dependent on $\frac{\delta\alpha}{\delta Q}$. α_0 is orders of magnitude larger than $\frac{\delta\alpha}{\delta Q}$ due to the statistical probability of a scattering event. While Rayleigh scattering is a first order process, Raman scattering is a second order process requiring the simultaneous interaction of electrons in a molecule with optical photons and optical phonons (quanta of vibrational motion). Furthermore, Raman scattering selection rules make only certain energetic transitions possible, further limiting the likelihood of an inelastic scattering event. Overall only one out of every $10^8 - 10^9$ photons undergoes Raman scattering, usually amounting to mere femtowatts of optical power[14,41].

Raman scattering's strong wavelength dependence is a pertinent aspect in the design of Raman systems. For example, aqueous samples are best excited in the NIR wavelength range (785-830nm) where radiation absorption is minimal (see Figure1.5)

and where autofluorescence is lower[58,59]. However, the Raman signal is severely diminished compared with visible wavelengths excitation. Additionally, common silicon detectors suffer from reduced quantum efficiency for NIR wavelengths (discussed further is Section 0).

Despite the inherently low signal levels of Raman scattering, with the development of compact, powerful laser sources, sensitive detectors and cameras, the detection of Raman scattering has become significantly more accessible, yet requires careful consideration of many parameters, as is detailed in the next Section.

1.3.2 Signal and Noise Model

The Signal to Noise Ratio (SNR) is canonically defined as the ratio of signal power to noise power. Since optical photons are converted to electrons in standard detectors and cameras, the signal to noise ratio can be written in Equation 1.8, where $\bar{S}$ is the mean of detected electrons and $\bar{\sigma}_{tot}$ is the standard deviation in the number of electrons.

$$\frac{S}{N} = \frac{\bar{S}}{\bar{\sigma}_{tot}} \tag{1.8}$$

In order to evaluate the feasibility of using Raman spectroscopy for measurement of a specific analyte, a model of the SNR, including the excitation, sample attributes, collection optics, and detection, needs to be constructed[14,15,60]. Figure 1.8 shows a general experimental setup with a sample comprising of analyte A and host material B which will be used to illustrate the model.

We begin by estimating the signal resulting from Raman scattering of a sample. An excitation laser emitting n_p photons illuminates a sample with spot size $A_s(z)$. The excitation photon flux, P_0 $\left[\frac{photons}{cm^2 \cdot s}\right]$, can be calculated from Equation 1.9, where

$\dot{n_p}$ is the temporal derivative:

$$P_0 = \frac{\dot{n_p}}{A_s(z)} \tag{1.9}$$

We assume a specific analyte, A, with concentration C_a $[\frac{moles}{cm^3}]$, in a sample volume surrounded by another material, B, with concentration C_b. The number of analyte molecules in a cubic cm of sample is then $C_a N_A$, and the number of background host molecules per cubic centimeter is $C_b N_A$, (N_A is Avogadro's number). From Equation 1.6 we know that the Raman scattering intensity depends on the analyte's specific molecular vibration as well as the excitation wavelength. We conveniently lump the total wavelength and analyte dependency into the Raman cross section[14,15,61,62], γ_a $[\frac{cm^2}{molecule}]$ for analyte A and γ_b for the host material B.

Assuming the total Raman scattering occurs in all directions into a sphere with a 4π solid angle, we can write the Raman radiance, R $\left[\frac{photons}{cm^2 \cdot s \cdot sr}\right]$ from a sample depth dz and area $A_s(z)$ by Equation 1.10[14]:

$$R = \frac{\dot{n_p}}{A_s(z)} \left(\frac{d\gamma_a}{d\Omega}\right) (C_a N_A dz) \tag{1.10}$$

We now move to address the optical collection system, which we model to have an aperture A_D with an acceptance angle Ω_D. The number of Raman photons collected per second are therefore:

$$N_S = R(A_D \Omega_D) \tag{1.11}$$

It is important to note that according to the Radiance theorem (discussed in detail in Section 1.4.1) the collection system's ability to gather the scattered photons is bound by the component (or aperture) with the lowest product of $\mathrm{A_D}\Omega_\mathrm{D}$ throughout the system.

We now further consider transmission losses, T_x, in the optical collection system due to reflections, absorbance, and imperfections of the optical components

such as filters and lenses. Additionally, the detector (or camera), discussed in detail in Appendix B, has a finite quantum efficiency, $\eta \left[\frac{e^-}{photons}\right]$, in which only part of the impacting photons are converted to electrons.

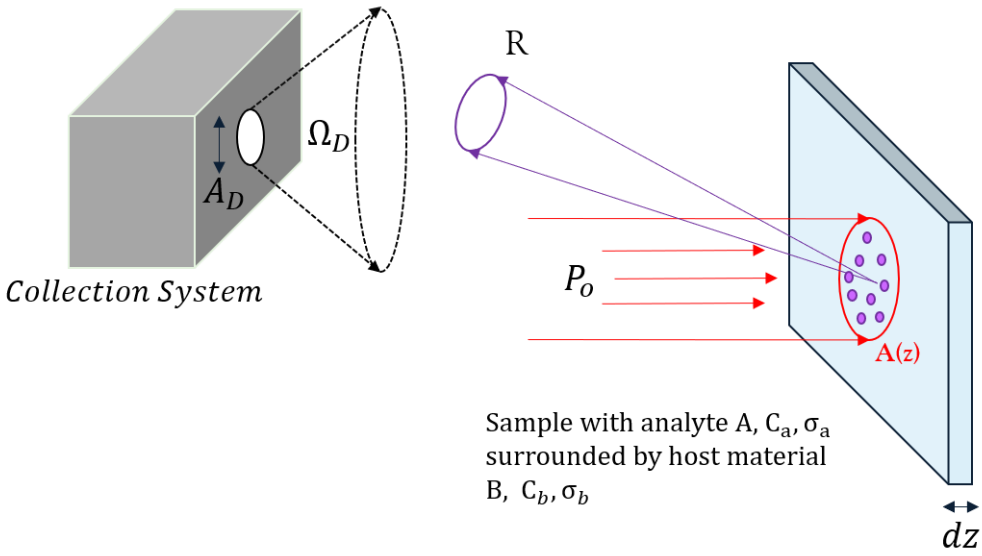

Figure 1.8: An illustration of a general experimental setup where a laser light with photon flux P_O excites a sample comprised of analyte A and host material B and an optical collection system with aperture A_D and acceptance angle Ω_D.

We now combine Equations 1.10 and 1.11 to write the total detected electrons from the sample due to the Raman scattering from analyte A over an integration period of τ seconds:

$$S = \tau\eta T_x \int \frac{\dot{n_p}}{A_s(z)}\left(\frac{d\gamma_a}{d\Omega}\right)(C_a N_A)(A_D\Omega_D)dz \tag{1.12}$$

Similarly, we can write the total number of electrons collected from the host background material with effective cross section σ_b:

$$B = \tau\eta T_x \int \frac{\dot{n_p}}{A_s(z)}\left(\frac{d\gamma_b}{d\Omega}\right)(C_b N_A)(A_D\Omega_D)dz \tag{1.13}$$

It is important to note that while this example models the background contribution as Raman scattering from another material, a similar effect could occur due to any other optical emission such as autofluorescence of the host material or the

target analyte itself. In that case, B would have a different mechanism that could be modeled by using a different effective cross section, incorporating all other contributions.

Now that we have a model for the signal intensity, we move to consider the noise in our model system. We assume the following noise factors in the system, each with a standard deviation associated with it: σ_s is the Raman shot noise, σ_b is the shot noise from autofluorescence and all other background Raman signals, σ_d and σ_r are dark noise (thermal) and readout noise, respectively, and σ_F is flicker noise[14].

Under the reasonable assumption that all noise factors are un-correlated random variables, their combined distribution can be modeled by Equation 1.14 which provided the total standard deviation in the system:

$$\sigma_{tot} = \sqrt{(\sigma_s^2 + \sigma_b^2 + \sigma_d^2 + \sigma_F^2 + \sigma_r^2)} \cong \sqrt{\sigma_s^2 + \sigma_b^2} \tag{1.14}$$

Advanced cooled detectors and cameras have exceptionally low thermal, flicker and readout noises, which allows to reach a shot-noise limited system. For example, a cooled Si CCD camera (Andor, Oxford Instruments) can have a readout noise of 6 electrons per pixel, and thermal noise (cooled to -20C°) lower than 0.015 electrons per pixel per second.

Shot noise, due to both the Raman signal and background contributions, follows a Poisson distribution[14,40,63] and given in Equations 1.15a and 1.15b, respectively:

$$\sigma_s = \sqrt{S} \tag{1.15a}$$

$$\sigma_b = \sqrt{B} \tag{1.15b}$$

Combining Equations 1.12, 1.13 and 1.15a, 1.15b we get:

$$\frac{S}{N} = \frac{S}{\sqrt{S+B}} = \left(\tau\eta T_x \int \left[\frac{\frac{\partial \gamma_a}{\partial \Omega} C_a}{\frac{\partial \gamma_a}{\partial \Omega} C_a + \frac{\partial \gamma_b}{\partial \Omega} C_b} \right] N_A \frac{\dot{n_p}}{A_s(z)} (A_D \Omega_D) dz \right)^{1/2} \tag{1.16}$$

A powerful conclusion from Equation 1.16 is that in a shot-noise limited system, the signal itself is the dominant cause of noise. Increasing the SNR for a given hardware system can be accomplished by increasing the excitation or by increasing the integration time.

Another common and efficient way to further enhance the SNR is by repeating the measurement K times, yielding an SNR increase of $\sqrt{K}$. This holds true only when the signal power is constant, and the noise is un-correlated with a constant variance, σ_{tot}^2, as is the case for shot-noise with a Poisson distribution. We assume the signal to be $\mathrm{S_i}$ for each i out of K measurements. We further assume the noise is $\mathrm{N_i}$ for each measurement so that the average signal $\bar{S}$ is:

$$\bar{S} = \frac{1}{K} \sum_{i=1}^{K} S_i = S \tag{1.17}$$

And the average noise is $\bar{N}$:

$$\bar{N} = \frac{1}{K} \sum_{i=1}^{K} N_i \tag{1.18}$$

The variance of a sum of uncorrelated random variables is the sum of variances since all cross-covariance terms cancel out so we can write:

$$Var(\bar{N}) = Var\left(\frac{1}{K^2} \sum_{i=1}^{K} N_i \right) = \frac{1}{K^2} K \sigma_{tot}^2 = \frac{\sigma_{tot}^2}{K} \tag{1.19}$$

Finding the Standard Deviation (SD) we take the square root of the Variance to get:

$$\bar{\sigma}_{tot} = \frac{\sigma_{tot}}{\sqrt{K}} \tag{1.20}$$

And finally plugging Equations 1.17 and 1.19 into Equation 1.8 and 1.16 we

get the SNR for K averages to be:

$$\text{SNR}=\frac{\bar{S}}{\bar{\sigma}_{tot}}=\frac{\sqrt{K}S}{\sigma_{tot}}=\left(K\tau\eta T_x\int\left[\frac{\frac{\partial\gamma_a}{\partial\Omega}C_a}{\frac{\partial\gamma_a}{\partial\Omega}C_a+\frac{\partial\gamma_b}{\partial\Omega}C_b}\right]N_A\frac{\dot{n_p}}{A_s(z)}(A_D\Omega_D)dz\right)^{1/2} \quad (1.21)$$

From Equation 1.21 it is possible to gain some fundamental understanding regarding the sensitivity of Raman systems; in a shot-noise limited system, the sensitivity is not linear with the signal but rather has a square-root dependency. A factor of 10 increase in any of the signal factors (excitation power, number of acquisition repetitions, étendue, integration time…), would enhance the sensitivity only by a factor of $\sqrt{10}$.

Practically, it is often quite challenging to measure or accurately estimate all of the parameters required for Equation 1.21, particularly for commercial systems which are enclosed and don't provide access to the internal optics. A common practical way to compare different systems' sensitivity is done by measuring the Limit of Detection (LOD).

The LOD is defined as the concentration (per specific analyte) for which the Raman signal is three times that of SD, $\bar{\sigma}_{tot}$, (i.e. SNR=3) [14]. Practically, measurement of the Raman spectra of several analyte concentrations in ranges similar to the expected LOD are performed. Each measurement is repeated K times to estimate $\bar{S}$, and $\bar{\sigma}_{tot}$ of the peak intensity (or the area under the peak) per analyte concentration. The selection of K is not arbitrary but rather meant to establish a reliable estimation of the noise SD.

In order to calculate the LOD, a linear fit of the peak signal intensity as a function of analyte concentration is calculated, often by the Classical Least Squares (CLS) method (see Section 1.6.2.3). Figure 1.9 shows the data for an LOD of a glucose-water solution with excitation power of 100mW at a wavelength of 830nm. The intensity of the strongest glucose Raman peak (at 1125 cm^{-1}) is plotted vs. the glucose

solution concentration (blue error bars). The measurement was repeated 50 times for each concentration, from which the mean, $\bar{S}$, and $\bar{\sigma}_{tot}$ are calculated. After a linear fit of the mean values is performed, the $3\bar{\sigma}_{tot}$ line is plotted above the background signal (red dashed line). The intersection of the $3\bar{\sigma}_{tot}$ line with the linear fit is the LOD concentration, corresponding to 7.6mmol/L of glucose in this example.

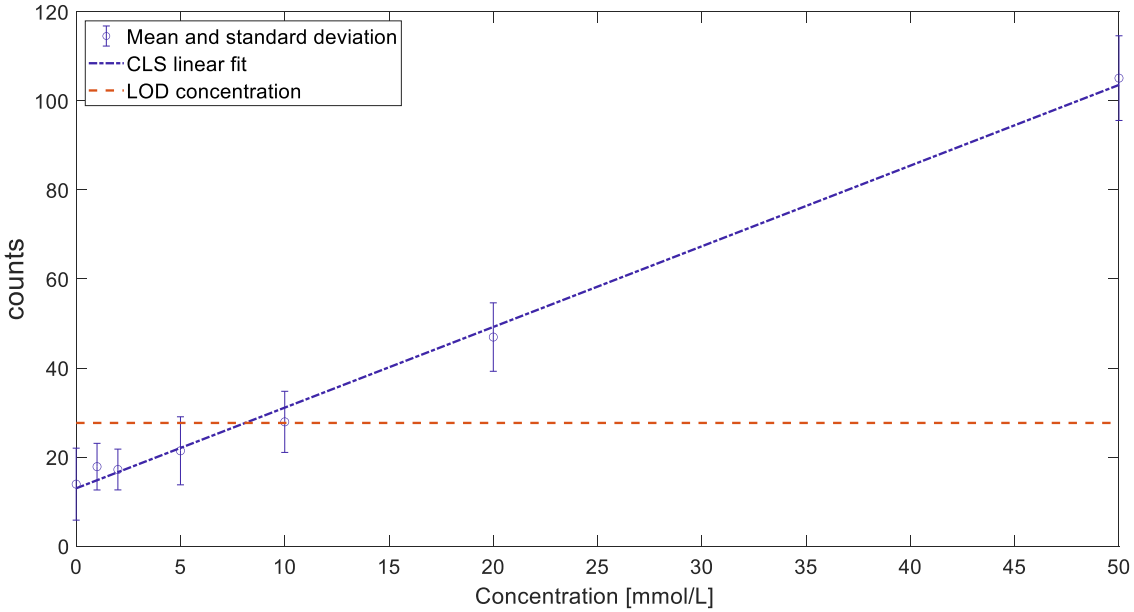

Figure 1.9: A plot of a glucose 3σ LOD measurement showing the glucose Raman peak (1125 cm^{-1}) mean intensity and STD vs. the concentration and the calculated LOD measured which shows the linear fit intersection with the 3σ line.

LOD can be used to benchmark a number of optical configurations for Raman spectroscopy[14,42,64], varying in their excitation wavelength, their footprint, optics for both excitation and collection, confocality, and many other design parameters [65–70]. In applications that have stringent environmental conditions such as in-vivo measurements, sterile environments, in-situ or submerged measurements, high pressure or temperature conditions, Raman fiber probes are widely used[70–72]. A review of the most common methods for spectral decomposition and signal detection with the goal of optimizing the SNR is given in 1.4, followed by a detailed review of Raman

probes design and applications in Section 1.5.

1.4 Spectral Acquisition and Detection Methods

Spectral acquisition methods divide into three main groups: Dispersive spectrometers, interferometric methods and Swept Source Raman (SSR). Before diving into a review of common spectral acquisition methods, it is worth noting two key definitions for étendue and spectral resolution. This will allow us to quantitatively compare the spectral acquisition methods with clear performance metrics.

1.4.1 Étendue

The French word *étendue* translates literally to the English word extent. In the field of optics, étendue is a measure of the extent of a beam of light in both area and solid angle. Alternative names for étendue include optical throughput and light-gathering power, but they are all one and the same since an optical system's ability to gather light translates into the extent of beams it can gather with an aperture A_D and acceptance angle Ω_D.

Étendue, G, is defined by Equation 1.22:

$$G = n^2 A\,(cos\,\theta)\Omega \tag{1.22}$$

Where n is the refractive index of the medium, A is the surface area or aperture with normal $\hat{n}_a$ and Ω is the acceptance solid angle through which light enters or exits the aperture at angle θ with normal $\hat{n}_a$, see Figure 1.10.

Assuming the light travels in air and propagates parallel to normal $\hat{n}_a$, i.e. $\theta = 0$, we get a simplified Equation 1.23:

$$G = A\Omega \tag{1.23}$$

The solid angle of a cone with apex angle 2φ is:

$$\Omega = 2\pi(1 - cos\,\varphi) \tag{1.24}$$

Many optical components and systems, including optical fibers, lenses, and spectrometers often specify their acceptance angle using Numerical Apertures (NA) which is defined in Equation 1.25:

$$NA = nsin\,\varphi \tag{1.25}$$

For small angles we approximate $cos\,\varphi \approx 1 - \varphi^2/2 \approx 1\,, sin\,\varphi \approx \varphi$ and conveniently re-write the throughput as follows:

$$G = A \cdot \pi(NA)^2 \tag{1.26}$$

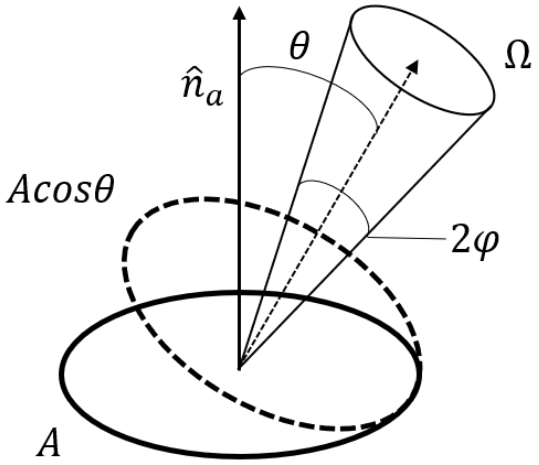

Figure 1.10: Geometrical illustration of surface (or aperture), A, emitting or reflecting a beam of light which is confined to a solid angle Ω, at an angle θ with the normal n_a.

Étendue is conserved in passive ray-optical systems[73]. This conservation is also called the Brightness Theorem[74] or Radiance Theorem[75] , or alternatively the "you can't smoosh light theorem"[76]. The conservation can be derived from thermodynamic considerations[77,78] or from Hamiltonian mechanics (Liouville's theorem)[79,80]. Effectively, for optical systems the conservation takes a form limiting the ability to concentrate light into a spot or collimate light to a perfectly parallel beam. The use of lenses can focus a beam of light but as shown from Equation 1.22 that would require the solid angle to compensate for the change in beam size.

Figure 1.11 illustrates an example where light is emitted from aperture A_1 positioned at the focal length of lens L_1 with focal length f_1. The light is emitted with solid angle Ω_1. For 2D representation, we take the half cone angle of $\Omega_1$to be θ_1. An intermediate image of the aperture A_2 with radius r_2 is created. The light is then focused by lens L_2, with focal length f_2, creating an image A_3. We assume a thin lens approximation as well as a paraxial approximation, i.e. small angles in which $tan\,\theta \approx \theta$.

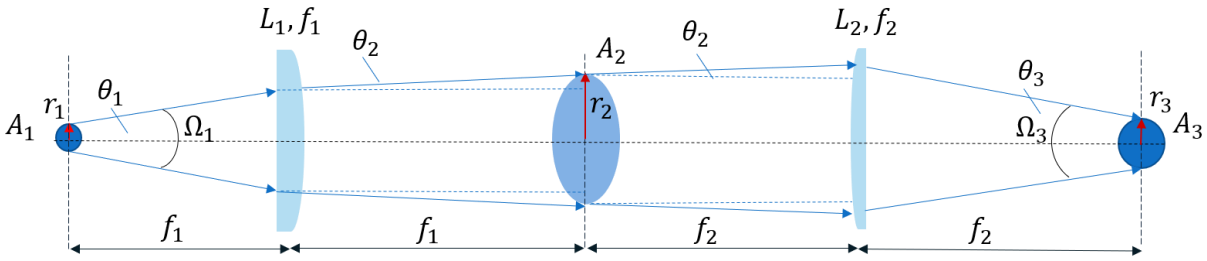

Figure 1.11: An illustration of a collimation an focusing setup from a light source A_1, being collimated by lens L_1 and then focused down to a spot size A_2 by lens L_2 demonstrating étendue conservation. The results are derived under the thin-lens and paraxial propagation approximations.

For an extended incoherent source with a finite size, such as A_1, the divergence angle after collimation can be shown to be:

$$\theta_2 = \frac{r_1}{f_1} \tag{1.27}$$

Since optical systems are reciprocal, the same can be said for lens L_2 so that

$$\theta_2 = \frac{r_3}{f_2} \tag{1.28}$$

Combining Equations 1.27 and 1.28 we get:

$$\frac{r_1}{r_3} = \frac{f_1}{f_2} \tag{1.29}$$

From geometrical considerations we can also show that:

$$r_2 = f_1\, tan(\theta_1) \approx f_1\theta_1 \tag{1.30}$$

And additionally, that:

$$r_2 = f_2\theta_3 \tag{1.31}$$

Combining Equations 1.30 and 1.31 we get

$$\frac{\theta_3}{\theta_1} = \frac{f_1}{f_2} \tag{1.32}$$

And finally, we see from Equations 1.29 and 1.32 that:

$$r_1\theta_1 = r_3\theta_3 \tag{1.33}$$

Returning to the 3D scenario, according to Equations 1.23, and 1.24, we get:

$$A_1\Omega_1 = A_3\Omega_3 \tag{1.34}$$

Showing that the étendue of this system is indeed conserved and poses a limitation on our ability to gather and collect light.

Generally, the Brightness Theorem can be shown to be applicable to arbitrarily complex optical systems, implying that the light collection of the entire system is determined by the component with the lowest étendue value. This value, $\mathrm{G} = \mathrm{A_D}\Omega_\mathrm{D}$, (see Equation 1.2) sets the maximal bound of the system's light collection efficiency.

1.4.2 Spectral Resolution

Raman spectral lines naturally take the shape of a Lorentzian[41,81], see Equation 1.35, which can be derived by using a damped harmonic oscillator model for the molecular vibrations[41,82,83]:

$$L(\nu) = L_0\frac{\nu_L^2}{(\nu - \nu_{L0})^2 + \nu_L^2} \tag{1.35}$$

Where $\mathrm{L_0}$ is the Lorentzian's maximal value, ν_{L0} is the wavenumber for which the Lorentzian is at its' peak, and ν_L is the Full Width Half Maximum (FWHM) point, for which $\mathrm{L}(\nu_L) = \frac{1}{2}L(\nu_{L0})$.

Due to thermal effects or vibrational relaxation (in liquid solutions), there is usually a Gaussian broadening of the linewidth[84,85]. Equation 1.36 gives a Gaussian

function where Γ_0 is the maximal value, $\nu_{\Gamma 0}$ is the expected value and where the Gaussian is at its' peak, and ν_σ is the standard deviation.

$$\Gamma(\nu) = \Gamma_0 exp\left[-\frac{1}{2}\left(\frac{\nu - \nu_{\Gamma 0}}{\nu_\sigma}\right)^2\right] \tag{1.36}$$

Additionally, the instrumentation itself has a finite spectral resolution and so the Raman linewidth is further broadened. Both the sample and the instrumentation broadening results in a Voigt line shape[82,86,87] which is the convolution of a Lorentzian and a Gaussian. Equation 1.37 gives the convolution for a case where the Gaussian broadening is symmetrical with the Lorentzian peak location, i.e. $\nu_{\Gamma 0} = \nu_{L0} = \nu_0$:

$$\Gamma * L = \int_{-\infty}^{\infty} L_0 \frac{\nu_L^2}{(\nu - \nu' + \nu_0)^2 - \nu_L^2} \Gamma_0 exp\left[-\frac{1}{2}\left(\frac{\nu' - \nu_0}{\nu_\sigma}\right)^2\right] d\nu' \tag{1.37}$$

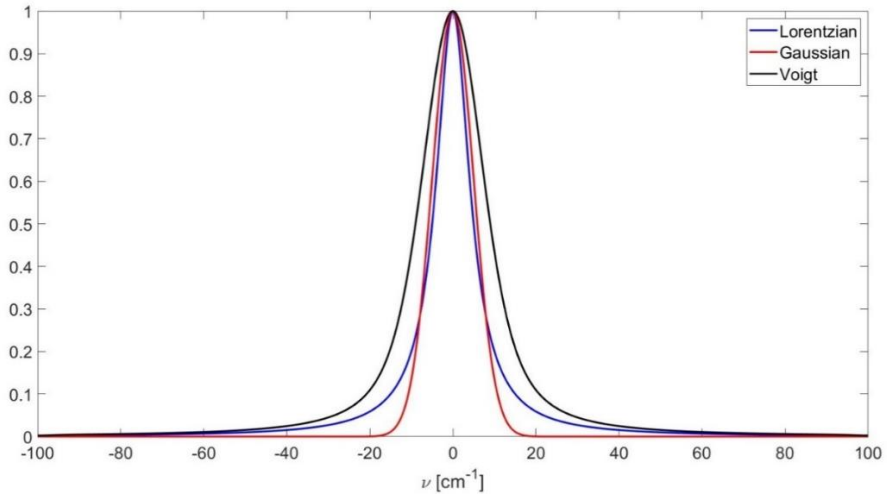

Figure 1.12: A normalized Lorentzian line shape (blue), centered around $\nu = 0$, with a FWHM of 5 cm^{-1}, compared with a normalized Gaussian, centered around $\nu = 0$ with a SD of 5 cm^{-1} (in red) along with their normalized convolution resulting in a Voigt line shape (black).

Figure 1.12 shows a Lorentzian with $L_0 = 1, \nu_0 = 0$ and $\nu_L = 5cm^{-1}$ (blue) and a Gaussian with $G_0 = 1, \nu_0 = 0$ and $\nu_\sigma = 5cm^{-1}$(red). Their convolution, resulting in a Voigt line shape and normalized to 1, is given in black.

In mixtures and complex materials, there are often close and overlapping

Raman spectral lines in addition to various background signals such as fluorescence, resulting in complex spectra. Resolution is a measure of how close two different spectral lines can be but still be differentiated as separate signals[44,88]. Furthermore, resolution is subject to various definitions.

While the relation is not always intuitive or straight forward, in many Raman spectroscopy systems there is a tradeoff between the étendue and the spectral resolution. These tradeoffs will be discussed in the following Subsections, detailing common Raman spectral acquisition instruments.

1.4.3 Dispersive Methods

Spectral decomposition by a dispersive element spectrometer is by far the most common method used for spectral detection[14,88]. There are a few possible dispersion elements such as prisms but diffraction-grating spectrometers are predominantly used[40,88].

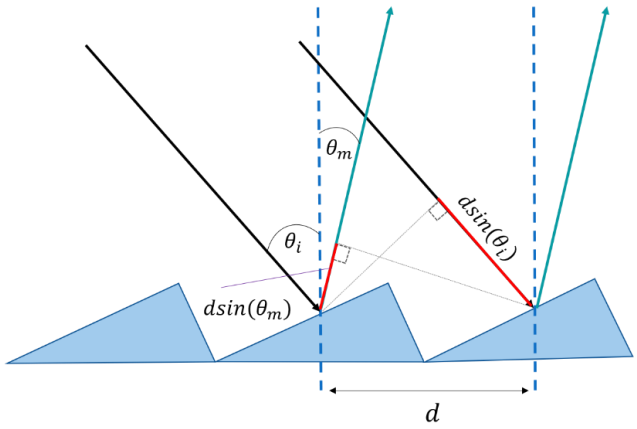

Figure 1.13: A schematic diagram of an echellette diffraction grating by which the optical path difference between adjacent grooves determines the constructive or destructive interference which is wavelength dependent, creating the diffraction pattern on the detector plane.

There are many types of gratings; holographic, echelle, grisms, concave, and

transmission gratings, to name a few[89]. While these gratings operate in slightly different ways, they achieve a dispersion of an incoming polychromatic beam of light into its constitutive wavelengths.

Figure 1.13 is a schematic illustration of an echelle diffraction grating, which is grooved (or blazed). The angled reflections from each of the broad faces allows interference among the reflected beams to occur. Equation 1.38 describes the condition for constructive interference per a specific wavelength, λ. m is the diffraction order, and d is the distance between neighboring grooves [40,89].

$$m\lambda = d(sin\theta_i - sin\theta_m) \tag{1.38}$$

The number of groves per millimeter and their angle determines the spectral range on the spectrometer's focal plane, which is set to coincide with the detection pixel array[14,44].

There are many spectrometer designs based on a single-grating geometry but the Czerny-Turner configuration, shown in Figure 1.14, is particularly popular. In this design there are two mirrors, acting as a collimator and as a focusing element. This design often houses several gratings on a rotating motor, providing flexibility in selecting both the spectral range and the resolution. Czerny-Turner is considered preferable since it also minimizes internal reflections, and generally suffers from less stray light[14,89]. Since this design is very common, it is beneficial to use it to demonstrate the resolution-étendue tradeoff.

As seen in Figure 1.14, the light enters the spectrometer through an input slit which has height h_s and width w_s. The height of the slit is usually fixed to accommodate the finite size of the detection pixel array. The width, however, can be adjusted to allow various inputs and determine resolution. The spectrometer's étendue, G_s, is therefore $G_s = \pi w_s h_s (NA)^2$ as shown in Equation 1.26. The spectrometer's NA is determined by the optical components and the light that can

effectively be focused onto the detector pixel array.

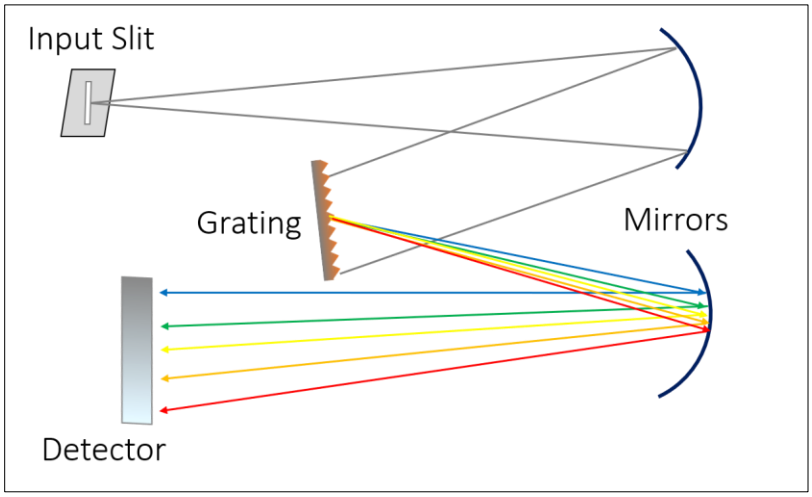

Figure 1.14: A diagram of a dispersive single-grating spectrometer in the Czerny-Turned configuration where light enters the spectrometer through a slit, and then collimated using the first concave mirror to hit the grating. The diffracted light is then refocused onto the detector using the second mirror.

The theoretical spectral resolution (FWHM) in Czerny-Turner spectrometers can be approximated by Equation 1.39 if we consider we need at least 3 pixels to detect the spectral resolution[14,44,90,91]:

$$\delta\lambda \cong RF\frac{\Delta\lambda w_s}{Mw_p} \tag{1.39}$$

Where $\Delta\lambda$ is the spectral range of the spectrometer (dependent on the spectrometers focal length, dimensions and the specific grating used), w_p is the pixel width, M is the number of pixels in the detector array (in the dimension parallel to the beam dispersion), and RF is a resolution factor which is determined by the ratio of the slit width and pixel width[90]. From Equation 1.39 it can be shown that the larger the slit width, w_s, the worse the spectral resolution becomes. If we were to fix the slit width and grating, and require greater resolution, only enlarging the spectrometer's focal length and physical size could accomplish this goal.

Figure 1.15 shows a simulation of the étendue-resolution tradeoff for a

benchtop spectrometer (Acton SP-300i) with a 300mm focal length and 0.13 NA. The spectrometer's étendue changes with the slit's opening and corresponds to a worsening of the spectral resolution (assuming a single fiber input, dashed blue line). A red circle marks the theoretical highest achievable resolution, ~2 cm^{-1}, as specified by the spectrometer specifications (corresponding to 0.1 nm at 830nm with a 1200g/mm grating).

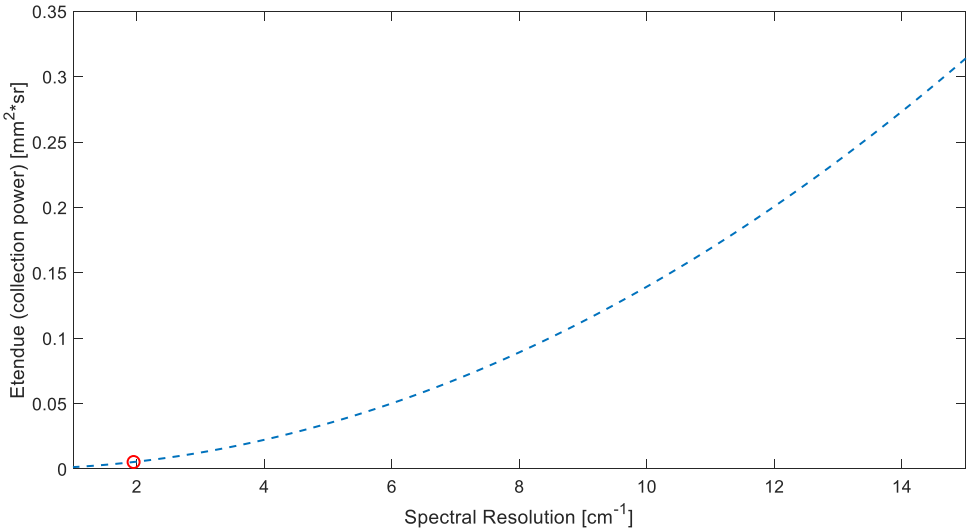

Figure 1.15: Simulated étendue-resolution tradeoff resulting for a dispersive spectrometer with a 300mm focal length, NA=0.13 (blue dashed line) and the performance of a 200µm slit width setting (red circle) with a collection power of 0.013mm^2/sr.

Minimizing dispersive spectrometers and making them more compact, comes with a performance cost and non-trivial fabrication complexity[24,92]. Other spectroscopy detection methods, which are less sensitive to physical size, are more easily adapted to compact footprints.

For interferometric and SSRS spectral acquisition methods, the resolution and étendue are determined by other system parameters which is given in Appendix A. The various detectors used for both dispersive, interferometric and Swept Source are given in Appendix B.

1.4.4 Swept Source Raman Spectroscopy

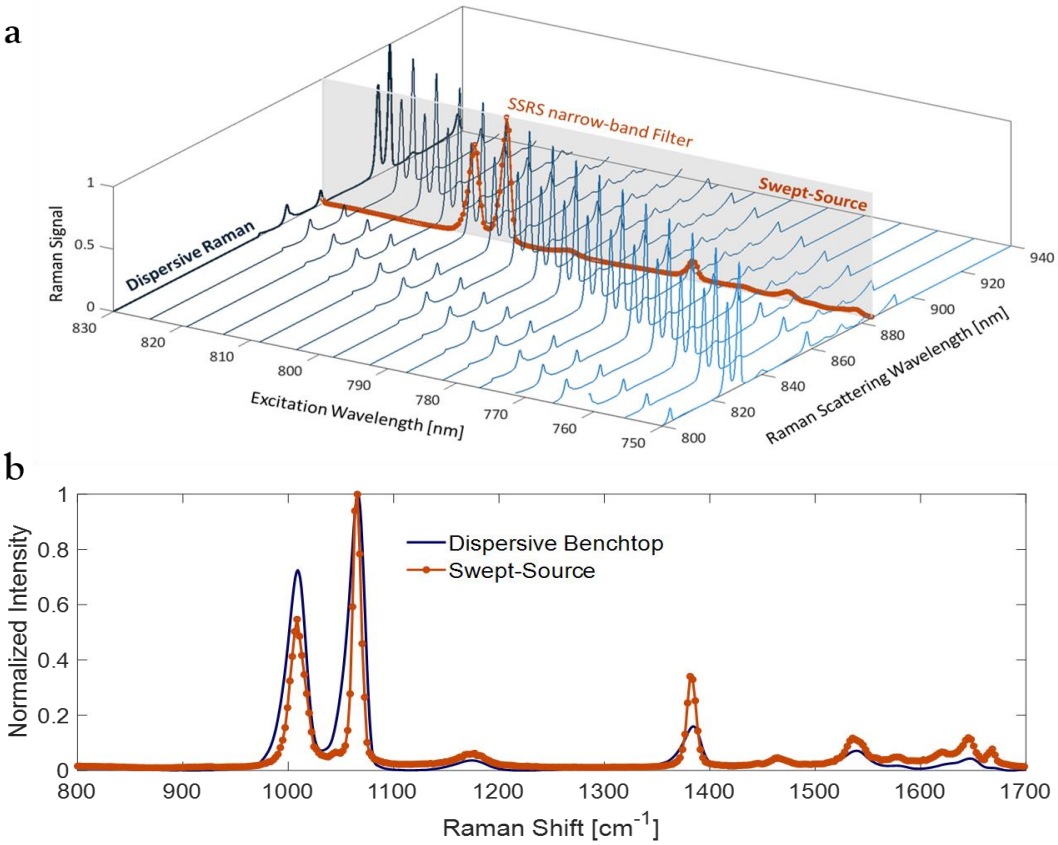

Figure 1.16: a) A diagram illustrating the operation of SSRS. A different segment of the Raman spectrum is detected as the laser excitation tunes and the scattered photons are detected through a narrow optical filter with a fixed wavelength. b) A comparison of SSRS spectrum and one acquired with a liquid nitrogen cooled benchtop system 830nm excitation and 150mW of a mixture of urea and sodium nitrate.

Swept Source Raman Spectroscopy (SSRS)[36] is based on the use of a tunable laser that replaces the fixed wavelength laser for excitation. The detection of spectra is accomplished by using a large area photodetector and an optical Ultra Narrow Band Filter (UNBF) that is mounted in front of the detector, see Figure 1.2. As the laser tunes, the Raman scattering shifts relative to the excitation, and the fixed wavelength filter detects a different segment of the spectrum.

Figure 1.16a illustrates the SSRS mode of operation. The blue spectra are those

acquired with a dispersive system at several fixed excitation wavelengths from 750 to 830nm. The SSRS UNBF has a central wavelength of 884nm and a FWHM of 0.45nm, represented by a semi-transparent screen. The data acquired by the SSRS photodetector is overlaid on the filter screen, in orange, showing how with the tuning of the excitation, the complete spectrum is acquired.

Figure 1.16b compares the final normalized spectra of a urea and sodium nitrate mixture, acquired with the SSRS and that of an 830nm, liquid nitrogen cooled, dispersive system. Importantly, the SSRS spectrum has not been corrected to account for the varying Raman scattering intensity, as predicted by Equation 1.6 and so the longer wavenumber region appears elevated compared with that of the dispersive system. By removing the spectrometer from the loop, SSRS offers a significant, if not complete, decoupling of the throughput and spectral resolution, similar to that of FT-Raman and SHRS, but without the complexity of added interferometry.

In SSRS, the spectral range is determined by the tuning range of the laser and the wavenumber is determined by the difference between the excitation wavelength, λ_{ex} and the UNBF central wavelength, λ_{UNBF}. Equation 1.40 gives the SSRS wavenumber:

$$\nu(\lambda_{ex})[cm^{-1}] = 10^7 \left(\frac{1}{\lambda_{ex}[nm]} - \frac{1}{\lambda_{UNBF}[nm]}\right) \tag{1.40}$$

The SSRS spectral resolution depends solely on the UNBF. The FWHM of the filter sets the hardware resolution limit. FP filters have a Lorentzian transfer function, as can be shown from Figure 1.17, showing the data from an 884nm PF interference filter with a FWHM of 0.448nm (specified as 0.45nm by the manufacturer, Alluxa Inc.).

The étendue in SSRS is dependent upon the optical components used in the Raman collection path. Particular attention is given to the UNBF and the

photodetector: If a large area detector is used, and a filter that has a large area and a large acceptance angle, as was done by Atabaki et al. [36], see Figure 1.18, then a 1000 fold throughput enhancement compared with a dispersive spectrometers can be achieved. The filter technology is therefore of the utmost importance as it could present the throughput bottleneck of the system.

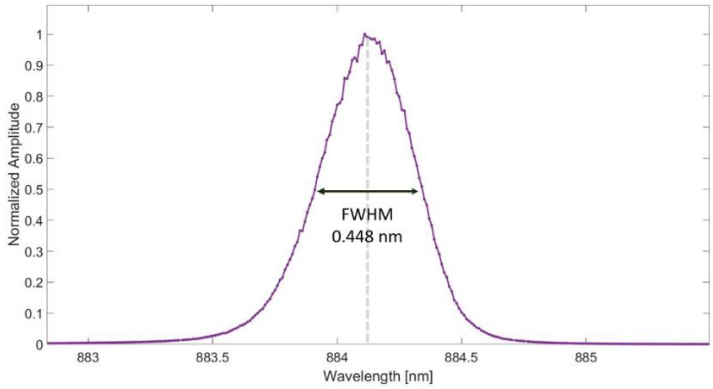

Figure 1.17: Normalized Lorentzian transfer function of an 884nm FP interference filter used as the UNBF in the SSRS system showing the measured FWHM of 0.448nm (specified by the manufacturer as 0.45nm)

In order to calculate the étendue of the UNBF, we need to know both the aperture area and NA (see Equation 1.26). The first is straight forward but the latter requires some consideration. The central wavelength of FP interference filters shifts with the angle of incidence, θ, according to the following equation:

$$\lambda_f^* = \lambda_{UNBF}\sqrt{1-\left(\frac{n_0}{n_{eff}}sin\theta\right)^2} \tag{1.41}$$

Where λ_{UNBF} is the central wavelength of the filter at $\theta = 0$, λ_f^* is the shifted central wavelength and $\mathbf{n_{eff}}$ is the effective refractive index of the filter. To find the acceptance angle of the filter, we calculate the incidence angle for which the shifted wavelength is no longer within the FWHM of the filter around $\boldsymbol{\lambda_{UNBF}}$. For a filter centered at 884nm, with a FWHM of 0.45nm and n_{eff}=1.58, the acceptance angle is 2.04 degrees while for a FWHM of 0.75 the acceptance angle is 2.08 degrees.

From these results it's evident that the NA (and étendue) of the UNBF does depend on the spectral resolution, but is not inversely proportional (as for dispersive systems). The use of Fabry-Perot (FP) interference filters guarantees relatively low sensitivity to the light incidence angle, and therefore SSRS has a performance advantage over dispersive spectrometers and Michaelson interferometers.

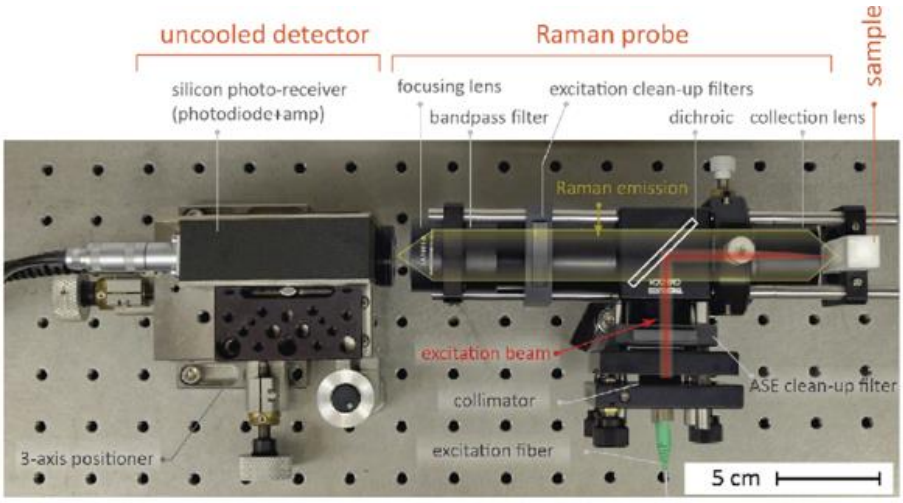

Figure 1.18: A SSRS free-space setup: The input excitation light is collimated and filtered using a short pass filter. The beam is diverted using a LP dichroic beam splitter. The light is focused onto a sample placed in a quartz cuvette The back-scattered Stokes-shifted Raman photons pass the dichroic where the thin-film interference UNBF filtere allows only a small fraction of the photons through. The passing photons are detected using a large-area uncooled silicon detector (reproduced from [36]).

Figure 1.19, reproduced from [36] compares the étendue-resolution tradeoff of dispersive, FT, and SSRS systems. The black arrow shows the performance of the free-space SSRS system, using a 1mm diameter silicon photodetector (Femto, GmbH) and a 25mm diameter UNBF centered around 935nm with a FWHM of 0.45nm.

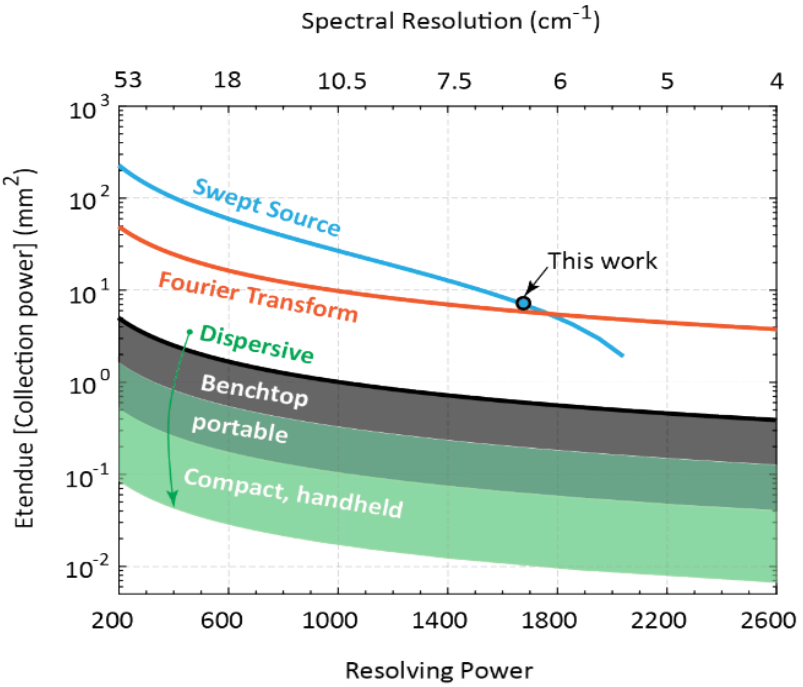

Figure 1.19: SSRS collection power vs. the resolving power and spectral resolution compared with those of both dispersive and Fourier transform spectrometers (reproduced from [36])

1.5 Raman Spectroscopy Fiber Probes

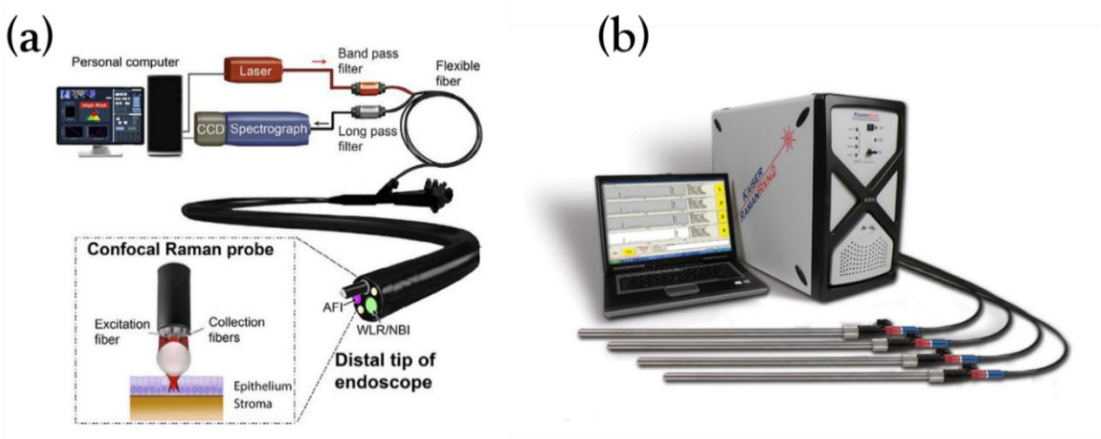

Figure 1.20: (a) An endoscope system which contains a Raman probe for real-time in-vivo imaging and (b) A commercial Kaiser Raman RXN4 4-probe system for bioreactor monitoring using 400mW of power at 785nm and switched channel operation

Raman fiber probes are portable, miniaturized Raman optical setups that

replace the large, benchtop optical ones and allow measurements in challenging conditions such as in-situ inside a bioreactor[17,93,94] or integrated into a catheter or endoscope for in-vivo measurements[68,70,95,96]. They often out-perform hand held Raman devices since they guide the light back to a benchtop spectrometer with enhanced resolution.

An added benefit of probes is the ability to customize them to various configurations and measurement conditions, also integrating other sensing modalities such as Optical Coherence Tomography (OCT)[68,97,98], or fluorescence and other imaging modalities[60,99]. Figure 1.20 (reproduced from [95]) shows (a) an endoscope incorporating a confocal Raman fiber probe and (b) a commercial Kaiser Raman Rxn2 system (Endress and Hauser) with four probes meant for bioreactor monitoring.

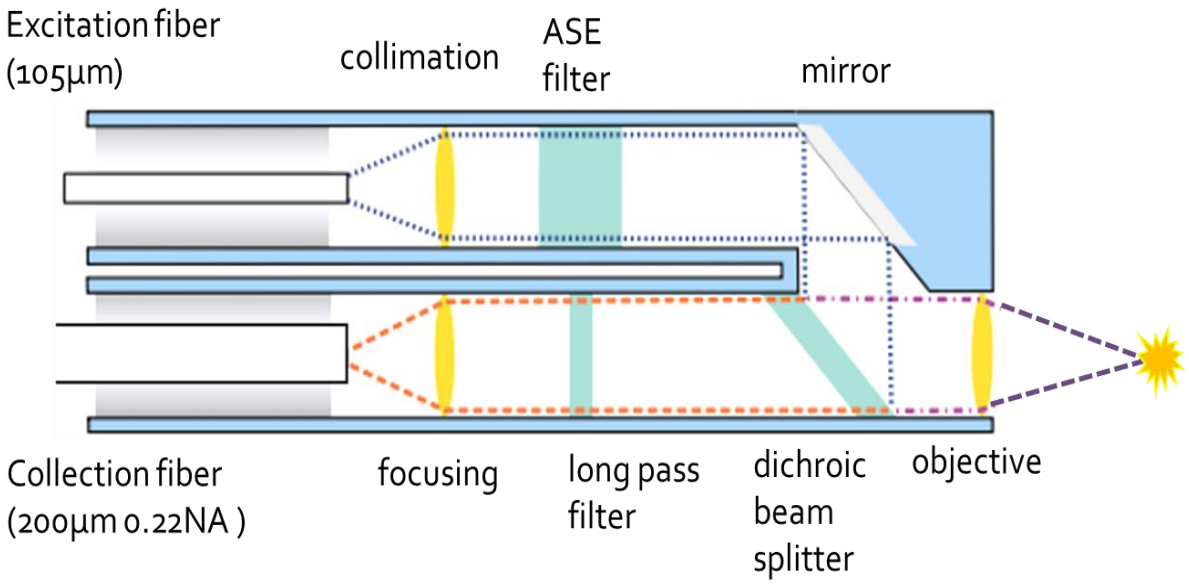

Figure 1.21: A diagram of a basic dispersive Raman fiber probe. The fixed-wavelength light is collimated and filtered to remove ASE. A combination of a mirror and a LP dichroic beam splitter divert the light onto the sample and allows the back-scattered Stokes-shifted photons to pass. The light is then passed through a long pass filter to remove residual excitation after which it is focused into the collection fiber which is matched to the spectrometer input slit.

Raman fiber probes deliver excitation light onto a sample and then collect and guide the Raman scattered light back through an optical fiber to a spectrometer for detection. The need to guide the Raman light back to the spectrometer dictates the entire design of the probe.

Figure 1.21 shows a diagram of a traditional Raman probe. On the excitation side, light enters the probe and passes through a narrow ("Linewidth") optical filter that allows a single laser wavelength while attenuating Amplified Spontaneous Emission (ASE) from the laser source. A short-pass dichroic beam splitter allows the excitation to pass to the objective and onto the sample. The Stokes-shifted backscattered Raman light is collected through the same objective and passed through the dichroic into the collection path. An additional long pass filter further attenuates any residual excitation light and the beam is then focused into the collection fiber. Notably, some probes have completely separate optical paths for excitation and collection, particularly probes designed for Spatially Offset Raman Spectroscopy (SORS), which has benefits in highly diffusive and scattering samples[100,101].

The collection fiber is chosen to match the étendue of the spectrometer, thus limiting its' core diameter and NA. In most benchtop dispersive spectrometers, see Section 1.4.3, a slit width guaranteeing sufficient spectral resolution is between 100-200μm, posing an upper bound on the fiber core diameter. Additionally, as spectrometers usually have fairly low NA values, ranging between 0.1-0.2, any fiber with a higher NA would result in light missing the detector leading to reduced SNR.

Since the signal collection is limited using a single fiber, it is quite common to use fiber bundles, comprised of anywhere between 7-64 fibers, to increase the collection area[19,66,70,102]. In order to detect the signal from all fibers, they are stacked, using the vertical dimension (height) of the spectrometer slit. Figure 1.22 shows the image captured on a spectrometer detector array with a 7 fiber-bundle input. The total

spectrum is computed via the summation of the vertical pixels in the array.

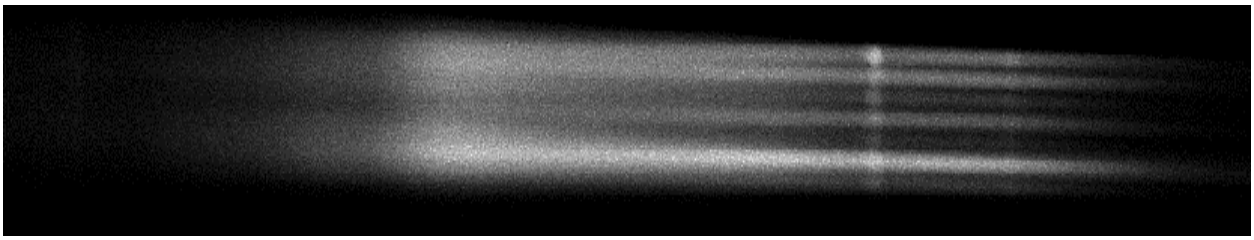

Figure 1.22: An image created on the spectrometer's detector plane when spectra is collected with a 7-fiber 200μm diameter core bundle. The vertical dimension of the slit is used to house the bundle while maintaining the slit width and corresponding resolution. This configuration allows to enhance collection but makes the use of simultaneous input detection impossible.

Spectrometer detector arrays are, however, limited in size. When multiple fibers are used for a single probe, the spectrometer cannot be used for additional probes, limiting the operation to a single sensor at-a-time. The multiplexing of multiple signal channels comes at the expense of SNR, or by switching inputs, which does allow multiple probes operation, but not simultaneously.

Étendue, however, is not the only limitation of the standard probe collection fibers. 100 and 200μm core fibers are not communication-grade fibers and they suffer from high attenuation, T_x, of 8dB/km (at 808nm)[103]. Since these fibers guide the already weak Raman scattered light, they must be limited in length to maintain SNR. There have been limited reports of long fiber probes, 100[104,105] and 1000[106] meters long, but these used laser sources with 1.25-2.5W output powers to compensate for the signal loss. Commercially available Raman probe systems limit the fiber length to 5-10 meters in order to minimize signal attenuation.

In summary, Raman probes offer many advantages and enable Raman measurements to be conducted in extreme conditions robustly and reliably. However, they are limited in both deployment distances and numbers due to the need to guide the collected light back to a spectrometer for detection and cannot be significantly

scaled up with traditional Raman spectroscopy instrumentation.

1.6 Chemometrics: Spectral Signal Processing and Analysis

Previous sections of this chapter described various hardware systems used in order to excite, collect and detect Raman spectra. However, acquiring spectra is only the first step, followed by the application of chemometric methods. Chemometrics is the term used for the various signal processing and analysis methods that detect and extract multivariate information from Raman spectra and other spectroscopy methods[107].

The first step in chemometrics is signal processing that ensures that the spectra is "clean" and ready for the analysis step. Common signal processing procedures include various filters and background removal algorithms which help to reduce noise and enhance the desired spectral features. In FT-Raman an additional mandatory step is of course a Fourier transform that produces the spectrum from the interferogram.

In SSRS the spectral acquisition is performed without a spectrometer and with tunable excitation, fundamentally changing the sample fluorescence response and instrumentation-related artifacts. While these things result in different spectral features, similar approaches to those used for dispersive and FT-Raman can be applied, while adjusting their parameters (filter order, bandwidth, etc').

The majority of spectral analysis work, however, is the application of algorithmic methods to calibrate, classify, quantify, and predict multiple analyte concentrations in the sample in a reliable and robust manner.

The following sections will give an overview of common signal processing steps of dispersive spectra (or post FT spectra), followed by a brief summary of spectral

analysis methods with key examples, and conclude with feature selection techniques that optimize predictive models.

1.6.1 Spectral Signal Processing

Raman spectroscopy systems are designed to enhance signal and reduce noise; however, the high sensitivity of the detectors introduces susceptibility to noise factors such as inter-pixel responsivity variations and cosmic rays.

Cosmic rays are high energy particles, mostly atomic nuclei arriving from space and travelling at velocities close to the speed of light[108]. Cosmic rays create spuriously positioned narrow peaks on top of the Raman spectrum. Figure 1.23a shows unprocessed 50 water spectra acquired with a liquid nitrogen cooled spectrometer where the cosmic rays are visible in some of the measurements. Cosmic ray related peaks are often only a single pixel wide and are removed using a 3rd order median filter or a 2D Laplacian filter[107] operating on the same pixel of consecutive spectral acquisitions. Since SSRS operates with a single pixel detector, cosmic ray events are rare, but do occasionally create signal peaks that are uncorrelated with excitation or sample and are therefore removed using a conditional 3rd order median filter that operates for spurious outlier peaks.

An additional filtering step is performed to smooth features that are below the spectral resolution limit. A common method is the Savitzky-Golay (SG) filter[109], which is a local least squares method. The advantage of SG is that it does not introduce delays (i.e. peaks do not shift) and it handles some degree of missing data well. Figure 1.23b shows a segment of water spectra before and after it has been smoothed by a SG filter. The inter-pixel variability along with detector reflection create the semi-periodic noise. The filter parameters - 2nd order polynomial with a span of 11 pixels in the filter

window- are chosen to smooth out any features that are below the spectrometer's resolution limit (2-3 cm^{-1} in this particular case), but these need to be modified depending on the spectrometer, grating, and often the sample itself, due to spectral broadening (see Section 1.4.2).

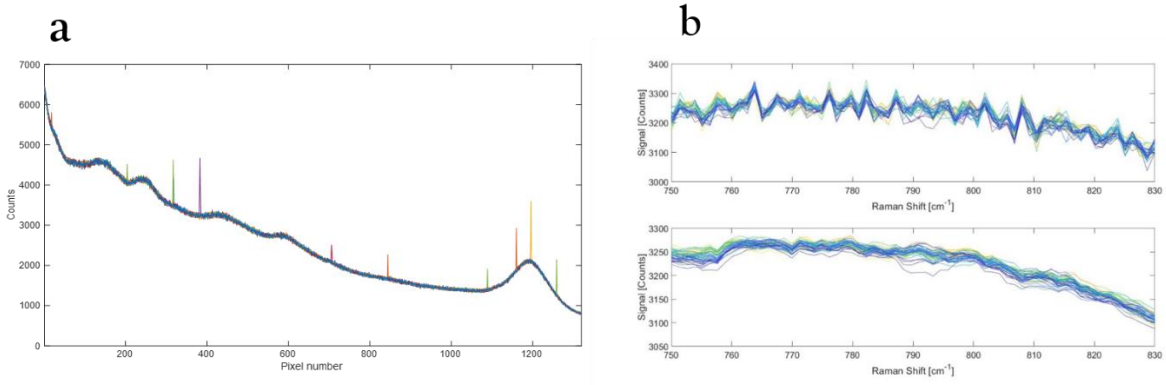

Figure 1.23: a) Unprocessed Raman spectra of water acquired with a benchtop liquid nitrogen cooled spectrometer showing spurious cosmic ray peaks. **b)** Top- raw partial spectra of water before smoothing and bottom- smoothed spectra using a 2nd order, 11th degree Savitzky-Golay filter which account for inter-pixel variability in the detector.

Particularly for the case of SSRS, both the span and order of the filter need to be tailored for the UNBF to filter laser excitation variations while leaving the Raman features intact. There are alternative techniques that accommodate more sparsely sampled data or introduce regularization that controls the roughness of the smoothed spectra[110–112].

Once data had been smoothed, the signal and noise are estimated from the complete set of K spectral acquisitions (see Section 1.3.2, Equations 1.17-1.20). The signal, $\bar{S}$, is computed from the arithmetic mean of the spectra. Let Y_i be the measurement value and $i = [1{:}K]$ is the spectral repetition number then the signal (including background) is:

$$\bar{S} \cong \bar{Y} = \frac{1}{K}\sum_{i=1}^{K} Y_i \tag{1.42}$$

In some cases, a weighted mean can be used, where the weights are normalized power measurements of the excitation laser, correcting for fluctuations and drift.

The noise $\bar{\sigma}_{tot}$ is estimated from the standard deviation of the measured spectra. However, since we only have access to the noise process sample and not the entire population, we use the formula for corrected sample standard deviation:

$$\bar{\sigma}_{tot} \cong \sqrt{VAR(Y)} = \sqrt{\frac{1}{K-1}\sum_{i=1}^{K}(Y_i - \bar{Y})^2} \tag{1.43}$$

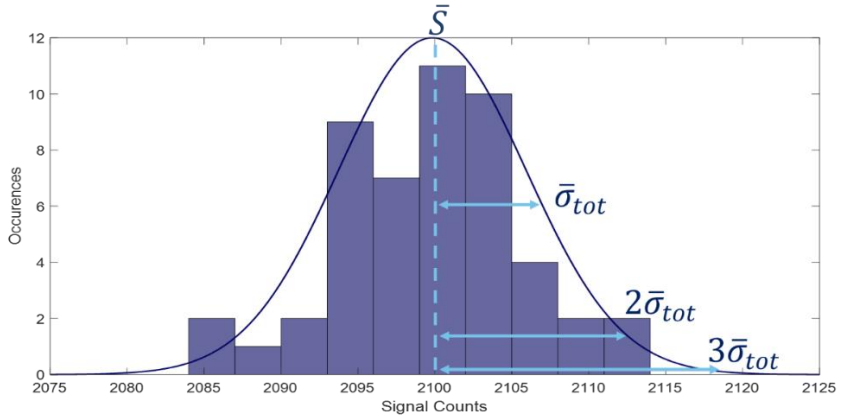

Figure 1.24: A histogram of the Raman water peak (1640cm^{-1}) signal counts when repeated 50 times. A gaussian fit centered on the signal counts mean and with the computed STD is overlaid which represent the signal and noise estimation.

Figure 1.24 shows a histogram of the Raman water peak signal (1640 cm^{-1}). The signal mean and standard deviation are calculated as described in Equations 1.42 and 1.43 and a Gaussian fit with those parameters is overlaid on the histogram to show the signal and noise estimations based on the measurement distribution.

Background removal methods are used when there is a significant fluorescent background or Raman spectrum from the sample itself, the sample holder, or the optical components in the system (see Figure 1.25a). Algorithmic techniques are used to enhance the Raman features but the shot noise emanating from the background signal cannot be removed. Hardware methods for removing fluorescence signals exist

but these require significant system modifications such as time gating, SORS, and are outside the scope of this thesis[113–115].

If possible, the spectrum of an empty sample holder or one with the analyte matrix (and no analyte) is subtracted from the spectrum containing the analyte. This measurement is also useful for self-calibration. Figure 1.25a shows the spectra of various glucose solutions used for the LOD measurement and one sample of water (Figure 1.23). Figure 1.25b shows the glucose solutions spectra after the water spectrum has been subtracted. The main glucose peaks (800-1500cm^{-1}) are visible and the water Raman peak is no longer present. When it is not possible to have a pure background measurement, algorithmic methods are used to remove the background signal. Raman peaks have higher spectral variation (see Section 1.4.2) than fluorescence, and so a frequency-based separation of signals is possible.

The Lieber[116] algorithm is an iterative method that performs automatic polynomial curve fitting based on least squares and then removes the lower order components. The order of the polynomial is chosen to remove as much of the background without sacrificing the Raman features. Additionally, it is preferable to truncate the spectra before applying the Lieber fit since the filter does poorly with zero values at the spectral edges. Figure 1.25c shows the result of a 6^{th} order Lieber polynomial fit over 200 iterations applied to the raw glucose solution spectra in Figure 1.25a in the range of 400-1700cm^{-1}. The result shows that some residual fluorescence background remains but the Raman glucose peaks are clearly visible compared with the raw spectra in Figure 1.25a. The glucose double-peak structure (1000-1200 cm^{-1}) is better accentuated in the water subtraction (Figure 1.25b) than with the Lieber fit due to a spectrometer artifact that overlaps with the peaks and is only partially removed with the polynomial fit.

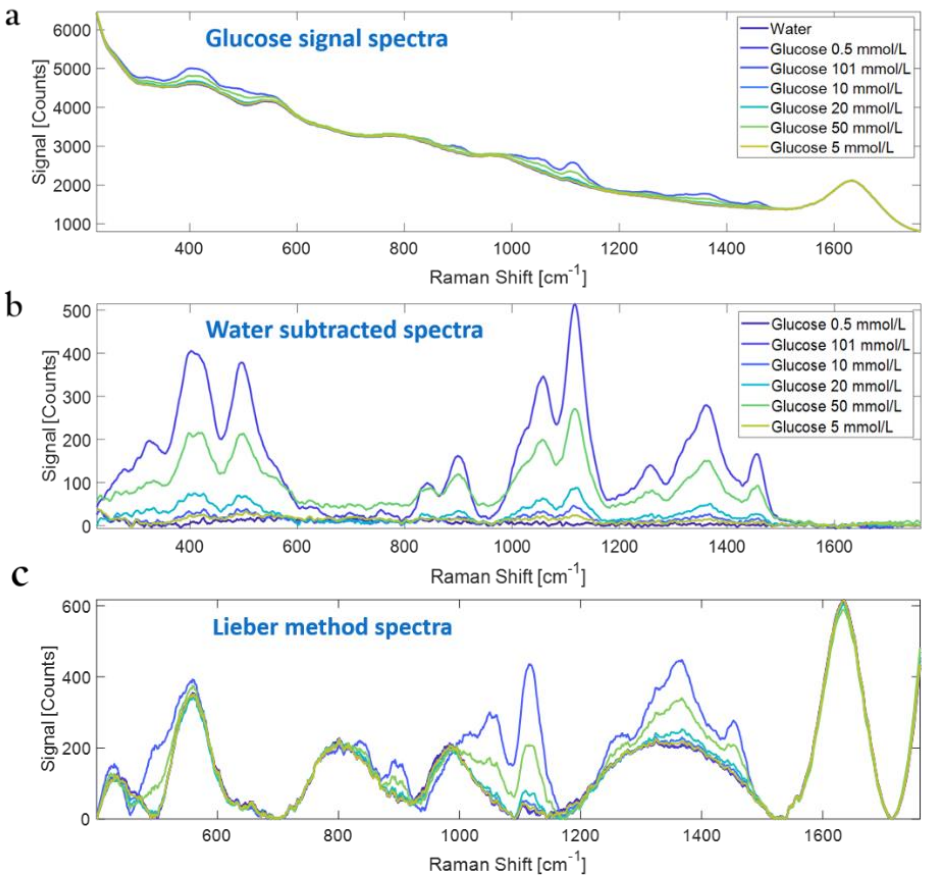

Figure 1.25: (a) Spectra of glucose solutions of various concentrations with dominant water background signal. (b) The signal of the glucose solutions after the water spectrum has been subtracted, revealing the analyte Raman peaks. (c) Spectra after a 6th order Lieber fit algorithm has been implemented on the raw spectra in (a), removing low order polynomial signal from the spectra.

Other algorithmic methods for background fluorescence removal implement spectral decomposition methods such as wavelet transform[117–119], local spline-fitting techniques[120], spectral derivatives, Bayesian modeling[121], and more[107,122].

Often times, after all the previous steps have been performed, an additional spectral normalization is performed between different samples. This final processing step aims to remove inter-sample variations that are due to instrumentation drifts and defocusing, after inter-sample corrections have been performed.

A simple and useful method uses a stationary Raman peak that is common to all samples and should not change in intensity, e.g. the water peak, see Figure 1.25a,

and normalize all sample spectra so that peak (single maximal wavenumber value) has an equal intensity for all samples. Variations of this method use the area under the peak, several Raman peaks, or even the mean of the entire spectrum[107].

1.6.2 Spectral Analysis

The objective of spectral analysis is to use slight variations in spectra to classify, quantify and ultimately predict molecular variations in the sample solely based on spectra. In many cases the spectrum of each sample is in itself a complex superposition of multiple Raman peaks in addition to background signals. Furthermore, many factors can alter the spectra of a sample, not just variations in analyte concentration, and these need to be considered throughout the experiment steps; starting from the experimental design, continuing to the actual measurement methodology, and finally while analyzing the spectra[107]. Sample inhomogeneity, sample preparation (e.g. freezing, thawing), biological and environmental changes (e.g. temperature, pH), and sample degradation are a few of the factors that could introduce spectral variations. Additionally, system drifts, and external light sources contamination could all contribute to spectral changes that the analysis aims to distinguish from the target analyte variations.

Spectral analysis methods are numerous and varied, spanning multiple mathematical and algorithmic approaches. There are several ways in which we can categorize these methods; Firstly, we can distinguish between classification methods and regression methods, although some techniques can do both. Secondly, we can separate linear methods and non-linear methods, and thirdly, a distinction between supervised, semi-supervised and unsupervised methods can be made[60,123]. Practically, there are a few analysis techniques that have gained more traction for Raman

spectroscopy[124], namely Direct Peak Analysis (DPA)[60], Principal Component Regression[125] (PCR), Partial Least Squares Regression[126] (PLSR), and more recently, unsupervised Machine Learning (ML) approaches[107,127,128] including Support Vector Regression[129] (SVR), and Neural Networks[130].

The following will define common terms regarding training, validation and prediction of models, followed by a brief description of some common methods, focusing on PLSR and feature selection methods that are particularly relevant for SSRS.

1.6.2.1 Training, Validation and Prediction

Most analysis algorithms consist of three steps: training, validation, and prediction. In order to perform these key three steps, a dataset that contains both spectra and an independent "ground truth" is necessary. Notably, these datasets are often a statistical sample of the population and considerable care needs to be given to making sure the sample size is adequate and not under-sampled or the model will perform poorly on new datasets[107,121] ("over-fitting").

Training and Validation

The training and validation steps, often performed together, are also termed the learning step, in which an estimation or classification model is constructed using both spectra and the ground truth measurements. We assume to have a total of N_L samples in our learning dataset which are split into N_T training samples and N_V validation samples. We additionally have a separate dataset for prediction (also termed test set) including N_P samples. Importantly, training, validation and prediction datasets have to contain different samples to ensure that the model isn't biased. Particular care is given to the splitting of the training and validation sets while considering the scarcity, cost and time required to acquire adequate learning data[107,131].

For simplicity, we describe a case where we wish to build a model estimating the concentration of a single analyte, A, with concentrations C_t where t is the sample index number. Generally, a model may estimate any sample attribute which affects the Raman spectra including concentration, but also diagnosis[95,132,133], or species[26,60,134]. The model produces an estimation $\hat{C}_t$ for the analyte concentration and we can measure the model agreement with the ground truth by the Root Mean Square Error of Estimation (RMSEE):

$$RMSEE = \sqrt{\sum_{t=1}^{N_T} \left(C_t - \hat{C}_t\right)^2} \tag{1.44}$$

Following the model building, we apply this model to the validation dataset, which serves to estimate the model's performance on previously unseen data. The model agreement is measured by the Root Mean Square Error of Validation (RMSEV) in a similar fashion as described in Equation 1.44.

The validation step is often iteratively intertwined with the training step in order to create a more robust estimation model. In this technique, termed Cross-Validation (CV)[131,135], the learning dataset is split into different training and validation subsets in each iteration, creating numerous variations of models and their respective RMSEE and RMSEV values. The final model's RMSEE and RMSEV are the averages of the values over all iterations, minimizing the likelihood of selection bias or over-fitting[136].

Within the family of CV methods, "k-fold" is very common where the learning dataset is randomly shuffled and then split into k equal parts. One segment is used as validation while the others are used to build k-1 models and this process is repeated k times, each time with a different validation set. For many biological experiments, in which technical replicates are made, it has been shown that splitting the datasets so

that training and validation are done on different technical replicates produces the most reliable models[131].

When the available learning dataset is smaller, (under 15-20 samples), an extreme version of k-fold is used where $k=N_L$. This method is also called "Leave-One-Out" (LOO) i.e. the learning dataset is repeatedly split so that $N_V=1$ until all splitting permutations are accomplished. LOO is an exhaustive method that uses all available data to build a model and can be quite computationally prohibitive. In the LOO method, the model parameters (regression coefficients, estimation and validation errors) are the average of those computed in each round. Alternative CV methods that are more common with larger datasets include "Bootstrapping"[135,136] which randomly samples the dataset in order to build a statistical model.

Prediction

Prediction is in many ways similar to independent validation, i.e. the constructed model is tested on previously unseen data. However, the prediction step is not used to iteratively test the model but to benchmark the final model using the Root Mean Square Error of Prediction (RMSEP) [107,131,136], similar to Equation 1.44.

1.6.2.2 Direct Peak Analysis

The most fundamental way of analyzing Raman spectra is DPA[60]. The main benefit of this technique lies in its simplicity and the fact that no training dataset is required for the analysis algorithms, though *a-priori* information is required.

Most DPA methods require the spectra to have visible Raman peaks, and some *a-priori* information regarding the peaks in the sample which are relevant for analysis, e.g. the target analyte pure spectrum or general curve fitting parameters. The relative increase or decrease of peak height or of the area under a peak can give both qualitative and quantitative estimations on analyte concentration. In fact, this is exactly how the

LOD of Raman systems is measured (see Section 1.3.2).

Often, libraries of pure analytes which are expected to be in the sample are pre-compiled and the sample spectrum is then decomposed and fitted to the various components while estimating the relative analytes concentrations[137]. Other, more computational demanding methods use deconvolution (blind[138] or based on prior knowledge[139]) to deconvolved the spectrum into Gaussian, Lorentzian and Voigt functions[140,141], finding the likeliest ratios of components in a mixture.

DPA, however suffers from some disadvantages. First, it uses a single peak even if the analyte has several known Raman peaks. Second, when SNR is low, peaks may not be visible above the noise or background signal, rendering DPA useless. Furthermore, in complex samples, multiple overlapping Raman peaks can create ambiguity as to the analytes affecting the spectral variation. In these situations, Bayesian modeling[142] often complements DPA by estimating both the peaks and background signals using likelihood probabilities, often improving model performance[121,143].

1.6.2.3 Linear Regression Methods

Linear Regression (LR) methods are the most popular Raman spectroscopy analysis techniques to date.[60,107] Where DPA looks for direct peak--analyte agreement, LR assumes that multiple regions in the spectrum can vary in different ways which are not always straightforward. These methods are robust even for relatively small datasets (containing between 10-20 spectra), which makes them a good fit for Raman spectra, particularly for biological datasets that tend to have a limited number of samples. Latent-variable LR (PCR, PLSR) have the added benefit of requiring no prior knowledge of the spectra or target analytes, making them extremely attractive for exploratory applications[107,121,124].

Generally, LR methods assume that a linear system model, represented by matrix H, exists which connects the target analyte concentration, C, and the spectrum X. The spectrum contains M spectral data points (independent variables): $[x_1, x_2, \dots x_M]$, and has been mean-centered[144], i.e. the mean of X and C equals zero. We can extend this formulation to a set of N_L samples where C is the analyte concentrations vector with dimensions $[N_L \times 1]$ (one for each of the samples), X is a matrix of spectra with dimensions $[N_L \times M]$, forcing H to be a vector $[M \times 1]$[125,144]. We assume ε to be the error or residual, also sized $[N_L \times 1]$ so that:

$$C = XH + \varepsilon \tag{1.46}$$

Importantly, some LR methods support a formulation where C is a matrix containing multiple analytes (each column represents the concentrations of a different analyte), and the model estimates the analytes simultaneously. However, model performance in these cases has been shown to do poorly compared with models tailored for a single analyte when the responses aren't strongly correlated [145,146].

The goal of LR is to find a model estimating H *by* using a training and validation dataset, so that it could be used for the inverse problem to find estimations of the analyte concentrations from the spectra:

$$\hat{C} = X\hat{H} \tag{1.47}$$

LR methods, described in more detail in the following, take different approaches for estimating $\hat{H}$, relying on various assumptions regarding the data.

Multivariate Linear Regression

Multivariate Linear Regression (MLR) is the multivariate version of Classical Least Squares (CLS). MLR is used as a standard fitting tool in order to find a straightforward linear relation between C and X. In MLR we find $\hat{H}$ according to the following equation[144,147], where X^T denotes the transpose matrix of X:

$$\hat{H} = (X^T X)^{-1} X^T C \tag{1.48}$$

Equation 1.48 alludes to a common problem with LR which is the need to find the inverse matrix $(X^T X)^{-1}$ *which may not exist or may introduce solution instability due to noisy data or significant variable collinearity*[144]*. Particularly for the common case where* $M > N_L$, i.e. there are more spectral datapoints than there are samples in the dataset, the problem is considered ill-posed without a single solution[147]. Weighted Least Squares (WLS) and various regularization methods are designed to limit the possible solutions and produce reliable models[148–150]. For latent-variable models, variable deletion (also known as "feature selection", described in more detail in Section 1.6.2.4) limits the number of variables in order to produce stable predictive models.

Principal Component Regression

PCR is based on Principal Component Analysis (PCA)[125]. PCA is a method by which a matrix $\mathbf{X}$ is projected onto a new coordinate system where the data's variance is maximized along the new axes (latent variables). The maximal variance axes of $\mathbf{X}$ are found by computing the eigenvalues and eigenvectors of the covariance matrix: $COV(X) = XX^T$, and once those are found, they are ordered by the magnitude of variance. In the regression step, the number of principal components is limited based on cumulative variance explained in the data[144]. $\mathbf{X}$ is then projected onto the lower dimensionality representation, $\mathbf{X}^*$, and use it to ensure a solution to the regression problem posed in Equation 1.48.

PCR is a semi-supervised method which allows the user to limit the number of input matrix components and reduce the dimensionality of the ill-posed problem. PCR is also used to easily identify key similarities and differences in spectra, and to simplify spectra and reduce noise as a pre-step before classification or other analysis algorithms are applied[60,151]. Importantly, PCR does not consider the output, $\mathbf{C}$, and variance in the input data does not necessarily correlate to variance in the output data, limiting its usefulness in predictive applications.

Partial Least Square Regression

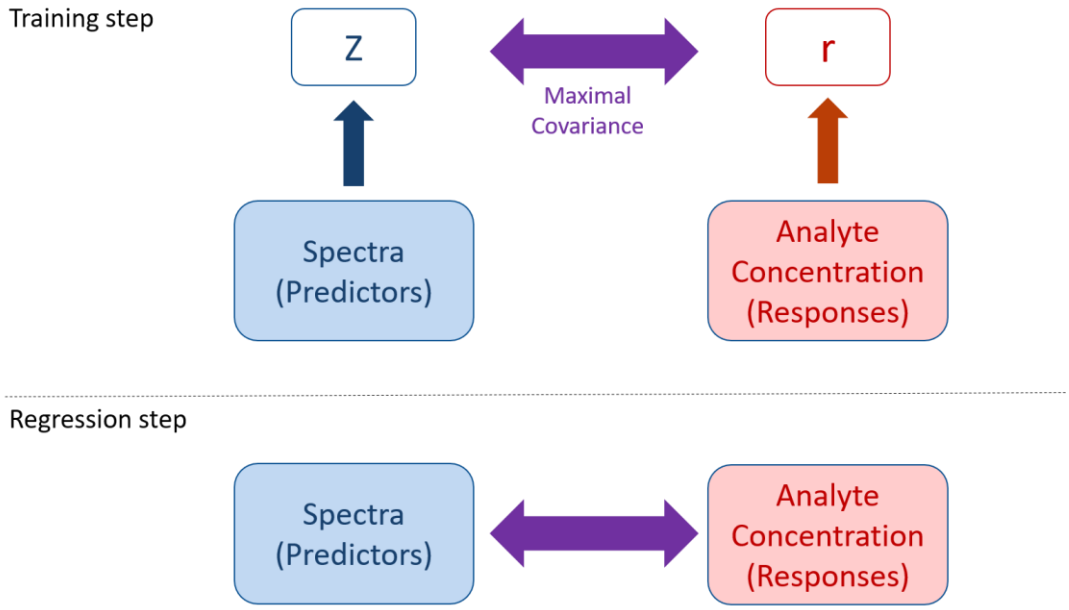

Figure 1.26: A diagram of the PLS regression using intermediate variables z, r to maximize the covariance of the input and output. The training step models the latent variables and then uses the model to predict previously unseen spectra

PLSR is the dominant analysis method for the estimation of analyte concentration from Raman spectra, particularly in biological applications[60,107]. The premise of PLS is that small principal components in the input (latent variables) may be highly correlated with the output and therefore should be incorporates in the estimation model. In PLSR, both the input ("predictor") spectra matrix, $\mathbf{X}$, and the analyte concentration $\mathbf{C}$ ("response"), are used in order to build the latent-variable model, maximizing their covariance[126]. The maximal covariance is found through intermediary variables, as shown in Figure 1.26. A complete mathematical formulation of the PLSR algorithm is found in Appendix C.

PLSR is a supervised iterative algorithm that finds a single latent variable in each iteration. The user defines the number of latent variables, N_{comp}, used for creating the estimation model. The cumulative variance explained in the output, (see Figure

1.27) can be used to determine the number of required latent variables, and in most cases a cumulative variance of 80-90% is chosen to avoid over-fitting the model.

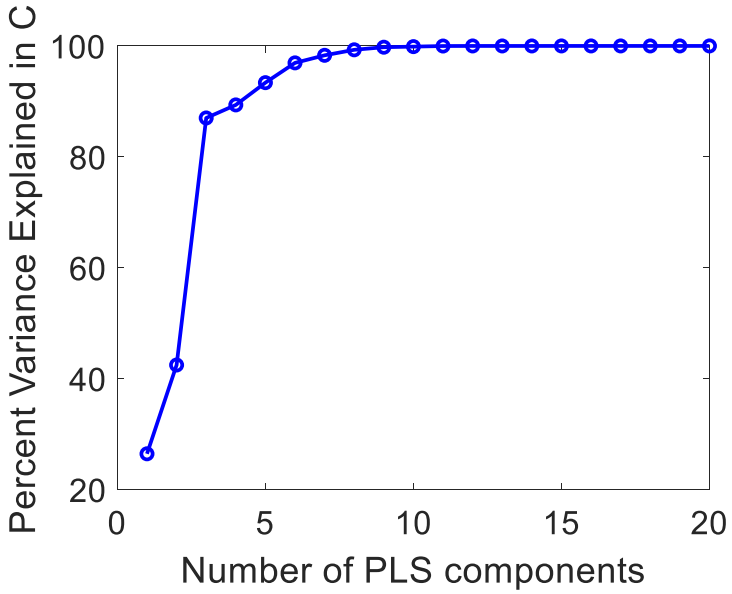

Figure 1.27: A plot showing the percentage of explained variance in the output (analyte concentration) as a function of the number of latent variables (iterations) used for the PLSR algorithm. Choosing a component number that correspond to 80-90% of variance tends to perform well for regression without over-fitting the data.

1.6.2.4 Feature/Variable Selection

In many spectral analysis methods, and particularly PLSR and PCR, an additional step of Variable Selection (VS), also called feature or wavelength selection, is performed to mitigate the excess in spectral data points (variables) compared with the number of observations (samples). This step helps to identify high SNR regions and avoid incorporating noise and low-importance regions into the prediction model. It has also been shown to improve predictions for high-collinearity in the observations[152,153]. The success of VS methods is often measured by comparing the RMSEP of the full and trimmed spectra but could also incorporate other metrics such as total variance explained[152,154].

There are three large categories of VS methods: filter methods, wrapper, and embedded[123,155]. Importantly, VS is extensively used for model optimization but rarely to affect the actual spectral acquisition[156]. In SSRS there is full control of the excitation wavelength and so VS could be used in order to direct the acquisition and reduce the total acquisition times while still maintaining low model errors.

The following will give a brief overview of VS methods used for Raman spectra and focus on the Variable Importance in Projection (VIP)[126].

Trimming

The most fundamental variable selection method is manual trimming (also truncating)[153,157], meaning that areas that have no known Raman peaks (i.e. the "silent region" between 1800-2800 cm^{-1}) are removed completely from analysis. In specific cases where a well-known Raman peak region is of interest, only that spectral region is considered in the analysis. In some real-time Raman imaging applications, only partial Raman spectra bands are acquired based on a-priori sample information to expedite acquisition[156,158]. While trimming is quite common, it is not strictly considered a VS method. It also assumes expert knowledge by the user, and tends to limit selection to regions which are visibly affected by changes, and are often collinear.

VS Filter and Wrapper Methods

In this family of methods, a model based on all variables is constructed and then only a subset of variables are selected based on some threshold criteria[123,155]. Common threshold metrics are the magnitude of the regression coefficient, $|\beta_m|$,*VIP* scores, and others[155]. *The* VIP score method, which quantifies the variance explained in the response for each spectral data point is described in detail in Chapter 4.

Wrapper and embedded VS methods extend filter methods and use optimization approaches, often iteratively, in order to find a subset of variables that produces the lowest RMSEP for a certain number of variables. Optimization

techniques include iterative-PLS (iPLS)[152,153,155,159], Uninformative Variable Elimination (UVE -PLS)[152,153,159], Artificial Neural Networks (ANN)[152,159], and many more[146,160–163].

1.7 Example Applications of Continuous Optical Chemical Sensing

In this section, two different applications of continuous optical chemical sensing are given. The first is the monitoring of nitrogen components, i.e. nitrate and urea in water sources. The second is the monitoring of the metabolic activity of cells in a pharmaceutical production process. These applications were chosen because they showcase the potential of SSRS NIR Raman spectroscopy while representing a diverse range of real-world applications, measurement setting, and analyte concentrations.

Both cell metabolism and nitrogen compounds monitoring have previously been accomplished using traditional Raman spectroscopy apparatus, providing a benchmark for comparison with our SSRS system. However, they have not been equally adopted and implemented as PATs. Nitrate monitoring requires low LODs, which are challenging, particularly in field conditions, and with unprocessed or unfiltered samples. The high cost, and limited availability of rugged Raman spectroscopy apparatus have made it an unlikely choice for water monitoring so far, despite its many advantages.

On the other hand, bioreactor monitoring has become a widely used PAT in pharmaceutical production and has gained acceptance in the scientific and pharmaceutical communities. Cell-based production has a highly controlled measurement environment with regards to temperature, pH, dissolved oxygen and other conditions, making Raman monitoring and model-based analysis a reliable

predictive tool. Additionally, as these production processes are meant for high-density cell cultures, reaching 30 million cells per milliliter, analyte concentrations are significant, providing good SNR data.

1.7.1 Monitoring of Inorganic Nitrogen and other fertilizers in Water

Inorganic nitrogen pollution has been shown to have many adverse effects on the environment[164,165]. The excess of inorganic nitrogen increases the density of plant life, promoting eutrophication of aquatic water systems, reducing oxygen levels necessary for the support of animal life. Additionally, excess nitrogen compounds, particularly nitrate (NO_3), nitrite(NO_2), and ammonium (NH_4), can reach toxic levels that impair the reproduction, growth and survivability of many aquatic life-forms while also posing a health threat to humans as these chemicals reach surface and groundwater systems[166–171]. The excess of hydrogen ions from these compounds contributes to the acidification of fresh-water as well as to that of soil, impairing eco-systems, reducing nutrients availability for crops, and increasing the mobility of heavy metals into the soil[172–174].

Industrial agricultural fertilizers along with animal manure runoffs, are the main contributors to the ten-fold increase in inorganic nitrogen flux over the last century, followed by industrial and wastewater treatment discharges[175,176]. However, fertilizers are also the driving force enabling increased food production that is paramount for supporting the world's growing nutritional demands[177]. Nitrogen fertilizers vary in their nitrogen content, acidification tendencies, and are selected based on the crop, drainage, aeration, and price point. Nitrate, ammonia and urea are common and available forms of nitrogen that are frequently used in fertilizers. Nitrate

and ammonia can be directly absorbed by plants while urea has a delayed nitrogen release. Ammonia is also a known cell metabolite that is converted to nitrite as part of the natural nitrification process[172,178]. Common fertilizers, their nitrogen (N) percentage as well their nitrate percentage are provided in Table 1.1[179].

Fertilizer	N [%]	NO3 [%]
ammonium-nitrate - NH_4NO_3	35.0	77.5
calcium-nitrate - $Ca(NO_3)_2$	17.1	75.6
ammonium-sulfate - $(NH_4)_2SO_4$	21.2	
potassium-nitrate - KNO_3	13.9	61.3
sodium-nitrate - $NaNO_3$	16.5	73.0
Urea - $CO(NH_2)_2$	46.6	-

Table 1.1: Common nitrogen fertilizers and their N and NO3 percentages

Recommended total nitrogen quantities for crops varies greatly depending on soil type, irrigation and required yield. On the lower range, crops like cotton and tobacco require 55-65 kg /hectare of nitrogen (50% of which should be in Nitrate form) , while high yielding corn and hay require 400-450 kg/hectare [180]. If we assume the weight of one hectare of soil in a depth of 20cm to be an average of 2.24e6 kg, we reach N concentrations of up 200 Parts Per Million (ppm) in soil. With the high density of farmland clustered around specific areas, and all excess fertilizer leeching into the same waterways, excess inorganic nitrogen accumulates[171,176].

The need to balance the use of fertilizers while mitigating their impact on the environment has led to a worldwide regulation of Maximum Contamination Levels (MCL) of nitrates in water. Table 1.22 shows MCLs for different countries and regions[171]. It is important to note that MCLs are often reported in units of nitrate-nitrogen (NO3-N) but since nitrogen accounts for 22.6% of the nitrate molecule by mass, this implies that the total nitrate (NO3) is 4.43 times higher in concentration than that of the reported nitrate-nitrogen level.

Country/Region	Nitrate-nitrogen MCL [NO3-N mg/L]	Nitrate MCL [NO3 mg/L]
USA, Canada[181,182]	10	44.3
EU[183]	11.3	50
WHO[184]	11.3	50
India[185,186]	10.1	45
China[187,188]	20	88.6

Table 1.2: MCL of nitrate in various countries and regions, their monitoring method and frequency

Surveillance and enforcement of the MCLs vary greatly depending on location. In the USA, the Environmental Protection Agency (EPA) is charged with implementing the regulations and goals set by the Clean Water Act (CWA)[189]. The actual monitoring and reporting is delegated to the State and Tribe levels [190,191] which follow the National Aquatic Resource Surveys (NARS) requiring an annual report[192]. In Europe the national authorities are charged with reporting once every 4 years to the European Commission while in India reporting is also done annually unless elevated levels are detected, where monitoring frequency is increased to once every quarter.

Despite regulations and monitoring practices, nitrate levels have continued to increase globally in surface and subsurface water systems and are expected to continue rising without significant mitigation[176,193]. If nitrate runoffs are to be truly reduced and addressed as they happen, and not just detected in hindsight, then a continuous, real-time, measurement methodology needs to be implemented instead of periodic sampling[194–196].

Over the past 50 years, numerous methods have been developed to measure nitrate and nitrite in various matrices, many of which are aqueous environments[196–202]. These methods largely divide into two main categories: direct measurements of the nitrate/nitrite contents, and indirect measurements that require the reduction of

nitrate or another chemical reaction that creates a new complex whose concentration is measured[203]. The nitrate or the chemical reaction product are then quantified with colorimetry[196,204,205], ion chromatography[196,200,206], High Performance Liquid Chromatography (HPLC)[199–201,204], hyperspectral or multi-band imaging couple with in-situ data[207–210], electrochemical methods[196,200,201,205], optical fiber methods[170,196,199,200], spectroscopic methods such as ultraviolet (UV) absorbance spectroscopy[170,196,199,201], Fourier Transform Infrared spectroscopy (FTIR)[170,197,198] and Raman Spectroscopy[200,204,211–215]. Out of the many methods in existence, only a handful are adequate for persistent, real-time nitrate measurement [196,197].

Methods based on periodic sampling, requiring chemical reagents or those that require extensive sample preparation and specialized lab equipment such as HPLC, ion chromatography, UV spectroscopy, and FTIR are not suitable for continuous or real-time monitoring. Periodic sample collection coupled with cost of labor, of transportation, and of reagents and of specialized labs, make them economically infeasible to conduct more frequently. These methods are also likely to miss detection of short-term runoff events. Remote sensing methods or in-situ electrochemical and optical methods have therefore emerged as possible alternatives[196,205,216].

Remote sensors, mostly based on hyperspectral data and Radio Frequency (RF), offering a global sensing scales and coverage of extremely remote locations are unfortunately not very well suited for nitrate detection due to its relatively low optical activity resulting in poor SNR and are also limited to surface water sensing. Electrochemical methods, that can be used in-situ, while reaching high sensitivity with Limits of Detection (LOD) lower than 1µg/L[170,196,203], suffer from poor selectivity and can only operate in fresh-waters. Improved electrochemical selectivity requires the use of exotic materials such as foam-based graphene, carbon nanotubes, or nano-wires, as recent examples that often degrade with continued use[170,196,204].

Raman has been used to detect nitrate and other chemicals in water since the1970s [204,214,215,217]. Raman is a particularly favorable method for this application, for reasons previously mentioned in Sections 1.2 and 1.3. Additionally, Raman can be used in highly turbid samples, which is favorable for environmental samples that are affected by temperature, particles and other objects in the water. Lastly, Raman is agnostic to the water salinity, making it effective in fresh as well as salt water[31,218]. Spontaneous Raman has been reported to achieve a 62ppm LOD[214] with a 90mW 532 excitation whereas SERS has achieved an LOD of 0.5ppm using a gold particle substrate[213]. A water monitoring system that mitigates drinking water contamination should have a LOD which is equal or lower than that of the EPA (10 NO3-N mg/L).

1.7.2 In-situ Monitoring of Cell Metabolism in Pharmaceutical Protein Production

Raman spectroscopy has gained traction as a PAT in pharmaceutical production applications[17–19,115,219]. There are numerous ways in which Raman is used in multiple steps of production, both upstream and downstream[157,219], but the most dominant example has been to monitor cell metabolism in the production of therapeutic proteins. Therapeutic proteins are a family of materials including antibodies, enzymes, coagulation factors, hormones, and cytokines[220]. Key examples out of the 350 FDA approved protein-based drugs[221] include many recombinant insulin products, and numerous cancer treatments such as Herceptin (Tastuzumab) targeting breast cancer.

Most therapeutic proteins are produced by recombinant technology, i.e. the genes that encode the desired protein are introduced into cells such as yeast[94], bacteria[222], and mammalian cells[223,224], which then produce the protein as they

proliferate. The cells cultures are often grown in bioreactors, vessels that provide the cells with a sterile environment in which oxygen and nutrients e.g. glucose and amino acids, are supplied and the waste products (metabolites) like lactate and ammonia are removed.

Most cell cultures today are grown in a fed-batch processes where nutrients are constantly added to the bioreactor and are slowly depleted. Alternatively, a perfusion process, also termed continuous manufacturing, aims to reach a chemical steady state ("chemostat") where some of the culture is harvested, waste is removed and replaced with fresh media and nutrients, maintaining steady cell-culture conditions[225]. Perfusion requires an increased level of monitoring and control but has been shown to have significant financial benefits and also improve product uniformity[226].

Figure 1.28: Left- standard ports on a bioreactor for probes including pH, oxygen and Raman, Right - a bioreactor with the probes introduced into the cell culture.

Sterile Raman probes, introduced into ports in the bioreactor, see Figure 1.28, provide continuous data on the concentration of nutrients and metabolites as well as other cell proliferation indicators and quantity of produced therapeutic[227,228] in a sterile, non-destructive manor, without the need to physically remove samples from the culture. The incorporation of Raman probes enhanced visibility, safety and promotes enhanced control of the culture conditions to optimize the therapeutic

production[228,229].

Performing a sensitivity comparison of reported Raman spectroscopy in bioreactors is extremely challenging. First, the cell cultures themselves are varied in type and cell densities. Additionally, there are differences in reported instrumentation (probes optics, excitation wavelength and power, spectrometers), spectral acquisition parameters (integration time and number of repetitions), on top of multiple chemometric algorithms and feature selection methods used to analyze spectra[154]. Table 1.3 shows a summary of major analytes and other markers monitored by spontaneous Raman in Chinese Hamster Ovary (CHO) cells, which are commonly used mammalian cells, with their respective analyte concentration ranges (across multiple bioreactor scales)[112]. Notably, additional materials are monitored in other types of cell cultures that are not produced in mammalian cells such as alcohols, phenylalanine etc'.[230–232].

Analyte/Marker	Concentration	References
Glucose	0-77.7 mM	112,137,145,233–238
Lactate	0.5-100 mM	93,112,134,137,236–241
Glutamine	0.2-15 mM	93,230,234,236,237
Glutamate	1-6 mM	93,112,134,230,234,238
Ammonium	1-20 mM	93,112,145,234,237,238
Total Cell Density (TCD)	1-35 [x10^6 cells/ml]	93,112,145,234,238
Viable Cell Density (VCD)	1-30 [x10^6 cells/ml]	93,112,145,157,234,238,239
IgG Antibody	1-140 [g/L]	145,157,227,238,242

Table 1.3: Analytes detected with Raman spectroscopy in bioreactors and their respective concentration in

PLSR is predominantly used for the analysis of Raman spectra and analyte concentration prediction in CHO[219], though other methods, including PCR, SVM, and others have been shown to be as successful in certain processes[60,107,124,151].

1.8 Thesis Objectives

This thesis aims to establish SSRS probes and sensor network as a chemical sensing method that not only serves as a practical utility but also matches or exceeds benchtop systems in sensitivity, resolution, scale, and efficiency.

In order to accomplish these goals, and demonstrate the SSRS probe performance for both cell-culture monitoring and fertilizer run-off detection, the LOD for glucose should be around 1g/L, which is comparable to dispersive Raman systems, and required for most mammalian cell cultures. Similarly, the LOD for nitrate should be lower than the EPA standard for drinking water, which is 44ppm. Moreover, a spectral resolution of 5-10 cm^{-1} is needed, as it adequately addresses the requirements for most liquid samples and aligns with the capabilities of typical dispersive spectrometers with an input slit width of 200μm.

To demonstrate that SSRS is capable of providing a practical utility service, a proof of scalability is necessary. The design objectives include the operation of multiple probes (ideally, over a dozen) either sequentially or concurrently to monitor various processes. Furthermore, the deployment distances should accommodate monitoring in diverse settings, ranging from large industrial complexes to outdoor applications, spanning hundreds of meters.

Lastly, the duration of spectral acquisition needs to be on the same order of magnitude as that of dispersive or interferometric method for the same class of samples: 30-60 minutes for cell cultures and up to several hours for slow varying processes such as water monitoring.

Chapter 2 of the Thesis will detail the design and validation of the SSRS probe in regard to sensitivity, resolution and provide a demonstration of nitrate uptake monitoring in a small hydroponic system. Chapter 3 will describe the scaling up of

the SSRS to a 16-channel sensor network using a standard optical data communication switch and leveraging the tunable laser as a shared resource. A demonstration of a 100m deployment distance is given as well as the economic models that support the superiority of SSRS over dispersive methods for multiple-sensor large-scale systems. Chapter 4 will explore efficient spectral sampling methods to reduce the total acquisition time and demonstrate these techniques on CHO cell-culture supernatant samples. Finally, Chapter 5 will present potential new directions for SSRS for both a single and network level systems.

CHAPTER 2

Swept-Source Raman Fiber Probe

The SSRS network relies on the single SSRS sensor as a basic building block. The utility of the single sensor, and the successful expansion to a multi-sensor network depend on the sensitivity, robustness, ease of use, and cost of both a single sensor and the entire sensor network.

This chapter will detail the design and fabrication evolution of the SSRS sensor, including the fiber probe and the receiver hardware (Section 2.1). A performance evaluation of the SSRS probe prototype is given and benchmarked against a dispersive benchtop system in Section 2.2. Finally, a proof of concept demonstration monitoring the nitrate in a hydroponic system and in unprocessed water samples is given Section 2.3.

2.1 SSRS Design Evolution

SSRS aims to offer a small-footprint alternative to dispersive benchtop spectrometers without compromising resolution or sensitivity and while also maintaining or reducing the cost. On top of that, the goal of having an easy-to-use SSRS probe which is also autoclavable, compatible with standard bioreactor ports, and can be easily expanded to be used in a network formation, poses optical and mechanical limitations that need to be balanced.

The SSRS sensor is comprised of two parts: the fiber probe and the optical

receiver which includes the UNBF assembly and the photodetector. The fiber probe houses the optical components that makeup a SSRS Raman system in a compact and user-friendly way (see Sections 1.5 and 1.4.4) while the receiver replaces the spectrometer and detects the back-scattered Raman photons.

Moving from free-space SSRS[36] and adjusting the design to a fiber-probe sensor was performed in a few steps detailed in the following table. Performance metrics for the Kaiser Rxn785 commercially available Raman probe system (Endress & Hauser) are provided for comparison.

	Commercial system	**Previous work**	**This work**		
Raman System	Kaiser Rxn785	Free Space SSRS	Gen 1	Gen 2	Gen 3
Laser and power	400-500mw	250mW	Superlum 15mW	Ti:Sapph 100mW	Superlum 6mW
Detector NEP	Dispersive 0.002fW	Femto 0.7 fW	Femto 0.7fW	SPAD 0.012fW	SPAD 0.012fW
Normalized Probe collection efficiency	1	900	3	12	12
Glucose 3σ LOD [mM/L]	~	3.3	100	4.5	5.17

Table 2.1: SSRS design evolution with various laser sources, detectors and probe optimization

The design and testing of the SSRS probes were accomplished at MIT and the fabrication was done by InPhtonics (Norwood, MA). As seen from Table 2.1, two laser sources and two detectors were used, but the probe collection efficiency continued to increase due to design improvements, which are detailed in the following Section.

2.1.1 SSRS Fiber Probe

The SSRS probe went through several iterations due to both changing design and fabrication issues. The design of the probe was affected by all the constraints previously mentioned. However, even after the design was agreed upon and sent for production, fabrication issues plagued the quality of the probes, resulting in performance variations between seemingly identical probes. The next sections will describe the design considerations of the probe as well as the fabrication iterations.

2.1.1.1 SSRS Probe Design Space

The need to balance the multiple design constraints led to engineering tradeoffs which are illustrated in Table 2.2. The lightly green shaded items the ones selected for the final design which was used for all the measurements given in the following sections.

Part name and specifications	**Design Notes**
Excitation Fiber	
780HP Single Mode (SM) Attenuation: 4dB/km	Both tunable sources are polarized SM lasers by default (but MM versions exist). Single mode probes were manufactured but had lower laser coupling efficiency (55% compared with > 80% for the MM options). Additionally, MM peripheral equipment is more readily available than SM. The 62.5µm fiber was selected due to the switch availability though the 50µm Ø fiber has lower attenuation and should be considered for future revisions.
50µm Ø Multi-Mode (MM) GRIN (low-OH) Attenuation: 2.3dB/km	
62.5µm Ø MM GRIN (Low-OH) Attenuation: 2.9dB/km	
Dichroic Beam Splitter	
Short-Pass (SP) 830nm	Both dichroic beam splitters serve the same function of separating the excitation and collection photons into different optical paths. However, high Optical Density (OD) LP filters are more commonly available in all wavelengths.
Long-Pass (LP) 830nm	
Objective Lens	
0.25NA, 5mm Working-Distance (WD)	Both probe versions were fabricated and used extensively. The 0.5NA objective has a higher throughput but is not

0.5NA, 3.2mm WD	suitable for the standard quartz cuvette with 1mm thick walls. However, it does improve collection efficiency for solid and opaque samples.
Collection Fiber	
Low -Oh 600µm Ø 0.5NA MM silica-core/clad	The collection fiber was chosen by balancing the need for higher étendue with the material constraints due to autoclaving. Increasing the size of the collection fiber is possible for different environmental measurement conditions.
>1000 µm Ø MM silica-core/Polymer clad	
Probe dimensions	
1/2" Ø stainless steel immersion probe	The immersion probe dimensions were chosen to match existing 7/8" ports in commercially available Applikon bioreactor (also accommodating an immersion sleeve). Importantly, for étendue to be maximized, the internal optics need to be carefully chosen to match the collection fiber. The Box probe was mostly used to select internal optics but was not meant for practical use.
1/8" Ø stainless steel hand-held probe	
"Box probe" (Demo)	

Table 2.2: Partial list of the design contingencies for the SSRS probe

2.1.1.2 Probe Fabrication Evolution

The probe evolution steps are described in Figure 2.1, marking in red the significant changes in each version. Having never designed a probe before, the first-generation probe failed to recognize the internal structure of Raman probes which included a baffling pinhole and also had collection optics matching a smaller collection fiber. Our design focused on the filters and collection fiber without properly addressing the optical components to match those changes, resulting in only a x3 collection enhancement compared with the theoretical predicted enhancement. Additionally, as is evident from Table 2.3, the SM input had the lowest excitation, aiding in the decision to move to MM fibers.

In the second generation, the pinhole was removed and back propagation was suggested to aid the fabrication, helping to co-align the excitation and collection optical paths which resulted in a probe version with a x9 collection enhancement.

Finally, in the third probe generation the internal collection focusing lens (6.2mm focal length and a clear aperture of 3.7mm, C171TMD-B, Thorlabs, NJ) was replaced with a lens that has a 5mm clear aperture and a 0.4NA (355110-B, Thorlabs better matching the objective lens' clear aperture and collection fiber NA. Moving to this lens proved helpful in reaching a x12 collection enhancement (see Section 2.2.2) but created difficulties with fabrication, resulting in moving to smaller collection fiber (500 µm Ø 0.5NA).

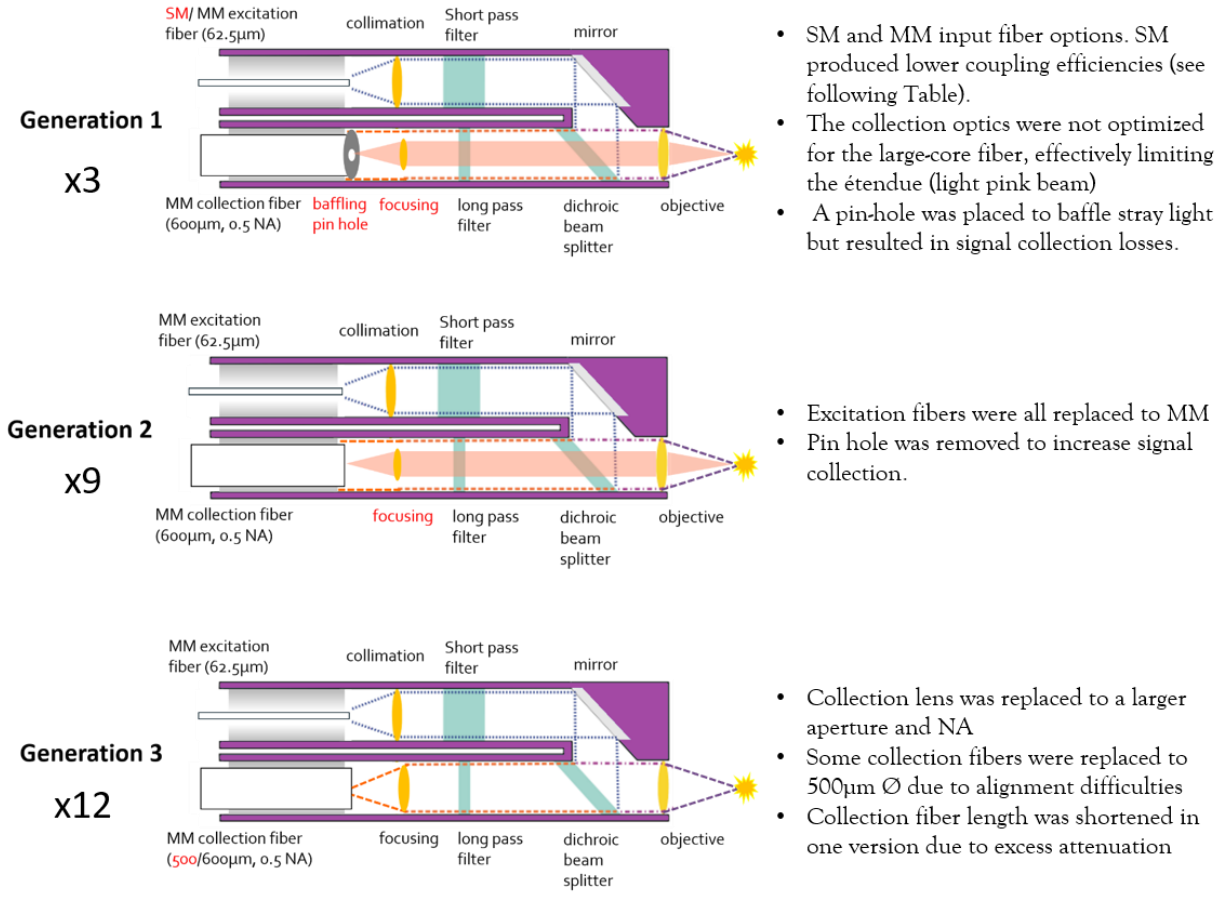

Figure 2.1: The evolution of the SSRS probe due to design and fabrication iterations.

After the SSRS probe iterations we had 5 operation probes whose performance was considered adequate, though not perfect. The probes were measured for the excitation efficiency by measuring the ratio of input power (785nm) and the power on

the sample plane. A similar measurement was performed by measuring the collection side by "back propagating" light (884nm) through the collection fiber and measuring the light on the sample plane. As the process is reciprocal, it gives a bound on the collection efficiency (Table 2.3) The product of these two efficiencies (right most column) gives the upper bound for the efficiency of the probe relative to a 100% efficient probe without insertion or collection losses.

It is important to note that these efficiency measurements give maximal bounds for the insertion losses but cannot fully predict the Raman signal collection. One of the challenges in aligning Raman systems is the matching of the excitation focal point on the sample and the collection focal point (in back-propagation mode). Even when the optical paths are well designed and work well independently, their mutual co-alignment sets the ability to effectively collect the Raman photons.

These results demonstrate that fabrication had a crucial effect of probe performance and even with identical optical components the probe variability was significant, reducing yield.

Objective NA	**Input fiber**	**Output fiber core diameter and length**	**Excitation efficiency [%] (@785nm)**	**Collection efficiency [%] (@884nm)**	**Bound efficiency [%]**
0.5	62.5µm MM	600 µm (2m)	85	80	68
0.5	62.5µm MM	500 µm (1m)	82	36	29
0.5	62.5µm MM	500 µm (2m)	79	38	30
0.25	62.5µm MM	600 µm (2m)	90	60	54
0.25	780HP SM	600 µm (2m)	65	55	36

Table 2.3: Final SSRS probes input and output coupling efficiency

The magnified illustration of the final SSRS fiber probe is given in Figure 2.2 and pictures of the fabricated probes are given in Figure 2.4. Full technical details of the final probe (0.25NA, 600 µm fiber and marked in the green square above) which

was used for all following measurements are given bellow.

The excitation input fiber is a low-OH Graded Index (GRIN) silica fiber with a 62.5µm core diameter (GIF625, Thorlabs, NJ, USA). This fiber is a standard datacom optical fiber that has an attenuation of ~2.9dB/km at 850nm[103] compared with ~8dB/km for 105 µm fiber, often used for Raman excitation (FG105LCA, Thorlabs, NJ). The use of this fiber allows one to guide the excitation light to longer distances and leverage existing optical datacom components, as will be further detailed in Chapter 3.

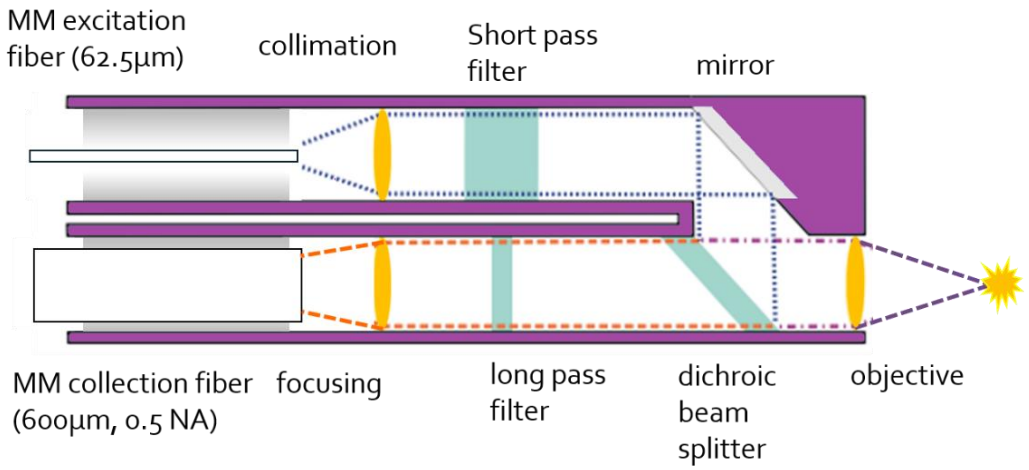

Figure 2.2: SSRS Probe Diagram showing the internal optical components. The tunable excitation light is introduced using a GRIN fiber with low attenuation. It is then collimated and filtered using a SP filter A combination of a mirror and a LP dichroic beam splitter divert the light onto the sample and allows the back-scattered Stokes-shifted photons to pass. The Raman light is then passed through a long pass filter to remove residual excitation after which it is focused into the collection fiber which is matched to the large core collection fiber and the large area-detector.

Secondly, the excitation input filter is replaced by a short-pass or a bandpass filter that accepts a range of excitation wavelengths to illuminate the sample. In the prototype SSRS probe, a short-pass filter with a sharp cutoff at 840nm (see Figure 2.3) was chosen, allowing excitation in the 760-840nm range to pass (FWHM bounds), which matches existing NIR tunable laser sources (see Section 2.2.1).

The objective lens which focuses the excitation onto the sample while also collecting the Raman photons can be made to accommodate a variety of samples. Two variations of objective lenses were designed: a 5mm diameter 0.25NA objective with a working distance of about 5 mm, and a 5mm diameter 0.5NA objective with a 3.2mm working distance. While the latter has a higher collection efficiency, it is sometimes beneficial to use a longer working distance and larger depth of field which corresponds to a larger illumination volume and is less sensitive to sample positioning.

The collection path of the SSRS probe has similar filters to those in standard Raman fiber probes. An 830nm long-pass dichroic filter (shared with the excitation path) diverts the excitation beam onto the sample while allowing the Stokes-shifted Raman photons into the collection port. An additional 843nm (FWHM) long-pass filter attenuates any residual excitation from reaching the collection fiber. The SSRS probe's collection path transmission was measured by "back propagating" light from the collection fiber port onto the sample and is shown in Figure 2.3 (orange curve). While it is possible to use shorter excitation wavelengths with these probes, a significant attenuation of the signal is expected because of the filters.

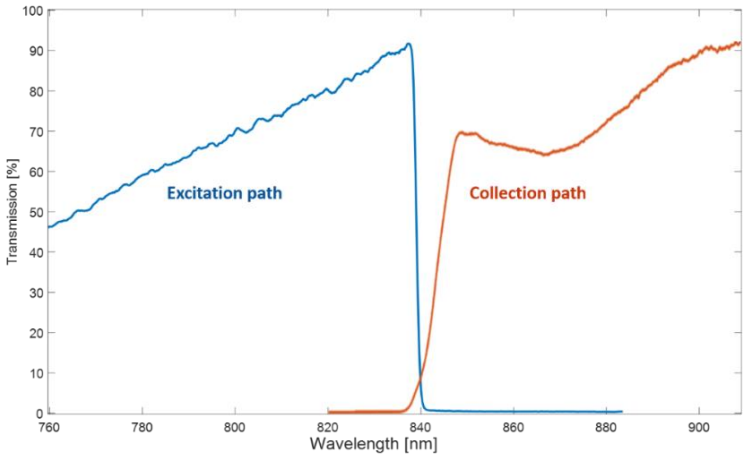

Figure 2.3: Measurements of the SSRS excitation transmission (blue) and the collection transmission (orange) in the expected NIR wavelength ranges of 760-910nm, showing the broad range of possible tuning excitation wavelength and filter effect on the excitation and collection paths.

The most significant change in the SSRS probe collection path is, however, the collection fiber and optics which is designed to maximize étendue. The collection silica fiber has a 600µm diameter core with 0.5NA (FP600ERT, Thorlabs, NJ). According to Equation 1.26, the probe étendue is therefore 0.22mm^2, limited by the collection fiber. While larger core fibers exist, this was (at the time of the design) the largest available silica fiber, which allows the probe to be autoclaved, ensuring sterile conditions for use in cell cultures, or high temperatures (200C°).

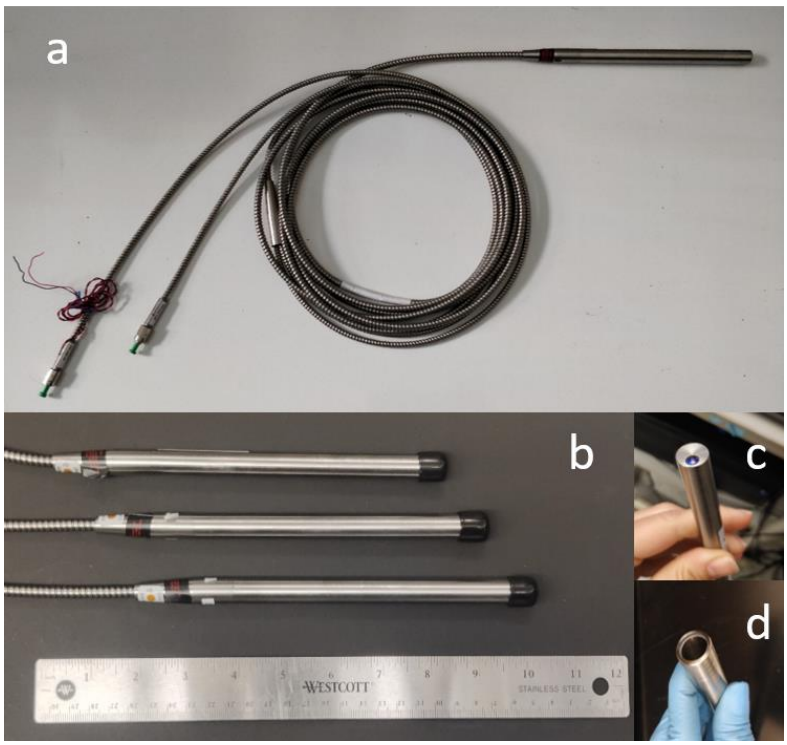

Figure 2.4: a) An SSRS immersion probe with 2m of armored optical fibers b) Three SSRS immersion probes, all made with the same stainless-steel incasing, measuring 8" long and ½" in diameter. c) a top look at the probe objective lens. d) An immersion sleeve silica window 1mm thick.

The probes were made 8" long and ½" in diameter (see Figure 2.4a, b), to match commercially available optical holders, and to also fit within a 7/8" stainless-steel immersion sleeve that matches standard port sizes on many commercially available bioreactors. A custom immersion sleeve with a 1mm thick fused silica window was made to accommodate the probes with either objective lens, allowing the focal length to extend beyond the sleeve window (see Figure 2.4b, c)

A standard 830nm excitation Raman probe with a 0.25NA objective, and 200µm, 0.22NA collection fiber was also fabricated to benchmark against the SSRS probes.

2.1.2 SSRS Optical Receiver

Part name and specifications	Design Notes
Photodetector	
SPAD (cooled) Noise Equivalent Power (NEP): 0.012fW Diameter 500μm	Initial design of the SSRS probe used high excitation power (>80mW) making the un-cooled Femto detector suitable achieving a glucose LOD of 4.5mM/L. However, when moving to lower excitation powers using the Superlum the Femto noise floor proved too high and LOD was reduced to 100mM/L. The large area SPAD, despite its smaller area compared with the Femto, proves sufficient for the probe collection fiber and has significantly lower noise.
Femto (un-cooled) Noise Equivalent Power (NEP): 0.7fW Diameter 1100μm	
UNBF	
853.75nm (central wavelength) 0.75nm (FWHM) ~ $12cm^{-1}$ (#853.75-0.75 OD6, Alluxa, CA)	The UNBF filter selection affects three main performance metrics: spectral range (Equation 1.40), and resolution (see Equation 1.41). Additionally, as the detection is done at a longer wavelength, the silicon quantum efficiency decreases (see Figure B.1), affecting SNR. The final filter (884nm) was chosen since it allowed detection of the main Raman fingerprint region as well as other biologically and environmentally relevant samples in the 730-1670 cm^{-1} range even with the Superlum laser (see below).
935.12nm 0.45nm (FWHM) ~ $12cm^{-1}$ (#935.125-0.45 OD5, Alluxa, CA)	
884.00nm (central wavelength) 0.45nm (FWHM) ~ $7cm^{-1}$ (#884.00-0.45 OD6, Alluxa, CA)	
Collimating/Focusing lenses	
Since the two different detectors used had significantly different active areas and mechanical specifications, the collimation and focusing had to be matched in regards to étendue, magnification and focal lengths that match the distance between the detector housing to the active area. The lenses chosen for the SPAD (detailed in the following) were the only commercially available options that allowed for all of these requirements to be met.	

Table 2.4: Partial list of the design alternatives for the SSRS receiver

The SSRS receiver is designed to match the probe in regards to étendue and optical magnification, while also determining the spectral resolution with the UNBF. The mechanical dimensions of the detector play a crucial role in adjusting the receiver optics to make sure light is collected and focused efficiently onto the detective's active

area. Additionally, if the detector noise floor isn't sufficiently low, it affects the total SNR of the system (see Equation 1.14). Since the probe went through several design iterations, the receiver was also continually evolved to match the probe and tunable laser source.

The final SSRS receiver is comprised of a small optical setup that collimates the light from the probe, passes it through the UNBF, and then focuses it back onto the detector (See Figure 2.5). Importantly, the optical receiver must match or surpass the étendue of the probe so that the collection enhancement achieved by the SSRS probe is not lost (see Figure 1.11). Additionally, the optical magnification of the receiver should guarantee that the beam spot size is smaller or equal to the detector's active area.

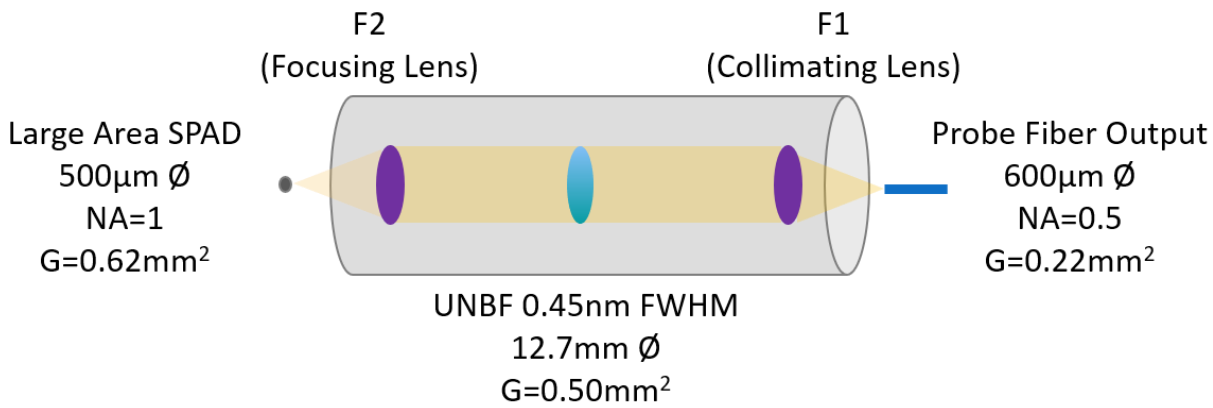

Figure 2.5: A diagram of the optical receiver which collimates the light from the probe, passes it through the UNBF and then focuses it onto the SPAD active area.

The UNBF used in this setup was a ½" Ø, with a central-wavelength of 884nm and a FWHM of 0.45nm (Custom filter by Alluxa, CA). The acceptance angle of this UNBF was calculated in Section 1.4.4 and found to be 2.04 degrees. The étendue of this filter is therefore 0.5mm^2 (see Equation 1.26), and does not pose a limitation on the light collected with the SSRS probe.

The detector used is a large area, electrically cooled Silicon SPAD (ID

Quantique, Switzerland). This SPAD has a 500μm diameter active area and can be cooled down to -40C°. Additionally, this SPAD has very low dark count rate (<300Hz specified and measured ~50Hz), making it suitable for extremely low Raman signal detection. Previous SSRS fiber probe implementation[37] as well as free-space SSRS[36] have used a un-cooled zero-biased high transimpedance photodetector (Femto, Germany). This was possible since the excitation power exceeded 80mW (for the fiber probe) or since the free-space SSRS system has a much higher étendue compared with the probe, ensuring high signal compared with detector noise (dark counts). However, moving to a lower excitation power (<12mW) while using the SSRS probe, requires the use of this ultra-low noise detector. The SPAD dark noise count (at -40C°) has an equivalent incident power of 0.012fW (~50 photons per second at 884nm) while the Femto's is 0.7fW, making the SPAD almost 60 times more sensitive.

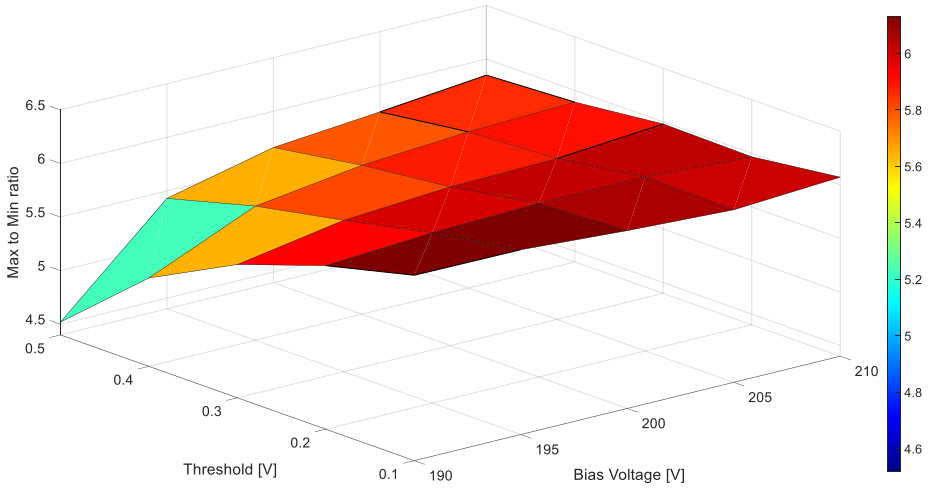

Figure 2.6: The ratio of the polystyrene peak signal and the low-signal spectral point with various SPAD bias and threshold voltage settings, which allowed to determine the SPAD operating parameters to optimize SNR.

The SPAD, which has an internal avalanche quenching circuit (see Subsection 0) requires the setting of both the bias voltage and the quenching parameter ("threshold voltage") which determines the SPAD recovery time after an avalanche

has occurred. If the threshold is set too high, the detector is idle for longer periods but if set too low, after pulsing from previous avalanches can create "false counts" and enhance the noise. In order to determine the optimal operation parameters, the SPAD was cooled to -40C° and signal of the polystyrene Raman peak (1001 cm^{-1}) and of a low Raman signal area (970 cm^{-1}) were measured (see Figure 3.2) using 100mW of excitation over an integration period of 10 seconds. The objective was to find the voltage settings for which the contrast between these values would be greatest, i.e. where the SNR would be the greatest. Figure 2.6 shows the contrast results where the darkest red colors achieved the best contrast. Based on these results, the bias voltage was set to -200V and the threshold setting to 0.1 for all future measurements.

Importantly, SPADS sometimes exhibit signal instability, independent of incoming photons but rather due to trap states in the junction which are excited due to the high voltage applied[243]. This, and the device dark count rate, are unit-specific characteristics that need to be individually assessed before integration into the system. Figure 2.7 shows an example of trap-assisted bistability which was discovered in one of the SPADS.

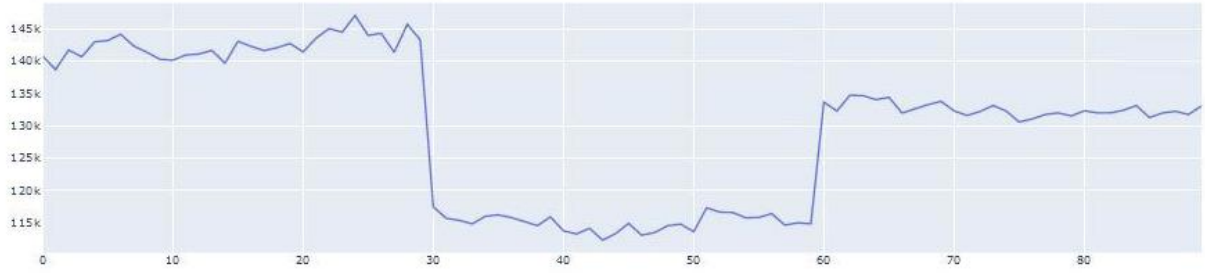

Figure 2.7: A trap-assisted bi-stability phenomenon where signal levels are constant but SPAD output counts differ due to released trap states. This phenomenon is rare and dependent on the specific detector which requires testing of each SPAD unit.

With the SPAD's acceptance solid angle of 2π (NA=1), étendue is calculated from Equation 1.26 and is equal to 0.617mm^2, posing no limitation on the collection

efficiency of the probe or the receiver in a fiber-based system. However, the SPAD's étendue can pose a limitation in a free—space system.

Since the probe's collection fiber is 600µm in diameter, and the SPAD's active area is 500µm in diameter, the collimating and focusing lenses in the receiver must create an optical magnification of 0.83 or less. For a system of two lenses as described in Figure 1.11, the optical magnification M is defined as the ratio of the lenses focal lengths:

$$M = \frac{f_2}{f_1} \tag{2.1}$$

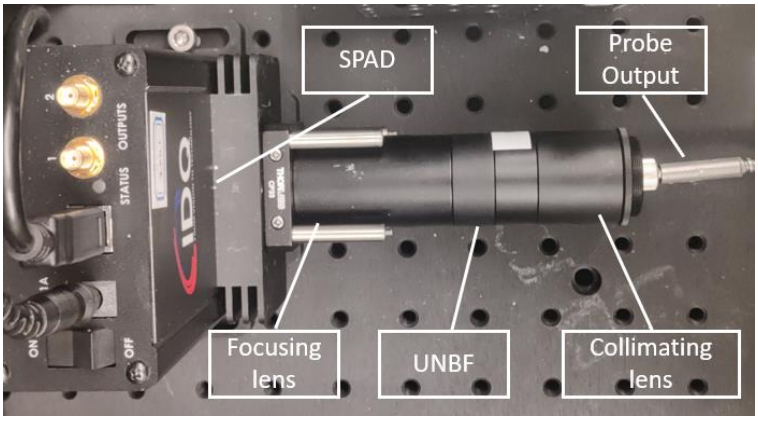

Figure 2.8: A picture of the SSRS optical receiver assembly from Figure 2.5, housed in a black anodized tube to reduce room-light leakage into the detector.

The collimating lens, L_1, was chosen with a focal length of f_1=7mm and a diameter of ½" (ACL12708u-B, Thorlabs) while the focusing lens, L_2 was chosen with a focal length of 10.5mm, and a 12mm diameter (ACL1210u-B), ensuring a suitable magnification of 0.66. These lenses were also the only commercially available options that allowed for both the magnification, and mechanical constraints to be met.

The position of the focusing lens was fixed to be as close as possible to the lip of the SPAD housing, but remained unchanged afterwards. Both lenses have NIR anti-reflective coating and the receiver assembly was housed in a black anodized tube to minimize room light from entering the detector, see Figure 2.8. Additionally, the

entire receiver was housed in a black box to prevent stray light from entering the detector.

Overall, the SSRS probe, UNBF and SPAD have theoretical étendue values of 0.22mm^2, 0.5mm^2, and 0.617mm^2 respectively. The total sensor étendue is therefore currently bound by the collection fiber. The spectral resolution, calculated from Equation 1.40 is 7 cm^{-1}. Compared with a standard Raman probe, designed for dispersive spectrometer with a single collection fiber (200µm Ø, 0.25 NA), the SSRS probe has an expected 36-factor improvement in collection power. The measured collection and resolution the SSRS probe and receiver are given in Section 2.2.2.

2.2 SSRS Proof of Concept

This section will include the proof of concept demonstration of the SSRS probe and provide performance metrics, benchmarked against a dispersive benchtop system. The hardware implementation including two different tunable lasers is detailed in Subsection 2.2.1. The SSRS probe light collection efficiency, and sensitivity are given in Subsection 2.2.2.

2.2.1 SSRS System Implementation

The heart of SSRS is the tunable laser. It carries considerable weight in the design and performance of the SSRS sensor and network. Excitation power, excitation stability, total tuning range, tuning accuracy and repeatability are determined by the laser. Two tunable lasers were used in this work, showcasing opposite ends of the available tunable laser spectrum (pun intended). These lasers differ in every possible aspect: size, cost, pump method, output power, tuning range, tuning resolution and accuracy, yet they both produce successful Raman spectra (see Figure 2.18).

The first is a high power, Continuous-Wave (CW) Titanium:Sapphire (Ti:Sapph), (M Squared, UK) pumped with a 10W frequency-doubled 1064 diode laser (Coherent, CA USA), providing an output power exceeding 2W (approximately 1.2W after fiber coupling). The laser tuning is controlled with a High Finesse WS7 wavemeter, guaranteeing a wavelength resolution of 1e-5nm. The laser tunes between 700-1000nm, corresponding to a theoretical spectral range of 0-4285 cm^{-1} but practically limited by the SSRS probe excitation filter to 0-2237cm^{1}. Importantly, the Ti:Sapph tuning mechanism, having an internal control loop requires between 5-30 seconds to tune between wavelengths (depending on the distance between them) and so while the wavelength accuracy is very high, the tuning overhead is significant for multiple data points.

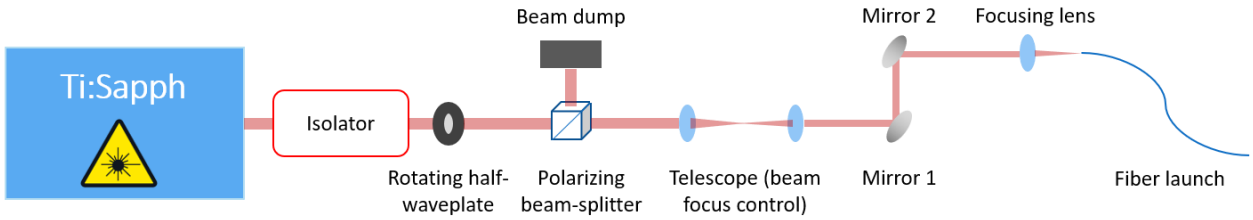

Figure 2.9: An optical setup diagram showing the components required to couple the Ti:Sapph output beam into an optical fiber while controlling the power. An isolator prevents light from returning into the cavity. The polarized output of the laser can be rotated with a half wave-plate after which a portion of the power can be passed through a polarizing beam-splitter. A telescope adjusts the focusing point of the beam and two mirrors are used to adjust the beam angle and location to couple into an optical fiber.

The cost of this laser system exceeds $200k and it takes a considerable amount of space on top of a vibration-damping optical table. Figure 2.9 shows a schematic diagram of the laser and fiber coupling assembly. This setup allows to adjust the power coupled to the fiber through a polarizing beam-splitter and control beam parameters (position, angle) to better couple the beam into an optical fiber (SM 780HP, Thorlabs, NJ)

On the other end of the spectrum lies the Superlum. This second tunable laser is an electrically pumped diode (OEM-BS-790-1, Superlum, Ireland). The laser is followed by a booster amplification unit (OEM Booster, Superlum, Ireland), outputting 20mW. The Superlum tunes between 770-825nm in 0.1nm increments. The laser linewidth is 0.05nm and the tuning is done based on a lookup table without an active control or external wavelength measurement.

This laser is compact, lightweight and arrives ready for fiber coupling with the provided Polarizing Maintaining (PM) SM fibers (PM780-HP, Thorlabs, NJ), proving easy to use without any optics know-how. Additionally, tuning between wavelengths is very fast, and takes less than 1 second, significantly shortening the tuning time overhead. The optical fiber launch diagram and pictures of the laser and booster units are given in Figure 2.10a and Figure 2.10b, respectively.

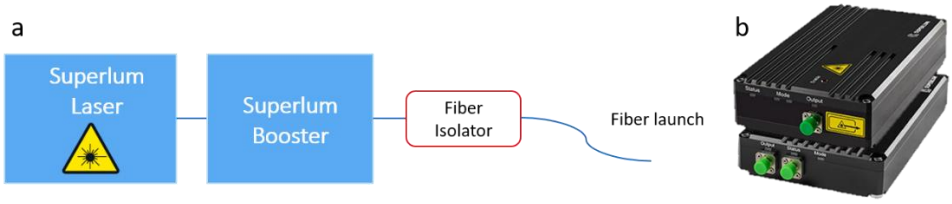

Figure 2.10: a) The Superlum laser and booster units connected to an additional fiber isolator unit minimizing laser output instability. b) A picture of the superlum laser and booster units

As seen in Figure 2.10a, an isolator (IO-F-780APC, Thorlabs, NJ) was introduced after the booster since the laser showed power fluctuations due to internal reflections when the SSRS probe was connected (but not when inspected as a stand-alone without additional devices connected). Figure 2.11 shows the power fluctuations recorded simultaneously in both the SPAD and a 1% SM tap and power meter (see details below).

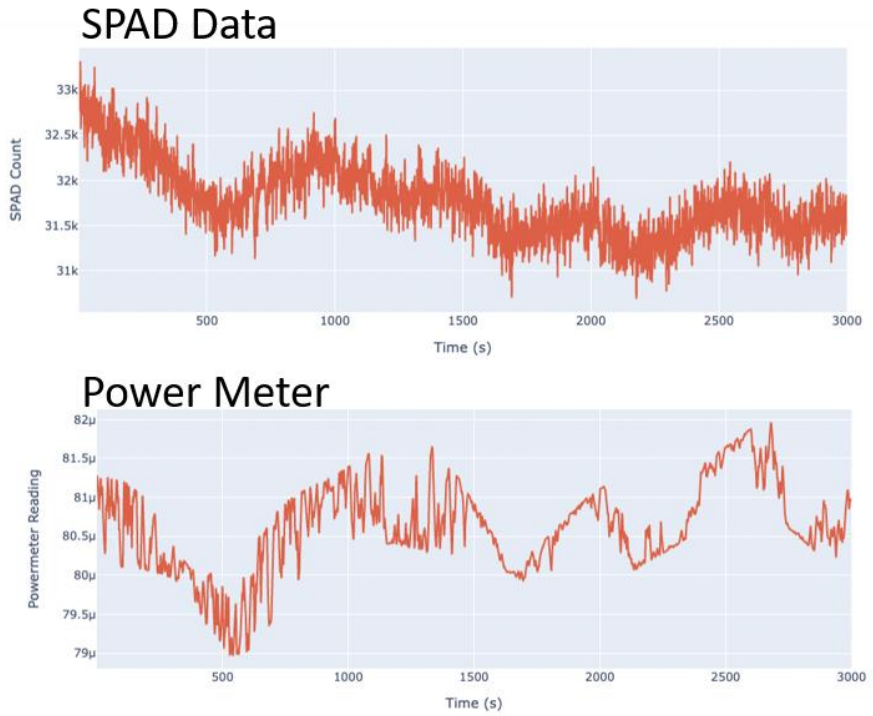

Figure 2.11: Top: the SPAD counts showing the modulation caused by power fluctuations from the laser source, Bottom: the recorded power fluctuations as seen by the 1% tap and power meter.

The total available optical power after the fiber isolator is approximately 12mW at the fiber launch and effectively limited to 6-8mW on the sample after coupling losses into the probe (due to butt coupling losses and probe insertion losses which will be detailed in the following section).

Since the Superlum lacks an active wavelength measurement, the output wavelength of the Superlum was measured in 1nm steps and repeated 100 times per each wavelength using a wavemeter (Bristol 621, Bristol Instruments, NY). The results, given in Figure 2.12, show that the output wavelength is constantly shifted by +0.25nm compared with the requested wavelength. Additionally, towards the edges of the Superlum gain curve (see Figure 1.19a) the wavelength fluctuates significantly and can reach deviations of up to 2-3nm in the 770-785nm tuning range, limiting the effective tuning range of this source.

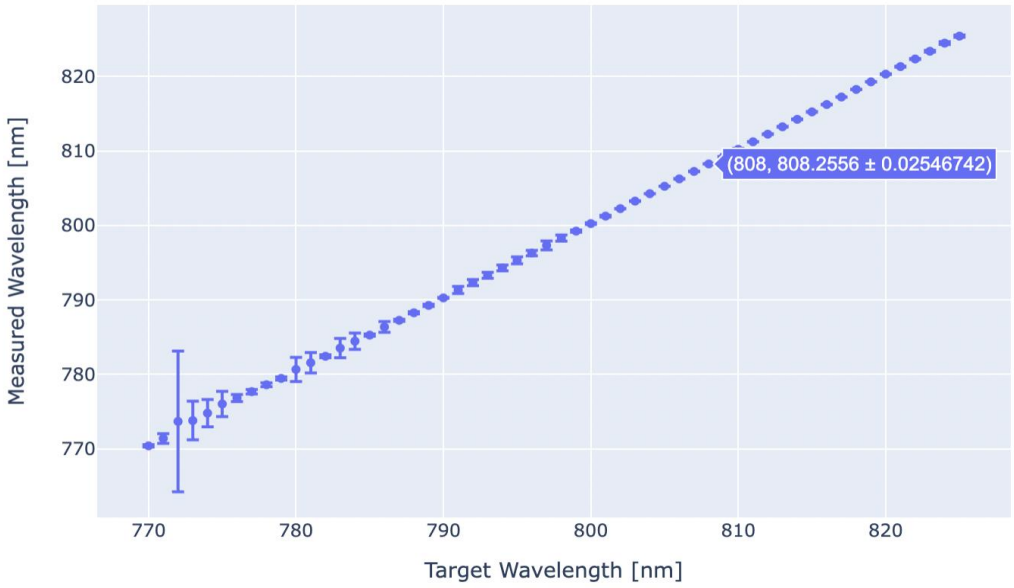

Figure 2.12: Superlum wavelength output stability vs. requested wavelength. The laser has significant wavelength fluctuations at the edge of the operation range and generally suffers from a +0.25nm offset compared with the requested wavelength, which needs to be calibrated for.

These results are further illustrated in Figure 2.18, showing glucose spectra acquired with both tunable sources and showing the spectral shift due to the Superlum wavelength shift.

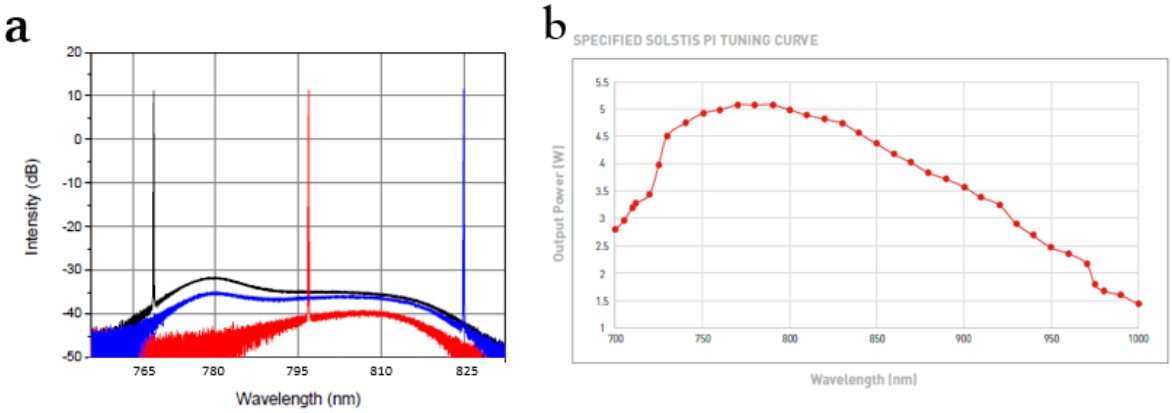

Figure 2.13: The output power as a function of wavelength for the (a) Superlum and for the (b) SolsTis Ti:Sapph, showing the dependency of output power on wavelength which affects the spectra baseline.

Both tunable lasers above have gain curves, i.e. the output power depends on

the wavelength. Figure 2.13 shows the output power as a function of wavelength for the Superlum (a) and the Ti:Sapph (b). To adjust and correct for the output power variation as well as power drifts, a 1:99 SM broadband fiber tap (TW805R1A1 for the Superlum and TW850R1A1 for the Ti:Sapph, Thorlabs, NJ) was introduced to continuously monitor the laser output using a power meter (PM101, with a s S120C power head, Thorlabs, NJ).

The SPAD, power meter and Superlum are USB controlled while the Ti:Sapph control module is accessible via ethernet or internet connection. A complete system diagram is given in Figure 2.14. The instrumentation was controlled using python drivers and libraries (written by Gavin West, Jaehwan Kim, Dodd Gray, Nili Persits and Dahlia Dry) and had a webpage-based graphical user interface written by Dahlia Dry to facilitate instrumentation control and data analysis and visualization (see Figure 2.15).

One of the concerns in the early stages of the design was that using a SM source and MM fibers would create mode instability in the excitation. Initially, a few SM probes were manufactured (see Section 2.2.2) but once MM fibers were found to be preferable in regards to coupling efficiency, attenuation and cost, the probes were made with MM excitation. To mitigate possible effects of mode instability, a mode scrambler was introduced immediately after the laser output SM fiber (#SMC085001014AS21011, AC-Photonics, CA). The scrambler has a SM 780HP fiber input and a 50/125µm MM GRIN output, which is also compatible with the 62.5µm probe input fiber. When the scrambler was connected, a 1:99 broadband 50µm MM tap (TM50R1F1B, Thorlabs, NJ) would replace the SM tap and be placed after the scrambler (see Figure 3.4). Notably, when the system was connected no effects of mode instability were detected without the scrambler and so it was removed from following measurements as it was introducing additional attenuation.

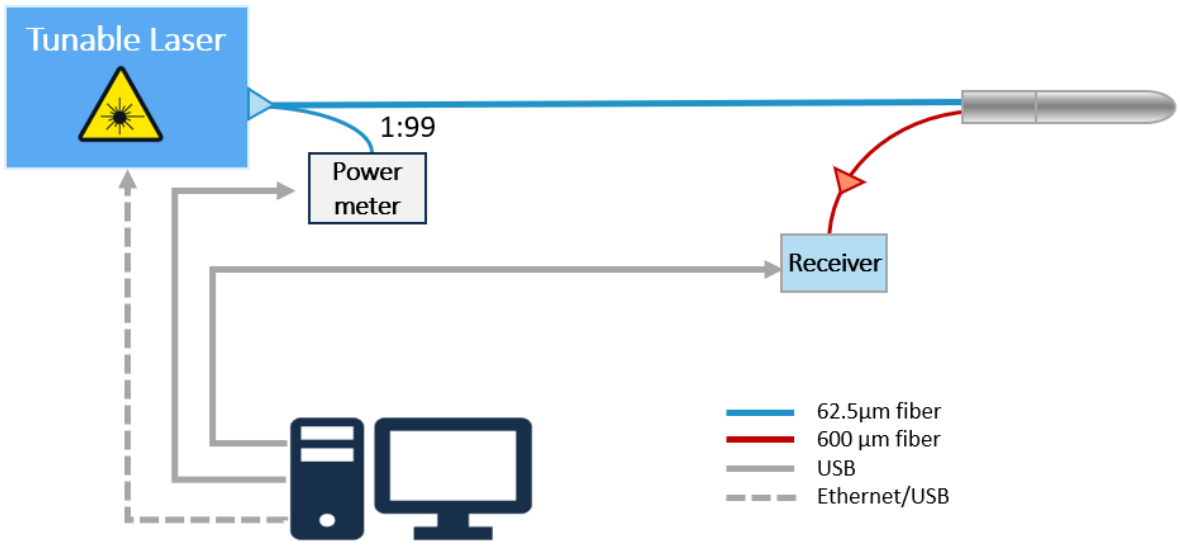

Figure 2.14: A single probe SSRS system diagram showing major components and connections. The laser power is monitored externally using a 1:99 optical tap connected to a power meter. The lion's share of the light passes through to the input of the SSRS probe. The SRSS output is connected to the optical receiver which detects the light. All components: the laser, power meter, and SPAD are controlled via USB and a custom python script by the main computer.

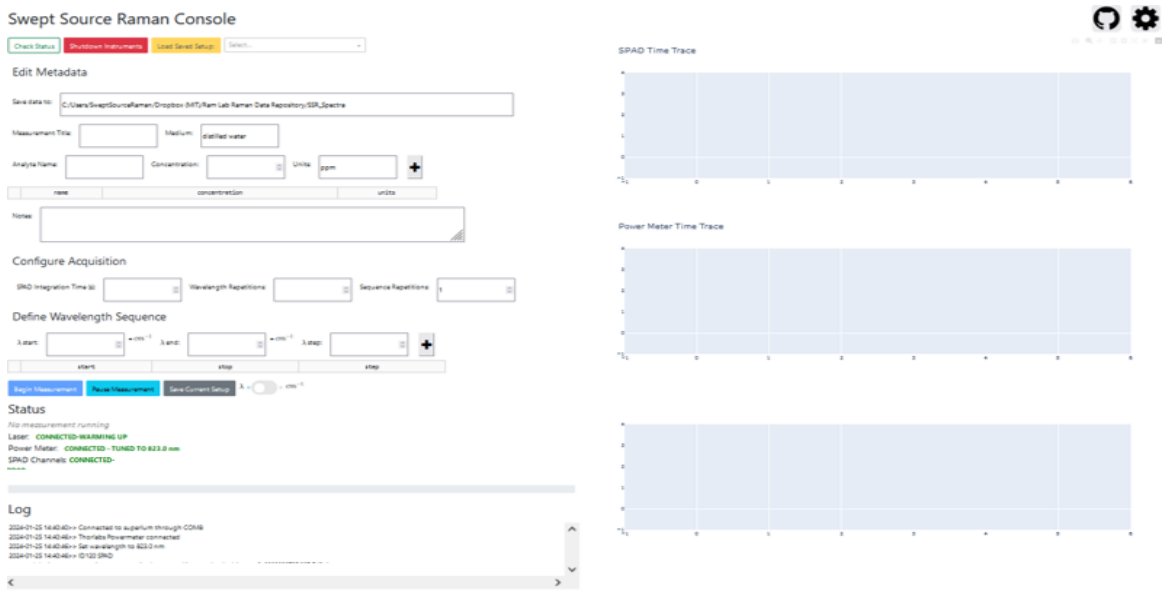

Figure 2.15: A screen shot of the Python GUI interface to control the measurement and perform quick data analysis written and maintained by Dahlia Dry.

Both lasers were measured for power output and stability in their relevant tuning range, and show output powers and fluctuations with wavelength dependency, as seen in Figure 2.16, that mostly follow the lasers gain curves (see Figure 2.13).

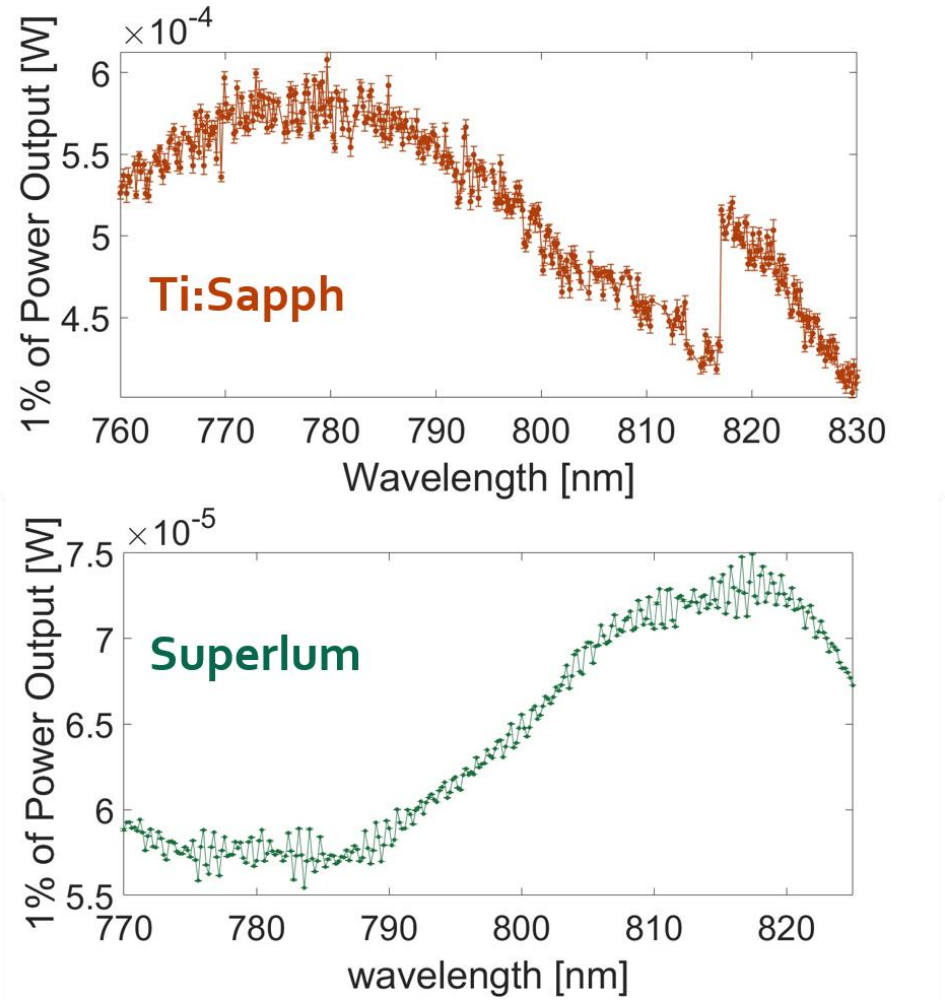

Figure 2.16: Power output and stability as a function of wavelength in the range of 760-830nm for the Ti:Sapph (top) and 770-825nm for the Superlum (Bottom).

From the above figures, a few additional important details emerge. The Ti:Sapph has a tuning hop around 818nm, which has to do with a coarse change in the laser cavity tuning (etalon). Attempting to tune to wavelengths in the immediate vicinity of this wavelength resulted in extreme wavelength instability and errors. Furthermore, the Ti:Sapph requires between 2-3 hours to heat up and reach thermal

equilibrium and should not be used before then. Both lasers don't show smooth power curves due to the step-wise tuning and while they are capable of continuously tuning the wavelength in a way that might increase tuning smoothness, the scanning speeds (>1nm/sec) are too fast for the SPAD and would compromise the spectral resolution.

When comparing the power stability for a single wavelength, it was evident the Ti:Sapph has significantly higher power fluctuations compared with the Superlum (see Figure 2.17). The output was measured at the lasers' fiber launch at a wavelength of 800nm over 30 minutes. The Ti:Sapph power had a STD which was 1.1% of the mean value, while the Superlum had a STD of only 0.29% of the mean value, making the Ti:Sapph "noisier" by a factor of 3.5. For comparison, the 830 nm IPS laser used with the dispersive system only has a 0.04% STD over mean value. Importantly, Ti:Sapph lasers are affected greatly by the optical laser pump that drives them. The measured fluctuations shown below are indicative of an old pump laser and can be reduced with a newer laser.

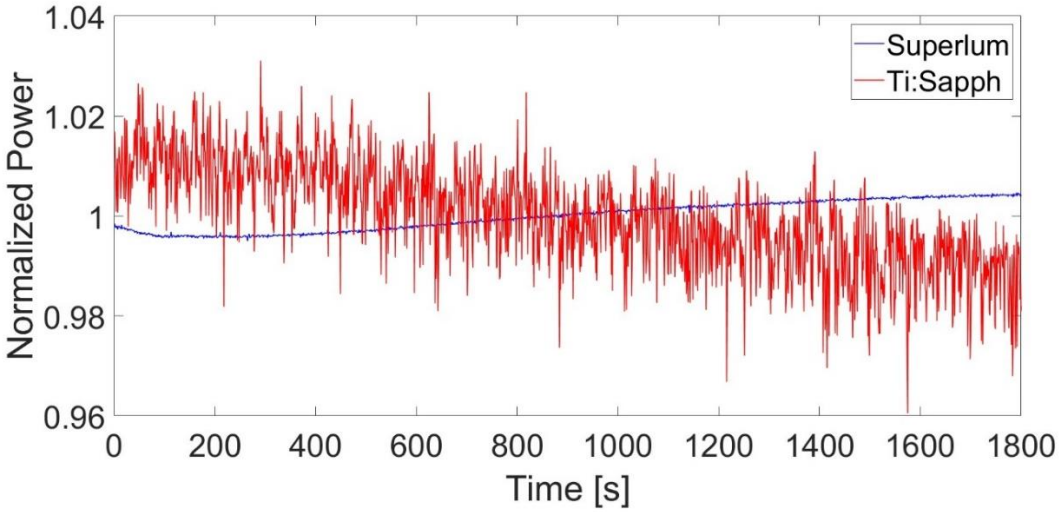

Figure 2.17: Tunable sources output power stability versus time with the Superlum in blue and the Ti:Sapph in red for 800nm excitation. The measurements were normalized to the mean, showing the large variance in output power for the Ti:Sapph, introducing measurement noise.

These results further emphasize the importance of closely monitoring the output power for each measurement in order to evaluate the added noise and correct for significant power drifts or hops in the data during post-processing.

2.2.2 SSRS Probe System Performance

Figure 2.18 shows normalized unsmoothed spectra of a glucose solution (50 g/L) taken with both the Ti:Sapph and Superlum lasers in the 770-825nm wavelength range (809-1675cm^{-1}) with the 0.25. Both spectra were collected over 367 wavelengths, with 1 second integration time per data point, repeated 10 times and the sample was placed in a quartz cuvette with 1mm thick walls (CV10Q35, Thorlabs, NJ). The power on sample was 6mW for the Superlum and 60mW for the Ti:Sapph. The Superlum shows a slight wavenumber deviation of 2-4cm^{-1} compared with the Ti:Sapph since tuning is not based on active control but rather on a look-up table (see Figure 2.12). The spectrum is weighted according to the excitation power per wavelength so that the laser gain curve isn't reflected in the spectra.

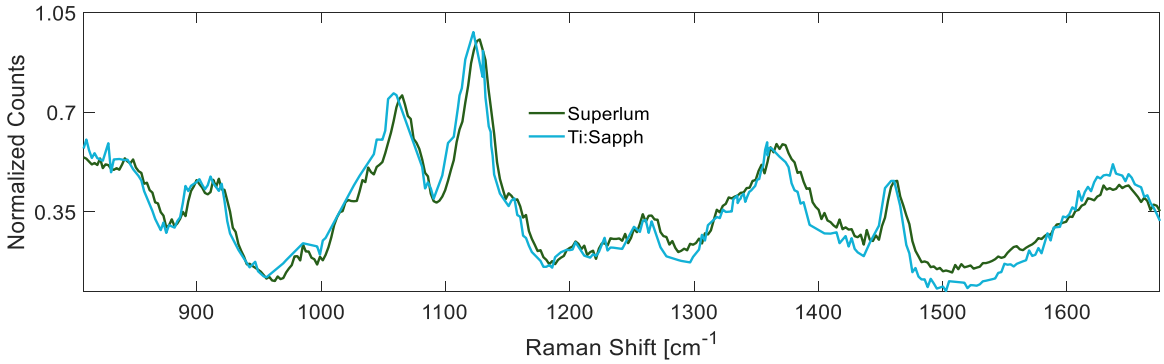

Figure 2.18: Glucose solution, 50g/L in water spectra acquired with the SSRS probe using the Superlum with 5-6mW (dark green) and Ti:Sapph with 50-60mW (light blue) showing slight wavenumber shifts due to tuning differences. Both spectra were acquired with 1 second integration repeated 10 times per data point using a quart cuvette

2.2.2.1 Étendue

As calculated in Section 2.1.2, the SSRS probe system has an expected theoretical étendue of 0.22mm^2, which is 36 times that of a standard dispersive Raman probe. Along with the insertion losses, and collection losses caused by misalignment and fabrication non-idealities (see Table 2.3), the collection is bound by 60% collection efficiency, effectively limiting the possible collection enhancement to a factor of x21.

A pure comparison of the SSRS probe and a standard Raman probe is quite challenging since the standard Raman probe only allows 830nm excitation, and the SSRS probe cannot be used with a dispersive spectrometer (without adversely affecting the resolution).

Therefore, a partial comparison is made solely for the throughput by using an 830nm excitation source (IPS, NJ) and measuring the collected output power directly at the output fiber port from a highly fluorescent black frosted quartz cuvette (CV10Q14, Thorlabs, NJ) with a calibrated power meter (Thorlabs, NJ). In this manner, both probes, which have identical 0.25NA objective lenses, observe the same sample, with the same excitation, creating a strong signal so that it can be measured via a standard un-cooled power meter.

The SSRS probe showed a consistent 12-factor enhancement in power collection compared with the standard probe, lower than the upper bound of x21. This discrepancy between theory and practice is attributed to misalignment of the large collection fiber that was reported as problematic by the probe manufacturer and was iterated upon several times (see Subsection 2.1.1.2). Even when the optical components are carefully considered and optimized, final alignment of the input and output should be done simultaneously while observing a Raman sample, and this was

not carried out during the probe assembly.

2.2.2.2 Spectral Resolution

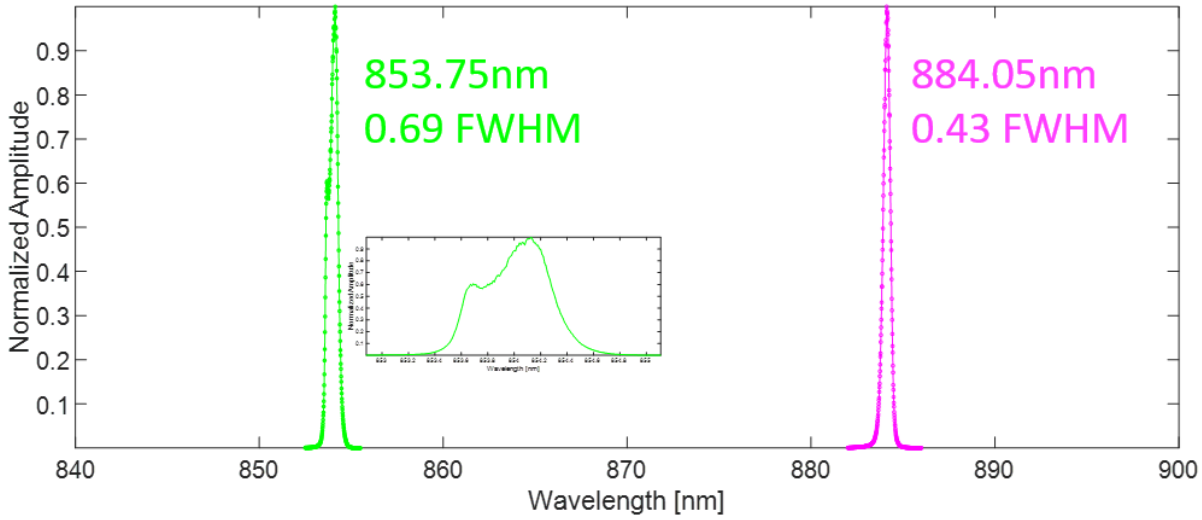

Figure 2.19: Alluxa UNBF filters transmittance as measured in lab, and an inlay showing a manufacturing problem for the 853.75 filter showing an irregular jagged profile. The transmittance was measured by tuning the Ti:Sapph in the filter wavelength range and measuring the ratio of output to input power.

The SSRS spectral resolution is determined by the UNBF. Our custom 884nm 0.45nm FWHM filter was measured by the manufacturer (see Figure 1.17) (Alluxa, CA) and also verified in lab, by measuring the transmittance when the Ti:Sapph laser was tuning across the filter spectral range. The 853.75nm filter was also measured and both filters are shown in Figure 2.19.

The 884nm filter showed similar results to the ones reported by the manufacturer, however, the 853nm filter shows a deviation from the expected Lorentzian profile (see small inlaid figure). These thin-film filters are made in batches by various coating layers and some processes can deviate from specification and result in artifacts. An evaluation of each batch should be performed to guarantee performance.

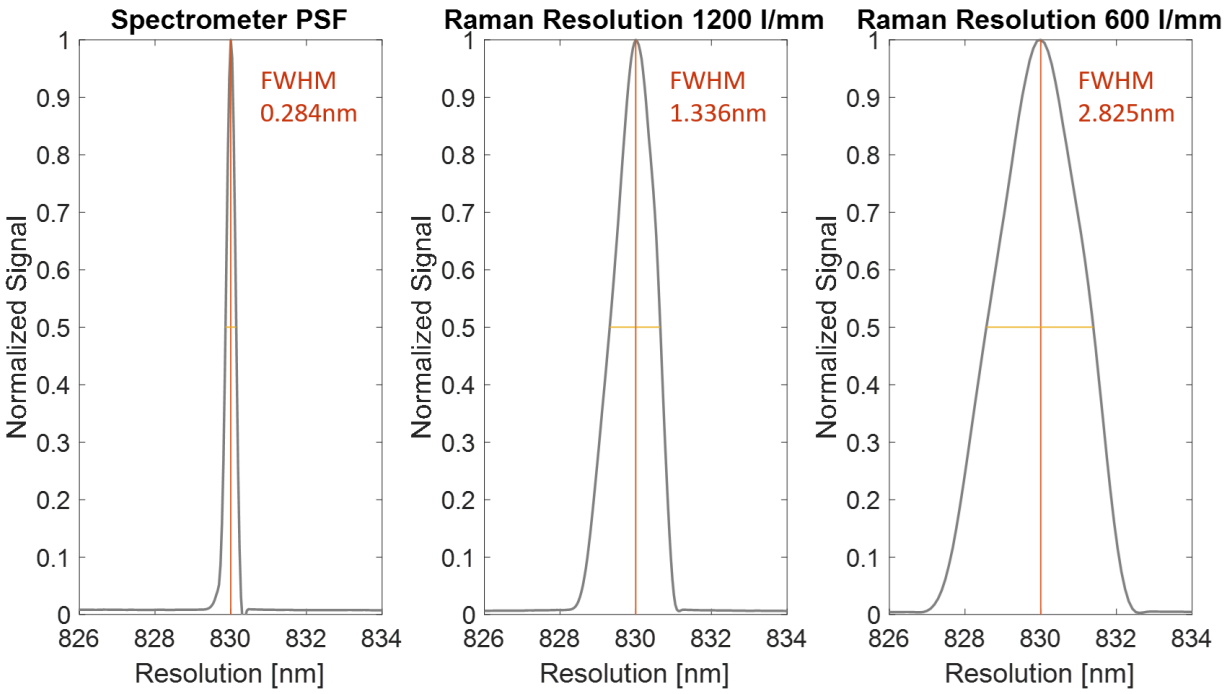

Figure 2.20: Spectral resolution for the dispersive Biomod system. Left- PSF estimation with a SM fiber input, center –laser line resolution with 200µm slit and 1200 lines/mm 750nm blazed grating, right – laser line resolution with 200µm slit and 600 lines/mm 1µm blazed grating.

The SSRS probe spectral resolution was benchmarked against our custom backscatter dispersive benchtop system (named Biomod). The Biomod uses 120-150mW of 830nm excitation and a LN2 cooled spectrometer (Acton SP-300i), with a 1µm-blazed grating with 600 lines per mm. A custom small-volume (40µL) sample holder with a 0.15mm fused silica window holds the sample. A 0.75NA objective is used for excitation and collection of the Raman photons which are then coupled into a 7-fiber bundle with 200µm, 0.22NA fiber cores (62% fill factor - BFL200LS02, Thorlabs, NJ).

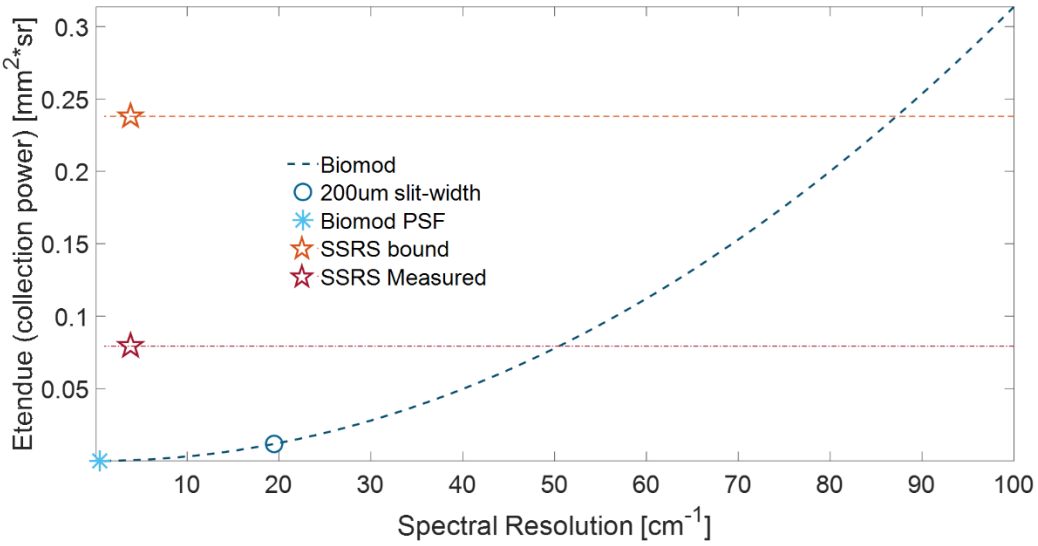

Figure 2.21: A plot of étendue vs. spectral resolution for the SSRS probe (orange line: theoretical bound) where the star shows the current UNBF filter, (red line – measured value) and our custom dispersive system with a 7 collection fiber bundle (blue circle) and PSF in light blue star.

The Point Spread Function (PSF) of the Acton spectrometer was estimated by measuring the laser-line width when inputted by a SM fiber (5μm core, P3-780Y-FC-1, Thorlabs, NJ) into the spectrometer slit and using a 750nm-blazed grating with 1200 lines per mm. This measurement stands for the highest resolution achievable by this spectrometer which is 0.284nm or approximately 4.1 cm^{-1}. The laser line was also measured when the excitation was introduced using the 200μm 7-fiber bundle to show the resolution decrease with enhanced slit-width. This measurement was done for both gratings to show the effect of the grating on the resolution. Figure 2.20 shows the resolution of the Biomod and demonstrates that the SSRS resolution is better than that achieved with the dispersive spectrometer with a 200μm slit width.

Figure 2.21 (based on Figure 1.15) compares the SSRS probe collection power and spectral resolution with that of our dispersive Biomod (assuming a x7 étendue enhancement due to the fiber-bundle collection). Since the collection is bound by the fiber, the SSRS étendue is constant, regardless of the spectral resolution which is

determined by the UNBF. The orange line and star show the upper theoretical bound for the SSRS probe, and the red line and star show the measured values, described in 2.2.2.3. The blue light star shows the PSF of the Biomod and the blue circle shows the measured resolution and calculated étendue for the 7-fiber bundle.

Importantly, by increasing the fiber diameter to 1000µm (FP1000ERT, Thorlabs, NJ), and using a 1" Ø UNBF, it is possible to reach the SPAD étendue value of 0.617mm^2 and almost tripling the bound for the theoretical collection efficiency without compromising resolution.

2.2.2.3 SSRS Probe Sensitivity (SNR)

As detailed in Subsection 1.3.2, the sensitivity, i.e. the expected SNR of a Raman system for a known sample, can be evaluated by two methods: the analytical route, using Equation 1.21, by which many parameters of the setup and sample need to be measured or approximated, or by conduction an LOD measurement (see Figure 1.9) which provides a fast and efficient estimate of the system sensitivity without getting into the weeds.

The glucose LOD was measured with a NA=0.25 SSRS probe using both tunable sources. Due to the Superlum wavelength shift between command and output, the wavelength was first scanned for the glucose peak exact position (1125cm^{-1}) with a high concentration (50g/L) solution and found to be at 803.9nm (versus 804.0nm with the Ti:Sapph). The Superlum was used with 5mW of output power (on sample) while the Ti:Sapph had approximately 32mW and the Biomod used 150mW. The glucose solutions were placed in a quartz cuvette.

All spectra were acquired over 10 seconds, repeated 50 times to establish mean and standard deviation values and compared for the primary glucose Raman peak. Figure 2.22 shows the LOD plots for all measurements.

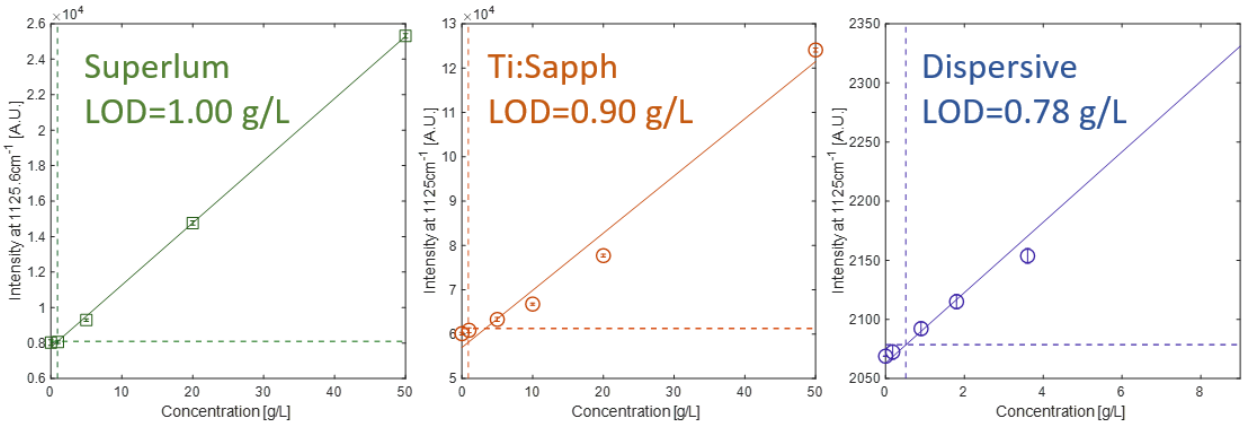

Figure 2.22: Glucose SSRS probe 3σ LOD results for the Superlum with 6mW (green, left)), Ti:Sapph with 40mW (red, center) and a dispersive benchtop using 150mW at 830nm excitation with a 7-bundle fiber collection. All spectra were acquired with 10 seconds integration repeated 50 times.

The LOD values were 1.00g/L, 0.90/L, and 0.78 g/L for the Superlum, Ti:Sapph, and dispersive system respectively. Despite significantly lower excitation power (20% for the Ti:Sapph, and 4% for the Superlum), the SSRS glucose LODs are lower than 1g/L (5.55mmol/L) and on the same order of magnitude as that of the dispersive system. The SSRS probe proved to be over 4 times more sensitive than the custom benchtop dispersive system for every milliwatt of excitation.

As a reminder, Equation 1.14, repeated below for convenience, lists the noise contributing elements in our system:

$$\sigma_{tot} = \sqrt{(\sigma_s^2 + \sigma_b^2 + \sigma_d^2 + \sigma_F^2 + \sigma_r^2)} \cong \sqrt{\sigma_s^2 + \sigma_b^2} \tag{1.14}$$

Where the background shot noise, σ_b^2 and the Raman peak signal shot noise, σ_s^2 are assumed to be dominant and the dark noise was assumed to be negligible. In the case of the Superlum water measurement (0g/L of glucose), the signal due to the water background was $\sigma_b^2 \cong 8030$ counts per 10 seconds, and the dark counts $\sigma_d^2 \cong 500$ counts per 10 seconds, justifying our assumption that this measurement is shot-noise limited. The theoretical total noise, $\sigma_{tot} \cong 90$ closely matched the noise measured of 84 counts per 10 seconds. For the 50g/L glucose solution, the signal

intensity is sufficiently high, becoming the dominant shot noise factor and increasing the total noise to an expected 160 counts, with 141 counts measured.

When using the Ti:Sapph with 6.4 times the excitation power compared with the Superlum, the water background signal increases to 60130 counts per 10 seconds, corresponding to an expected $\sigma_b \cong 250$, however, the data is significantly noisier with measured values of $\sigma_{tot} = 310$. The laser fluctuations were consistently measured to be between 3.4 and 4 times larger than those of the Superlum, as seen in Figure 2.17, adding noise to the process.

Despite the x6.4 increased power of the Ti:Sapph compared with the Superlum, and the shot-noise limited receiver, expected to yield a $\sqrt{6.4} \cong 2.5$ SNR enhancement (see Equation 1.21), the enhancement is impaired by the addition of laser fluctuation noise. Noting the added laser noise as σ_L^2, we can be model the total noise according to the following Equation:

$$\sigma_{tot} \cong \sqrt{\sigma_s^2 + \sigma_b^2 + \sigma_L^2} \tag{2.2}$$

Looking at the Ti:Sapph water measurement, and plugging the values, we reach an estimation that $\sigma_L^2 = 35470$ counts per 10 seconds.

We can further calculate the expected SNR gain for the Ti:Sapph compared with the Superlum with the added laser noise when the excitation power is increased by a factor of p_x:

$$SNR\ Gain = \frac{SNR\ (Ti{:}Sapph)}{SNR\ (Superlum)} \cong \frac{\frac{p_x(B+S)}{\sqrt{p_x(B+S) + \sigma_d^2 + \sigma_L^2}}}{\frac{B+S}{\sqrt{B+S+\sigma_d^2+\sigma_L^2}}} \tag{2.3}$$

Plugging the data from the Superlum water measurement where the signal due to the Raman peak is 0 and the background comprises the entire signal counts, the SPAD dark noise is negligible, as is the laser noise for the Superlum, we reach:

$$SNR\ Gain \cong \frac{\frac{6.4B}{\sqrt{6.4B + \sigma_L^2}}}{\frac{B}{\sqrt{B}}} \tag{2.4}$$

The results are plotted in Figure 2.23 where the red dot stands for the measured excess laser fluctuation counts, reducing the SNR gain to 1.15, matching the results for the Superlum and Ti:Sapph LOD.

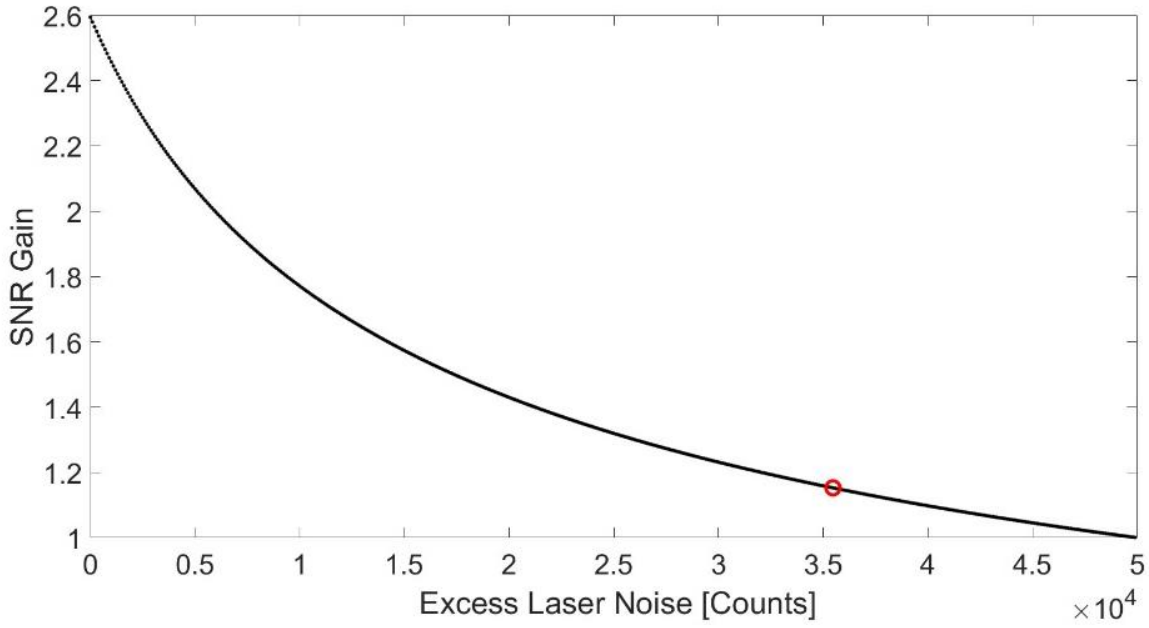

Figure 2.23: SNR gain enhancement of the Ti:Sapph laser compared with the Superlum when accounting for both the excess laser power and additional laser fluctuations as described in Equation 2.4. The red dot marks the gain enhancement in the LOD measurements in Figure 2.22.

These results illustrate the significance of the tunable source stability for the overall system sensitivity and the need to reduce power fluctuations.

2.3 Application Demonstration: Nitrate Monitoring

Now that the SSRS probe sensitivity has been verified and benchmarked, we move to show the usefulness of SSRS probes in monitoring nitrate in a hydroponic

setup and the monitoring of additional agriculture pollutants in water.

2.3.1 Nitrate LOD

Figure 2.24: Immersion sleeve insertion setup for nitrate in water measurements with the sleeve inserted into a custom fabricated bottle cap to allow easy replacement of measured liquids without disturbing the probe.

Nitrate is an important agricultural fertilizer and a significant environmental pollutant (see Subsection 1.7.1). To establish the sensitivity for nitrate monitoring with SSRS, a nitrate LOD measurement was performed with the SSRS probe and using the Ti:Sapph at a wavelength of 809.2nm and our Biomod benchtop dispersive system (detailed in the previous Section). The SSRS probe was used with an immersion sleeve (1mm fused silica window) and inserted into a 100ml bottle with a custom-made cap that help the immersion sleeve in place. It is crucial to prevent any relative movement between the probe and sleeve since they create varying background spectrum counts (due to the changing distance to the sleeve window)

The SSRS probe used 50mW with 1ml samples placed in a quart cuvette. The dispersive benchtop used 100mW illuminating a small 40µl droplet which was placed in a high-collection (0.7NA) free space system. As before, the integration period was

10 seconds, repeated 50 times. the LOD results for the dispersive system (blue) and SSRS probe (orange) are 48ppm and 22ppm respectively (see Figure 2.25), resembling previous works on the subject (see Subsection 1.7.1). Additionally, the EPA standard of 44ppm is represented by the gray-shaded area, showing the SSRS sensitivity is adequate to enforce regulatory standards in drinking water.

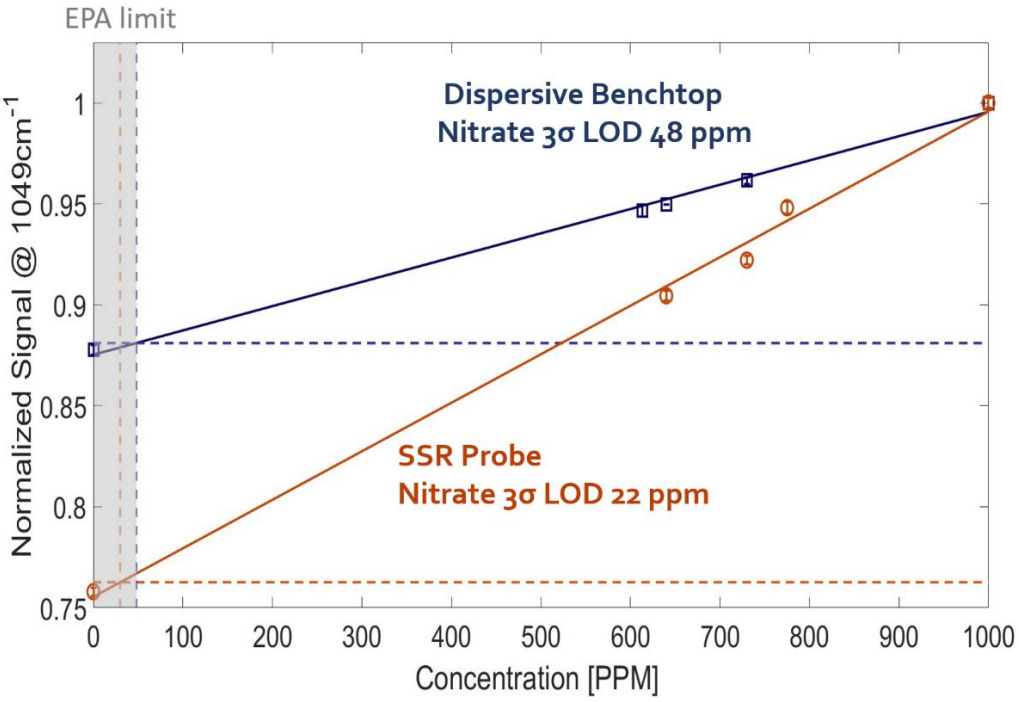

Figure 2.25: Nitrate 3σ LOD measurement using the Ti:Sapph and the SSRS probe with 50mW of excitation (orange) and the dispersive benchtop (blue) using 100mW of 830nm excitation for the nitrate peak at 1049cm^{-1} (10 second integration repeated 50 times)

Notably, the nitrate LOD is higher for the SSRS compared with the dispersive system, in contrast to the glucose LOD. Firstly, the laser output power was 50mW compared with 32mW on sample and accounts for an SNR improvement of $\sqrt{50/32} = 1.25$. Additionally, the laser power fluctuations at 809.2nm are a factor 2.2 lower in magnitude (STD over mean value) compared with the power stability for the glucose wavelength (804.0nm, see Figure 2.26), reducing the noise which impaired the glucose LOD measurement with the Ti:Sapph.

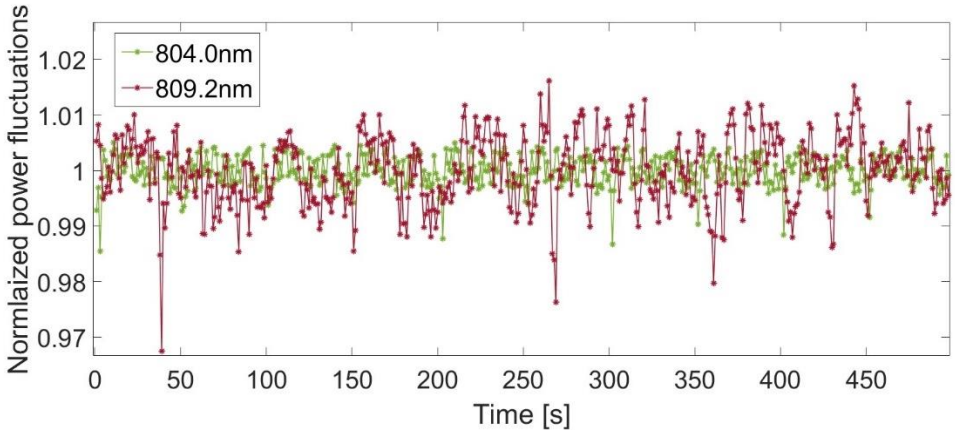

Figure 2.26: Ti:Sapph power fluctuations for the glucose peak wavelength (green) and the nitrate peak wavelength (red) showing the laser output power as well as stability depend on the wavelength.

To illustrate the difference in sensitivity between the SSRS and dispersive systems, Figure 2.27 shows mean-normalized histograms of the 50-nitrate peak[215] (1049 cm^{-1}) signal measurement repetitions for the 1000ppm standard nitrate solution (traceable to SRM from NIST, Millipore-Sigma).

The histograms show the signal distribution, and a gaussian fit, which is used to estimate the measurement noise (see Equations 1.42, 1.43 and Figure 1.24). The narrower distribution for the SSRS correlates to a lower standard deviation and enhanced SNR.

After the nitrate LOD was established for the SSRS, providing an important benchmark, a monitoring demonstration for a real-world application was necessary. The following Section describes the use of the SSRS probes to monitor the nitrate in a small-scale hydroponic setup.

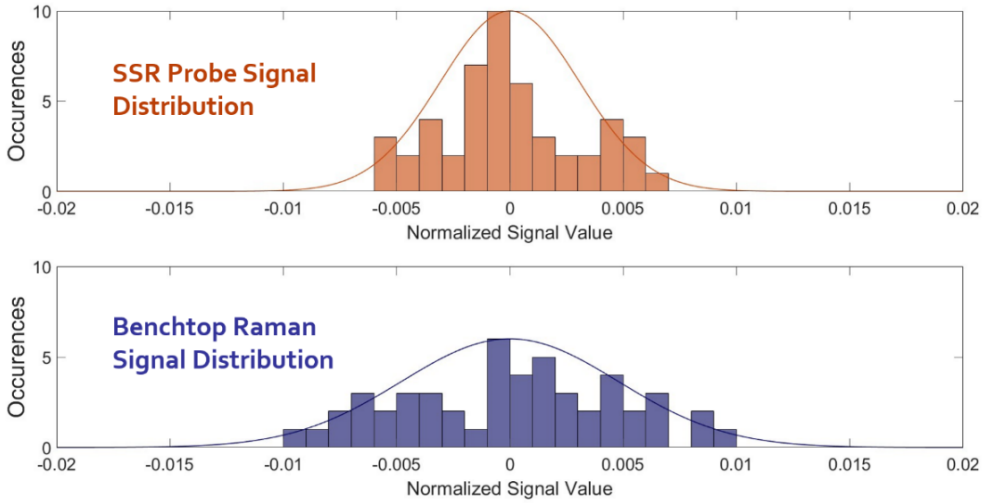

Figure 2.27: Histograms of the normalized standard deviation of Raman signal measurements for both dispersive Biomod and SSRS system on the nitrate 1000ppm NIST standard Raman peak signal with 50 repetitions and fitted Gaussian curves with the equivalent STD.

2.3.2 Hydroponic Nitrate Monitoring

Figure 2.28: Pictures of the Rise hydroponic lab setup used to grow a variety of plants. In the right-side picture, the nitrogen deficient system is on the left showing smaller, yellowing plants while the nitrogenous system on the right has large green plants.

Two small-scale, 5-liter water-recycling hydroponic system (Rise Gardens) were used to grow Pak choy (Toy choy hybrid, 2 units), Chinese broccoli (Early jade hybrid, 1 unit), mint (Peppermint, 2 units) and cilantro (Santo hybrid, 1 unit). The nutrient

media composition in the first system was nitrogenous and was prepared based on known recipes[244,245]. The second system had no nitrogen compounds and calcium chloride (CaCl) replaced the nitrogen salts. After media dilution in to the first water reservoir, the concentration of nitrate was 700ppm. Monitoring began exactly 5 weeks after planting and lasted for a week. Each hydroponic system contained 6 mature plant units, considered to be in a period of higher nitrate uptake[246]. Nutrient uptake depends on the plant strain and age and so is expected to vary throughout the growth cycle.

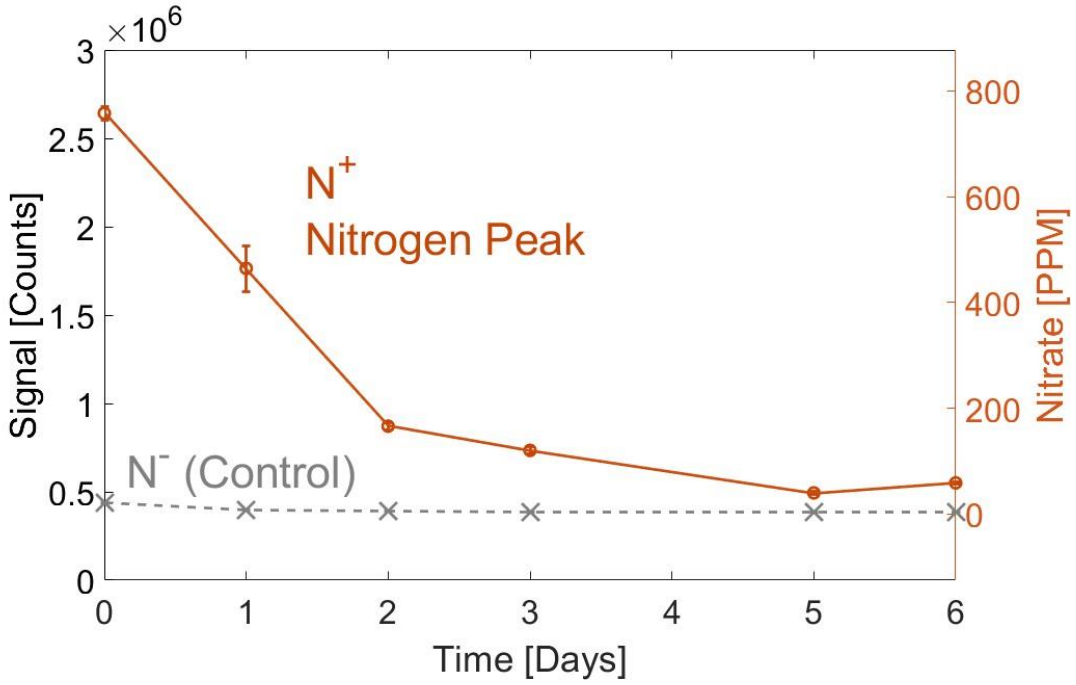

Figure 2.29: SSRS Nitrate peak signal as a function of time with 10mW of excitation 5 seconds integration repeated 10 times, monitoring both hydroponics systems water reservoir after media with nutrients was introduced on Day 0. The nitrate deficient system nitrate peak is in gray and the nitrogenous system is o in red.

Water from both reservoirs was measured daily in immersion mode by the SSRS probe using 10mW of excitation over a 30 seconds integration period, repeated 50 times to establish the standard deviation.

Figure 2.29 shows the nitrate peak (1049cm^{-1}) signal level for the two

hydroponic systems as it was recorded by the SSRS probe as a function of time (left Y axis), while also showing the approximated nitrate level (right Y axis) (Orange for nitrogenous and gray for nitrogen deficient). The nutrient media was introduced on Day 0 and a clear downward trend is visible through Day 6 where a replenishing of the media is necessary (The error bars on the control are not visible and are on the order of 1000 counts, approximately 0.2% of the signal level).

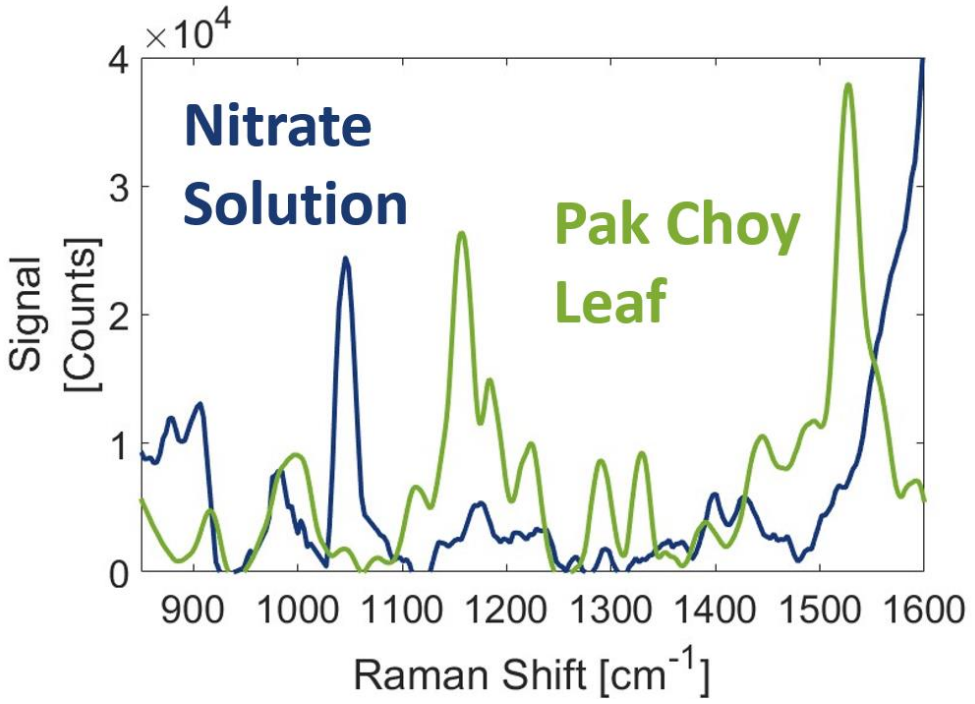

Figure 2.30: Spectra of a Pak Choy Leaf (green) and a NIST standard 1000ppm nitrate solution (blue) acquired with the SSRS using 10mW of excitation with 5 second integration repeated 10 times over 225 spectral data points between 770-825 nm.

The SSRS probe was also used to acquire the full spectrum of a Pak Choy leaf from the nitrogenous system with 10mW excitation, 5 seconds integration time repeated 10 times over 225 equally spaced data points between 770-825nm. Figure 2.30 shows both the leaf spectrum and the spectrum of the standard nitrate 1000ppm solution. The nitrate peak is clearly visible in the solution and in the leaf, while the leaf spectrum additionally has known carotenoid[247,248] (1521, 1153 cm^{-1}) and

cellulose[247] (1320 cm^{-1}) peaks. The nitrate solution spectra shows an artifact of Lieber-fit in the are of the water peak.

2.3.3 Estuary Water Sample

While nitrate is one of the most significant agriculture-related environmental pollutants, it is by no means the only one (see Table 1.1). Raman spectroscopy is particularly useful in identifying different compounds due to their distinctly different spectra. Figure 2.31 shows spectra of three common fertilizer compounds acquired with the SSRS probe (50mW, 1 second integration repeated 10 times): sodium nitrate (blue), urea (red) and ammonium sulfate (green). These compounds have clear Raman peaks that can be easily distinguished: nitrate (1049, 1382 cm^{-1}), urea (1005cm^{-1}), and sulfate (971cm^{-1}) where ammonium has known Raman peaks in the longer wavenumber region, approximately 3276, 3380 cm^{-1}.

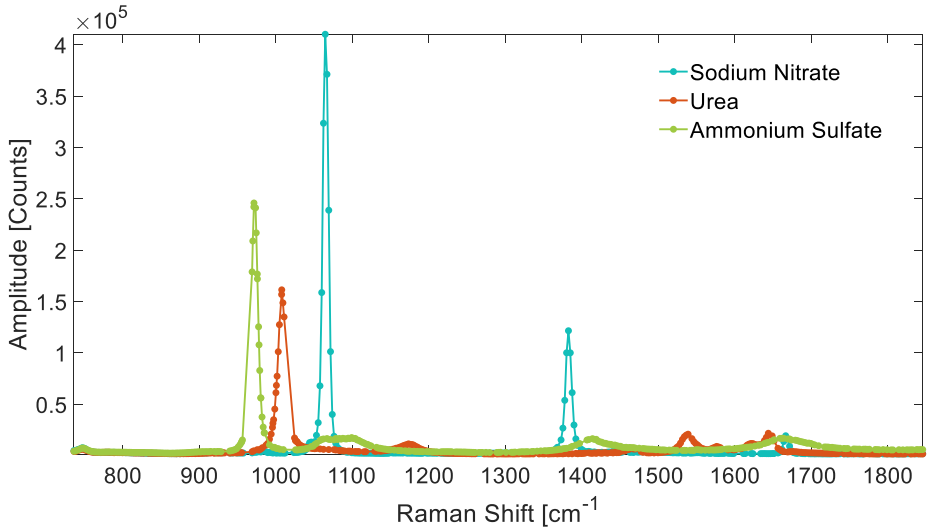

Figure 2.31: Raman spectra of fertilizer salts including Sodium nitrate(blue), urea(red) and ammonium sulfate(green), acquired with the SSRS probe with 50mW of excitation with 1 second integration repeated 10 times.

To prove the usefulness and utility of the SSRS probe on less familiar and controlled water samples, a sample was taken from the Falmouth estuary in Cape Cod,

Massachusetts in January 2022 (see Figure 2.32b) and measured in lab and compared to tap water and distilled water meant for cell culture (Gibco). Spectra were acquired with an immersion sleeve using 50mW with 5 second integration repeated 12 times. Figure 2.32a shows the comparison of these three water samples with a distinct sulfate peak centered on 971cm^{-1} in the estuary sample, exhibiting a spectral broadening compared with the solid sample in Figure 2.31 (see Subsection 1.4.2). While the tap water shows some spectral features, the distilled water sample shows no evidence of sulfate or other materials (other than the background signal generated by the 1mm thick fused silica immersion sleeve window). These water samples were not measured with any other method and so the results are not conclusive. However, sulfate enrichment in estuary waters has been documented[249] and is assumed to be related to the biochemical activity which depends on the hydrological conditions, affected by drought and climate change.

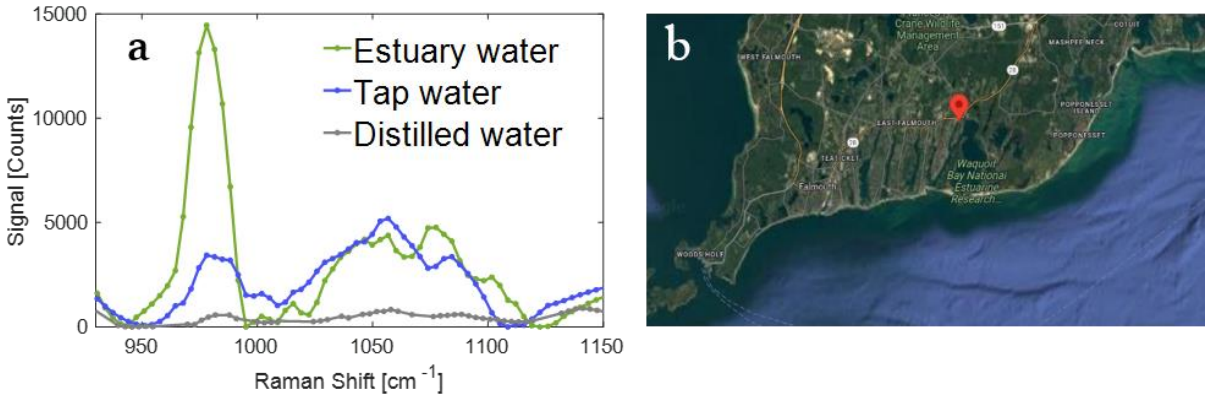

Figure 2.32: SSRS Spectra (50mW, 5 seconds integration repeated 12 times) of a a) Falmouth estuary water sample (green), tap water (blue) and distilled water (grey) showing a clear sulfate peak in the estuary water. b) Location of the sample origin in the Falmouth Estuary in Cape Cod.

2.4 Conclusions

In this chapter the SSRS probe design and proof-of-concept demonstration

were discussed. The étendue of the probe, bound by the collection fiber, closely matches that of the SPAD and UNBF, with some room for theoretical improvement by a factor of 2.8 which is the SPAD limitation. The fabricated probe performance, achieved a x12 throughput enhancement instead of the predicted x36 enhancement which is attributed to alignment and non-idealities in the probe's internal optics.

The probe's sensitivity was benchmarked using a quantitative LOD against a custom, high-throughput, dispersive Raman system which uses a 7-fiber bundle collection and was found to be 4 times more sensitive for every milliwatt of excitation. Additionally, the system was used to monitor nitrate in a small-scale hydroponic setup in both the water reservoir and growing plants, monitoring the fertilizer uptake. Lastly, the utility of the system was demonstrated for environmental water monitoring by measuring an estuary water sample without any sample preparation.

CHAPTER 3

Swept-Source Sensor Network

The sensitivity and resolution of the SSRS probe have been established in Chapter 2, proving it is comparable to dispersive benchtop systems as well as FT-Raman (see Section 1.4). However, in order for Raman to become a practical utility, a single-sensor system is insufficient. Utilities require a service to not only be essential, easy-to-use, and general, but also scalable [4,5]. Scalability includes both the size of the service area and the economical scalability, both of which determine the cost-effectiveness of the service. This chapter will demonstrate the scalability of SSRS using an optical fiber network, see Figure 3.1, and further illustrate the economic scalability of this approach.

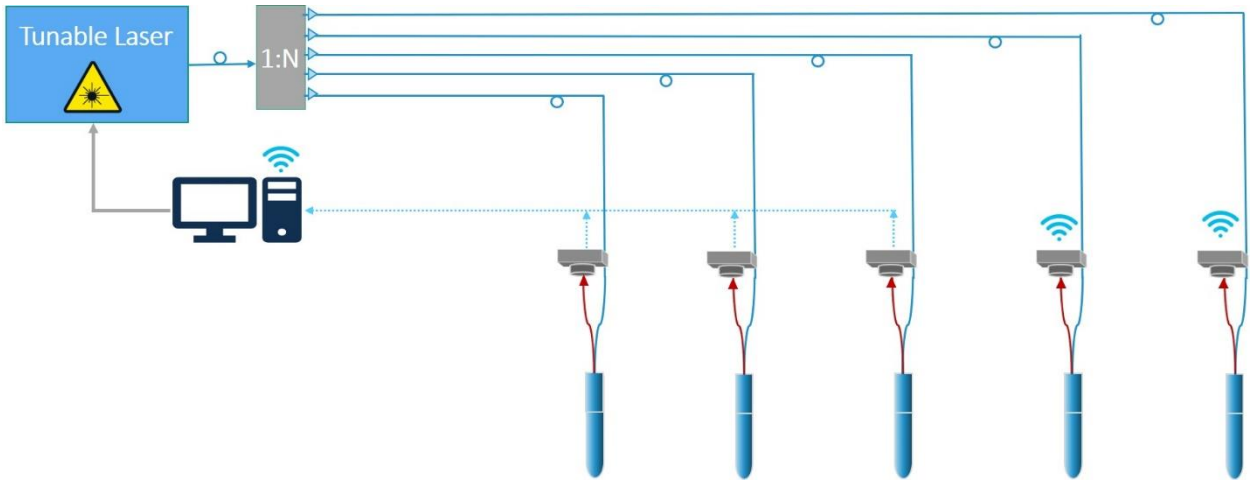

Figure 3.1: A diagram of the SSRS sensor network with multiple probes used with a single shared laser source. The laser is switched between different channels using a 1:N datacom switch and delivers excitation using GRIN optical fibers. The optical receivers can collect the data via USB ethernet or Wi-Fi modules.

Section 3.1 will detail the design and implementation of deploying a SSRS probe over large distances, enabling a large coverage area for sensing with a remotely positioned laser source. Section 3.2 will detail the optical data communication infrastructure enabling the use of a single tunable laser as a shared resource that can drive dozens of sensors simultaneously. Section3.3 will show a cost analysis of this method from a consumer stand-point and benchmark it against similar Raman sensor deployments using commercially available Raman systems. Finally, several potential applications for the SSRS sensor network will be given.

3.1 Long Distance Deployment

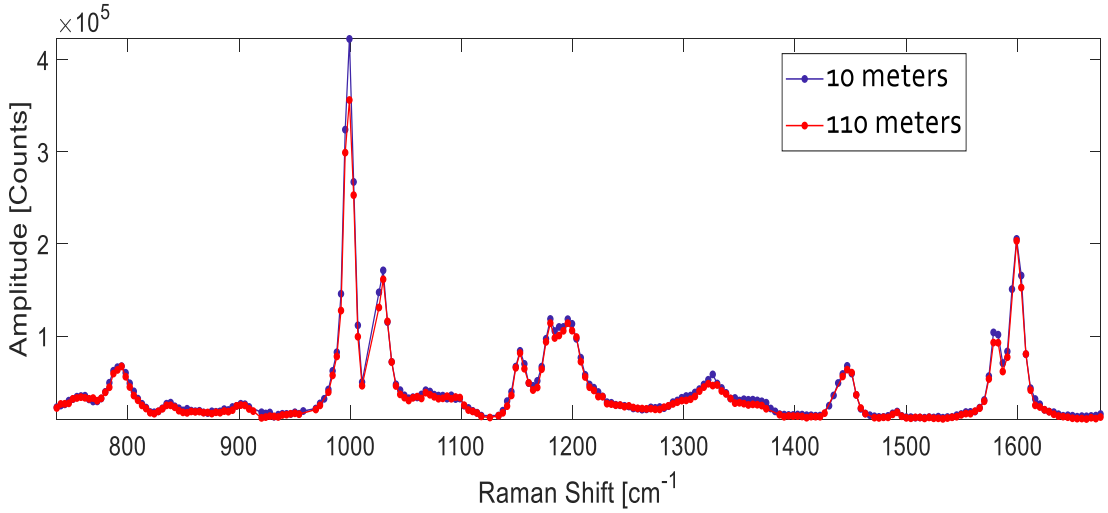

Figure 3.2: Polystyrene spectra (5mW, 2 seconds integration repeated 30 times) acquired for both a 10m long GRIN fiber (blue) and a 110 m long GRIN fiber (red), demonstrating the possibility of long-distance deployment with minimal changes to the acquired signal.

The feasibility of long-distance deployment of SSRS probes is demonstrated through the acquisition of polystyrene spectra with two different fiber lengths connecting the laser to the probe: 10m and 110m (62.5µm NIR GRIN fibers, Thorlabs, NJ). The spectra were acquired using 5mW of excitation with the Ti:Sapph

laser in the 770-830nm range with 2 seconds integration repeated 30 times, see Figure 3.2. The fiber attenuation is 2.9dB/km at 808nm[250], and this value is used as an approximation for the entire wavelength range.

The 110m polystyrene spectrum was attenuated by -0.74dB compared with that acquired with a 10m fiber, corresponding to 84.3% of the signal at 10m length. The expected attenuation due to the additional 100m length fiber is -0.29dB with two additional fiber butt-couples adding approximately -0.2dB each, totaling in -0.69dB, agreeing with experimental results. The silica Raman spectrum due to the fiber is not visible even with long fiber lengths since the probe has the cutoff filters integrated, attenuating the unwanted background. Mitigation of butt-coupling losses is easily accomplished by splicing the fibers together when the optical infrastructure is permanently deployed.

Importantly, a deployment of 1km of fiber would result in approximately 50% of the excitation power reaching the probe. As shown from the sensitivity analysis in Subsection2.2.2.3, even the Superlum laser source (20mW) can be used to deploy a SSRS probe to distances extending a kilometer and still reach comparable sensitivity to that of a dispersive benchtop system. Using a more powerful laser source such as the Ti:Sapph with output powers extending 1W, can be used to deploy an SSRS probe to distances greater than 7km while maintaining performance. An additional enhancement of this range can be done by moving to a design relying on 50μm diameter MM GRIN fibers which have lower losses (2.3dB/km)[250] and are also available Commercially Off-The-Shelf (COTS).

With the spectral data collected by the receiver deployed remotely, the issue of communication and data collection become pivotal. If sensors are deployed very close to the laser and control computer, USB connections can be used since they are fast and extremely reliable. USB 3.0 cables can reach lengths of up to 15 meters and have

been used successfully with the SPAD which has a built in USB port for control and data communication.

Alternatively, ethernet (using standard Cat5e or Cat6 cables) can reach lengths of up to 100 meters without requiring amplification. Most experiments in lab used either USB or ethernet to send the collected spectra from the receivers to the main control computer. Lastly, Wi-Fi module boosters with external antennas can reach distances of about 800 meters for reliable communication at speeds of up to 150Mbps. Longer deployment distances can leverage the optical fiber infrastructure already in place or require additional data communication installation which is beyond the scope of this thesis.

3.2 SSRS Sensor Network

On top of enabling remote deployment, the tunable source which has significant cost and considerable output power (particularly the Ti:Sapph), can be used as a shared resource to operate multiple sensors, thus allowing for physical and economical scalability of the SSRS network architecture. By additionally leveraging existing optical data communication infrastructure technology, chemical sensing as a utility is feasible.

To demonstrate the potential for large scale, multi-sensor deployment, the laser excitation from the Ti:Sapph was connected to a 16 channel optical fiber MEMS switch which controls the output using a dual axis tilting MEMS mirrors (DiCon Fiberoptics, CA) The switch has a 20ms switching time between channels. The insertion loss is specifried as 1.4 dB max (measured with an LED) but was measured for each of the channels at both 785 and 800nm and was found to be between 0.1-0.3 dB regardless of the wavelength, guaranteeing a high degree of uniformity between

the different network channels, see Figure 3.3.

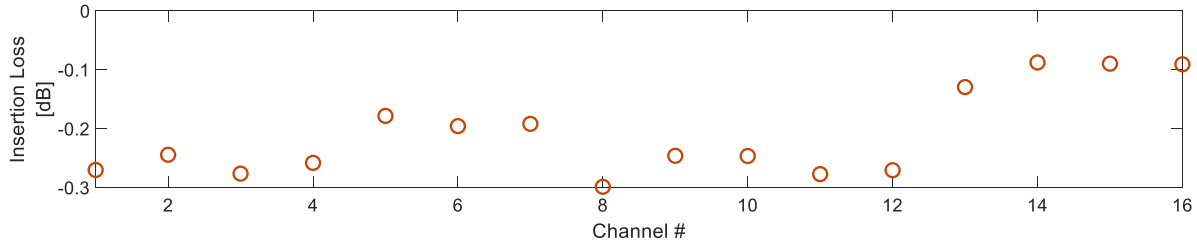

Figure 3.3: Insertion loss variation between all 16 channels of the DiCon optical fiber switch, not including insertion losses of the connectors, showing good uniformity between the channels.

Figure 3.4 shows a picture of the optical breadboard that hosts all the SSRS Raman network components connecting the laser and probes. Some of the components were introduced in early designs but are not part of the core design and their use is strictly optional.

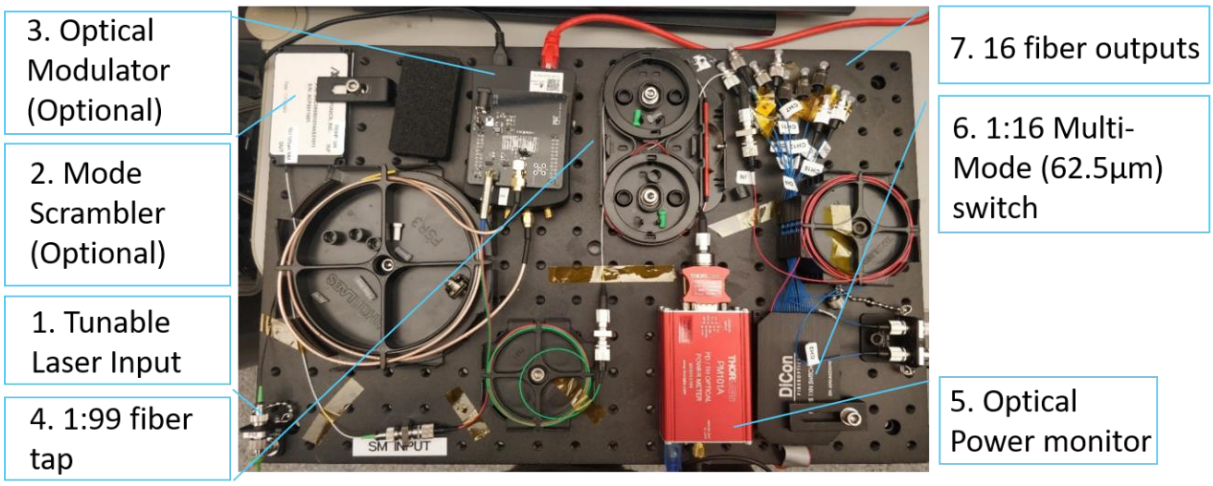

Figure 3.4: A picture of the SSRS optical board accepting the tunable excitation and delivering it to one of the 16 output switch channels with descriptions of the various components.

The first component of the network board is the tunable laser input (1), followed by a mode scrambler (2) (see Subsection 2.2.1). (3) An optical modulator (DiCon Fiberoptics, CA) with a Red Pitaya control unit was added to allow modulation of the excitation signal. Modulation of the laser allows us to perform lock-

in-detection and improve the SNR of the system when ambient light leaks into the detector[36]. Since the SPAD was particularly sensitive to room light and had to be covered to prevent saturation. (4) To monitor the laser output power (with or without modulation), a 1:99 MM broadband optical tap was introduced, similar to the 1:99 tap in the single-probe system. The 1% tap was connected to a Thorlabs power meter (5), connected via USB to the control computer. The 99% port was connected to the 1:16 switch (6) which was controlled via an RS232 port. Software control allowed to choose the required channel through which the excitation would be delivered.

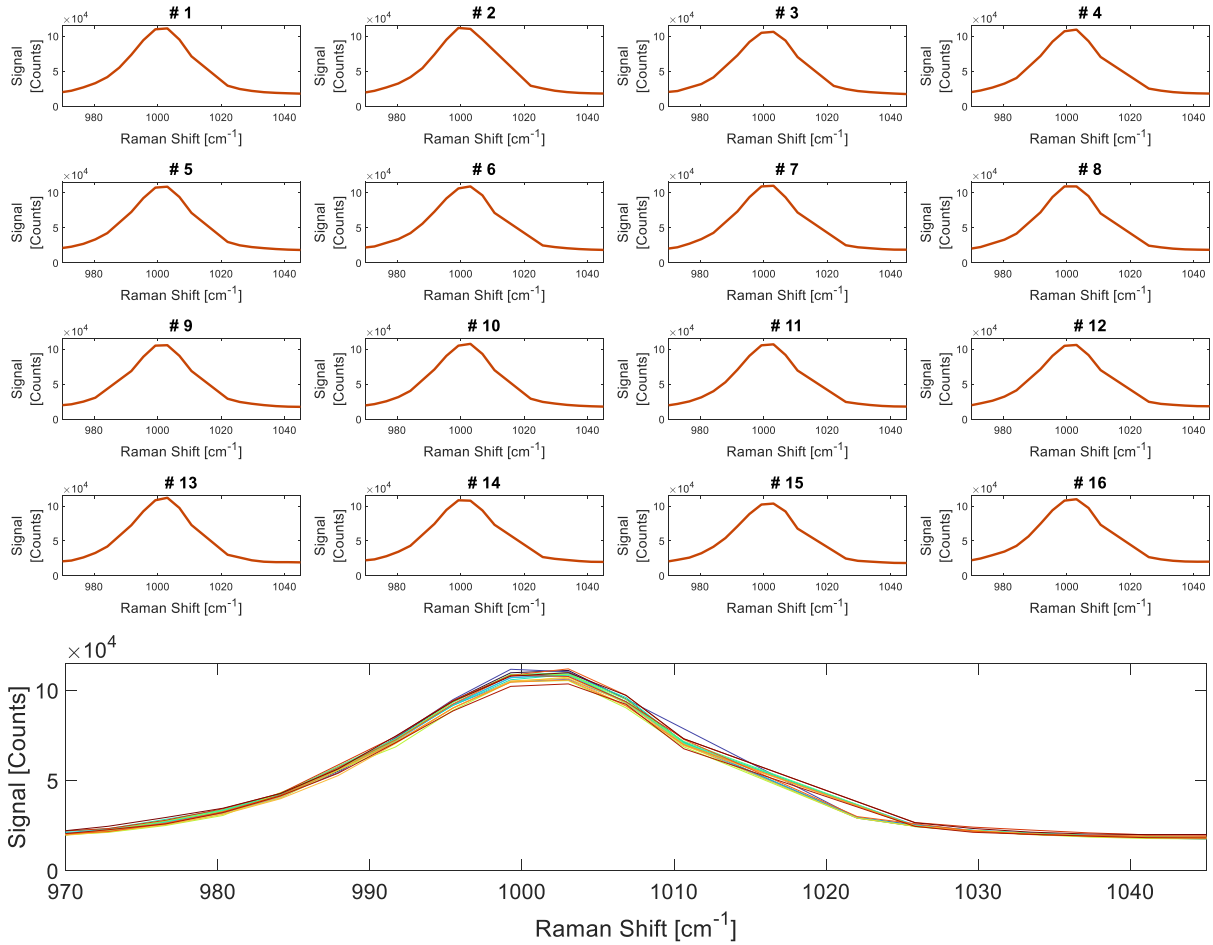

Figure 3.5: Top: Individual urea spectra acquired through all 16 channels of the optical switch using 50mW and 1s integration repeated 50 times, and bottom: all 16 spectra overlaid together to show their similarity.

To provide a proof of concept for the network operation, spectra of urea

($CO(NH_2)_2$) solution (10g/L), were acquired through all 16 channels using 50mW of excitation and 1s integration per each data point repeated 10 times. Figure 3.5 shows the signal acquired through each channel separately (top) and also the signals overlaid together for comparison (bottom).

The results show the feasibility of deploying a large number of sensors over significant distances while maintaining the desired sensitivity and resolution for chemical detection and quantification. Notably, the 1:16 switch allows only one channel to acquire spectra while the other 15 channels are idle. This approach is useful when data acquisition is infrequent and the laser must be time-shared, which could also be used to reduce the overall laser cost and use a lower power laser option. However, it is also possible to drive many sensors simultaneously using the Ti:Sapph. A full analysis exploring the performance and cost of multi-sensor systems is provided in the following section.

This section successfully demonstrated the feasible large-scale deployment of a SSRS network comprising16 sensors and covering large distances. However, to make this a utility, physical scale must be accompanied by an economic justification which will be given in the following section.

3.3 Cost Analysis and Potential Applications

The cost of a utility is key to ensuring it is scalable and can serve multiple applications and users. The cost also determines which users are most likely to be first adopters of a technology, particularly when it is emerging and costs of parts, labor and installation haven't been optimized. The following subsection will show a cost analysis of a few SSRS probe systems of varying size, followed by a few application examples that could be early adopters.

3.3.1 Economics of scale

In order to assess the economic feasibility of SSRS as a chemical sensing utility, it is helpful to frame a few key scenarios and estimate the cost of the SSRS approach vs deploying COTS Raman solutions with equivalent sensitivity. To facilitate the comparison, we focus on fiber Raman probes and not large imaging systems which have significantly higher costs.

The cost of the SSRS network can vary greatly based on system application and requirements. For example, if spectral measurements are infrequent and sensing can be performed by switching the laser between nodes, then a single laser can be used but the switch insertion losses and fiber attenuation need to be taken into consideration.

The following cost analysis is built around three main cases, each with some degrees of freedom regarding the system parameters:

i. Single probe system with a low power tunable source.
ii. Switched multi-probe system
iii. Simultaneous multi-probe system

Each case is analyzed from an engineering stand-point, detailing the design restrictions based on available component and their associated costs. The underlying assumption is that at least 6mW (on sample) of excitation is required for each node, guaranteeing equivalent sensitivity, resolution and spectral range described in Chapter 2. Additionally, we assume all fiber connections are spliced and not butt-coupled to reduce excess attenuation.

For the following analysis, it is assumed that fiber Raman probes, both SSRS and dispersive, are manufactured in the same manner and have equivalent optics. All prices are based on quotes received between 2021 and 2023 from various vendors and

are cost estimates, rounded to the nearest thousand and do not account for any recent price increase.

3.3.1.1 Single probe system with a low power tunable source

From the case of a single probe system, which has been described in detail in Chapter 2, and given in Figure 3.6, we can learn about the critical components in the system. The general power link budget is given in following Equation when quantities are in logarithmic scale:

$$P_{laser}[dBm] + Isolator_{loss}[dB] + tap_{loss}[dB] + probe_{loss}[dB] + fiber_{loss}[\frac{dB}{km}] \cdot L_s[km] = P_{sample}[dBm] \quad (3.1)$$

First, the Superlum laser outputs a maximum of 20mW (13.0dBm). The 1% fiber tap loss including insertion loss and excess loss is 0.5dB[251]. The isolator (IOF-850, Thorlabs, NJ) has an additional insertion loss of 1dB[252]. The probe insertion loss was measured to be 10%, equivalent to -0.45dB (see Table 2.3), resulting in 12mW of available power in the best-case scenario. Maintaining a minimal power of 6mW (7.78dBm) on the sample suggests we cannot allow any additional loss beyond 3dB.

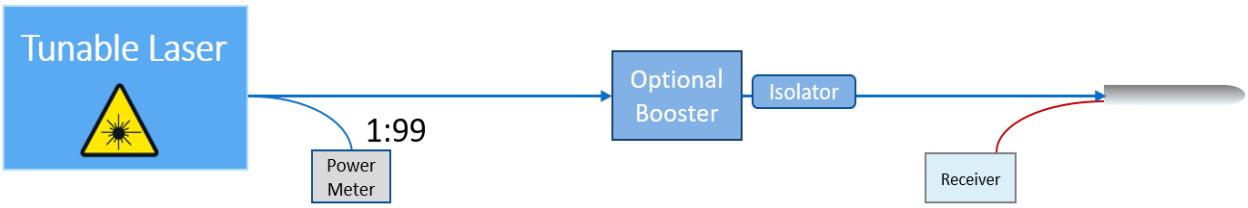

Figure 3.6: A diagram of a single probe system and an optional range extending booster at a minimum cost of $34K and maximal range of 1.3km without the booster.

The above calculation sets the bound on the deployment distance, L_S [km], of a single probe. Assuming we use the lower-loss 50μm Ø MM GRIN fiber attenuation of 2.3dB/km, the probe must be deployed at distance no greater than 1.3km from the laser source. A bare 50μm Ø GRIN optical fiber is $1.2/meter but one with a jacket

is approximately is $6/meter.

In Figure 3.6 an option for the extension of the deployment range is presented. It is possible to add an additional booster to amplify the laser. The booster unit requires a minimal input optical power of 1mW[253] and has a maximal gain of 13dB. If we position the isolator after the last booster, these specifications limit the distance to the range-extending booster to 3km from the tunable laser source.

The input to the booster has to be a 780nm or 850nm Polarizing Maintain SM fiber (PANDA) which has an attenuation of 4dB/km[254]. A bare PANDA optical fiber is $23/meter but one with a jacket is approximately $178/meter which adds considerable cost to the system.

	Component	Cost [$K]	# items	Total [$K]
SSRS	Fiber Probe	6	1	6
	Tunable Laser (Superlum)	17	1	17
	Fiber Isolator	2	1	2
	SPAD	6	1	6
	UNBF (1" Ø)	2	1	2
	Optics (lenses, tubes)	1	1	1
	Optical fiber	0.006	Ls	$0.006L_s$
				34 + 0.006Ls
Dispersive	Fiber Probe	6	1	6
	Fixed wavelength Laser	6	1	6
	Spectrometer	20	1	20
	grating	2	1	1
	Detector	35	1	35
				68

Table 3.1: Cost estimates for a single probe Raman system comparing SSRS and an equivalent sensitivity dispersive system, reaching a max range of 1.3km.

The cost of a single probe system without a range extension is presented in Table 3.1. The table shows that for this case, there is a clear cost advantage for the SSRS probe architecture. The use of a single tunable laser, which is the most significant cost factor, is still lower compared with a cooled, high-end detector and

spectrometer which are able to compete with the sensitivity and resolution of the SSRS. However, the point can be made that resolution and required sensitivity are dependent on the application and for some applications, lower-cost spectrometers with reduced performance can be in the same cost-range as the tunable laser. Additionally, as the SSRS requires slow tuning of the wavelength, monitoring fast-dynamic processes might also be better matched with dispersive solutions, despite the cost differences. Approaches to mitigate the extended acquisition time are presented in Chapter 4.

3.3.1.2 Switched Multi Probe System

One of the key advantages of the SSRS architecture is the ability to deploy multiple sensors using a single tunable source and a MEMS switch which directs the excitation to one of the channels. The switch has an insertion loss which depends on the number of channels and type of fibers used[255] but is below 0.8dB for all SM switches, and under 1.4dB for all MM switches. SM switches are available in configurations of 4-32 channels (~$6k) but is also available with 128 channels (~$18k).

If we use the Superlum laser as our shared laser, and add the SM switch insertion loss to the link budget calculation in Equation 3.1, we achieve 10.6mW of excitation per probe. This excess power can be used to enhance SNR or deploy sensor to distances of up to 1km.

Table 3.2 shows the cost analysis for a system using up to 32 switched channels. The base cost of the laser, booster and isolator are shared for all sensors and the cost of the system increases only as a function of the supported sensor number, K_S. For both SSRS and the dispersive options, a 1: K_S switch is assumed since using a cascade of switches would increase attenuation and the available switches are sufficient to

support over a hundred channels. Importantly, we have demonstrated in Subsection 3.2 that using a SM switch with MM fibers was technically possible.

For the dispersive option, it is assumed that an additional switch is placed at the input of the spectrometer. As detailed in Subsection 1.5, the option to have multiple spectrometer inputs is limited to about 4 probes with standard 200μm Ø collection. Most dispersive Raman probes have fiber bundles to enhance signal collection and so have to be replaced with single-fiber probes to take advantage of switches.

	Component	Cost [$K]	# items	Total [$K]
SSRS	Fiber Probe	6	K_S	$6K_S$
	Tunable Laser (Superlum) and booster unit	17	1	17
	isolator	2	1	2
	SPAD	6	K_S	$6K_S$
	UNBF (1")	2	K_S	$2K_S$
	Optics	1	K_S	K_S
	*Switch (1:k)	6	1	6
	Optical fibers	0.006 Ls	K_S	$0.006L_s$
				$25+15K_S+0.006L_s K_S$
Dispersive	Fiber Probe	6	K_S	$6K_S$
	Laser	6	1	6
	Spectrometer	20	1	20
	grating	2	1	1
	Detector	35	1	35
	switch (1:k)	6	2	12
				$74+6K_S$

Table 3.2: Cost estimates for a Switched Multi-Probe System with 1km max range and up to 32 nodes in both SSRS and dispersive architectures

Importantly, the dispersive option requires the probes to be at close proximity to the spectrometer, due to the Raman signal attenuation. If the sensors are positioned far from the laser or far from the spectrometer, the dispersive option becomes technically challenging requiring extremely powerful excitation lasers.

Figure 3.7 plots the price of a Raman sensor system vs. the number of sensing nodes. The plot assumes short deployment distances (L_S<10m) with anywhere between 1-32 probes. In the COTS option, the majority of cost is the spectrometer and so additional probes have a lower impact on the overall system cost. In the SSRS, the system cost scales with the number of sensors. Importantly, the actual market cost of a 4-probe dispersive system such as the Kaiser RXN4 includes much more than the price of components and includes labor, overhead and profit, reaching a price of approximately $240K.

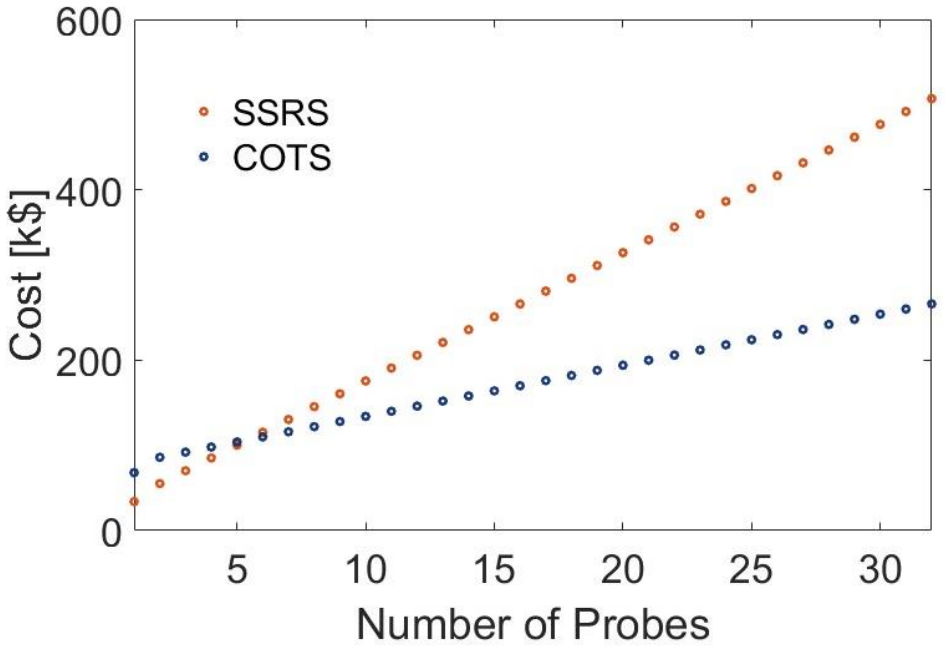

Figure 3.7: Cost comparison for a system comprising between 2-10 probes working one-at-a-time with either SSRS or dispersive COTS architectures showing both systems scale linearly with the number of probes but with significant excess cost for the dispersive spectrometer.

The above figure implies that for applications where all the sensors are positioned very (very) close together, and they do not need to be used simultaneously, there is an advantage for a dispersive system with more than 5 sensors. However, this option negates the utility model since it prevents the use of multiple sensors at the

same time or the deployment of such a system in any space larger than a medium-sized room.

3.3.1.3 Simultaneous multi-probe system

This last case describes an envisioned application where a number of sensors operate simultaneously. For dispersive systems this scenario is only possible by deploying multiple systems at each sensing point, multiplying the price of a single system given in Table 3.1. For the SSRS system, the burden falls on the tunable source.

In medium sized systems, it is possible to use the Superlum with additional booster units acting as amplifiers for each sensor.

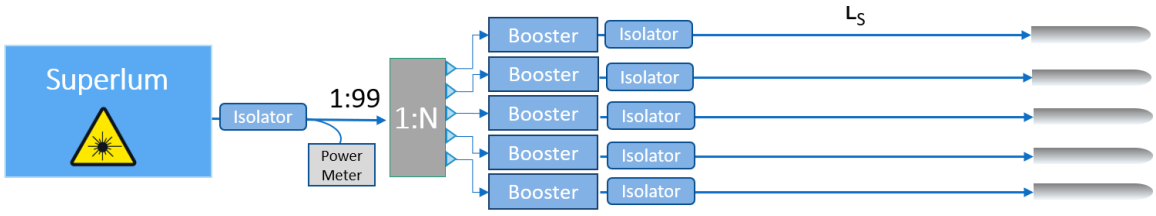

Figure 3.8: A diagram of a multi-probe simultaneous implementation using the Superlum and multiple booster units where each sensor branch requires laser amplification. This mid-scale system can support up to 10 sensors with a single amplification level but can be expanded using more amplification steps.

As discussed in Subsection, 3.3.1.1, each booster needs a minimum of 1mW to operate. Following the power tap and first isolator we have 14mW of available power. COTS 1:4 or 1:2 SM splitters (TWQ850HF, TW850R5F1, Thorlabs, NJ)[256] have approximately 0.6dB of insertion loss. If we cascade two splitters we are left with 10.3mW which enables a maximal of 10 sensors in this architecture. Following each booster an isolator has to be introduced leaving us with 15.8mW per probe, allowing for remote deployment of up to 1.7km or additional splitting into more sensor nodes.

In this method, the cost of each sensor node has an additional booster ($7K) and isolator ($2K) costs associated with it. Table 3.3 shows the cost breakdown for

this system in the SSRS architecture and with a dispersive COTS alternative.

Since the extra cost per sensor is significant when using the Superlum and booster design, above a certain number of sensors it is preferable to use a powerful laser such as the Ti:Sapph. Table 3.4 shows a comparable cost breakdown of a multi-sensor system using the Ti:Sapph and Figure 3.10 plots the Superlum, Ti:Sapph and dispersive COTS system costs for 2-20 sensor probes with a 200m deployment.

	Component	Cost [$K]	# items	Total [$K]
SSRS	Tunable Laser (Superlum)	17	1	17
	Splitters	1	Log2(K_S)	Log2(K_S)
	Isolators	2	K_S +1	2+2 K_S
	Boosters	7	K_S	$7K_S$
	Optical fiber	0.006xL_s	K_S	$0.006K_SL_s$
	SPAD	6	K_S	$6K_S$
	Fiber Probe	6	K_S	$6K_S$
	UNBF (1")	2	K_S	$2K_S$
	Optics	1	K_S	K_S
				$19+ Log2(K_S)+24K_S+ 6e^{-3}K_SL_s$
Dispersive	Single dispersive system (Table 3.1)	68	Ks	
				$68K_S$

Table 3.3: Cost estimate for a medium-scale sensor system with Ks probes operating simultaneously in dispersive and SSRS architecture.

	Component	Cost [$K]	# items	Total [$K]
SSRS	Tunable Laser (Ti:Sapph)	160	1	160
	Splitters	1	$Log_2(K_S)$	$Log_2(K_S)$
	Optical fiber	0.006xL_s	K_S	$0.006K_SL_s$
	SPAD	6	K_S	$6K_S$
	Fiber Probe	6	K_S	$6K_S$
	UNBF (1")	2	K_S	$2K_S$
	Optics	1	K_S	K_S
				$160+15K_S+ Log_2(K_S)+ 6e^{-3}K_SL_s$

Table 3.4: Cost estimates for a large-scale sensor system with Ks probes (10-100) operating simultaneously in SSRS and dispersive architecture.

Figure 3.10 shows that a dispersive solution is never cost effective for simultaneous measurements. Additionally, the Superlum approach is preferable for up to 15 sensors after which using the Ti:Sapph has a lower overall cost. The Ti:Sapph has additional benefits in regards to a broader spectral range, and the benefit of not requiring multiple amplifiers.

It is helpful to also illustrate the system maximal capability using the Ti:Sapph. Ti:Sapph lasers output more than 2W in either SM or MM versions. Approximately 60-80% of the Ti:Sapph output power can be efficiently coupled into a fiber. Using

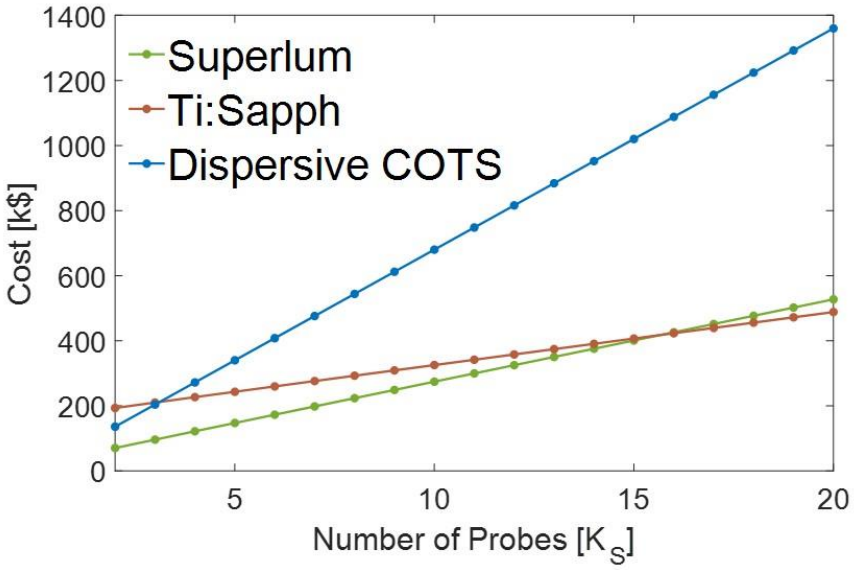

Figure 3.9: A cost comparison for a simultaneous multi-sensor system with the Superlum (green), Ti:Sapph (red), and dispersive COTS (blue) for K_S=2-20 sensors and L_S=0.2km deployment (Table 3.3) showing the clear advantage of SRSS over dispersive solutions.

60% as a conservative estimate, we have about 900mW of available power, $P_{available}$, after the power tap and switch. Again, assuming a minimum of 6mW on sample (effectively 6.7mW at the probe input), we can calculate the maximal number of supported probes per every deployment length according to the following Equation:

$$K_S = P_{available} \cdot (Fiber\ Loss)^{L_S} \tag{3.2}$$

Where the fiber loss is the linear loss per meter calculated as $10^{(-2.4e-3/10)}$. Figure 3.10 plots the results showing that more than 126 sensors can be supported at distances of 100m and down to 10 sensors at 5km deployment.

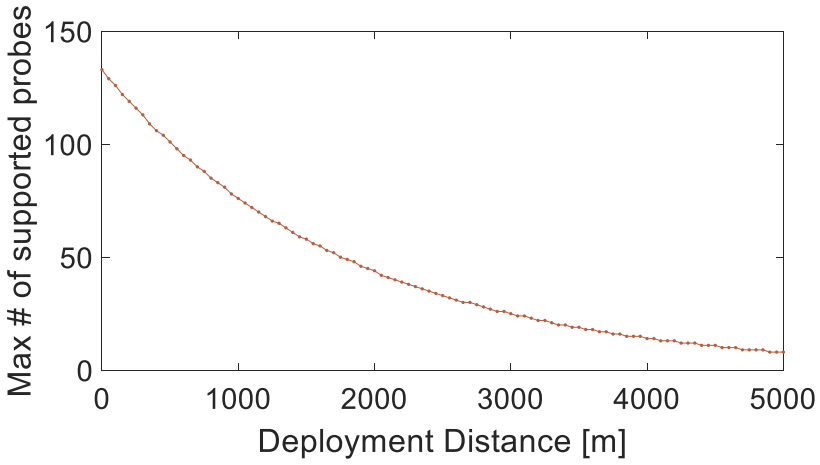

Figure 3.10: A plot showing the tradeoff between number of supported sensors and the maximal deployment distance for large-scale simultaneous operation illustrated in Table 3.4 using the Ti:Sapph.

This analysis demonstrates that SSRS provides a much more scalable solution for sensor deployment in regards to cost compared with dispersive systems in both a switched or simultaneous operation. Notably, these sensors are still not at a point to be priced for consumers but neither were many utilities when they first emerged such as computers or mobile-phones and it took many years of technological improvements and the reduction of material and fabrication costs to drive the prices down.

Now that we have demonstrated the scalability of SSRS in both size, number of sensors, and cost, we move on to explore potential applications.

3.3.2 Potential Applications

The integration of a multiple-sensor system is financially justified when it can provide added value to an existing process or when it can enable a completely novel process which was previously impossible. The added value can certainly be financial

in the form of reduction of consumables, shortening the process time, and optimizing process conditions in regards to energy use or product yield. However, value can also take the form of increased safety, quality assurance, and provide an insurance of sorts for the wellbeing of the process (see Section 1.7.2).

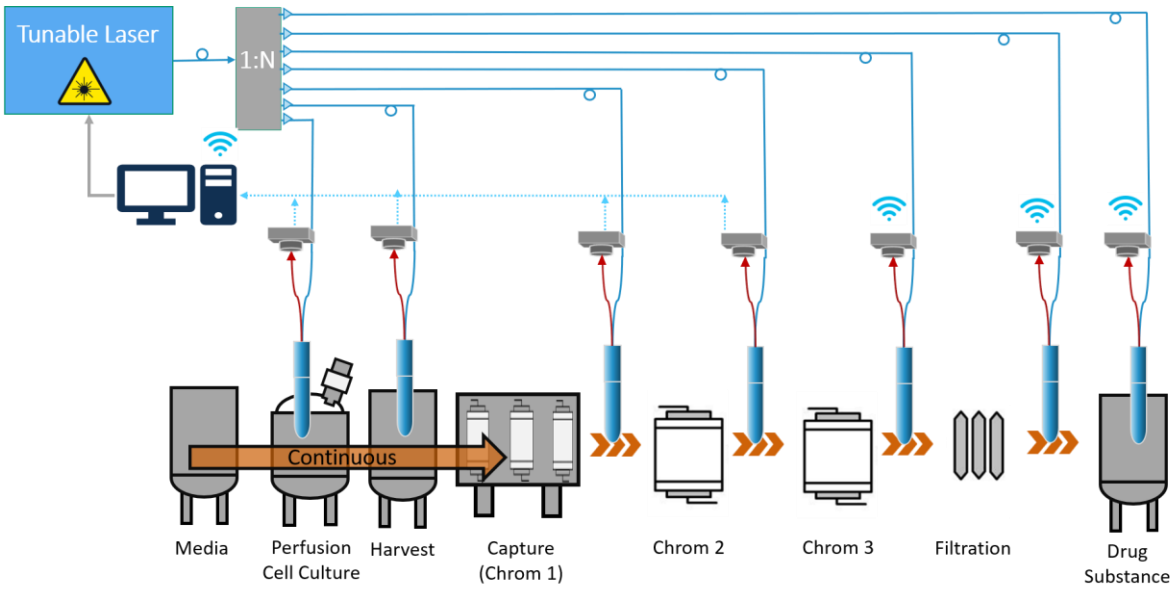

Figure 3.11: A possible application of the SSRS network integrated into a continuous pharmaceutical production line, monitoring the quality of consumables, providing visibility into the dynamic process of cell growth and metabolism, and aiding in the purification, and formulation steps.

As one example for a large-scale network application, we consider a possible integration of the SSRS network into a continuous pharmaceutical production line of therapeutic proteins (see Figure 3.11). Traditionally, pharmaceuticals have been made in batch processing[225]. Continuous manufacturing has been shown to reduce manufacturing costs by more than 55% as well as require a much smaller facility size[257] while also improving product uniformity since the process is kept at a chemical steady-state with enhanced monitoring and control[226]. However, continuous manufacturing comes with challenges of ensuring sterility, and requiring significantly more monitoring to maintain steady-state or to diagnose the root cause of deviations if they

occur.

Currently, Raman probes are mostly used in monitoring of the fed-batch bioreactor, however, the SSRS network system presents an opportunity for integration in multiple steps throughout production - in both upstream and downstream phases. In this application, a large-scale simultaneous network (Figure 3.9) would be required. Cell doubling-times are on the order of 24 hours, requiring monitoring of several times per day. Additionally, active control of feed, waste and product would demand simultaneous sensing architecture to provide adequate response times. SSRS probes could persistently monitor quality of the base media components and nurtients[137], provide metrics regarding cell metabolism and expansion inside the bioreactors[18], various purification and formulation steps, as well as provide quality and safety metrics in the final product[17,18,258]. In this application the number of sensors can be anywhere between K_S =10 for a process-development facility or K_S>50, for large scale production. Similarly, for small facilities the deployment distance, L_S, could be dozens to a few hundreds of meters, connecting different production halls.

The cost of therapeutic proteins can reach thousands of dollar per gram[226,257], so a strong financial incentive exists to increase production throughput while also enabling flexible production using a continuous process. The use of the SSRS probe on CHO perfusion culture samples is discussed in Chapter 4.

A different type of potential application, better suited for the switched network architecture (Figure 3.8) is where monitoring was not previously feasible, but it carries a great environmental and regulatory impact. The need to mitigate nitrogenous fertilizer leeching into water streams has been established in Section 1.7.1. The SSRS has successfully demonstrated the monitoring of nitrate levels and other fertilizer compounds in water in a small lab-scale hydroponic setup and estuary water (Section 2.3). This application can be significantly upscaled to large hydroponic and other

agricultural facilities to minimize fertilizer use, monitor the incoming and outgoing water quality concurrently with crop optimization. Particularly for agricultural use cases where monitoring frequency is low, and concurrent measurements are not essential, the lower cost switching multi-probe system is a promising solution.

Figure 3.12 shows an illustration of the integration of the SSRS sensors in a hydroponic facility where SSRS probes monitor the various nutrients concentration in aqueous media, the uptake of nitrate by the plants[247] and the residual fertilizer in the reservoir, aiding in minimizing excess fertilization and providing real-time measurement of the waste stream to mitigate environmental impact. In this type of system which requires deployment distances of hundreds of meters, and numerous sensors that do not to operate simultaneously, there is a cost benefit to the switched system.

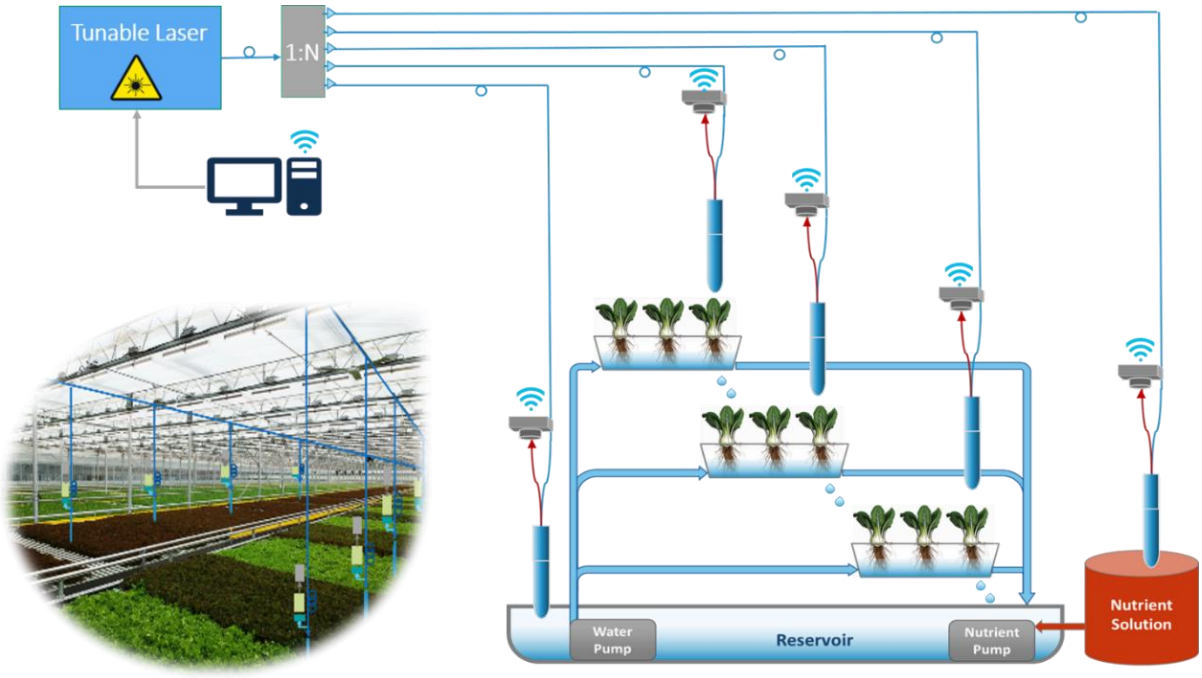

Figure 3.12: Visualization of a possible application of the SSRS network to monitor a greenhouse in which water quality, fertilizer and produce are monitored continuously to optimize growing conditions and reduce waste.

Certainly, for most production agricultural facilities, produce price is far lower

compared with pharmaceuticals. However, process development in agriculture requires high-throughput phenotyping to develop the most successful strains and optimize growth conditions. Integration of a large-scale monitoring system can reduce both the development time and cost while also providing measurable metrics for process success.

An additional incentive for system integration could be to adhere to regulation and ensure compliance. This approach requires that governing agencies lead the path by increasing enforcement of polluting industries and impose penalties linking the environmental damage with a financial one. Additional industries that could similarly make use of continuous chemical monitoring for both process optimization and adherence to regulation are for example petrochemicals, food and beverage, cosmetics, and wastewater treatment.

3.4 Summary

In this chapter, we validated the SSRS network architecture's viability as a utility service, examining both its technical capability and economic feasibility. We confirmed the efficacy of a network comprising 16 sensors, leveraging a single laser source alongside COTS infrastructure such as optical fibers and switches. We also established the network's capability for long-distance deployment across multiple sensors.

Our analysis included the exploration of cost models tailored for small and large-scale systems. These models show that SSRS is a superior alternative to dispersive systems, underscoring the economic advantages inherent in the SSRS architecture.

CHAPTER 4

Minimal Spectral Sampling

The SSRS sensor network presents a considerable advantage in regards to number and range of Raman sensors that can be deployed and operated. However, it is important to emphasize that spectral acquisition with SSRS is done sequentially. Raman spectra acquisition often require both a considerable integration time (1-30 seconds) and between 10-50 acquisition repetitions to enhance SNR (see Section 1.3.2). The throughput enhancement of the SSRS allows us to shorten the integration time (or alternatively reduce the excitation power) but total acquisition time is still considerably longer than with dispersive Raman because sampling must be repeated for each spectral datapoint. Dispersive benchtop systems have anywhere between 1300-3600 pixels and if we were to try and acquire spectra in the same spectral density, each spectrum would take days to complete. This challenge is exacerbated when considering the use of a single laser which is time-shared between multiple sensors.

This chapter describes the data acquired from a CHO-cell continuous manufacturing testbed and proposes the use of *a-priori* information regarding the spectra to minimize total spectral acquisition time. Three different approaches are proposed and examined: Down-sampling, Raman peak sampling and VIP-informed sampling. These methods are evaluated through a simulation using dispersive spectra and using SSRS to validate them.

4.1 CHO-cell Continuous Testbed

The samples presented in this chapter were all part of an integrated CHO-cell continuous testbed producing Adalimumab[259] (also commercially named Humira) a monoclonal antibody (mAb) used for treating various forms of arthritis. The continuous testbed was part of a collaboration between the Sinskey Lab at MIT, and Sartorius Stedim Cella GMBH which provided the CHO cell line.

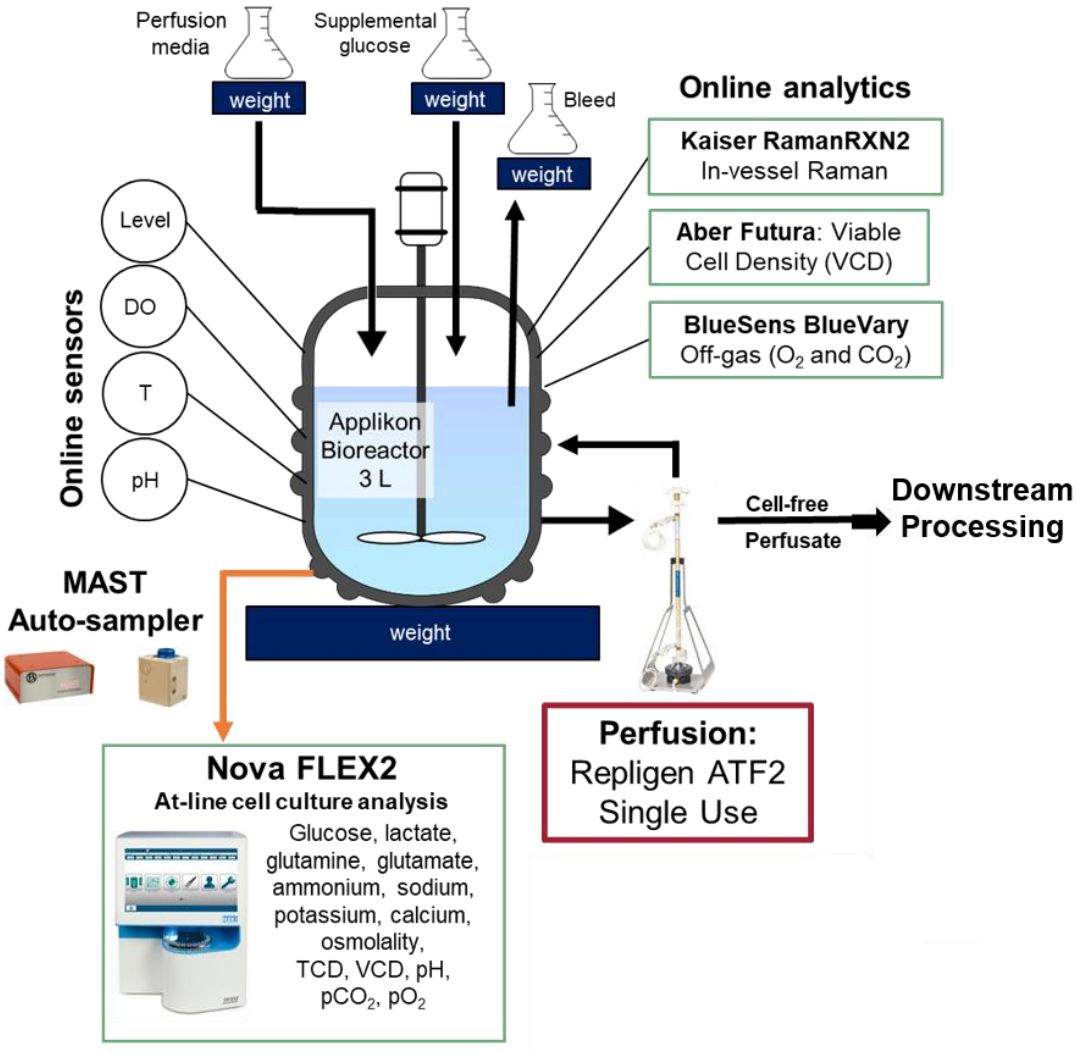

Figure 4.1: A diagram showing the main components of the upstream section of the CHO-cell continuous testbed which was produced samples of spent media and supernatant measured with three Raman systems. (Courtesy of Jackie Wolfram)

Figure 4.1 shows a diagram of the main components in the upstream section of the testbed. The cell culture was maintained in a 3-liter Applikon bioreactor. An automated MAST autosampler system (MilliporeSigma, USA) drew samples daily and transported them to an automated analyzer (Nova, FLEX2) measuring key metabolites including glucose, lactate, glutamine, glutamate, ammonium, as well as ions, gasses, cell densities, and pH. Online analytics were integrated into the bioreactor including a Viable Cell Density (VCD) sensor (Aber Futura capacitance sensor), an off-gas sensor (BlueSens) and a Kaiser Raman RXn2-785nm probe system which measured the spectra inside the bioreactor using 400-500mW of power (10s integration repeated 75 times). When mAb was produced it was measured off-line using an Octet RED96e biolayer interferometry system (Sartorius, USA).

Run #	Total Days	Maximal VCD (Nova) [cell/ml]	Number of spectra /Nova (Usable sets*)	Notes
R2	56	68.9e6	1329/ 214 (149)	1. Spectra was measured hourly 2. Samples were drawn manually for analysis
R3	32	41.4e6	187/289 (146)	Spectra and metabolites were automatically measured every 2 hours
R1	25	66.3e6	143/192 (133)	Spectra and metabolites were automatically measured every 4 hours

Table 4.1: Details regarding the three-perfusion cell culture runs conducted in the CHO testbed.

Three perfusion runs were conducted and are described in Table 4.1. As the testbed was also being developed as the runs were taking place, the runs were quite different from one another in regards to length, culture parameters and unexpected events which affected the in-line Raman spectra. As an example, see Figure 4.2 (courtesy of Naresh Mohan) which illustrates the progression of the first and second perfusion runs (R2, R3) and some of the unexpected events such as foaming and changes in media composition. Run R2 predates the automation using the MAST

system so samples were drawn manually once a day from the perfusate and measured in the Nova metabolite analyzer while spectra were acquired hourly.

Samples were drawn daily, approximately at noon, manually or automatically. A small volume was analyzed with the Nova while the rest was spun down to remove the cells and the supernatants was measured for mAb titer. The supernatant samples were frozen and kept in a -80C° freezer. 14 samples from run R3, each 1.5ml in volume, were aliquoted and measured with the Biomod and the SSRS probe using the Superlum laser (5 second integration, repeated 12 times with 5-6mW of power).

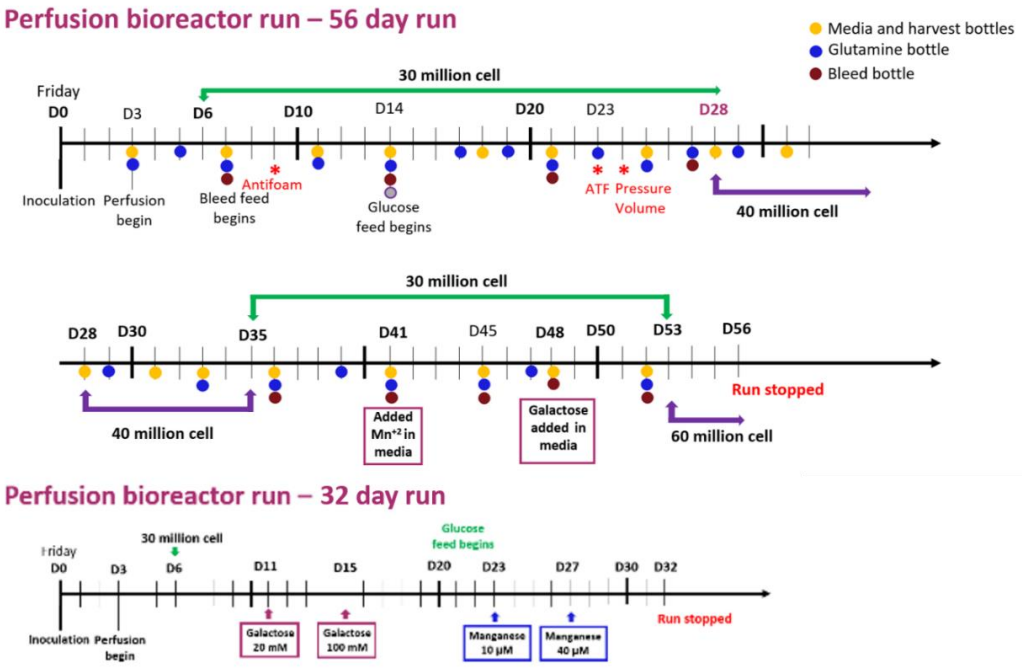

Figure 4.2: Chronological description of two CHO perfusion runs (R2, R3) in the testbed, illustrating the complexity of the process and multiple steps required to maintain the culture along with some unexpected events that required troubleshooting (courtesy of Naresh Mohan)

In order to train models based on Raman data from the integrated Kaiser probe, both spectra and ground truth, measured using the Nova analyzer are needed. To make sure spectra reflects the most accurate data, only spectra that was acquired up to an hour from the Nova measurement is used to build the models (this mostly

affected data for R2 since sampling was not automated). Additionally, some of the Nova measurements suffered from errors due to clogging, or calibration issues and could not be used. Table 4.1 shows the total number of Raman spectra and Nova measurements acquired during each run while noting the available dataset for model training as "Usable sets".

Ideally, the use of Raman spectra to build prediction models should be made with a well-characterized process, minimizing significant deviations from the training dataset to reduce model errors. However, that is not always possible both in process development or when malfunctions occur. The following sections explore several options for data acquisition and predictive-model building, illustrating the performance tradeoffs in "ideal" and non-ideal scenarios.

4.2 A-priori Information from Kaiser Spectra

Figure 4.3 shows spectra acquired with the Kaiser probe in-situ for all three runs. Since most of the relevant data for key analytes and the data we can currently acquire with the SSRS is in the fingerprint region (600-1800 cm^{-1}) the remainder of analysis will only use data from the Superlum spectral range between 810-1670 cm^{-1}. Ideally, spectra in the 400-810 cm^{-1} and 2700-3600 cm^{-1} ranges would also be acquired since it also holds important information regarding water, ammonium and other compounds[61].

The R2 spectra (top in Figure 4.3) shows sharp peaks that are attributed to room-light leaking into the bioreactor, which was corrected for future runs. All of the spectra exhibit an increase in the fluorescence background with time, which is a sign of increasing bio-mass as cells expand in the bioreactor. The output data from the Kaiser system is given in 1cm^{-1} intervals, (the inherent system resolution is 4 cm^{-1}).

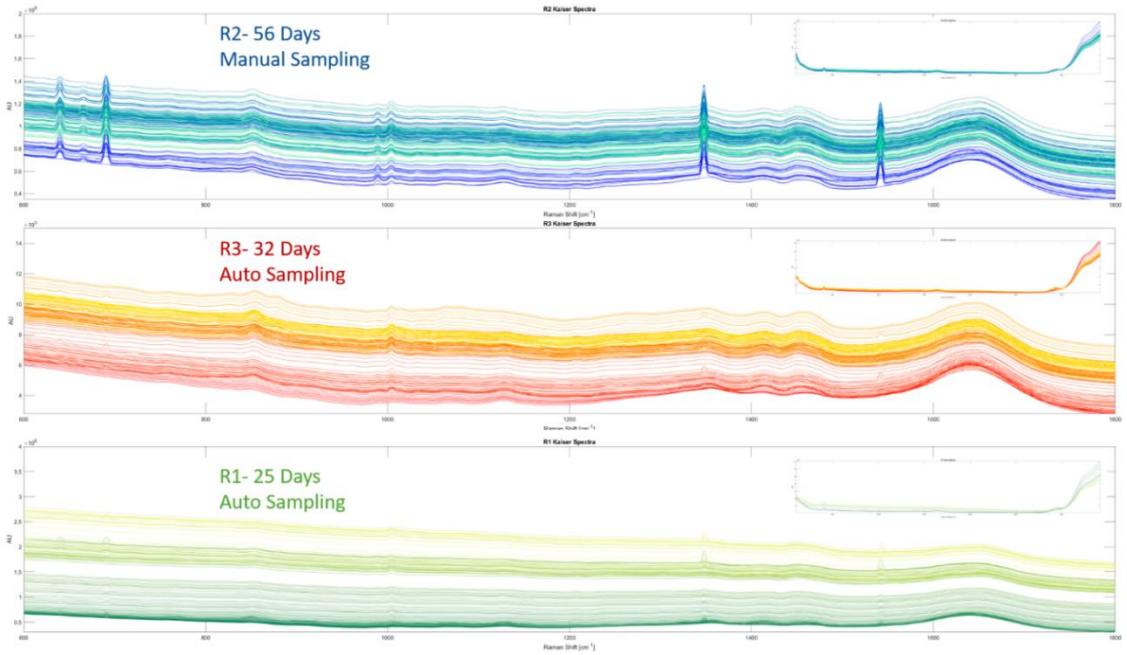

Figure 4.3: Kaiser spectra of all three CHO runs, focusing on the fingerprint region with an inlay of the entire spectral range (100-3425 cm-[1]). All spectra were acquired using 400mW and 10 second integration repeated 75 times.

To establish a baseline for comparison, we preform PLSR for 7 analytes: glucose, glutamine, glutamic acid, lactate, ammonium, Cell Density (CD) and mAb (see Section 1.6.2.3) in the 810-1670 cm^{-1} spectral range which includes 861 data points. Spectra from all three runs is used for the creation of the regression models. PLSR was chosen since the algorithm does not rely on background removal, which is significant in these spectra as seen from Figure 4.3. Additionally, PLSR performs better than PCA for highly colinear spectra, which has been shown to be the case for many cell-culture processes[107].

Two model-training methods were explored: In the first, the training set is chosen to be half of all usable dataset, but uniformly distributed throughout the runs' duration. This creates an evenly sampled process and the model represents all stages of the cell culture. The second method similarly used half of the usable dataset but chosen to be only at the beginning of the perfusion culture. The validation (in this

case also the prediction) is performed on the rest of the dataset, not including any of the data used for training. The number of PLSR components, N_{comp}, is chosen automatically for each analyte separately to correspond to 83-90% percent of cumulative variance (see details in Table 4.2)

Analyte	N_{comp} (Cumulative variance explained %)	# samples in training dataset	Uniformly Sampled		First Half	
			RMSEE	RMSEP	RMSEE	RMSEP
Glucose [g/L]	7 (87.49%)	214	0.61	0.60	0.680	1.51
Glutamine [mmol/L]	16 (84.7%)	189	0.43	0.56	0.44	3.14
Glutamic acid [mmol/L	19 (84.93%)	214	0.52	0.83	0.39	3.65
Lactate [g/L]	8 (85.43%)	214	0.38	0.44	0.21	0.94
Ammonium [mmol/L]	13 (83.88%)	195	0.76	0.63	0.42	3.71
CD [x10^5 cells/ml]	5 (86.89%)	213	51.4	62.8	37.62	109.90
mAb [mg/L]	7 (85.99%)	38	96.97	170.34	67.04	337.55

Table 4.2: PLS model parameters and results from two type of training methods

The above PLSR results on the spectra show that a process should be sampled uniformly throughout its duration in order to improve predictive modeling performance. All future PLSR models in this chapter use the uniformly-sampled training.

4.2.1 Down Sampling

The Kaiser spectra includes 860 data points in the Region of Interest (ROI). If we were to acquire equivalent spectra with the SSRS with 10 seconds integration time

and 10 repetitions for each spectral point, it would take approximately 24 hours. As the signal intensity cannot be changed with the Superlum, it is impossible to reduce integration or further decrease the number of repetitions without compromising the sensitivity. Therefore, a reduction in the number of acquired data points is necessary.

First, we explore uniform down-sampling of the spectra and identifying the largest interval that allows us to reduce the number of data points while trying to minimize the effect on our signal resolution and predictive model performance. To evaluate this method, a simulation was created in which the data from the Kaiser system was down- sampled in increasingly larger intervals between 2 and 20cm^{-1}. The performance was evaluated by performing PLSR on the original (see Table 4.2) and decimated spectra and comparing the RMSEE and RMSEP values Table 4.2.

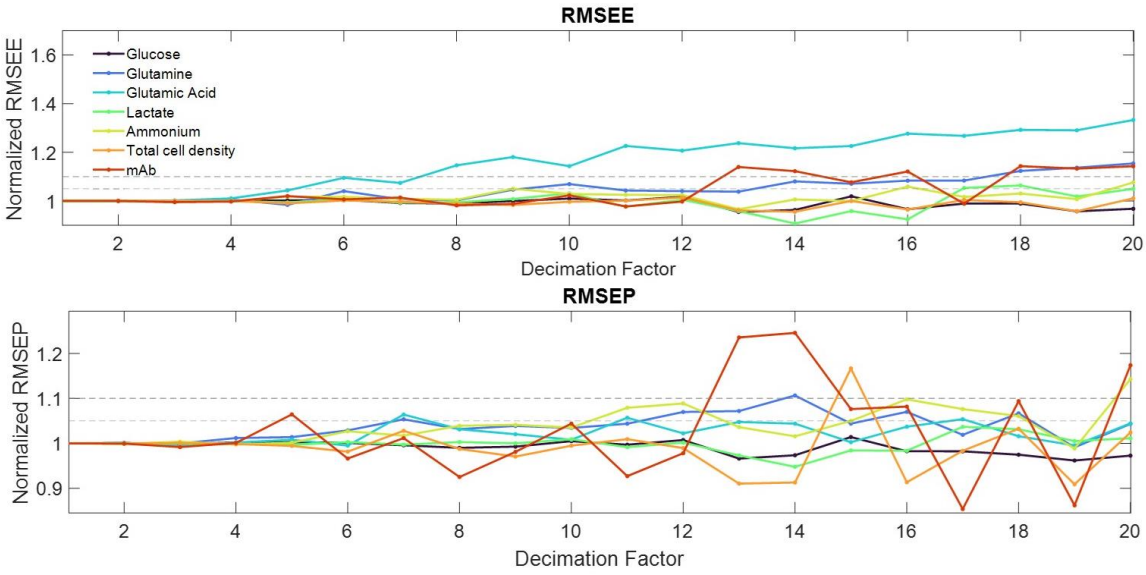

Figure 4.4: Simulation results in which the Kaiser spectra was sampled in increasingly larger intervals (decimation) and the effect of this decimation on the RMSEE and RMSEP of the PLSR model for all 7 analytes (normalized to no decimation data results).

Figure 4.4 shows the simulation results for all 7 analytes with RMSEE in the top panel and RMSEP in the bottom panel. The results are normalized to the RMSEE and RMSEP values when no decimation is performed. Dashed gray lines mark 5%

and 10% increase in error. Decimation by a factor of 4 had minimal effect on errors, resulting in only 1% increase for RMSEE and 1.2% for RMSEP. This result is expected as the resolution of the Kaiser system is $4cm^{-1}$, meaning that each data point contains information from a spectral range of $4cm^{-1}$. Adjacent pixels contain some overlapping information that can be recovered from sampling at larger intervals that overlap with the system resolution.

A factor of 4 reduction in sampling rate is equivalent to sampling in intervals of $4cm^{-1}$, corresponding to 0.24nm (at 770nm) and 0.27nm (at 825nm). Since the Superlum tunes in 0.1nm intervals it was decided to sample spectra at 0.2nm intervals, which would also provide some margin for laser wavelength instability (see Figure 2.13).

The suggested sampling interval results in 276 spectral datapoints in the Superlum spectral range and still requires significant sampling time. In order to acquire spectra in a somewhat reasonable time frame, each spectra data point was acquired for 5 seconds and repeated 12 times to establish mean and STD. The SSRS spectra acquired and the signal processing pipeline for the spectra is described in the following section.

4.3 SSRS Spectra Signal Processing

After the minimal sampling parameters for the SSRS were found, spectra were acquired for 14 CHO-cell supernatant samples using a quartz cuvette using 5-6mW of power. Spectra of the same samples were acquired with the Biomod system using 150mW 10s integration repeated 50 times. Figure 4.5 shows the spectra for 12 of the 14 days using all three systems.

Two of the SSRS spectra (corresponding to days 12 and 27 of the run) suffered

from severe power fluctuations which was traced back to issues with the AC power supply and are excluded from the analysis.

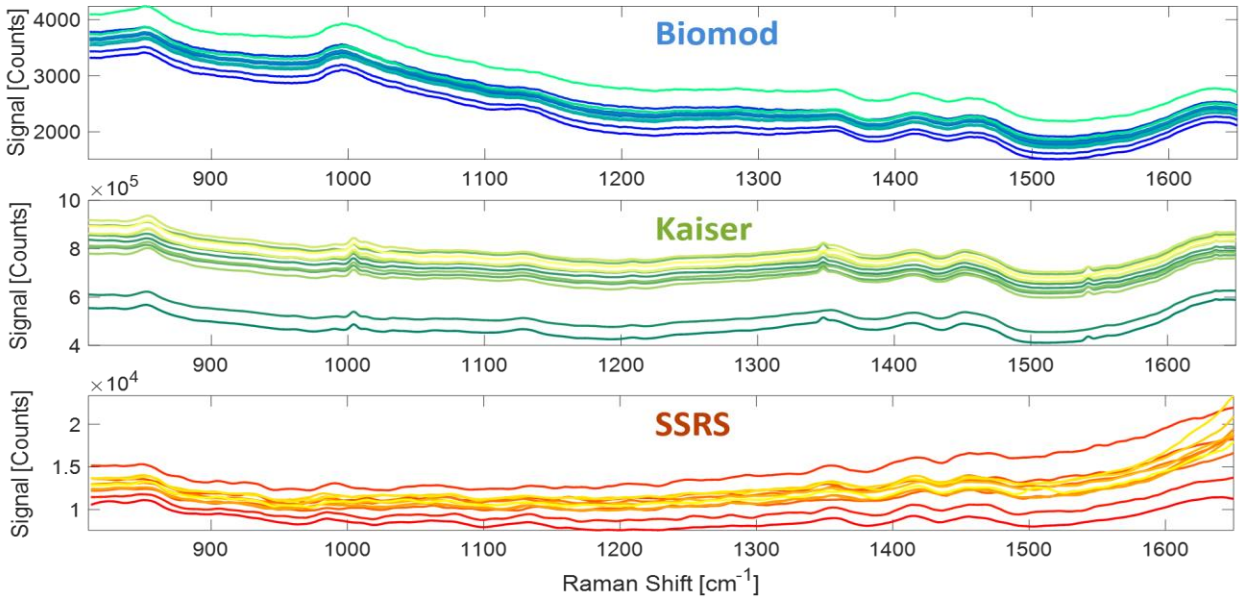

Figure 4.5: Comparison of 14 spectra from days in run R3 for the Biomod (top), Kaiser (middle) and SSRS (bottom). The Biomod (150mW, 10s repeated 50 times) and SSRS spectra (5-6mW, 5 s repeated 12 times for 276 data points) are of supernatant samples while the Kaiser spectra is of the in-situ culture (400mW, 10s repeated 75 times). All spectra were smoothed but no additional processing was performed.

The Kaiser spectra is presented after some internal processing that we are not privy to (presumably median filtering and smoothing) and had not gone through any additional processing steps. The Biomod data had been smoothed as described in Subsection 1.6.1 with a 3rd order median filter and a 2nd order, 11th degree Savitzky-Golay filter.

The SSRS spectra also requires some signal processing steps to enhance SNR and remove system artifacts. First, since the SPAD is a single-point detector, it is far less prone to cosmic rays than a CCD array. A median filter is applied conditionally only if extreme peaks are present in the signal (where the peak value is over 10 standard deviations above the mean signal for a specific wavelength).

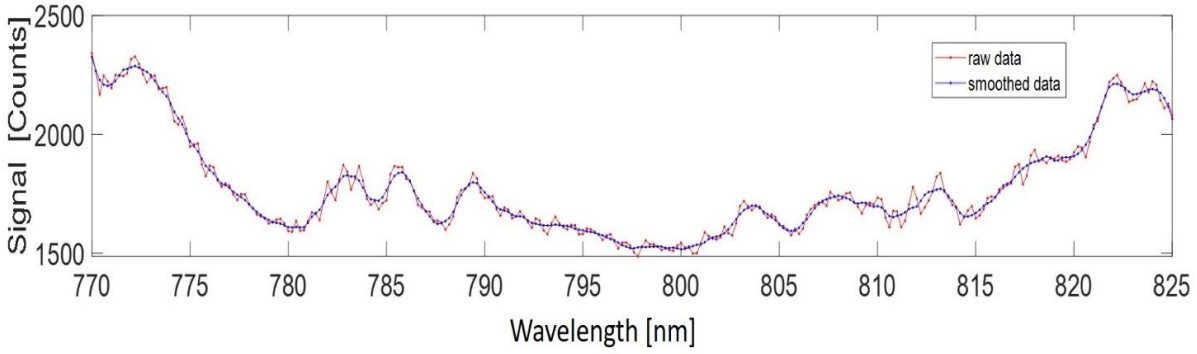

Figure 4.6: SSRS Spectra of one of the CHO supernatant before (red) and after (blue) smoothing with a Savitzky-Golay filter order 2, 3rd degree.

Secondly, due to the laser power fluctuations and wavelength dependency (see Figure 2.16) a Savitzky-Golay filter, 2nd order, 3rd degree, is applied to the spectra (see Figure 4.6). These filter parameters were chosen to filter out laser fluctuations which are below the SSRS resolution while minimally attenuating the Raman peaks.

To better illustrate the differences of spectra acquired with all three systems we inspect spectra acquired on Day 8 of the R3 run.

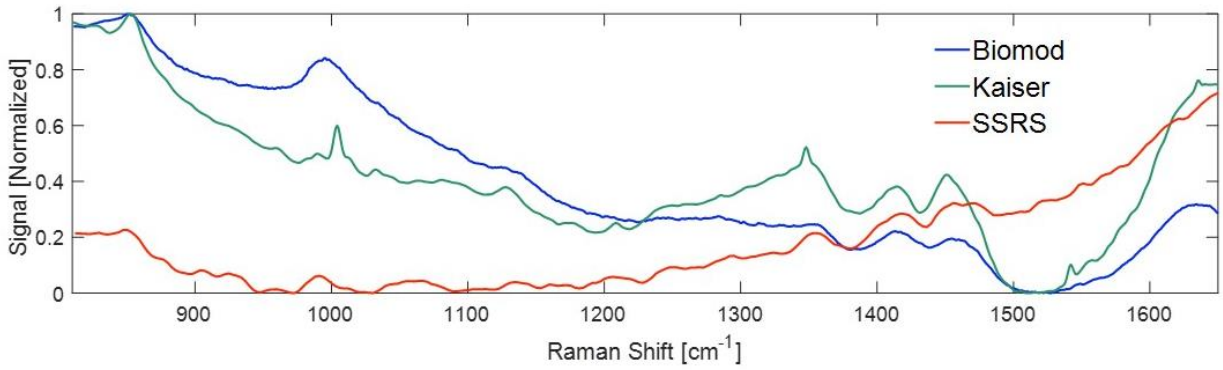

Figure 4.7: Normalized Spectra comparison of samples from day 8 of the R3 run, with the Kaiser in-situ (green), Biomod supernatant (blue) and SSRS supernatant (red) with acquisition parameters as mentioned before.

Figure 4.7 shows normalized spectra from three different Raman systems where the Kaiser data was acquired in-situ (green line) and includes both the supernatant and cells, while the SSRS (red) and Biomod (Blue) show spectra of the supernatant sample drawn that same day, frozen, and then thawed and measured by both systems.

All spectra have been smoothed as described above, but no additional processing steps were performed.

Notably, the slow-varying fluorescence background curve is similar for the dispersive Biomod and Kaiser systems, (830 and 785nm excitation, respectively), where the higher fluorescence is closer to the excitation (0 cm^{-1}). For the SSRS, however, the short wavenumber region is acquired at longer excitation wavelengths and the long wavenumber region is acquired with the shorter wavelengths (see Equation 1.40). This results in a "reverse" fluorescence curve.

Furthermore, the effective Raman cross-section is different for each spectral datapoint because each is acquired with a different excitation wavelength, and is proportional to $1/\lambda^4_{ex}$ (see Equation 1.6). In the case of photon counting detection (and not optical power), the dependency becomes $1/\lambda^3_{ex}$ due to the factor of $h\nu$ (photon energy) in the calculation[14]. This further exacerbates the background slant since the shorter wavenumbers suffer from a lower cross-section.

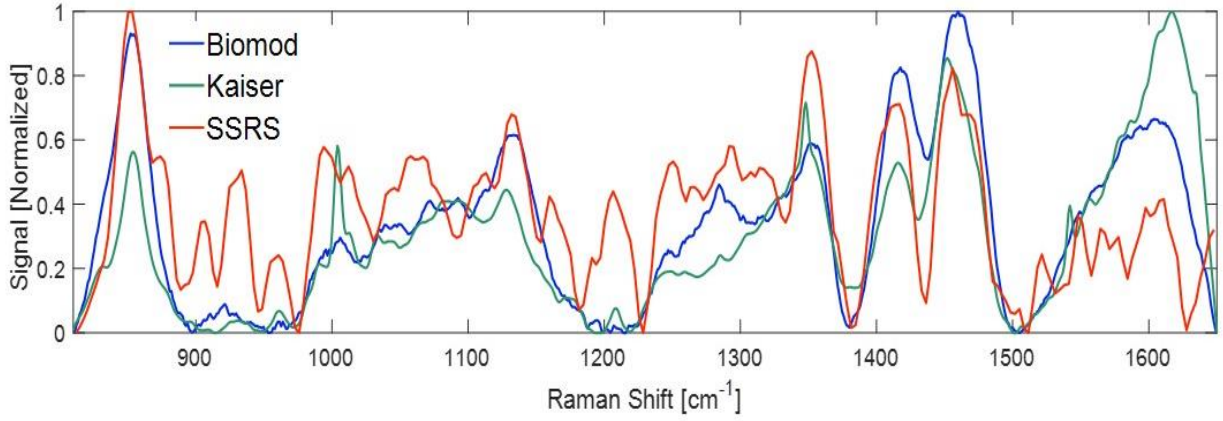

Figure 4.8: Normalized spectra of samples from Day 8 of the CHO R3 run from all three systems (as in Figure 4.7) after background removal using an empty sample holder subtraction and a 6th order polynomial Lieber fit.

In order to account for the Raman cross-section wavelength dependency, each spectral datapoint j, using excitation wavelength λ_j is multiplied by a correction factor

given in Equation 4.1, where λ_0 is the shortest wavelength used (i.e. 770nm).

$$w_j = \left(\frac{\lambda_j}{\lambda_0}\right)^3 \tag{4.1}$$

Standard background removal methods, i.e. spectral background subtraction of an empty sample holder (possible for SSRS and the Biomod) and a following Lieber algorithm (6th order, see Subsection 1.6.1) to remove residual fluorescence (for all systems) are used to reach the final spectra of Day 8 for all systems in Figure 4.8.

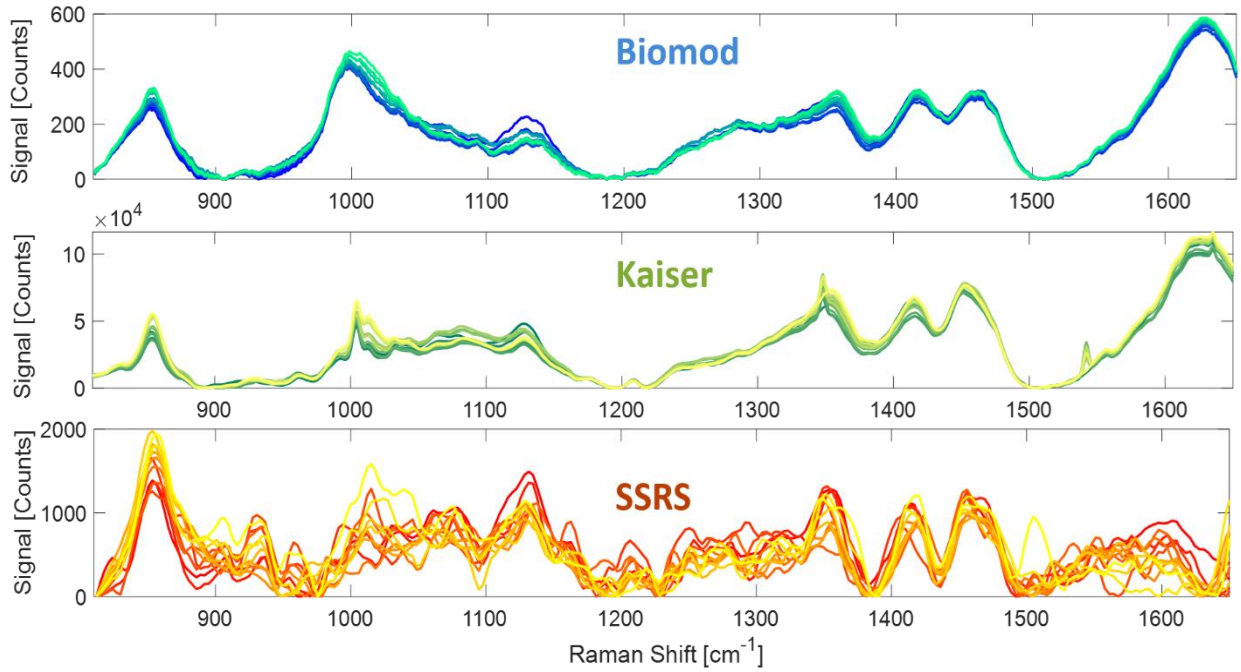

Figure 4.9: Comparison of 14 samples from different days in CHO run R3 for the Biomod (top), Kaiser (middle) and SSRS (bottom) after background removing techniques and cross-section correction has been applied. (see Figures 4.5-4.8).

The SSRS, Biomod and Kaiser all have distinct similarities with the amide III region[260] (around 1350cm^{-1}), glucose (1125, 1060 cm^{-1}) and Glutamine (850 cm^{-1}) clearly visible, while the Kaiser spectra is expected to have some differences due to the presence of cells. The SSRS spectra has better peak contrast in the lower wavenumber region due to reduced fluorescence,however, there are some unexplained peaks in the 900-1000cm^{-1} region, which do not appear in the Biomod or Kaiser data and need

further investigation.

Figure 4.9 shows the same 12 spectra presented in Figure 4.5 after background removal and cross-section correction. The final spectra of all systems is extremely sensitive to the backround removal algorithm, making diresct apectra analysis without the use of training data challeging. The next sections explore analyte concentrations analysis based on both DPA and PLSR.

4.4 Direct Peak Analaysis

DPA (see Subsection 1.6.2.2) is a relatively simple method of detecting trends in analyte concentrations where the location of Raman peaks is known in advance and the signal is strong enough, i.e. surpasses the background shot-noise, and can be detected.

Figure 4.10 shows an example for DPA of glucose and mAb. The top panel shows spectra of 50mg/ml glucose, the middle panel shows the spectra of Days 5,6 and 8 in run R3 and the bottom spectra is of 10 mg/ml NIST mAb (RM 8671, IgG1κ). While the NIST mAb is not the mAb produced in the CHO cells, it shares similar structure in the amide I, III regions[260]. All spectra were acquired in a quartz cuvette with the SSRS using 5s integration repeated 12 times. The blue shaded region is the location of glucose' Raman peaks (1060, 1125 cm^{-1}) and the green shaded shows some of the significant spectral region of mAb (995, 1250 cm^{-1}).

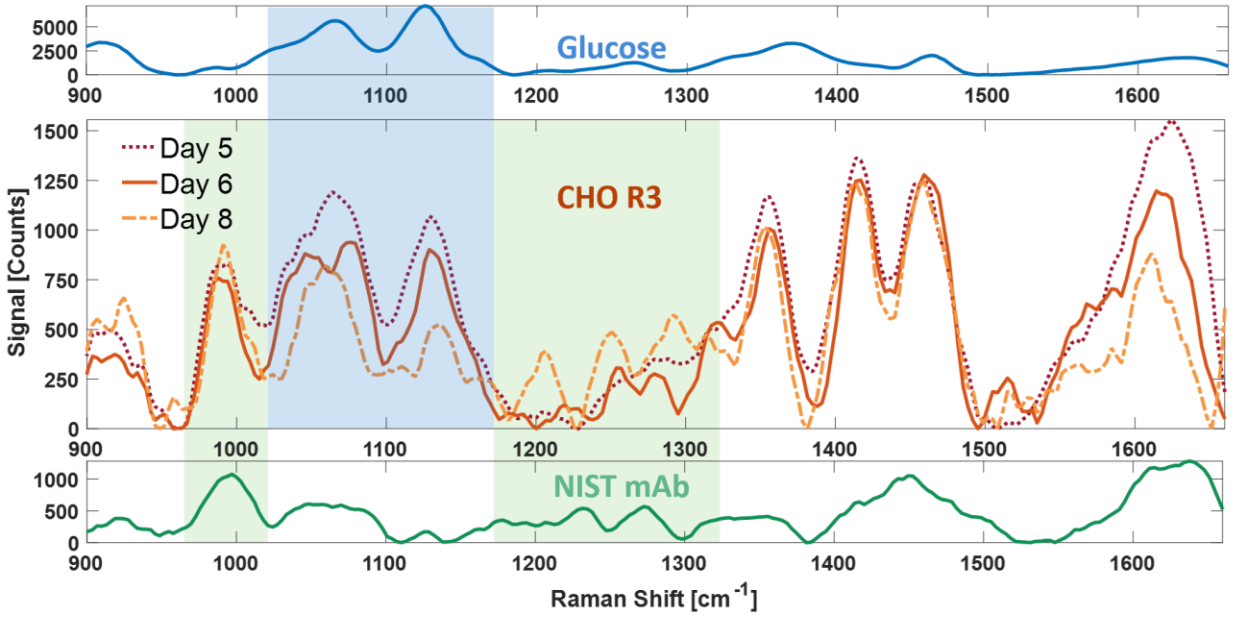

Figure 4.10: SSRS spectra of 50mg/ml glucose (top), R3 run supernatant from Days 5,6 and 8 (middle), and 10mg/mL of NIST mAb (bottom). All spectra were acquired with 506mW, 5 seconds integration and 12 repetitions with 276 wavelengths.

Importantly, the image also illustrates one of the challenges of DPA. The mAb spectra has other significant peaks, for example at 1650 cm^{-1} which is the Amide I band. However, it overlaps with the O-H stretching peak in water[261] making it extremely difficult to detect with the excess noise. Similarly, glutamine[262] has a Raman peak at 850cm^{-1} while lactate[263] has a primary peak at 860 cm^{-1}, making them very hard to distinguish. Furthermore, with varying fluorescence background levels, as is the case for cell culture (see Figure 4.5) prevent DPA from being useful without extremely accurate and consistent background removal methods.

Figure 4.11 shows the glucose peak (1125cm^{-1}) DPA as a function of time for the R3 run. The left Y axis shows the SPAD counts and the right Y axis shows the ground truth measured with the Nova analyzer.

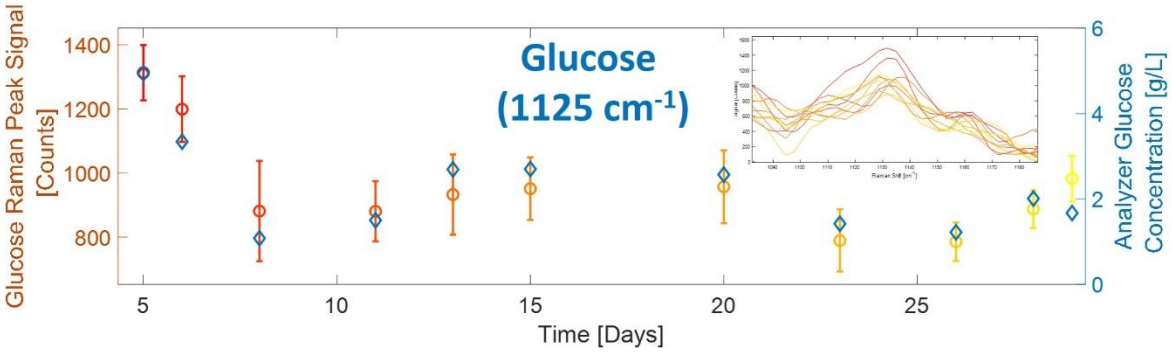

Figure 4.11: SSRS DPA of the main glucose peak (1125 cm^{-1}) with the SSRS signal values (red) presented on the left Y axis and the NOVA metabolite analyzer (blue) on the right Y axis for 12 samples of the CHO R3 run, showing good correlation of values.

Observing the SSRS data error bars in the glucose plot, we see a STD (1σ) of approximately 1g/L. Recalling the glucose 3σ LOD measurement (see Figure 2.22) which was also 1g/L (but with 10s integration and 50 repetitions), we reach good agreement, expecting the SNR to be a factor of 2.8 lower in the CHO glucose measurement due to half the integration time and only a quarter of repetitions: $(\sqrt{0.5 \cdot 0.25} = 0.35 = 1/2.8$.

Another two examples are given in Figure 4.12a and Figure 4.12b, where the mAb peak (1250 cm^{-1}) and lactate peak (850cm^{-1}) are monitored with DPA. While general trends of the lactate Raman peak are similar to those measured with the Nova analyzer, they do not have the same granularity and resolution, but are still able to provide useful information regarding the process without any training data. For mAb, however, the DPA fails to track the titer and is not correlated with the Octet data.

Despite the successful trend detection shown above for glucose and partially for mAb and lactate, these results generally do not transfer to other analytes since they typically have low concentrations, have lower Raman cross sections, or lack observable peaks in the ROI.

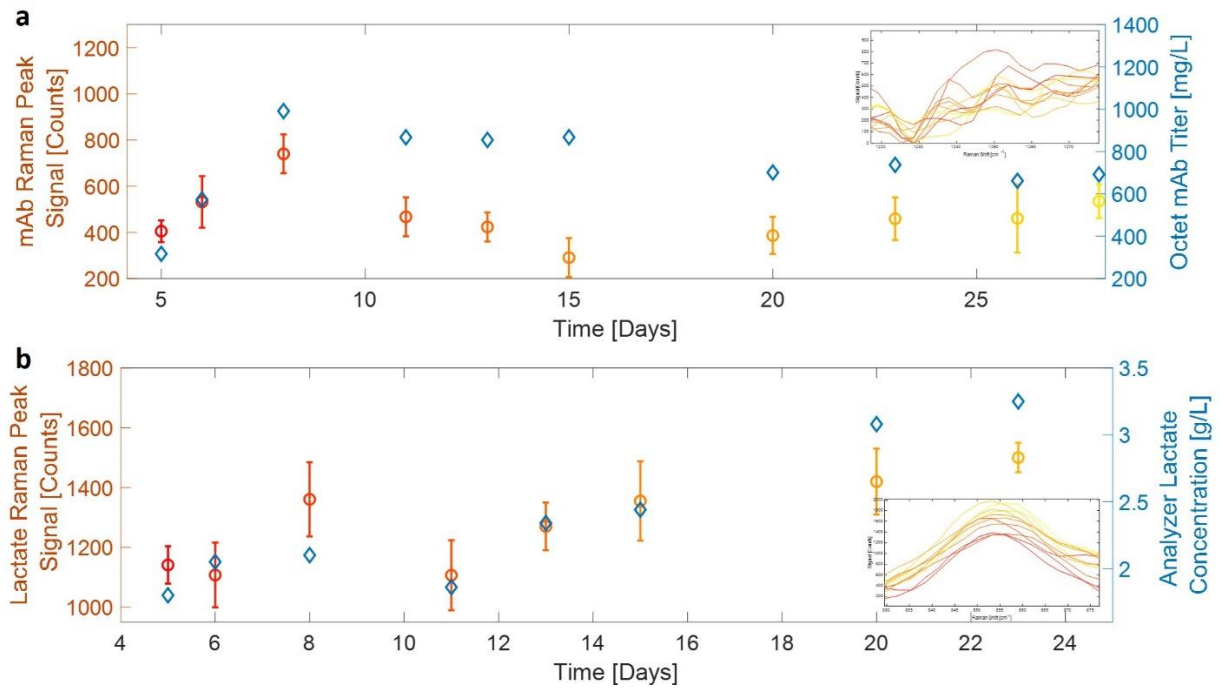

Figure 4.12: SSRS DPA for 12 samples of the CHO R3 run, a) of mAb peak (1250 cm^{-1}) with the SSRS signal values (red) presented on the left Y axis and the Octet mAb titer (blue) on the right Y axis and b) Lactate Raman peak (850cm^{-1}) with SSRS signal values(red) on the left and Nova metabolite analyzer on the right(blue).

Importantly, the main challenge around acquisition time is not resolved by using decimation and DPA. The total acquisition time for all Raman systems was 75x10s=750 seconds for the Kaiser, (3400 data points), 50x10s=500 seconds for the Biomod (1340 data points) and an overwhelming 16,560 seconds for the SSRS (5s repeated 12 times for each of the 276 datapoints). With the laser tuning overhead, the total measurement took 5 hours to complete. Such a long acquisition time makes the measurements more susceptible to drift due to the laser and also to changing environmental and sample dynamics, emphasizing the need to reduce the acquisition time to even shorter durations.

Figure 4.13 shows the effect of extended measurement time on a supernatant sample. The sample of Day 8 from run R3 was measured repeatedly with the SSRS 4 consecutive times. The spectra show clear changes in the fluorescence background

level, particularly for longer wavenumbers, and also changes in peak structure. Importantly, the sample placement in a quart cuvette, without the constant mixing which occurs in bioreactors, contributes to the degradation of the sample due to extended exposure to the excitation radiation.

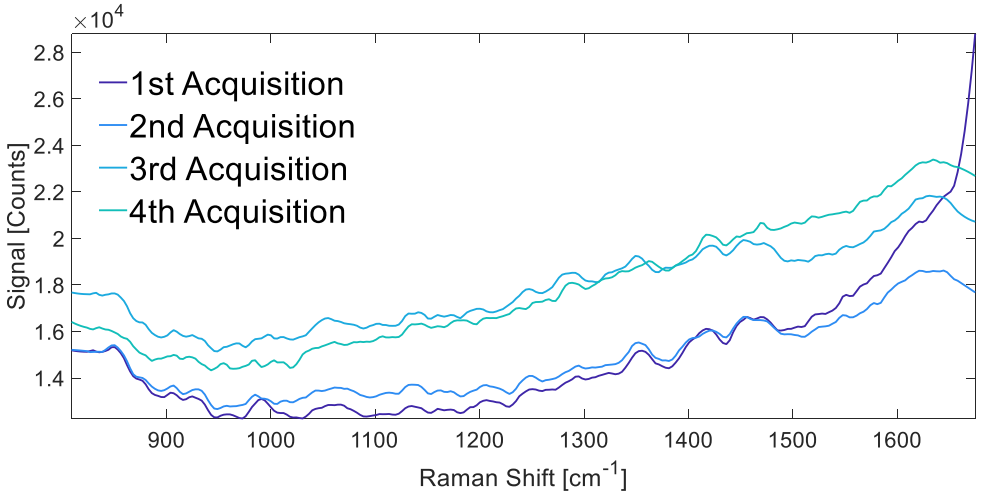

Figure 4.13: Example of sample degradation with extended acquisition time. Spectra of the Day 8 sample from run R3 acquired 4 consecutive times with each acquisition lasting 5 hours, showing sample degradation and varying fluorescent levels indicating denaturation.

If we attempt to perform a limited Raman peak acquisition, as was demonstrated for nitrate (see Subsection 2.3.2) or urea (see Figure 3.5), we discover the fluorescence background to be a limiting factor. In order to remove the background, polynomial fitting methods such as Lieber or other algorithms are used (see Subsection 1.6.1). These methods require a significant number of data points, particularly for complex spectra with many overlapping peaks and if we acquire only the peak region, we risk misinterpreting the data. Signal processing and spectral analysis methods that do not rely on background removal have a distinct advantage particularly for bioprocess monitoring.

4.5 Informed Sampling by Variable Importance in Projection

4.5.1 VIP

VIP, which was briefly introduced in Subsection 1.6.2.4 is a metric by which the importance of variables (spectral data points) on the output variance (analyte estimation) is measured[123,126,264]. The mathematical equation describing the derivation of the VIP scoring is given in Appendix C.

Once VIP scores are calculated, a threshold is set (often 1) and only variables above the threshold comprise the final model. Figure 4.14 shows the regression coefficients and VIP scores for a PLSR model estimating the glucose concentration in a cell culture dataset (see Section 1.7.2)

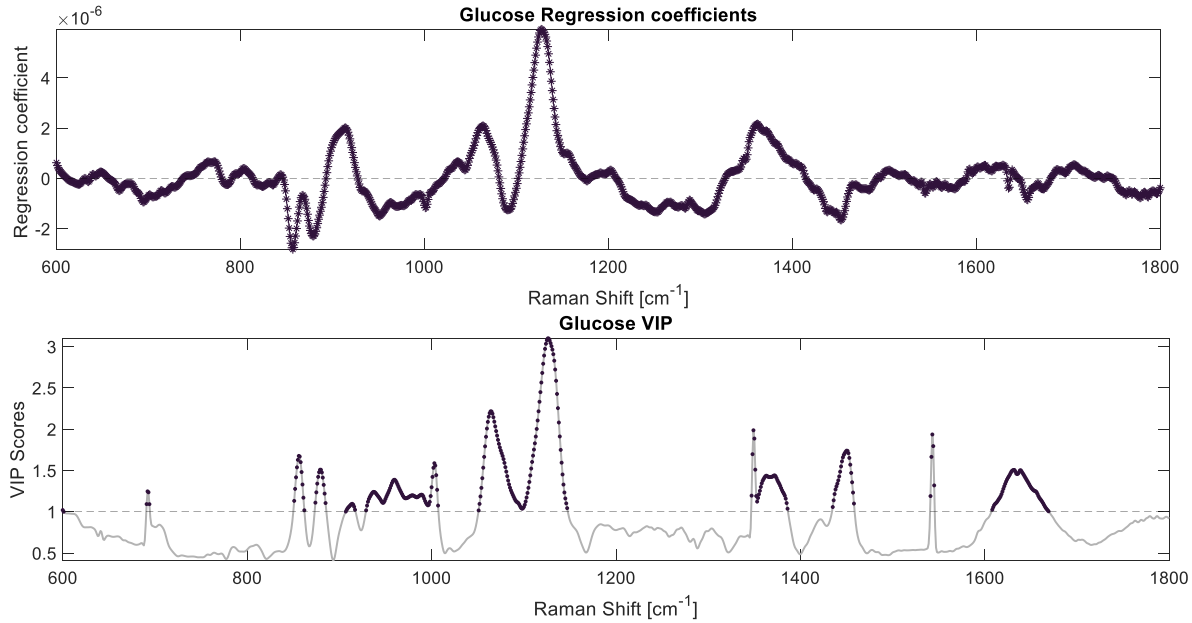

Figure 4.14: top: PLSR regression coefficients (β) computed from Kaiser Raman spectra of CHO cell culture, estimating the glucose concentration. Bottom: the VIP scores computed for each of the spectral data points, indicating their significance on the overall explained variance of the output.

In this Section we explore the use of a-priori Raman data for minimal spectral sampling, in order to further reduce the SSRS acquisition time. We propose to create an adaptive and selective sampling technique by which only high significance areas of the spectrum are sampled. The assignment of significance to spectral data points can be done in many ways, however, for this work we selected the use of PLSR and VIP scores. This approach supports the SSRS utility model for applications where a known set of analytes are used as metrics for a process progress or success. Importantly, if random samples are measured each time with different target analytes, a full spectrum would need to be acquired.

PLSR is an example for a widely-used spectral analysis technique that does not rely on fluorescent background removal. The PLSR algorithm (given in Subsection 1.6.2.4 and Appendix C) uses mean-centered spectra, $\mathbf{X}$, as inputs, i.e. the smoothed spectra which includes the fluorescent background shifted to have mean=0. The mean value of each spectrum is not lost, but used to build the regression coefficients). The regression coefficient vector, β, given in Equation C.10 and repeated here for convenience, provides the "weight" each data point is given for the final analyte prediction, $\hat{\mathbf{C}}$:

$$\hat{C} = X\beta = X\left[\sum_{i=1}^{N_{comp}} z_i \bar{q}_{0,i}\right] \tag{C.10}$$

In addition to the regression coefficients, we can calculate the VIP for each analyte (see Equation A.11 and Figure 4.14). The VIP allows us to map the useful parts of the spectra for the modeling of each analyte, but does not include information regarding the direction of correlation. As an example, we look at the regression coefficients and VIP scores for lactate which were calculated in Section 4.2 and given in Figure 4.15.

The regression coefficient and VIP show resemblance to lactate spectra[263] with a dominant peak in 860 cm^{-1}. This peak is marked as an area of importance by the VIP, with a value larger than 1, and also with a $\beta > 0$, indicating this peak positively contributes to the lactate concentration estimation. On the other hand, different regions marked as significant in the VIP map (910, 1130, 1348, 1542, 1635 cm^{-1}) have significantly lower β values which are even negative.

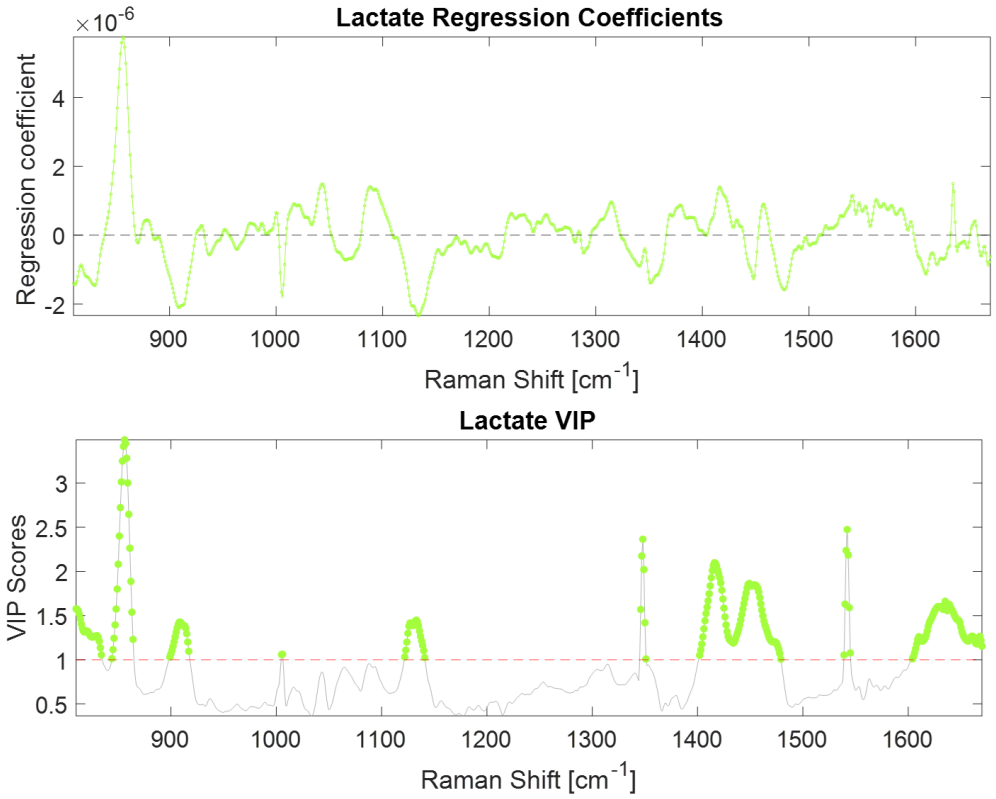

Figure 4.15: Lactate regression coefficients (top) marking the 0 line in dashed gray and the VIP scores (bottom) showing the highly correlated spectral points with the prediction of lactate concentrations. The two figures show that VIP alone might not be the best method to direct selective spectral acquisition since it also includes regions which are negatively correlated with the regression coefficients.

Inherently, for spectra containing hundreds of data points, Equation C.11 describes an ill-posed problem and so feature selection methods are used to reduce the dimensionality of the system. For the sake of predictive modeling, it is worthwhile

selecting high importance VIP regions as all the spectra had already been sampled, even regions with negative β values. Low VIP areas which are likely to add noise can safely be ignored. However, the same cannot be said for selective sampling.

With SSRS, the objective is to minimize the number of acquired points and so it is worth considering avoiding sampling points with negative β values all together. In order to test this hypothesis, a simulation based on Kaiser data was constructed, which is describe in the following Section.

4.5.2 VIP-Informed Sampling Simulation

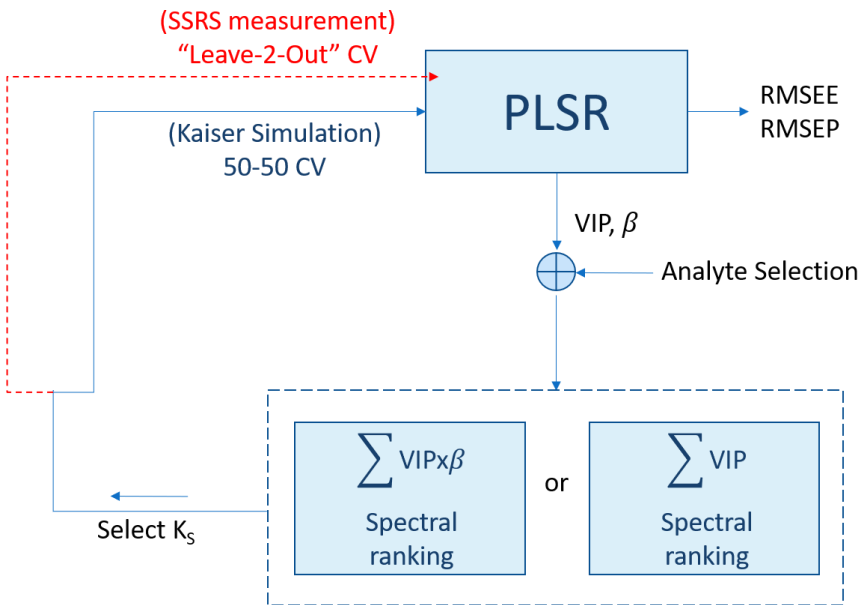

Figure 4.16: Diagram illustrating the selective VIP-informed spectral sampling and validation with SSRS. The first step of the algorithm calculates the full PLSR model after which selective points are chosen based on VIP scores or VIPxBeta scores, after which a reduced spectra is used to recalculate the PLSR model.

In order to assess the selective VIP sampling method a simulation and validation process was constructed, described in Figure 4.16. In the first step all data (861 data points) in the 810-1670 cm^{-1} spectral range was used to compute VIP scores and regression coefficients for all 7 analytes (see Section 4.2). The RMSEE and

RMSEP values (see Table 4.2) are used to benchmark the performance for future iterations. Figure 4.17 shows the VIP scores in the first step, where the colored markers indicate the significant VIP regions for which VIP >1.

The user then inputs the analytes for which selective sampling should be performed so only their respective VIP scores and β values are considered. In the simulation results presented below, all 7 analytes were considered.

The second step assigns a value for each data point. Two methods are used to evaluate the significance of each data point. In the first, the VIP scores of all analytes (Figure 4.17) are summed, creating a shared "VIP heat map" (Figure 4.18), where red markers indicate where the cumulative VIP score was greater than 1 for all analytes. In the second method, termed VIPxBeta, the products of the VIP scores and normalized β values are calculated for each analyte. Normalized β values allow us to compare analytes without accounting for their different units of measurement. Figure 4.18 shows the data point ranking of the second method in light blue.

4.5.2.1 Spectral Data Point Selection

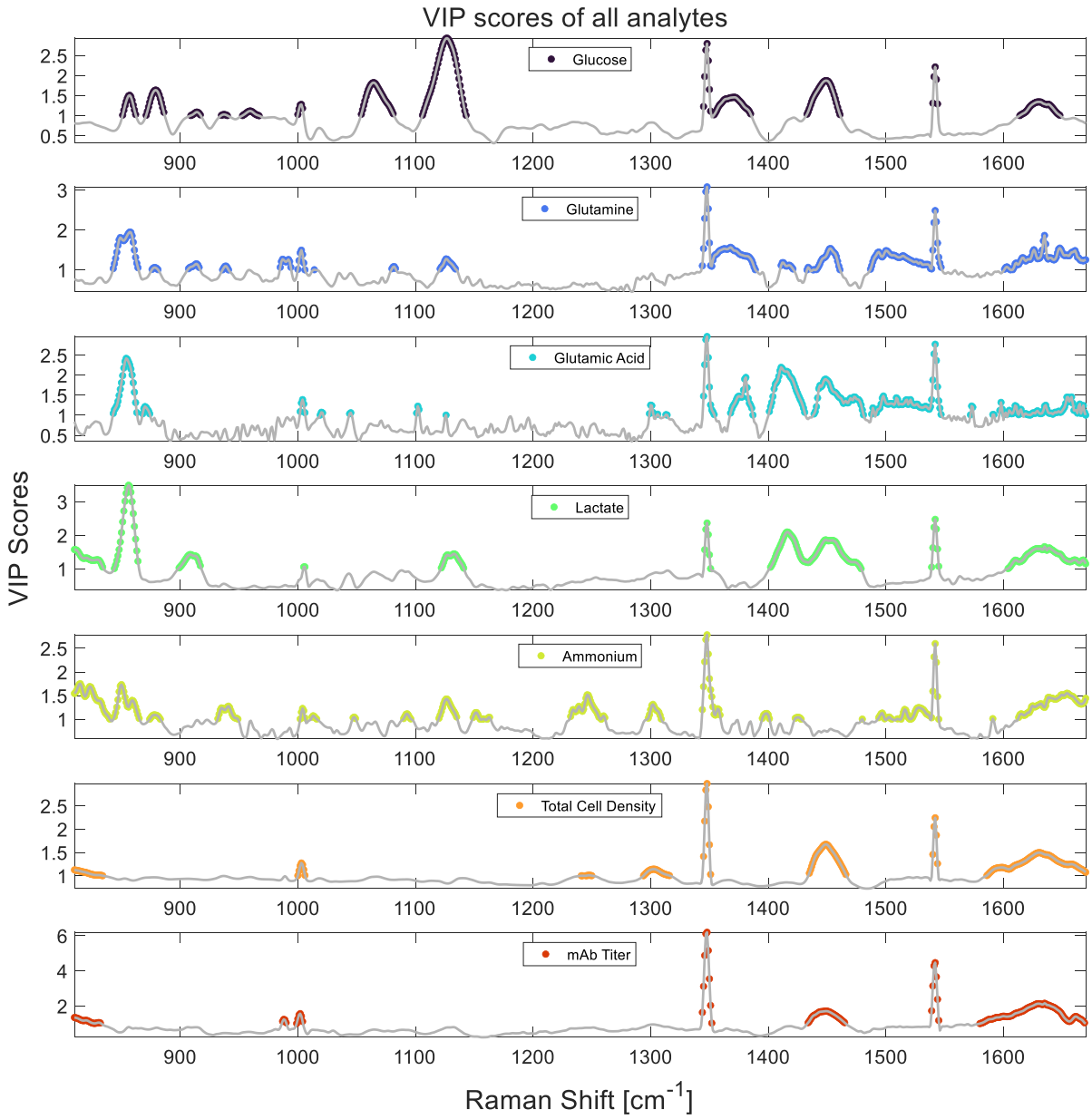

Figure 4.17: PLSR VIP scores for all 7 analytes in the full spectral range between 810-1670cm^{-1} where the colored markers correspond to VIP scores greater than 1.

After the VIP heat maps are created, the user selects the number of required spectral datapoint, K_P, and they are ranked according to their value.

Importantly, both VIP scores and regression coefficients have been previously

used to minimize spectral sampling[156], however, their combination has never been explored and the use of a weighted score sum for multiple analytes is also proposed and tested here for the first time.

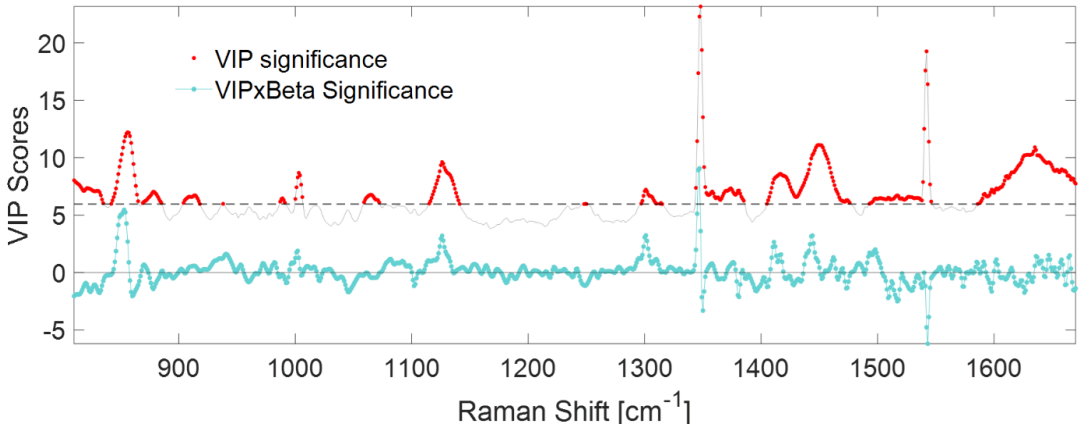

Figure 4.18: Two methods of ranking spectral data point significance. The first in red, using the sum of all analyte VIP scores, and the second, in light blue, which is the sum of products of VIP and regression coefficients.

Figure 4.19 shows an example of selecting 50 data points in both methods. The red values show the position of the highest-ranking scores in the VIP method and the blue shows the ranking in the VIPxBeta method.

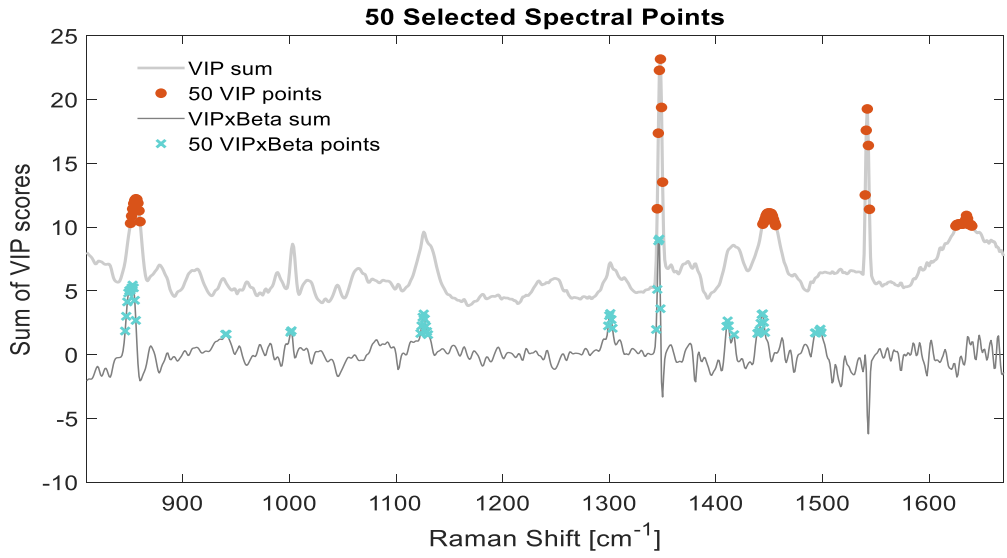

Figure 4.19: Example for the 50 selected spectral points in both methods showing the VIP method in red and the VIPxBeta method in blue.

In the third and final step of the simulation, the PLSR is computed again, but only on the reduced spectra with K_P data points. The PLSR models were computed as before with 50% of the CHO data used for training and 50% for prediction. The number of principal components, N_{comp}, was recalculated for each analyte to guarantee at least 83% explained variance based on the new partial spectra. For glucose, lactate, CD and mAb, N_{comp} remained fairly consistent, changing by 1 or 2 components even for 30 data points.

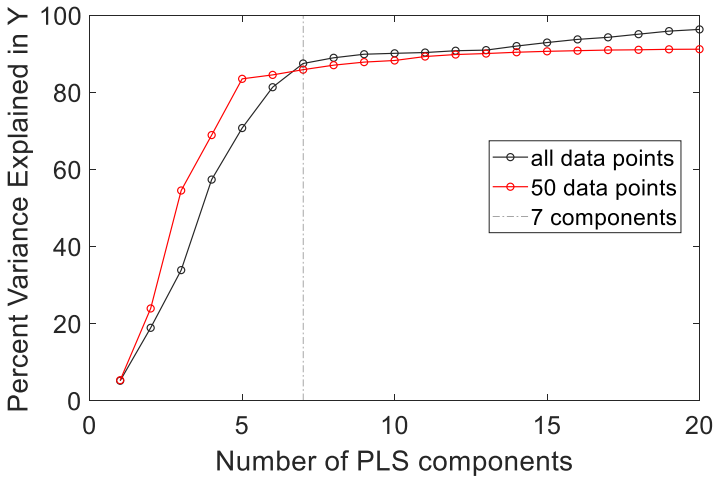

Figure 4.20: The percentage of variance explained in Kaiser spectra for glucose concentration as a function of number of PLS components for both a full-range spectra (black) and only 50 data points (red) showing the the number of components changes for the partial spectra.

An example of this is given in Figure 4.20 that shows the variance explained in glucose concentration estimation as a function of number of PLS components for both the full spectrum and a 50-point reduced spectrum. However, for glutamine, glutamic acid and ammonium, which require a larger number of components, there was a significant increase and particularly for $K_P<60$, the maximal variance explained did not reach 80% even for the maximal number of components. This is also attributed to the limited spectral range we examined in this simulation.

4.5.2.2 Simulation Results

The simulation was run for K_P values between 215 and 30 for all 7 analytes. Table 4.3 and Table 4.4 show the results in the VIP and VIPxBeta methods respectively. The results show that for both methods, it is possible to significantly reduce the number of spectral data points and have a relatively small effect on the RMSEE and RMSEP values where the VIPxBeta method tends to perform slightly better. As an example, for K_S=80, which signifies an order of magnitude reduction in acquisition time, results show only an average 19.6% increase in RMSEE and 12.4% increase in RMSEP (VIPxBeta).

VIP	K_P	Glucose [g/L]	Glutamine [mmol/L]	Glutamic acid [mmol/L	Lactate [g/L]	Ammonium [mmol/L]	CD [x10^5 cells/ml]	mAb [mg/L]
RMSEE	861	0.61	0.43	0.52	0.38	0.76	51.40	96.97
	215	0.67	0.45	0.55	0.38	0.76	51.06	96.18
	100	0.71	0.48	0.99	0.41	0.81	58.41	96.24
	90	0.68	0.56	1.06	0.40	0.83	58.65	95.26
	80	0.67	0.64	0.98	0.40	0.86	54.40	94.71
	70	0.63	0.67	0.75	0.38	1.00	55.11	93.42
	60	0.69	0.64	0.77	0.37	0.97	57.32	94.61
	50	0.77	0.56	0.80	0.40	0.99	58.58	98.96
	40	0.75	0.57	0.83	0.38	1.03	56.15	99.98
	30	0.78	0.59	0.88	0.37	1.06	57.42	99.11
RMSEP	861	0.61	0.56	0.83	0.44	0.63	62.81	170.34
	215	0.68	0.71	1.10	0.45	0.83	67.85	159.83
	100	0.69	0.93	1.16	0.46	1.31	74.92	169.54
	90	0.67	0.89	1.28	0.46	1.36	79.70	170.34
	80	0.66	0.90	1.25	0.46	1.34	156.99	170.17
	70	0.65	0.95	0.99	0.44	1.32	103.31	173.88
	60	0.70	0.87	1.01	0.43	1.35	93.79	175.45
	50	0.90	0.76	0.96	0.45	1.08	127.84	170.22
	40	0.89	0.69	0.97	0.43	1.10	89.12	170.48
	30	0.87	0.66	0.92	0.46	1.10	76.89	188.57

Table 4.3: Simulation results for analyte concentrations with various number of spectral data points with the VIP ranking method.

Figure 4.21 a-d show the predicted PLSR values versus the measured values for K_P =40 data points (40 minutes per spectrum) for glucose, lactate, total CD and mAb in the VIPxBeta method. Each color on the plots represents data from different CHO runs that were monitored using the Kaiser system (see Figure 4.3).

VIPxBeta	K_P	Glucose [g/L]	Glutamine [mmol/L]	Glutamic acid [mmol/L	Lactate [g/L]	Ammonium [mmol/L]	CD [x10^5 cells/ml]	mAb [mg/L]
RMSEE	861	0.61	0.43	0.52	0.38	0.76	51.40	96.97
	215	0.70	0.45	0.55	0.34	0.75	51.50	96.61
	100	0.63	0.45	0.67	0.36	0.76	51.20	93.80
	90	0.71	0.45	0.65	0.35	0.77	50.36	94.17
	80	0.70	0.47	0.68	0.38	0.78	49.57	96.13
	70	0.68	0.49	0.69	0.37	0.77	50.35	99.28
	60	0.69	0.54	0.72	0.38	0.78	49.38	101.48
	50	0.70	0.56	0.75	0.40	0.90	50.77	95.88
	40	0.71	0.57	0.77	0.40	0.95	49.11	96.21
	30	0.70	0.59	0.83	0.40	0.99	57.36	87.93
RMSEP	861	0.61	0.56	0.83	0.44	0.63	62.81	170.34
	215	0.65	0.69	1.11	0.43	0.77	61.61	158.37
	100	0.62	0.75	1.16	0.45	1.03	60.31	144.52
	90	0.70	0.77	1.06	0.45	0.98	59.40	148.17
	80	0.69	0.83	1.02	0.48	0.97	57.37	129.12
	70	0.68	0.77	1.01	0.46	1.02	59.27	152.08
	60	0.69	0.71	0.96	0.46	0.98	57.85	167.64
	50	0.70	0.66	0.93	0.48	1.07	60.75	149.02
	40	0.72	0.67	0.92	0.48	1.06	59.24	157.94
	30	0.70	0.70	0.95	0.48	1.10	69.49	191.86

Table 4.4: Simulation results for analyte concentrations with various number of spectral data points with the VIPxBeta ranking method.

a

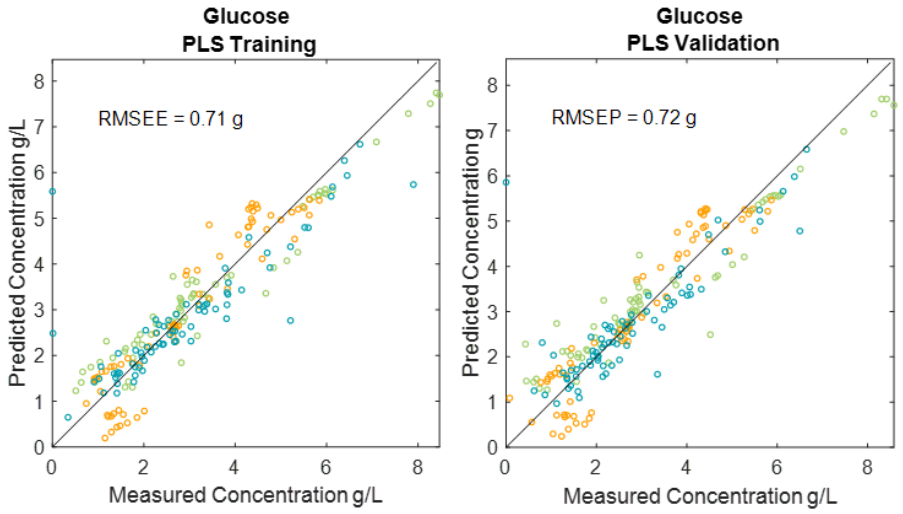
Glucose
PLS Training
RMSEE = 0.71 g
Predicted Concentration g/L
Measured Concentration g/L
Glucose
PLS Validation
RMSEP = 0.72 g
Predicted Concentration g
Measured Concentration g/L

b

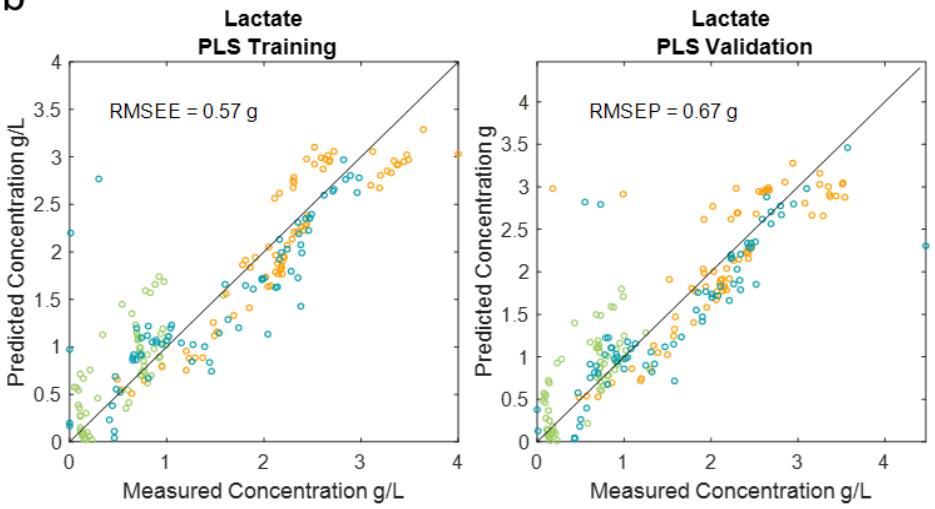
Lactate
PLS Training
RMSEE = 0.57 g
Predicted Concentration g/L
Measured Concentration g/L
Lactate
PLS Validation
RMSEP = 0.67 g
Predicted Concentration g
Measured Concentration g/L

c

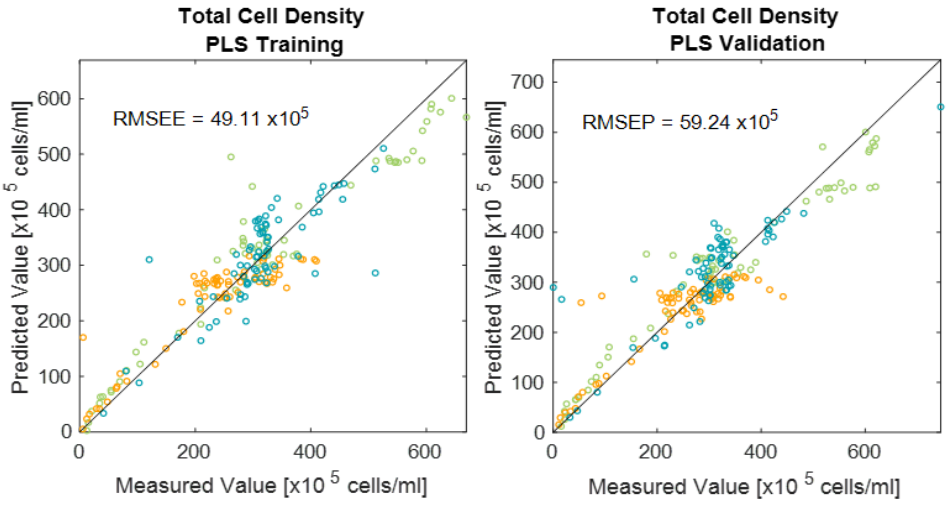
Total Cell Density
PLS Training
RMSEE = 49.11 x10^5
Predicted Value [x10 5 cells/ml]
Measured Value [x10 5 cells/ml]
Total Cell Density
PLS Validation
RMSEP = 59.24 x10^5
Predicted Value [x10 5 cells/ml]
Measured Value [x10 5 cells/ml]

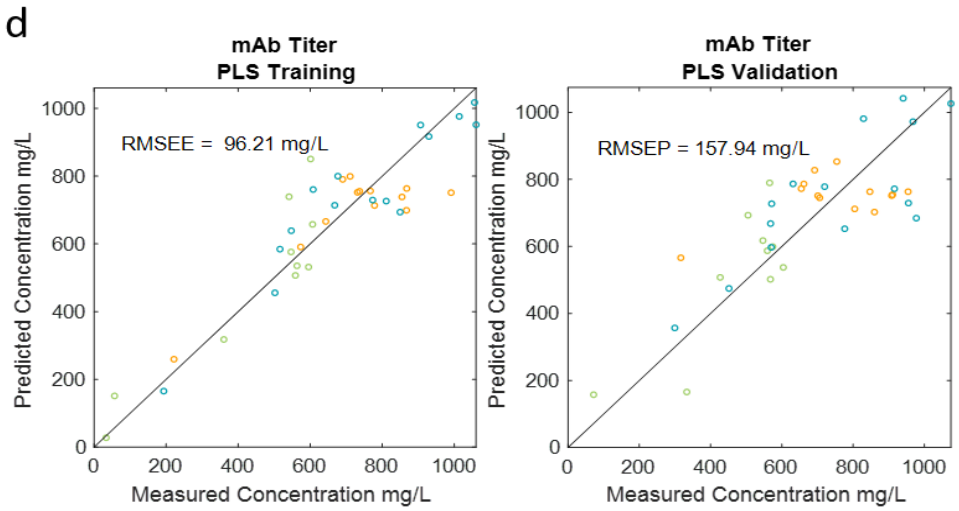

Figure 4.21: Kaiser spectra PLSR models results showing the estimated and predicted analyte concentration results for a) glucose, b) lactate, c) total CD and d) mAb with only 40 datapoints ranked in the VIPxBeta method. The different colors represent data from the three different CHO perfusion runs that were monitored using the Kaiser system.

The above results suggest that it is possible to significantly reduce acquisition time from approximately 5 hours to 40 minutes, and still maintain good prediction values using VIP-informed sampling. The following section will put this theory to the test by selectively sampling with the SSRS.

4.5.3 Validation by SSRS Measurement

It is generally quite difficult to transfer PLSR model results between different runs, let alone different Raman systems. Any Raman spectrum includes specific system spectral features from the lenses, filters, or optical windows, which are captured along with the sample under inspection. Particularly for the SSRS and Kaiser, which have completely different hardware and were also inspecting different samples (supernatants versus media with cells) it's extremely unlikely one model can be used to inform another. However, we can use the acquired SSRS spectra of the 12 CHO samples from run R3 (see Section 4.4) to evaluate the VIP-informed sampling strategy.

4.5.3.1 PLSR parameters for SSRS Spectra

Since only 12 CHO samples from run R3 were available for SSRS measurements, the data was not split into equal data sets of training and validation but rather a "leave-2-out" cross validation was performed iteratively. In each iteration, 10 of the 12 spectra were used for training and 2 spectra were used for validation until all permutations were exhausted (12*11/2=66). The regression coefficients and final RMSEE and RMSEP are the mean values computed in all iterations.

The number of PLSR components for each analyte were determined automatically to be the lowest number for which the explained variance would exceed 83%.

4.5.3.2 SSRS PLSR results

The reduced number of samples limits the PLSR ability to predict analyte concentrations from previously unseen spectra and also limits the number of possible PLS components, further hindering performance. Additionally, as was established before, the SNR of the SSRS spectra was lower compared with the LOD measurement due to short integration times (5 seconds) and a low number of repetitions (12). Table 4.5 and Table 4.6 show the measurement results for VIP informed sampling and VIPxBeta informed sampling respectively.

Overall, the RMSEE values were quite good, and remained so even for $K_P<70$ for both selection methods. There appears to be no advantage to sampling using VIPxBeta, however, there is not enough data to draw definite conclusions.

SSRS VIP	K_P	Glucose [g/L]	Glutamine [mmol/L]	Glutamic acid [mmol/L	Lactate [g/L]	Ammonium [mmol/L]	CD [x10^5 cells/ml]	mAb [mg/L]
RMSEE	276	0.48	0.08	0.17	0.24	0.15	18.35	86.90
	100	0.51	0.09	0.22	0.27	0.17	21.64	60.54
	90	0.52	0.14	0.24	0.27	0.17	21.91	62.65
	80	0.52	0.14	0.24	0.27	0.17	22.54	66.04
	70	0.52	0.13	0.26	0.28	0.22	25.25	75.71
	60	0.45	0.12	0.27	0.18	0.17	25.62	77.68
	50	0.45	0.12	0.17	0.20	0.19	25.90	78.39
	40	0.45	0.12	0.19	0.12	0.14	27.58	79.28
	30	0.35	0.13	0.22	0.14	0.10	24.73	66.99
RMSEP	276	1.65	0.61	4.41	1.96	1.42	238.71	609.52
	100	1.60	0.64	4.45	2.05	1.43	243.54	606.10
	90	1.60	0.64	4.46	2.05	1.43	243.02	605.66
	80	1.62	0.63	4.44	2.03	1.42	244.16	606.55
	70	1.65	0.62	4.42	2.01	1.41	241.59	611.68
	60	1.69	0.62	4.40	1.94	1.41	238.46	615.09
	50	1.70	0.63	4.41	1.92	1.42	236.01	615.55
	40	1.70	0.63	4.41	1.96	1.42	235.52	616.03
	30	1.66	0.64	4.40	1.96	1.45	241.26	609.28

Table 4.5: SSRS measurement results for analyte concentrations with various number of spectral data points with the VIP ranking method.

SSRS VIPxBeta	K_P	Glucose [g/L]	Glutamine [mmol/L]	Glutamic acid [mmol/L	Lactate [g/L]	Ammonium [mmol/L]	CD [x10^5 cells/ml]	mAb [mg/L]
RMSEE	276	0.48	0.08	0.17	0.24	0.15	18.35	86.90
	100	0.37	0.08	0.16	0.23	0.17	22.89	64.98
	90	0.38	0.10	0.19	0.24	0.17	23.84	90.59
	80	0.39	0.11	0.21	0.24	0.18	24.91	68.69
	70	0.40	0.07	0.23	0.25	0.15	21.47	69.72
	60	0.52	0.07	0.22	0.25	0.16	21.71	69.94
	50	0.52	0.07	0.23	0.25	0.16	22.19	71.11
	40	0.52	0.06	0.23	0.19	0.17	14.98	72.62
	30	0.43	0.07	0.16	0.19	0.12	18.90	73.80
RMSEP	276	1.65	0.61	4.41	1.96	1.42	238.71	609.52
	100	1.61	0.64	4.50	2.00	1.45	236.20	607.46
	90	1.60	0.65	4.53	2.04	1.45	236.79	605.36
	80	1.59	0.66	4.56	2.04	1.44	235.40	605.63
	70	1.59	0.65	4.54	2.03	1.44	235.38	605.38
	60	1.64	0.65	4.54	2.03	1.46	234.23	605.33
	50	1.61	0.64	4.54	2.04	1.45	234.50	605.94
	40	1.62	0.64	4.52	1.99	1.45	235.53	607.93
	30	1.65	0.66	4.44	1.98	1.43	231.89	609.54

Table 4.6: SSRS measurement results for analyte concentrations with various number of spectral data points with the VIPxBeta ranking method.

The RMSEP errors are significantly higher than RMSEE, attributed to the limited capacity of the PLSR model with such a limited sample number. However, the prediction errors remain similar even for a reduced number of K_P spectral points, indicating the usefulness of VIP informed sampling.

A "sanity check" was performed by sampling K_P random data points and comparing to the VIP-informed methods (Table 4.7). The random RMSEE errors were quite low, but RMSEP values were significant for all analytes and all values of K_P. The random selection method produced larger errors compared with the VIP-informed methods, further indicating that there is value in VIP- informed sampling.

Generally, the large differences between RMSEE and RMSEP values is indicative of over-fitting, which is not surprising due to the sample size. Conclusive validation of VIP -informed sampling requires additional SSRS measurements.

Random	K_P	Glucose [g/L]	Glutamine [mmol/L]	Glutamic acid [mmol/L	Lactate [g/L]	Ammonium [mmol/L]	CD [x10^5 cells/ml]	mAb [mg/L]
RMSEE	276	0.48	0.08	0.17	0.24	0.15	18.35	86.90
	100	0.52	0.08	0.19	0.22	0.15	18.32	93.49
	90	0.38	0.08	0.21	0.13	0.12	21.23	70.86
	80	0.49	0.08	0.17	0.23	0.15	18.81	89.00
	70	0.49	0.09	0.29	0.16	0.15	17.77	87.17
	60	0.39	0.07	0.20	0.23	0.15	20.42	90.68
	50	0.51	0.07	0.19	0.25	0.10	14.63	93.12
	40	0.53	0.08	0.18	0.16	0.17	21.21	71.06
	30	0.52	0.09	0.29	0.17	0.15	21.95	59.65
RMSEP	276	1.65	0.61	4.41	1.96	1.42	238.71	609.52
	100	1.85	0.72	4.59	2.06	1.47	249.99	649.74
	90	1.91	0.67	4.56	2.04	1.47	249.18	653.99
	80	1.85	0.67	4.60	2.07	1.47	249.94	649.40
	70	1.89	0.67	4.56	2.03	1.45	246.72	652.27
	60	1.87	0.71	4.58	2.05	1.47	248.53	654.09
	50	1.86	0.68	4.58	2.07	1.49	252.47	648.33
	40	1.81	0.68	4.59	2.04	1.47	249.50	656.11
	30	1.83	0.69	4.57	2.01	1.46	247.24	652.95

Table 4.7: SSRS measurement results for analyte concentrations with various number of randomly selected spectral data points.

Notably, the SSRS PLSR still allows us to track trends in analyte concentrations, despite errors. Figure 4.22 shows the SSRS PLSR results for K_P=40 and the ground truth of the Nova analyzer. These results mostly reflect the RMSEE errors and the model as a descriptive tool and not a predictive tool due to the limited dataset available.

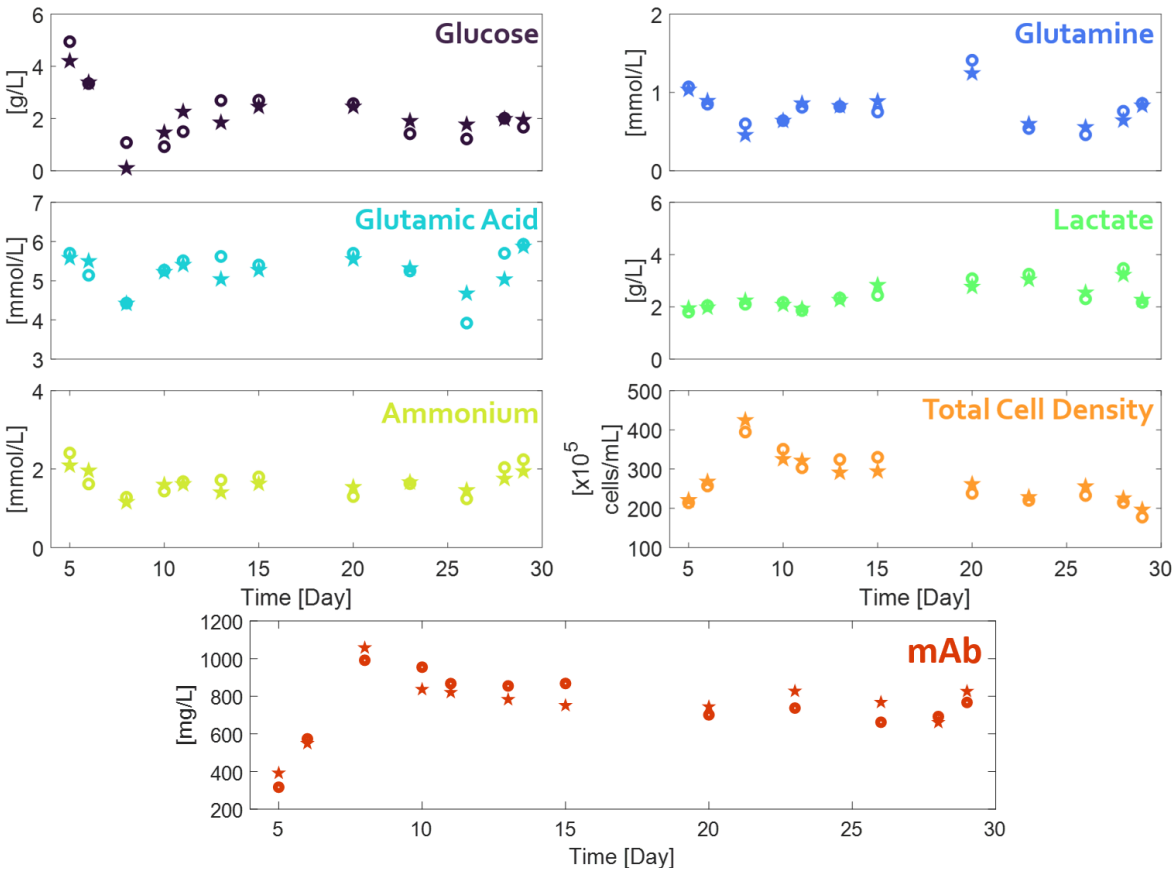

Figure 4.22: SSRS PLSR results with K_P=40 points for 12 CHO supernatant samples from Run R3, reflecting the model's RMSEE estimation errors of the data. The empty circles represent the Nova analyzer values and the stars represent the PLSR estimation results.

4.5.3.3 Summary

In this Chapter, samples from a CHO perfusion culture were measured using the SSRS and also two dispersive Raman systems. The SSRS achieved comparable spectra to the dispersive systems and enabled monitoring of key metabolites including glucose, lactate and also cell density and mAb titer using direct Raman peak analysis.

The hypothesis of using VIP scores and regression coefficients calculated by PLSR to minimize sampling time was investigated using a simulation with dispersive spectra and showed that VIP-informed sampling has potential to reduce acquisition time by a factor of 7, with minimal or no increase to estimation errors.

The Kaiser simulation data showed that based on VIP or VIPxBeta sampling, estimation and prediction errors were consistent, supporting this method for analyte prediction. While the RMSEE errors were larger than those of SSRS (e.g. glucose had an RMSEE value of 0.6-0.7 g/L and SSRS only 0.4-0.5 g/L), the Kaiser data was monitoring the testbed development processes that suffered from large variability in culture conditions. SSRS results, particularly in regards to validation errors was limited due to the small dataset but shows promise capturing essential metabolite and mAb values with as little as 40 data points.

VIP and regression coefficients informed sampling can support the use of SSRS as a utility, particularly when a sensor system is integrated into a well-defined process, e.g. a chemical manufacturing facility or pharmaceutical production where the process monitored has a set of analytes the indicate the process success. However, if multiple users monitor random and unrelated samples, a full spectrum would need to be acquired.

CHAPTER 5

Conclusion and Future Work

The pursuit of ubiquitous chemical sensing has long been a central objective within the scientific community, accelerated by increasing demands from both regulatory bodies and industrial stakeholders. Despite this, conventional chemical sensing predominantly takes place in centralized analytic laboratories and relies on reagent-based techniques. The deployment of wireless bio/chemical sensors, while promising, is hindered by constraints in sensing methodologies, data acquisition, and power consumption, limiting their practical utility.

In this thesis, a novel utility model for chemical sensing is introduced, building upon swept-source Raman spectroscopy to address previous challenges in the field. Drawing inspiration from recent advancements in cloud and edge computing, the proposed model is designed to meet the criteria of a utility service, encompassing hardware infrastructure, scalability, essential service provision, support for generic applications, and user-friendliness.

Demonstrating the feasibility of this chemical sensing utility service, Chapter 2 underscores the sensitivity of the SSRS network sensor system's basic component, the SSRS probe. Remarkably, this sensitivity matches that of high-end dispersive benchtop systems, with significantly reduced laser power. Validation was achieved through measuring LODs for glucose and nitrate, alongside monitoring nitrate concentrations in a hydroponics system reservoir and environmental water samples.

Chapter 3 demonstrates the scalability of the sensor network, leveraging readily available optical fibers and switches to extend sensor deployment over kilometers. Economic viability is assessed through cost analyses across various system sizes, comparing with commercially available Raman systems of similar performance.

Furthermore, samples from a CHO-cell line perfusion culture were evaluated using the SSRS, with comparisons drawn against both custom and commercially available Raman systems. Adaptation of linear regression algorithms, tested through simulations and SSRS measurements, demonstrated the potential to optimize spectral acquisition, reducing duration by an order of magnitude without compromising predictive accuracy.

These promising results warrant exploration of near and long-term directions for advancing SSRS technology further.

5.1 Near Term Applications

Continuous manufacturing Monitoring

Chapter 4 has shown the usefulness of SSRS for the monitoring of cells cultures producing therapeutic mAbs. The sensitivity of the SSRS probe with only 6mW of power to monitor metabolites and mAb production was demonstrated. However, PLSR informed sampling was validated only as a descriptive model due to the limited availability of samples. In order for SSRS to be a predictive tool, additional samples need to be tested to create a more robust model. An integration of the SSRS probes into a bioreactor and additional points in the mAb continuous testbed would enable the exploration of real-time data collection, analysis, and modeling.

Novel Cell-Therapy Development

An additional emerging category of therapies in which SSRS Raman can be

instrumental is cell-based therapeutics. In this family of products, the cells themselves are the therapeutic agent[265]. These cells can replace damaged tissue or produce compounds in-vivo such as hormones or cytokines which modulate the response of the immune system. Examples for such therapies are Chimeric Antigen Receptor T-cells, (CAR-T) which is a treatment for Leukemia[266], or Mesenchymal Stromal Stem Cells (MSCs) used to treat Graph Versus Host Disease[267].

The development of cell-based therapies often includes many iterations in which cells are harvested from a donor, genetically altered or activated, and then expanded in culture. These cell therapies depend not only on the cell culture process itself, but also on donor variability, which can be significant, particularly when cells are derived from sick donors. Cell therapies require an additional level of monitoring and control in both process development and manufacturing to enhance product uniformity and assure quality and safety.

Raman spectra of supernatant from MSC cultures or T-cell cultures can be used to build predictive models even for different donors and has been successfully demonstrated using the dispersive Biomod system with prediction errors of 0.15g/L of glucose and 0.2g/L lactate using PLSR[268] (see Figure 5.1).

A SSRS sensor network can be used to monitor multiple culture conditions and various donor products in a synchronized manner to optimize therapeutic development and also to monitor production in either large scale or in small, personalized manufacturing facilities. Excitation powers, particularly for small volume cultures, need to be kept as low as possible to reduce any harmful effect on the cells and their environment. The use of smart adaptive sampling techniques, as were described in Section 4.5, to minimize acquisition time but maintain model accuracy is paramount for fast culture screening.

Lastly, while Raman for 16-96 well plates has been developed[269], it relied on

sequential scanning using a single Raman probe to acquire the spectra. This process is extremely time consuming and could pose a threat to the samples due to high laser power. The SSRS could be integrated onto a robotic arm and enable fast spectral acquisition of all samples with significantly lower power and a short illumination period. However, a miniaturized probe would need to be fabricated for this application.

The high cost of such therapies along with their life-saving potential could justify a mid-level simultaneous sensor system or even a large-scale simultaneous system as describes in Chapter 3.

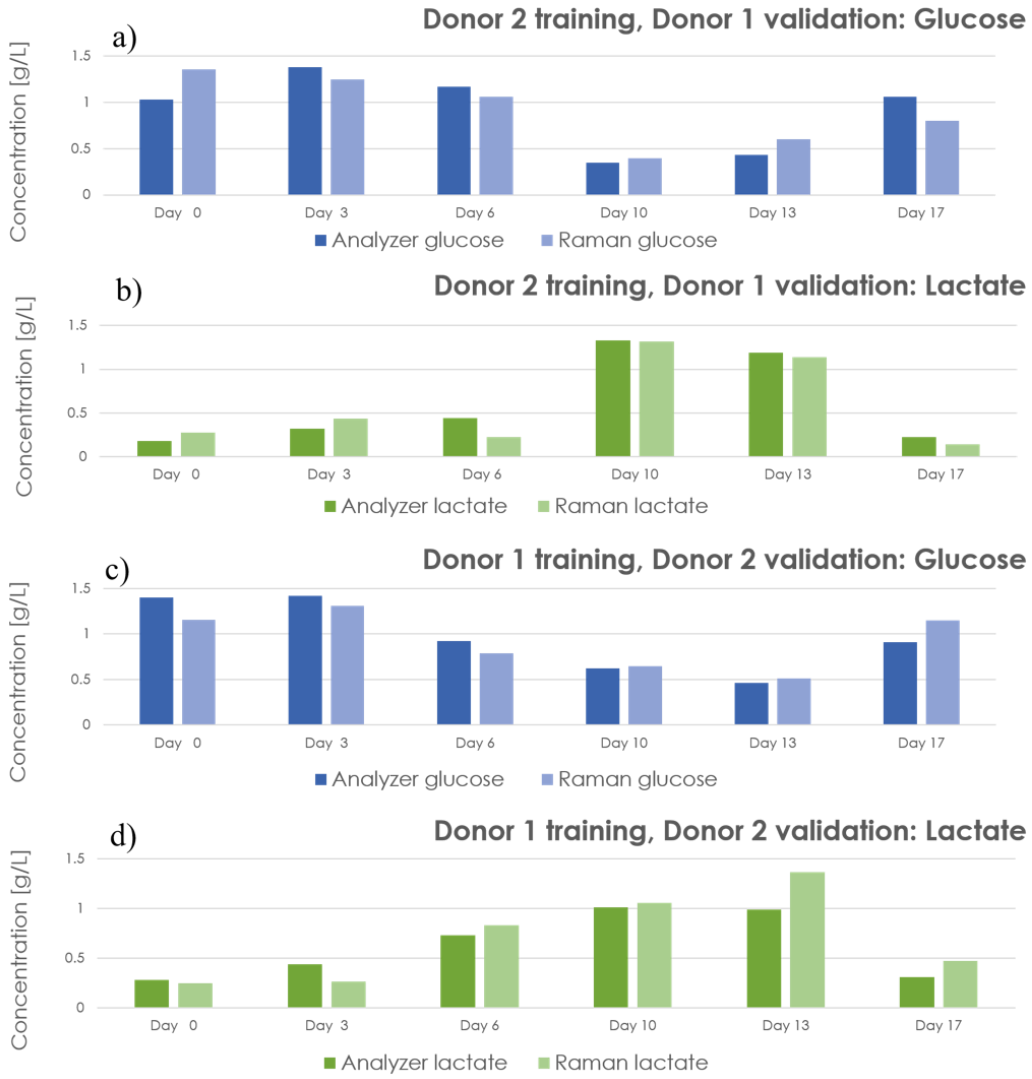

Figure 5.1: PLSR prediction results from MSC supernatant spectra taken with the Biomod which used cross-donor validations. The results show the model's predictive concentrations for (a) glucose and (b) lactate as learned from Donor 2 and used to estimate the values for Donor 1 along with the ground truth data from the Nova metabolite analyzer. Similarly, Figures (c) and (d) show the predicted values for glucose and lactate respectively, as learned from Donor 1 and used to predict values for Donor 2.

Agricultural and Horticular Monitoring

The SSRS has been demonstrated on a small-scale hydroponic system but full large-scale integration would benefit from several modifications. First, the SSRS probes were designed for sterile liquid immersion and while they perform well for free-space samples, but they can be significantly simplified. Probes can be modified for

longer probing distances on the order of centimeters and not millimeters by introducing new objective lenses or even using a collimated beam for probing large areas. A combination of probes can serve different sensing needs: liquid immersion or screening of plants in free space. Additionally, the fabrication of the probes can be facilitated if strict port dimensions do not pose a mechanical limitation and if autoclaving isn't necessary. These modifications might also allow for better internal alignment of optics and fibers.

Second, deployment of a large system requires housing the main laser and deploying a network of fibers which may be intrusive and expensive and require maintenance (beyond the cost of components). Calibration, multi-sensor acquisition protocols and multi-sensor data fusion need to be developed to both manage the system and to gain as much value from its' deployment. As illustrated in Chapter 4, large amounts of data would need to be collected for models to become reliable and provide good predictive assessments.

5.2 Long-Term Development

Medical Diagnostics

SSRS is unique for allowing the acquisition of Raman spectra with low excitation power. Low illumination is crucial in medical applications since high excitation can cause tissue damage due to phototoxicity or protein denaturation[270].

NIR Raman is used to monitor blood, serum and other bodily fluids for fast chemical screening or detection of infections. It is also used to classify various tissues as healthy or malignant during endoscopies, gastroscopies or other surgical operations. In all of these use cases, excitation levels must remain under the safety guidelines to ensure patient safety and are enforced by the FDA. These guidelines have so far

prevented the use of NIR Raman for human ophthalmic in-vivo measurements due to the high sensitivity of the eye.

Cytochrome C is a crucial heme protein which bears resemblance to hemoglobin[271,272]. This protein is abundant in mitochondria and exhibits a conformational change when it is oxidized, which alerts to the redox state of the tissue. This structural change has been previously monitored by resonant UV-Raman and is indicative of tissue health[273]. While UV-resonant Raman is destructive, SSRS can detect structural changes safely. Figure 5.2 shows the normalized spectra of 1mg/ml cytochrome C in PBS in oxidized and reduced forms for both our Biomod (120mW, 50x10s) and a resonant Raman spectrum (414nm, 4mW, 100x1s, provided by Dr. Bertan Cakir from MGH and the Harvard Medical School Department of Ophthalmology). Though the resonance Raman has spectral features which are not found in NIR Raman (1350-1400 cm-[1]), both spectra show changes in the spectral range between 1500-1700 cm^{-1} when oxidized.

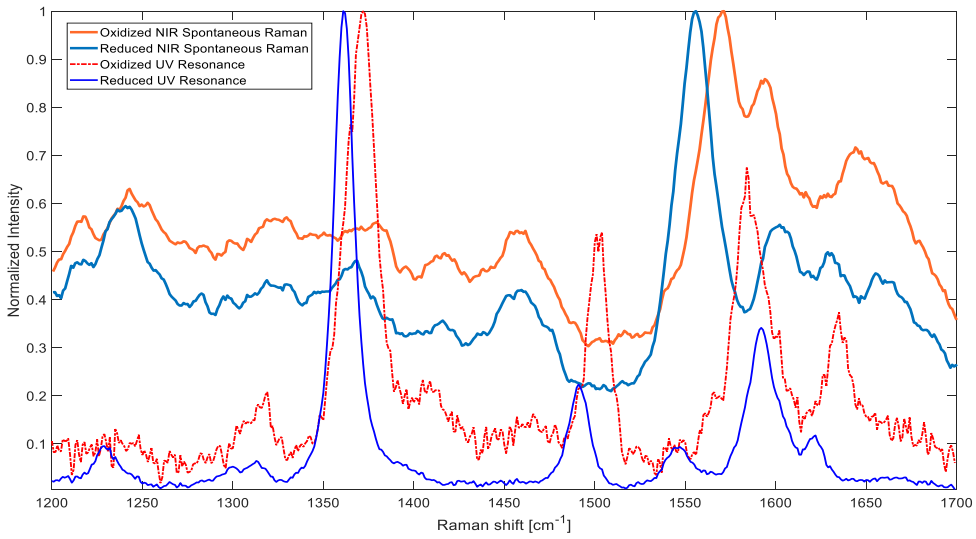

Figure 5.2: Comparison of spectra of cytochrome C in reduced (light blue) and oxidized (orange) forms acquired with the Biomod dispersive system (120mW, 10s integration repeated 50 times) and UV-resonant Raman of the same samples (in blue and red respectively, with 4mW at 414nm using 1s integration repeated 100 times, courtesy of Dr. Cakir Bertan)

The SSRS probe acquired spectra of 5mg/ml cytochrome C and found similar feature changes (770-800 nm, 5mW, 30x1s), see Figure 5.3.

Cytochrome C is abundant in the mitochondria-packed fovea layer of the retina which is the most energy demanding tissue in the human body. Monitoring the redux state in this tissue could provide an early diagnostic tool for age-related macular degeneration in which the tissue is unable to properly oxidize, leading to cell death and ultimate blindness.

In order for SSRS to become a viable diagnostical tool, the cytochrome C limit of detection needs to be improved and acquisition time shortened to approximately 120 seconds, which is the limitation for inspection recommended by medical doctors. Additionally, the redox state of cytochrome C needs to be measured in complex environments which include hemoglobin, which may interfere with the detection of conformational changes. Lastly, a system that can probe an area of the retina and not limit the inspection to a single point would allow to map the retina in an efficient and comprehensive way.

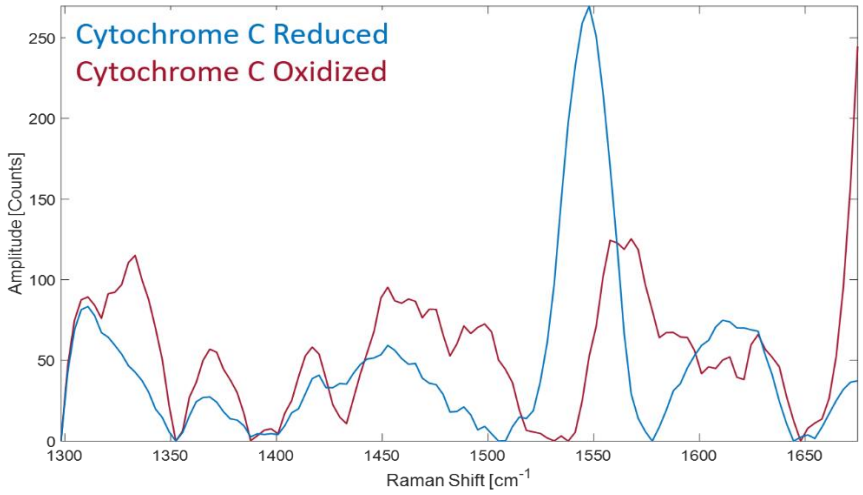

Figure 5.3 SSRS spectra of 5mg/ml cytochrome C in reduced and oxidized forms acquired with 5-6mW with 1 scond integration and 30 repetitions showing conformational chnages in the 1500-1650 cm^{-1} wavenumber range.

Remote and Mounted Sensing

SSRS significantly increases the scale of Raman systems but it has so far been limited to immersion or very close-range measurements due to the optics of the probe. Remote Raman sensing has been previously demonstrated by designing telescope-like probes that illuminate distant samples with a pulsed laser and employ gated detection[61,274]. Tunable sources are often used as pulsed sources with sufficient excitation powers to travel several meters (collimated) and scatter off a sample with enough intensity to provide adequate SNR for chemical detection.

Since SSRS already employs tunable lasers, SSRS could be similarly designed to enable standoff detection. A significant redesign of the detection would need to allow gating to determine the sample distance from the probe and distinguish between different samples, much like a radar pulse.

Remote systems can be mounted on combines or harvesters and be used for precise agriculture in which watering, fertilization and pest-control is done by-demand and only ripe produce is harvested. Remote detection of hazardous materials, or environmental monitoring using unmanned vehicles in the air or sea could significantly enhance our efforts to mitigate pollution.

To conclude, apart from the SSRS probe and sensor network extensively discussed in this Thesis, there are several other promising avenues for advancing SSRS technology, such as imaging, remote sensing, and medical applications. The most immediate and promising direction involves further integrating and measuring the CHO perfusion testbed and expanding PLSR-based minimal sampling for robust predictive modeling, which would significantly enhance monitoring capabilities.

APPENDIX A

Interferometric Methods

Fourier Transform Spectrometers

Fourier Transform (FT) spectroscopy was developed in the 1950's to study IR spectra of stars in astronomical measurements[40]. The basic principle relies on the interference of two beams of light in an interferometer and performing a FT to detect the spectral features[275], as is detailed in the following. The technique was adapted to chemical measurements in the FIR and MIR regions, where detector sensitivity is inherently low.

The main advantage of FT spectroscopy for Raman is the increased étendue compensating for the low detector sensitivity. Since the spectral resolution is decoupled from the size of the input aperture, more light can be collected into the system while maintaining resolution. Additionally, as the detection is based on the interference of coherent light, stray light is much less likely to introduce unwanted spectral artifacts. The étendue limitation of FT spectroscopy stems from the small acceptance angle required to align two beams of light in order to measure their interference. If the beams have an angular misalignment, an off-axis path difference error is introduced which affects the spectral resolution[276]. Effectively, in order to achieve a spectral resolution of 4 cm^{-1}, the acceptance angle is limited to approximately 1°.

It is worth noting a second advantage of FT spectrometers that is pertinent in

general but not applicable for shot-noise limited measurements, which is the case for Raman spectroscopy. In FT, all M_w spectral wavelengths, are observed simultaneously (multiplexed) and so the SNR is calculated for all spectral bands together in the interferogram. In cases where the noise is random and independent of the signal, the SNR would increase by $\sqrt{M_w}$. However, in a shot-noise limited regime, the noise increases as the squared root of the signal and so the noise would also increase by $\sqrt{M_w}$, offsetting the multiplexing advantage[56,275].

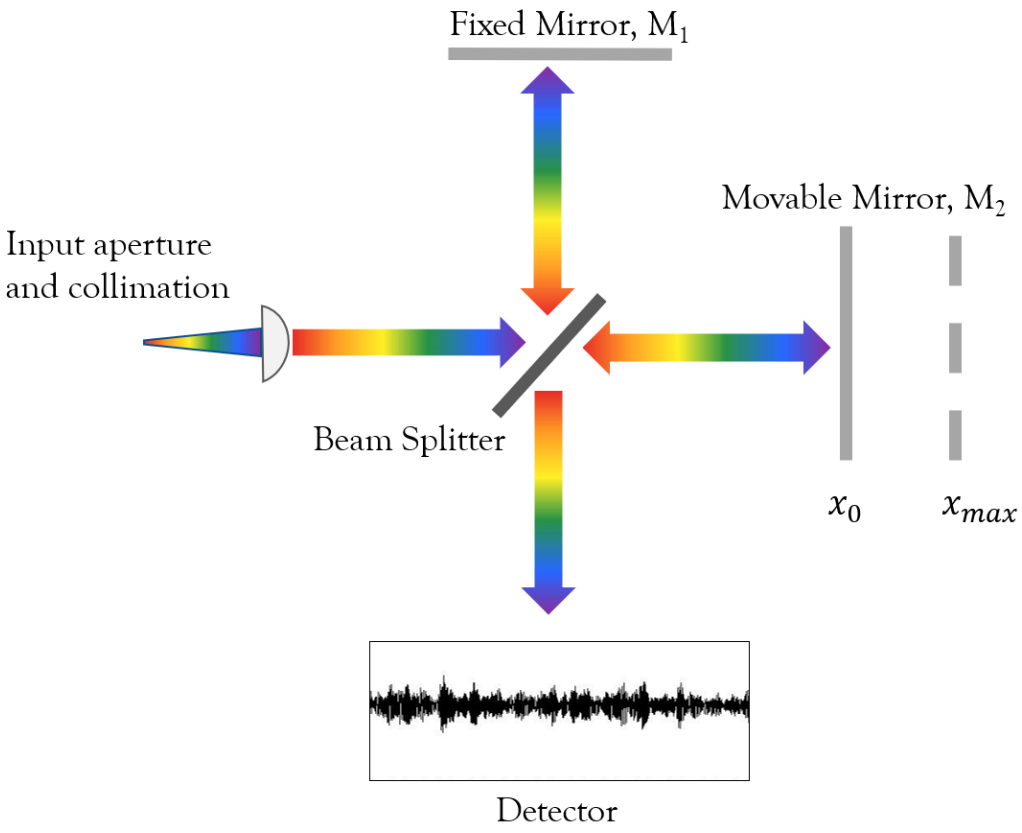

Figure A.1: An FT spectrometer based on a Michaelson interferometer showing the light input which is collimated using a lens and split using a beam splitter to two arms. One half of the light hits a reference fixed mirror and the other a movable mirror, creating a difference in path length leading to an interference pattern which is recorded on the detector.

Figure A.1 shows a top-view of an FT spectrometer based on a Michaelson interferometer used for detection of Raman spectra. The light from the sample is

collimated and enters the interferometer. A beam splitter halves the incoming light so that one beam is reflected of a fixed mirror and the other is reflected off a moving mirror, creating a modulation of the Optical Path length Difference (OPD). The beams interfere and hit the detector where an interferogram is created with M data points that correspond to M positions of the movable mirror from x_0 to x_{max}. If we assume for simplicity that the movable mirror as at distance x_0 from the mirror, then the maximal OPD is x_{max}.

The spectral resolution, $\Delta\nu$, in a FT spectrometer depends on the OPD according to the Nyquist theorem[277,278]:

$$\Delta\nu = \frac{1}{2x_{max}} \tag{A.1}$$

As seen from Equation A.1, $\Delta\nu$ is completely independent of the spectrometer's input aperture, allowing for significantly larger throughput compared with dispersive spectrometers. Spectral resolution values between 1-4cm^{-1} are very common in commercially available benchtop instruments with an OPD of a few centimeters, and custom instruments with an OPD extending 10 meters and a spectral resolution of 0.001cm^{-1} are also available[279].

The enhanced throughput allows the use of longer excitation wavelengths such as 1064nm, where fluorescence is negligible, and to compensate for lower Raman scattering, as seen from Equation 1.6. However, for these longer wavelength excitation, Ge or InGaAs detectors are used but as they are narrow direct bandgap materials, they suffer from significantly higher noise, limiting their sensitivity[248,280,281].

Furthermore, the use of a moving mirror to modulate the optical path difference comes with strict requirements of accuracy and repeatability, making instrumentation bulky and expensive. Alignment is of utmost importance in interferometry and is also particularly sensitive to temperature, humidity, and other

environmental conditions, making them extremely difficult to operate in the field. Another significant disadvantage has to do with aqueous samples, which absorb more of 1064nm excitation (see Figure1.5) limiting the usefulness of this technique. Lastly, only a single input can be introduced into the interferometer at any given moment and so the use of multiple signal channels (including multiple pixels for imaging), is accomplished by sequentially sampling each channel.

Spatial Heterodyne Raman Spectroscopy

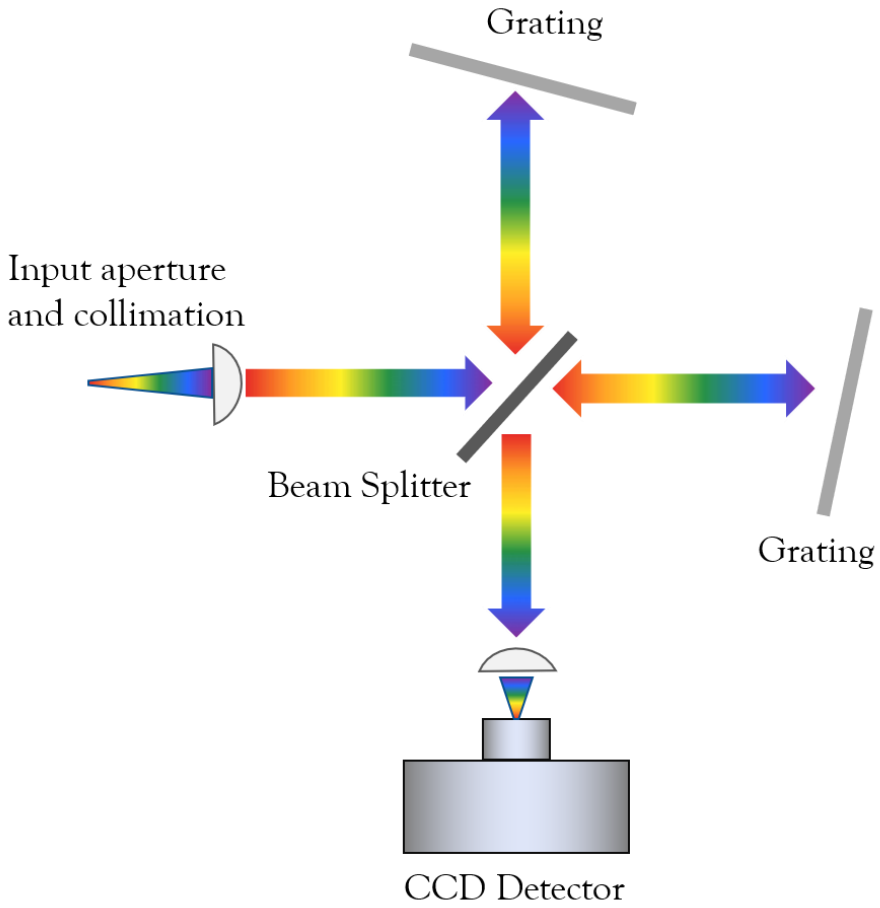

Figure A.2: a SHS spectrometer where two fixed gratings replace the moving mirrors of the FT spectrometer, creating multiple 2D diffraction patterns that interfere with one another, and a CCD array detects the interferogram of all OPD simultaneously, making the scanning redundant.

Spatial Heterodyne Raman Spectroscopy (SHRS)[282,283] is a fairly new technique,

based on the Spatial Heterodyne Spectrometer (SHS)[284]. This technique leverages the advantages of interferometry and enhanced throughput, while alleviating the complexity of a moving mirror operation by using tilted gratings and a detector array.

Figure A.2 shows a SHS. It resembles an FT spectrometer but instead of mirrors, there are two tilted grating and the interferogram is created on a CCD array so that all OPDs are simultaneously detected. A 2-Dimensional (2D) FT interprets the detector image to compute the Raman spectrum.

The spectral range of SHS is limited by the highest spatial frequency that can be recorded on the CCD array without aliasing[284]. Similar to dispersive systems, the spectral resolution of SHS depends on the physical dimensions of the setup: the dispersive grating size, tilt angles, and CCD. It has been shown that the étendue of SHS is equivalent to that of FT spectrometers[285] and that the resolution achievable is better than $5cm^{-1}$ in most systems[282].

The dimensions of the interferometer, gratings, and the CCD, usually limited to a few centimeters, dictate that this technique is most effective for UV and short visible wavelengths excitation[283,284,286]. The "one-shot" spectral measurement that negated the use of mirror tuning, further enables gating of the detection, crucial for standoff Raman measurements[283].

SHRS is still not widely used, certainly in comparison to established FT or dispersive systems, however, it is a fairly new Raman architecture and there have been interesting recent advancements. A monolithic SHRS[287] using a 532nm excitation reaching a resolution of $8cm^{-1}$ was demonstrated in 2021. Hyperspectral Raman imaging was performed combining SHRS and a micro-lens array[288]. In-situ measurements using a custom Raman probe with a 300μm core have also been reported[289].

SHRS leverages the throughput enhancement that FT spectrometers offer,

while mitigating alignment challenges with improved system robustness. However, it is mostly a method suited for short wavelength excitations that leave out applications with biological samples or highly fluorescent samples. Similar to FT Raman, it still only allows a single signal channel.

APPENDIX B

Common Detectors

In the early days or Raman experiments, before the invention of semiconductor devices and detector arrays, spectra were acquired by a scanning monochromator followed by a sensitive single-point detector based on vacuum tubes[290]. Today, detectors are predominantly built with semiconductors, either as single-point detectors, but most commonly as detector arrays comprising of many adjoint pixels.

Detectors are chosen first and foremost by their material responsivity, which determines the conversion rate of photons to electrons. Figure B.1, reproduced from reference [[291]] shows the photon-electron conversion efficiency curves of common semiconductor materials. Silicon, which is a non-direct bandgap material, is the most common material for detection of UV, VIS, and NIR wavelengths because of its low noise and low cost.

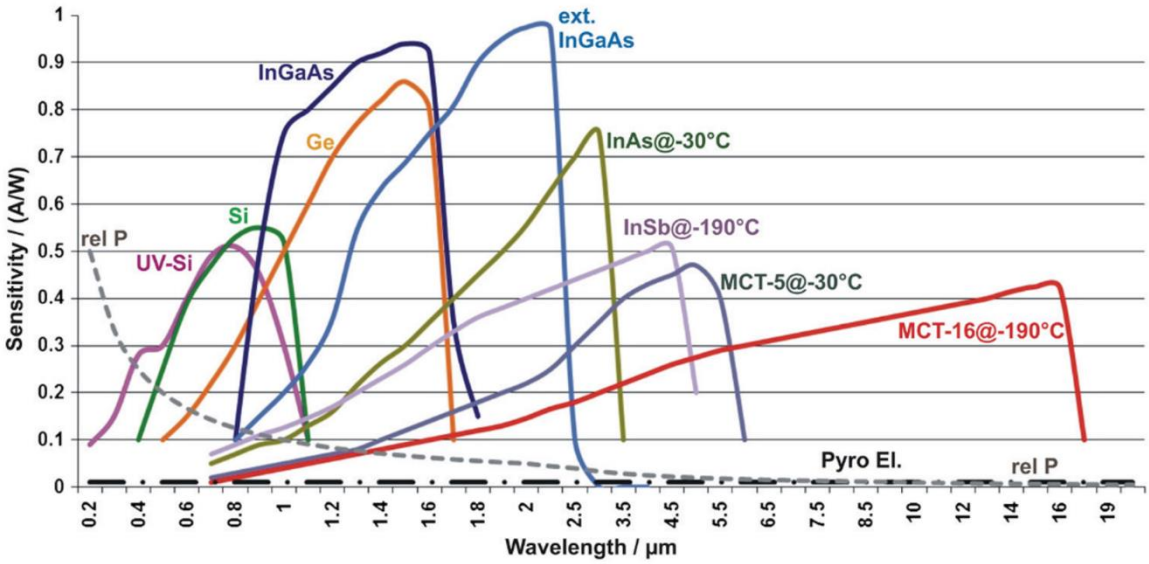

Figure B.1: Photon-electron conversion efficiency curves of solid-state materials (Reproduced from [291]) showing the appropriate wavelengths in which each material can function.

As mentioned in Section 1.3.2, there are many noise factors contributing to the overall noise in photon detection. The most significant noise in the detector itself is the thermal noise or Johnson noise. The Root Mean Square (RMS) value of the thermal noise current is given by Equation 1.43 and it is a uniformly distributed ("White Noise") process, where T is the temperature, Δf is the measurement bandwidth and R_Ω is the resistance value of the MOS element.

$$\sigma_d = \sqrt{\frac{4k_B T \Delta f}{R_\Omega}} \tag{B.1}$$

Since Raman is such a weak scattering process, most detectors need to be cooled in order to reduce the thermal noise and improve the SNR. Air or liquid convection cooling systems, Thermoelectric Cooling (TEC), and the use of liquid nitrogen are all methods used to reduce detector noise. Additional detector noise factors such as read-out and flicker noise, depend on the geometry and on the detector's architecture.

Single Point Detectors

Single point detectors are used today in many spectroscopy methods including FTIR, FT-Raman, CARS, and SSRS where spectra are acquired through scanning or tuning and only a single detector is used for signal acquisition. Single point detectors often have larger areas, and can accommodate additional amplification or photon counting modules.

Photon Multiplier Tubes

Photon Multiplier Tubes (PMT) are a class of vacuum phototubes that are one of the oldest single-point detectors. PMTs amplify the detected photon flux using secondary electron emission through the photoelectric effect[291]. When a photon impacts the photocathode, electrons are emitted and then amplified through a series of dynodes, which are high-voltage biased electrodes inside the tube. The amplified electrons reach the anode where they are detected. PMTs have a high gain ($\sim 10^8$), low-noise, high frequency response, and a large active area, making them extremely useful for a host of low-light applications in UV, VIS and NIR wavelengths. While PMTs have many advantages, they are fragile detectors that require vacuum tubes and have both a high voltage (~1kV) and a considerable power consumption. The quantum efficiency of PMTs depends on the photocathode material, but is often limited to 25% in the VIS-NIR ranges.

Semiconductor Photodiodes

In semiconductor photodiodes, light is absorbed in the detector material creating charge carriers, holes and electrons, which are then transported from the device and measured. There are many photodetector architectures bases on semiconductor doped junctions (p-n, p-i-n) and on capacitor structures like Metal-Oxide-Structure (MOS), to name a few. Without getting into detailed descriptions of

photodetector technologies, we can largely separate these detectors into two groups based on their mode of operation: Photovoltaic (PV) and Photoconductive (PC), where some devices can be operated in both modes.

PV mode is preferred for low bandwidth low-light applications. When the device is unbiased, light is absorbed in the active area (depletion region) of the device, and charge carriers are formed. These charge carriers are measured either as current, producing a linear response between the light power and detected current or as voltage on a resistor. PV mode has a lower signal bandwidth but also lower dark and thermal noise. Often, transimpedance amplifiers are attached to these detectors, creating an electronic gain and producing a measurable output voltage external to the photodiode which can be on the order of 10^8-10^{12} V/A.

In PC mode, a reverse bias is applied to the diode, creating a larger depletion region for the charge carriers. When light impacts the diode, charge carriers form, and are immediately transported due to the electric field on the device. PC mode produces both a smaller capacitance, thus increasing the detection bandwidth, but simultaneously increased the dark noise. Importantly, when the reverse bias is further increased (100-200V in silicon) close to the junction breakdown voltage, an "avalanche" effect occurs in which charge carriers gain enough kinetic energy to ionize other atoms, creating an amplification of charge carriers. This phenomenon is used to create a class of photodiodes called Avalanche Photodiodes (APD), discussed in the following. Figure B.2 shows a simplified diagram of the current created in a photodiode in PV, PC and avalanche mode for increasing illumination levels P_0, P_1, and P_2.

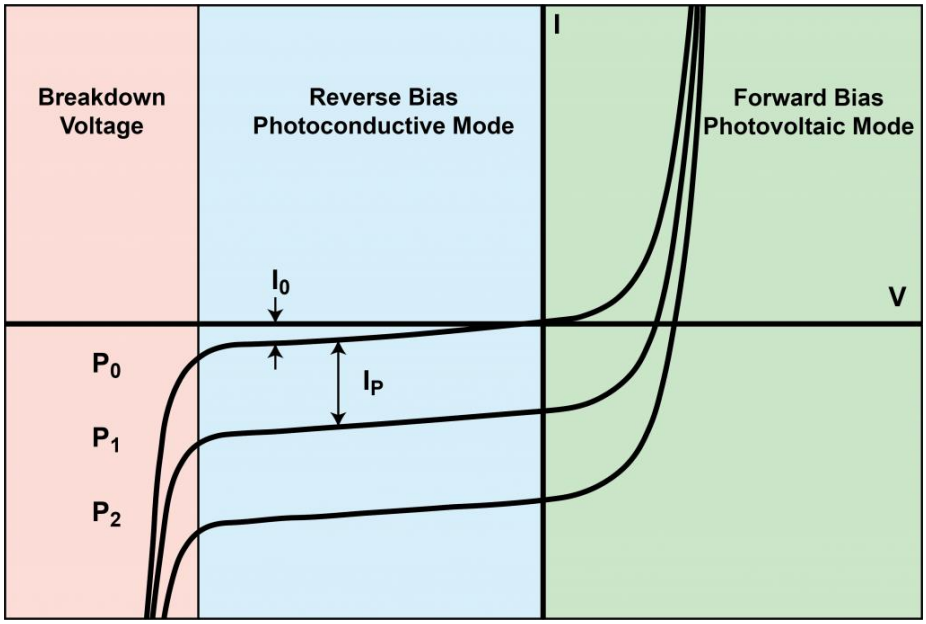

Figure B.2: A diagram showing the different modes of operation for semiconductor photodiodes in both PC, PV and avalanche modes. P_0 P_1 and P_2 stand for different illumination levels.

Avalanche Photodiodes and Single Photon Avalanche Detectors

APDs are the solid-state alternatives for PMTs. When they are combined with photon counting modules, they form Single Photon Avalanche Detectors (SPAD). The main difference in the operation of APDs and SPADs is the magnitude of the applied reverse voltage. In SPADs, the reverse bias exceeds the junction breakdown voltage, leading to a "Geiger-mode" operation, whereas APDs have a more linear gain characteristic[292]. SPADs are preferable for extreme low-light (single-photon) scenarios, where the amplification gain is significant and noise is fairly low. However, SPADs can saturate in the presence of noise or ambient light and require a quenching circuit that temporarily reduces the applied voltage to allow recovery.

Most SPADS have a smaller active area (junction) compared with PMTs, on the order of 10-100μm in diameter, but their quantum efficiency is often much higher reaching 50-70% in the UV-VIS-NIR regimes, depending on the semiconductor material. Recently, large-area SPADs with diameters between 200-500 μm have

emerged, opening the use of these detectors for high collection efficiency applications, including SSRS[293].

Detector Arrays

Most modern spectra detection, particularly that of dispersive Raman systems, is accomplished with Charge Coupled Device (CCD) arrays, located at the focal plane of the spectrometer. Each pixel in the CCD array is an independent MOS element that converts the incoming photons to electrons which are then read by a separate circuit to produce the electronic signal[291].

CCD technology is often mentioned alongside Complementary Metal Oxide Semiconductor (CMOS) technology. CMOS architecture has many benefits in regards to lower power consumption and readout speed, but suffers from reduced pixel uniformity, increased noise and often has smaller active pixel areas. For these reasons, spectrometers, particularly those used for NIR, and very low light levels, use CCD arrays.

The benefit of detector arrays is of course the ability to detect large spectral regions simultaneously in dispersive systems and have integrated readout circuitry. However, arrays have finite sizes, limiting the spectrometer's input aperture, and are expensive, often becoming the most significant cost components in Raman systems.

APPENDIX C

PLSR and VIP Mathematical Formulation

The following mathematical PLSR formulation is provided for a general case where C is a response matrix, i.e. including J analytes for each sample in the learning dataset and sized $[N_L \times J]$. In most PLSR Raman spectroscopy applications, C is a single analyte vector (i.e. J=1), but some have reported modeling several analytes simultaneously, often referred to as PLS2[145,146,294]

For iteration *i* we assume there are a pair of unit vectors, v_i in the input space and w_i in the output space so that:

$$z_i = {v_i}^T X_i \tag{C.1a}$$

$$r_i = {w_i}^T C_i \tag{C.1b}$$

z_i and r_i are called the input and output scores, respectively. We wish to find v_i *and* w_i which maximize the correlation of z_i and r_i, which is equivalent to maximizing the covariance of the mean-centered matrices X_i, and C_i*:*

$$COV(X_i, C_i) = [X_i \cdot {C_i}^T] \tag{C.2}$$

By using Equations C.1a, C.1b and C.2 we get the following expression:

$$max(z_i \cdot r_i) = max({v_i}^T X_i \cdot {w_i}^T C_i) = \ max({v_i}^T [X_i \cdot {C_i}^T]\, w_i) \tag{C.3}$$

There are several algorithms used for finding the unit vectors which maximize the scores correlation. Nonlinear Iterative PLS (NIPALS)[126] was the original method

used and it is still used for large datasets where the computational cost of other methods is prohibitive. PLS-Singular Value Decomposition (PLS-SVD)[295] takes a different approach for finding latent variables and is considered precise yet computationally costly. Simultaneous PLS (SIMPLS)[296] is the most commonly used method which also imposes orthogonality on the unit vectors, making the interpretation of latent variables easier.

After finding the scores, we wish to predict the concentration $\hat{C}_i$ from our score z_i using the output loading vector $\bar{q}_i$:

$$\hat{C}_i = \bar{q}_i z_i = \bar{q}_i {v_i}^T X_i \tag{C.4}$$

By minimize the estimation error (Equation C.5) a solution for the optimal loading vector $\bar{q}_{0,i}$ is found (Equation C.6):

$$argmin\left\{\left|C_i - \hat{C}_i\right|^2\right\} = argmin\{(C_i - \bar{q}_i {v_i}^T X_i)(C_i - \bar{q}_i {v_i}^T X_i)^T\} \tag{C.5}$$

$$\bar{q}_{0,i} = \frac{COV(C_i, X_i)v_i}{{v_i}^T COV(X_i, X_i)v_i} \tag{C.6}$$

In order to find the next latent component, we must first remove the first latent component from both the predictor (input) and response (output), a process called "deflation". The deflated output, C_{i+1}, can be found from Equations C.4 and C.6:

$$C_{i+1} = C_i - \hat{C}_i = C_i - \bar{q}_{0,i} {v_i}^T X_i \tag{C.7}$$

The derivation for the deflated input, X_{i+1}, is beyond the current scope but can be shown to be:

$$X_{i+1} = X_i - \hat{X}_i = X_i - \bar{p}_{0,i} z_i = X_i - \bar{p}_{0,i} {v_i}^T X_i \tag{C.8}$$

Where the input loading vector, $\bar{p}_{0,i}$, is defined as:

$$\bar{p}_{0,i} = \frac{COV(X_i, X_i)v_i}{{v_i}^T COV(X_i, X_i)v_i} \tag{C.9}$$

And finally, after N_{comp} latent variables have been computed, the final

regression coefficients vector, $\beta = \hat{H}$, is given by[296,297]:

$$\hat{C} = X\beta = X\left[\sum_{i=1}^{N_{comp}} z_i \bar{q}_{0,i}\right] \tag{C.10}$$

The VIP score can therefore be described by C.11a-b, where the index i stands for the index of latent variable so that $i = [1,2,\dots,N_{comp}]$ and the index $m = [1,2,\dots,M]$, stands for the variable index:

$$VIP_m = \sqrt{M \frac{\sum_{i=1}^{N_{comp}} SS(\bar{q}_{0,i}, z_i) \cdot \left(v_{m,i}/\|v_i\|\right)^2}{\sum_{i=1}^{N_{comp}} SS(\bar{q}_{0,i}, z_i)}} \tag{C.11a}$$

$$SS(\bar{q}_{0,i}, z_i) = \bar{q}_{0,i}{}^2 z_i{}^T z_i \tag{C.11b}$$

Bibliography

1. Stocker, J. H. *Chemistry and Science Fiction*. (American Chemical Society, 1998).
2. Gründler, P. Chemical Sensors: An Introduction for Scientists and Engineers. *Chem. Sensors An Introd. Sci. Eng.* **61**, 1–273 (2007).
3. Kassal, P., Steinberg, M. D. & Steinberg, I. M. Wireless Chemical Sensors and Biosensors: A review. *Sensors Actuators, B Chem.* **266**, 228–245 (2018).
4. Rappa, M. A. The Utility Business Model and the Future of Computing Services. *IBM Syst. J.* **43**, 32–42 (2004).
5. Hamdaqa, M. & Tahvildari, L. *Cloud Computing Uncovered: A Research Landscape*. *Advances in Computers* vol. 86 (Elsevier Inc., 2012).
6. Bajic, B. *et al.* Edge Computing vs. Cloud Computing: Challenges and Opportunities in Industry 4.0. *Ann. DAAAM Proc. Int. DAAAM Symp.* **30**, 864–871 (2019).
7. Kassal, P., Horak, E., Sigurnjak, M., Steinberg, M. D. & Steinberg, I. M. Wireless and Mobile Optical Chemical Sensors and Biosensors. *Rev. Anal. Chem.* **37**, 1–27 (2018).
8. Kishore, S. C. *et al.* Smartphone-Operated Wireless Chemical Sensors: A Review. *Chemosensors* **10**, 1–22 (2022).
9. Byrne, R. & Diamond, D. Chemo/Bio-Sensor Networks. *Nat. Mater.* **5**, 421–424 (2006).
10. Santos, J. L. Optical Sensors for Industry 4.0. *IEEE J. Sel. Top. Quantum Electron.* **27**, (2021).
11. Lu, X., Thomas, P. J. & Hellevang, O. A Review of Methods for Fibre-Optic Distributed Chemical Sensing. *Sensors* **19**, (2019).
12. Bado, M. F. & Casas, J. R. A Review of Recent Distributed Optical Fiber Sensors Applications for Civil Engineering Structural Health Monitoring. *Sensors* **21**, 1–83 (2021).
13. Raman, C. V. A New Type of Secondary Radiation. *Nature* **121**, 501–502 (1928).
14. McCreery, R. L. *Raman Spectroscopy for Chemical Analysis*. *Measurement Science and Technology* vol. 12 (2001).
15. Szymanski, H. A. *Raman Spectroscopy*. (1970). doi:10.1007/978-1-4684-3027-1.
16. Fallis, A. . *Raman Spectroscopy Theory and Practice*. *Climate Change 2013 - The Physical Science Basis* vol. 53 (1967).
17. Esmonde-White, K. A., Cuellar, M., Uerpmann, C., Lenain, B. & Lewis, I. R. Raman Spectroscopy as a Process Analytical Technology for Pharmaceutical Manufacturing and

Bioprocessing. *Anal. Bioanal. Chem.* **409**, 637–649 (2017).

18. Esmonde-White, K. A., Cuellar, M. & Lewis, I. R. The Role of Raman Spectroscopy in Biopharmaceuticals from Development to Manufacturing. *Anal. Bioanal. Chem.* **414**, 969–991 (2022).

19. Bakeev, K. A. *Process Analytical Technology: Spectroscopic Tools and Implementation Strategies for the Chemical and Pharmaceutical Industries: Second Edition*. *Process Analytical Technology: Spectroscopic Tools and Implementation Strategies for the Chemical and Pharmaceutical Industries: Second Edition* (2010). doi:10.1002/9780470689592.

20. Claßen, J., Aupert, F., Reardon, K. F., Solle, D. & Scheper, T. Spectroscopic Sensors for In-Line Bioprocess Monitoring in Research and Pharmaceutical Industrial Application. *Anal. Bioanal. Chem.* **409**, 651–666 (2017).

21. Yahya, M. N. *et al.* A Study on the Hydrolysis of Urea Contained in Wastewater and Continuous Recovery of Ammonia by an Enzymatic Membrane Reactor. *Processes* **9**, (2021).

22. MacDonald, G., Levison, J. & Parker, B. On Methods for In-Well Nitrate Monitoring Using Optical Sensors. *Groundw. Monit. Remediat.* **37**, 60–70 (2017).

23. Maleev, I., Khan, A., Peerzada, L., Khmaladze, A. & Sharikov, A. In-Line Monitoring of Water Quality by Combined Fluorescence and Raman Spectroscopy. *2017 Conf. Lasers Electro-Optics, CLEO 2017 - Proc.* **2017-Janua**, 1–2 (2017).

24. Li, Z., Deen, M. J., Kumar, S. & Selvaganapathy, P. R. Raman Spectroscopy for In-Line Water Quality Monitoring — Instrumentation and Potential. *Sensors (Switzerland)* **14**, 17275–17303 (2014).

25. Kong, K., Kendall, C., Stone, N. & Notingher, I. Raman Spectroscopy for Medical Diagnostics - From In-Vitro Biofluid Assays to In-Vivo Cancer Detection. *Adv. Drug Deliv. Rev.* **89**, 121–134 (2015).

26. Baker, M. J. *et al.* Clinical Applications of Infrared and Raman Spectroscopy: State of Play and Future Challenges. *Analyst* **143**, 1735–1757 (2018).

27. Orlando, A. *et al.* A Comprehensive Review on Raman Spectroscopy Applications. *Chemosensors* **9**, 1–29 (2021).

28. Xu, Z. *et al.* Topic Review: Application of Raman Spectroscopy Characterization in Micro/Nano-Machining. *Micromachines* **9**, (2018).

29. Vandenabeele, P., Edwards, H. G. M. & Jehlička, J. The Role of Mobile Instrumentation in Novel Applications of Raman Spectroscopy: Archaeometry, Geosciences, and Forensics. *Chem. Soc. Rev.* **43**, 2628–2649 (2014).

30. Vandenabeele, P., Edwards, H. G. M. & Moens, L. A Decade of Raman Spectroscopy in Art and Archeology. *Chem. Rev.* **107**, 675–686 (2007).

31. Moore, C. *et al.* Optical Tools for Ocean Monitoring and Research. *Ocean Sci.* **5**, 661–684

(2009).

32. Pasteris, J. D. *et al.* Raman Spectroscopy in the Deep Ocean: Successes and Challenges. *Appl. Spectrosc.* **58**, (2004).

33. De Oliveira Penido, C. A. F., Pacheco, M. T. T., Lednev, I. K. & Silveira, L. Raman spectroscopy in forensic Analysis: Identification of Cocaine and Other Illegal Drugs of Abuse. *J. Raman Spectrosc.* **47**, 28–38 (2016).

34. Li, Y. S. & Church, J. S. Raman Spectroscopy in the Analysis of Food and Pharmaceutical Nanomaterials. *J. Food Drug Anal.* **22**, 29–48 (2014).

35. Jianwei, Q. *et al.* Advances in Raman Spectroscopy and Imaging Techniques for Quality and Safety Inspection of Horticultural Products. *Postharvest Biol. Technol.* **149**, 101–117 (2019).

36. Atabaki, A. H., Herrington, W. F., Burgner, C., Jayaraman, V. & Ram, R. J. Low-Power Swept-Source Raman Spectroscopy. **29**, 24723–24734 (2021).

37. Persits, N. *et al.* Networked Swept-Source Raman Sensors. *Opt. InfoBase Conf. Pap.* **1**, 22–23 (2021).

38. Jaffrezic-renault, N. *The 1st International Electronic Conference on Chemical Sensors and Analytical Chemistry*. *The 1st International Electronic Conference on Chemical Sensors and Analytical Chemistry* (2022). doi:10.3390/books978-3-0365-4116-7.

39. Orellana, G. & Moreno-Bondi, M. C. *Frontiers in Chemical Sensors*. *Frontiers in Chemical Sensors* (Springer, 2005). doi:10.1007/5346_010.

40. Skoog, D. A., Holler, F. J. & Crouch., S. R. *Principles of Instrumental Analysis. Seventh edition. Australia: Cengage Learning, 2018.* (2018). doi:10.5111/bunkou.9.181.

41. Parson, W. W. *Modern Optical Spectroscopy*. *Modern Optical Spectroscopy* (2015). doi:10.1007/978-3-662-46777-0.

42. Hammes, G. G. *Spectroscopy for the Biological Sciences*. (Wiley, 2005).

43. Barone, V. *et al.* Computational Molecular Spectroscopy. *Nat. Rev. Methods Prim.* (2021).

44. Neumann, W. *Fundamentals of Dispersive Optical Spectroscopy Systems*. (SPIE, 2020).

45. Antosiewicz, J. M. & Shugar, D. UV–Vis Spectroscopy of Tyrosine Side-Groups in Studies of Protein Structure. Part 2: Selected Applications. *Biophys. Rev.* **8**, 163–177 (2016).

46. Hansen, S. K., Jamali, B. & Hubbuch, J. Selective High Throughput Protein Quantification Based on UV Absorption Spectra. *Biotechnol. Bioeng.* **110**, 448–460 (2013).

47. Roberts, J., Power, A., Chapman, J., Chandra, S. & Cozzolino, D. The Use of UV-Vis Spectroscopy in Bioprocess and Fermentation Monitoring. *Fermentation* **4**, (2018).

48. Guo, Y., Liu, C., Ye, R. & Duan, Q. Advances on Water Quality Detection by UV-Vis Spectroscopy. *Appl. Sci.* **10**, 1–18 (2020).

49. Sinha, R. P. & Häder, D. P. UV-Induced DNA Damage and Repair: A Review. *Photochem. Photobiol. Sci.* **1**, 225–236 (2002).

50. Rastogi, R. P., Richa, Kumar, A., Tyagi, M. B. & Sinha, R. P. Molecular Mechanisms of Ultraviolet Radiation-Induced DNA Damage and Repair. *J. Nucleic Acids* **2010**, (2010).

51. Carré, E., Pérot, J., Jauzein, V., Lin, L. & Lopez-Ferber, M. Estimation of Water Quality by UV/Vis Spectrometry in the Framework of Treated Wastewater Reuse. *Water Sci. Technol.* **76**, 633–641 (2017).

52. Wang, H., Ju, A. & Wang, L. Ultraviolet Spectroscopic Detection of Nitrate and Nitrite in Seawater Simultaneously Based on Partial Least Squares. *Molecules* **26**, (2021).

53. Lakowicz, J. R. *Principles of fluorescence spectroscopy, 3rd Principles of fluorescence spectroscopy, Springer, New York, USA, 3rd edn, 2006. Principles of fluorescence spectroscopy, Springer, New York, USA, 3rd edn, 2006.* (2006). doi:10.1007/978-0-387-46312-4.

54. Wang, L., Frei, M. S., Salim, A. & Johnsson, K. Small-Molecule Fluorescent Probes for Live-Cell Super-Resolution Microscopy. *J. Am. Chem. Soc.* **141**, 2770–2781 (2019).

55. Wei, D., Chen, S. & Liu, Q. Review of Fluorescence Suppression Techniques in Raman Spectroscopy. *Appl. Spectrosc. Rev.* **50**, 387–406 (2015).

56. Chase, B. Fourier Transform Raman Spectroscopy. *Anal. Chemsitry* **59**, 881–889 (1987).

57. Rolinger, L., Rüdt, M. & Hubbuch, J. A Critical Review of Recent Trends, and a Future Perspective of Optical Spectroscopy as PAT in Biopharmaceutical Downstream Processing. *Anal. Bioanal. Chem.* **412**, 2047–2064 (2020).

58. Berger, a, Wang, Y. & Feld, M. S. Rapid, Noninvasive Concentration Measurements of Aqueous Biological Analytes by Near-Infrared Raman Spectroscopy. *Appl. Opt.* **35**, 209 (1996).

59. Li, G. & Zhang, G. Raman Spectroscopy Application to Analyses of Components in Aqueous Solutions. 60472V (2006) doi:10.1117/12.710095.

60. Shipp, D. W., Sinjab, F. & Notingher, I. Raman Spectroscopy: Techniques and Applications in the Life Sciences. *Adv. Opt. Photonics* **9**, 315 (2017).

61. Acosta-maeda, T. E., Misra, A. K., Porter, J. N., Bates, D. E. & Sharma, S. K. Remote Raman Efficiencies and Cross-Sections of Organic and Inorganic Chemicals. *Appl. Spectrosc.* **71**, 1025–1038 (2017).

62. Schrötter, H. W. & Klöckner, H. W. *Raman Scattering Cross Sections in Gases and Liquids*. (1979). doi:10.1007/978-3-642-81279-8_4.

63. Klingshirn, C. *Frontiers of Optical Spectroscopy*. *Frontiers of Optical Spectroscopy* vol. 168 (2005).

64. Yang, W. *et al.* Raman ChemLighter: Fiber Optic Raman Probe Imaging in Combination with Augmented Chemical Reality. *J. Biophotonics* **12**, 1–7 (2019).

65. Smith, E. & Dent, G. *Modern Raman Spectroscopy: A Practical Approach*. vol. 5 (Wiley, 2005).

66. Schwab, S. D. & McCreery, R. L. Versatile, Efficient Raman Sampling with Fiber Optics. *Anal. Chem.* **56**, 2199–2204 (1984).

67. Hammes, G. G. *Practical Raman Spectroscopy*. (Springer-Verlag, 1989). doi:10.1201/9781420032345.ch5.

68. Cordero, E., Latak, I., Matthaus, C., Schie, I. & Popp, J. In-Vivo Raman Spectroscopy: from Basics to Applications. *J. Biomed. Opt.* **23**, 1 (2018).

69. Cordero, E. *et al.* Evaluation of Shifted Excitation Raman Difference Spectroscopy and Comparison to Computational Background Correction Methods Applied to Biochemical Raman Spectra. *Sensors (Switzerland)* **17**, (2017).

70. Latka, I., Dochow, S., Krafft, C., Dietzek, B. & Popp, J. Fiber optic probes for linear and nonlinear Raman Applications - Current Trends and Future Development. *Laser Photonics Rev.* **7**, 698–731 (2013).

71. Wang, C., Zeng, L., Li, Z. & Li, D. Review of Optical Fibre Probes for Enhanced Raman Sensing. *J. Raman Spectrosc.* **48**, 1040–1055 (2017).

72. Stevens, O., Iping Petterson, I. E., Day, J. C. C. & Stone, N. Developing Fibre Optic Raman Probes for Applications in Clinical Spectroscopy. *Chem. Soc. Rev.* **45**, 1919–1934 (2016).

73. Boyd. *Radiometry and the Detection of Optical Radiation*. (Wiley, 1983).

74. Quimby, R. S. Solid Angle and the Brightness Theorem. in *Photonics and Lasers: an Introduction* 495–498 (2006).

75. Lax, M. & Nelson, D. F. Radiance Theorem and Optical Invariants in Anisotropic Media. *J Opt Soc Am* **65**, 668–675 (1975).

76. Spoor & Rogier. XKCD. https://what-if.xkcd.com/145/.

77. Ries, H. Thermodynamic Limitations of the Concentration of Electromagnetic Radiation. *J. Opt. Soc. Am.* **72**, 380 (1982).

78. Winston, R., Wang, C. & Zhang, W. Beating the Optical Liouville Theorem: How Does Geometrical Optics Know the Second Law of Thermodynamics? *Nonimaging Opt. Effic. Des. Illum. Sol. Conc. VI* **7423**, 742309 (2009).

79. Winston, R. Light Collection within the Framework of Geometrical Optics. *J. Opt. Soc. Am.* **60**, 245–247 (1970).

80. Jannson, T. & Winston, R. Liouville's theorem and Concentrator Optics. *J. Opt. Soc. Am. A* **3**, 7 (1986).

81. Ulness, D. J., Kirkwood, J. C., Stimson, M. J. & Albrecht, A. C. Theory of Coherent Raman Scattering with Quasi-cw Noisy Light for a General Line Shape Function. *J. Chem.*

Phys. **107**, 7127–7137 (1997).

82. Meier, R. J. On Art and Science in Curve-Fitting Vibrational Spectra. *Vib. Spectrosc.* **39**, 266–269 (2005).

83. Griffiths, P. R. & de Haseth, J. A. Monitoring Atmospheric Water Vapour: Ground-Based Remote Sensing and In-situ Methods. in *Fourier transform infrared spectrometry* vol. 10 (2006).

84. Myers, A. B. Molecular Electronic Spectral Broadening in Liquids and Glasses. *Annu. Rev. Phys. Chem.* **49**, 267–295 (1998).

85. Watanabe, J. & Kinoshita, S. Spectral Broadening in Phonon Raman Scattering and its Stokes to Anti-Stokes Intensity Ratio. *Phys. Procedia* **13**, 50–53 (2011).

86. Sadat, A. & Joye, I. J. Peak Fitting Applied to Fourier Transform Infrared and Raman Spectroscopic Analysis of Proteins. *Appl. Sci.* **10**, (2020).

87. Schulze, H. G., Rangan, S., Blades, M. W., Piret, J. M. & Turner, R. F. B. B. Smoothing Raman Spectra with Contiguous Single-Channel Fitting of Voigt Distributions: An Automated, High-Quality Procedure. *Appl. Spectrosc.* **73**, 47–58 (2019).

88. Ball, D. W. *Field Guide to Spectroscopy*. (SPIE press, 2006).

89. Neumann, W. The Dispersion Elements: Diffraction Grating and Refraction Prism. *Fundam. Dispersive Opt. Spectrosc. Syst.* 69–81 (2014) doi:10.1117/3.1002528.ch3.

90. Resolution Power. *SPIE* https://spie.org/news/resolving-resolution?SSO=1.

91. James, J. The Prism Spectrograph. in *Spectrograph Design Fundamentals* 57–62 (Cambridge University Press, 2009). doi:10.1017/cbo9780511534799.008.

92. Yang, Z., Albrow-Owen, T., Cai, W. & Hasan, T. Miniaturization of Optical Spectrometers. *Science (80-.).* **371**, 1–23 (2021).

93. Abu-Absi, N. R. *et al.* Real Time Monitoring of Multiple Parameters in Mammalian Cell Culture Bioreactors Using an In-Line Raman Spectroscopy Probe. *Biotechnol. Bioeng.* **108**, 1215–1221 (2011).

94. Schalk, R. *et al.* Non-Contact Raman Spectroscopy for In-Line Monitoring of Glucose and Ethanol During Yeast Fermentations. *Bioprocess Biosyst. Eng.* **40**, 1519–1527 (2017).

95. Heng, H. P. S., Shu, C., Zheng, W., Lin, K. & Huang, Z. Advances in Real-Time Fiber-Optic Raman Spectroscopy for Early Cancer Diagnosis: Pushing the Frontier into Clinical Endoscopic Applications. *Transl. Biophotonics* **3**, 1–31 (2021).

96. Banerjee, H. & Verma, M. Intraoperative brain cancer detection with Raman spectroscopy in humans. *Ann. Transl. Med.* **4**, 1–10 (2016).

97. Klemes, J. *et al.* Non-invasive diagnostic system and its opto-mechanical probe for combining confocal Raman spectroscopy and optical coherence tomography. *J. Biophotonics* **10**, 1442–1449 (2017).

98. Mazurenka, M., Behrendt, L., Meinhardt-Wollweber, M., Morgner, U. & Roth, B. Development of a combined OCT-Raman probe for the prospective in vivo clinical melanoma skin cancer screening. *Rev. Sci. Instrum.* **88**, (2017).

99. Schie, I. W., Stiebing, C. & Popp, J. Looking for a perfect match: multimodal combinations of Raman spectroscopy for biomedical applications. *J. Biomed. Opt.* **26**, 1–18 (2021).

100. Matousek, P. Spatially offset Raman spectroscopy for non-invasive analysis of turbid samples. *TrAC - Trends Anal. Chem.* **103**, 209–214 (2018).

101. Nicolson, F., Kircher, M. F., Stone, N. & Matousek, P. Spatially offset Raman spectroscopy for biomedical applications. *Chem. Soc. Rev.* **50**, 556–568 (2021).

102. Paudel, A., Raijada, D. & Rantanen, J. Raman spectroscopy in pharmaceutical product design. *Adv. Drug Deliv. Rev.* **89**, 3–20 (2015).

103. Thorlabs optical fiber specification - attenuation. https://www.thorlabs.com/newgrouppage9.cfm?objectgroup_id=6838.

104. Myrick, M. L. & Angel, S. M. Elimination of background in fiber-optic Raman measurements. *Appl. Spectrosc.* **44**, 565–570 (1990).

105. Schoen, C. L., Cooney, T. F., Sharma, S. K. & Carey, D. M. Long fiber-optic remote Raman probe for detection and identification of weak scatterers. *Appl. Opt.* **31**, 7707 (1992).

106. Ahmad, H., Sumpf, B., Sowoidnich, K., Klehr, A. & Kronfeldt, H.-D. Insitu Raman Setup for Deep Ocean Investigations Applying Two 1000 m Optical Fiber Cables and a 785 nm High Power Diode Laser. *Mar. Sci.* **2**, 132–138 (2012).

107. Guo, S., Popp, J. & Bocklitz, T. Chemometric analysis in Raman spectroscopy from experimental design to machine learning–based modeling. *Nat. Protoc.* **16**, 5426–5459 (2021).

108. Aab, A. *et al.* Observation of a large-scale anisotropy in the arrival directions of cosmic rays above 8 × 1018 eV. *Science (80-.).* **357**, 1266–1270 (2017).

109. Savitzky, A.; Golay, M. J. E. Smoothing and Differentiation of Data. *Anal. Chem* **36**, 1627–1639 (1964).

110. Eilers, P. H. C. A perfect smoother. *Anal. Chem.* **75**, 3631–3636 (2003).

111. Berry, B. N. *et al.* Quick generation of Raman spectroscopy based in-process glucose control to influence biopharmaceutical protein product quality during mammalian cell culture. *Biotechnol. Prog.* **32**, 224–234 (2016).

112. Berry, B., Moretto, J., Matthews, T., Smelko, J. & Wiltberger, K. Cross-scale predictive modeling of CHO cell culture growth and metabolites using Raman spectroscopy and multivariate analysis. *Biotechnol. Prog.* **31**, 566–577 (2015).

113. Rehrauer, O. G. *et al.* Binary Complementary Filters for Compressive Raman Spectroscopy. *Appl. Spectrosc.* **72**, 69–78 (2018).

114. Kiefer, J. Instantaneous shifted-excitation Raman difference spectroscopy (iSERDS). *J. Raman Spectrosc.* **45**, 980–983 (2014).

115. Matousek, P. *Emerging Raman applications and techniques in biomedical and pharmaceutical fields*. (Springer, 2010).

116. Lieber C.A., M.-J. A. Automated Method for Subtraction of Flourescence from Biological Raman Spectra. *As* **57**, 1363–1367 (2003).

117. Hoang, V. D. Wavelet-based spectral analysis. *TrAC - Trends Anal. Chem.* **62**, 144–153 (2014).

118. Galloway, C. M., Le Ru, E. C. & Etchegoin, P. G. An iterative algorithm for background removal in spectroscopy by wavelet transforms. *Appl. Spectrosc.* **63**, 1370–1376 (2009).

119. Chen, D., Chen, Z. & Grant, E. Adaptive wavelet transform suppresses background and noise for quantitative analysis by Raman spectrometry. *Anal. Bioanal. Chem.* **400**, 625–634 (2011).

120. Baradez, M.-O., Biziato, D., Hassan, E. & Marshall, D. Application of Raman Spectroscopy and Univariate Modelling As a Process Analytical Technology for Cell Therapy Bioprocessing. *Front. Med.* **5**, (2018).

121. Han, N. & Ram, R. J. Bayesian modeling and computation for analyte quantification in complex mixtures using Raman spectroscopy. *Comput. Stat. Data Anal.* **143**, 106846 (2020).

122. Guo, S., Bocklitz, T. & Popp, J. Optimization of Raman-spectrum baseline correction in biological application. *Analyst* **141**, 2396–2404 (2016).

123. Cocchi, M., Biancolillo, A. & Marini, F. Chemometric Methods for Classification and Feature Selection. in *Data Analysis for Omic Sciences : Methods and Applications.* (ed. Jaumot, Joaquim, Carmen Bedia, and Romà Tauler i Ferré, E.) 265–299 (Elsevier, 2018).

124. Rafferty, C. *et al.* Analysis of chemometric models applied to Raman spectroscopy for monitoring key metabolites of cell culture. *Biotechnol. Prog.* **36**, 1–16 (2020).

125. Tormod, N. & Martens, H. Principal Component Regression in NIR Analysis: Viewpoints, Background Details and Selection of Components. *J. Chemom.* **2**, 155–167 (1988).

126. Wold, S., Michael, S. & Errikson, L. PLS-regression: a basic tool of chemometrics Svante. *Chemomerics Intell. Lab. Syst.* **58**, 109–130 (2001).

127. Qi, Y. *et al.* Recent Progresses in Machine Learning Assisted Raman Spectroscopy. *Adv. Opt. Mater.* **11**, 1–22 (2023).

128. Tulsyan, A., Coufal, M., Schorner, G. & Wang, T. A machine - learning approach to calibrate generic Raman models for real - time monitoring of cell culture processes. 2575–2586 (2019) doi:10.1002/bit.27100.

129. Brereton, R. G. & Lloyd, G. R. Support Vector Machines for classification and regression. 230–267 (2010) doi:10.1039/b918972f.

130. Chen, T. & Baek, S. J. Library-Based Raman Spectral Identification Using Multi-Input Hybrid ResNet. *ACS Omega* (2023) doi:10.1021/acsomega.3c05780.

131. Guo, S., Bocklitz, T., Neugebauer, U. & Popp, J. Common mistakes in cross-validating classification models. *Anal. methods* **9**, 4410–4417 (2017).

132. Kong, K. *et al.* Towards intra-operative diagnosis of tumours during breast conserving surgery by selective-sampling Raman micro-spectroscopy. *Phys. Med. Biol.* **59**, 6141–6152 (2014).

133. Mitchell, A. L., Gajjar, K. B., Theophilou, G., Martin, F. L. & Martin-Hirsch, P. L. Vibrational spectroscopy of biofluids for disease screening or diagnosis: Translation from the laboratory to a clinical setting. *J. Biophotonics* **7**, 153–165 (2014).

134. Buckley, K. & Ryder, A. G. Applications of Raman Spectroscopy in Biopharmaceutical Manufacturing: A Short Review. *Appl. Spectrosc.* **71**, 1085–1116 (2017).

135. Kohavi, R. & Edu, S. A study of cross-validation and bootstrap for accuracy estimation and model selection. *Proc. 14th Int. Jt. Conf. Artif. Intell.* **2**, 1137–1143 (1993).

136. Clark, J. S. *Model Assessment and Selection. Models for Ecological Data* (2020). doi:10.2307/j.ctv15r5dgv.9.

137. Singh, G. P., Goh, S., Canzoneri, M. & Ram, R. J. Raman spectroscopy of complex defined media: Biopharmaceutical applications. *J. Raman Spectrosc.* **46**, 545–550 (2015).

138. Liu, H., Zhang, Z., Sun, J. & Liu, S. Blind spectral deconvolution algorithm for Raman spectrum with Poisson noise. *Photonics Res.* **2**, 168 (2014).

139. Sane, S. U., Wong, R. & Hsu, C. C. Raman Spectroscopic Characterization of Drying-Induced Structural Changes in a Therapeutic Antibody: Correlating Structural Changes with Long-Term Stability. *J. Pharm. Sci.* **93**, 1005–1018 (2004).

140. Zhang, B. *et al.* In Situ High-Temperature Raman Spectroscopy via a Remote Fiber-Optic Raman Probe. *IEEE Trans. Instrum. Meas.* **72**, 1–8 (2023).

141. Pablo Tomba, J., Carella, J. M. & Pastor, J. M. Interphase evolution in polymer films by confocal Raman microspectroscopy. *Appl. Spectrosc.* **60**, 115–121 (2006).

142. van de Schoot, R. *et al.* Bayesian statistics and modelling. *Nat. Rev. Methods Prim.* **1**, (2021).

143. Moores, M. *et al.* Bayesian modelling and quantification of Raman spectroscopy. 1–24 (2016).

144. Geladi, P. & Kowalski, B. Partial Least Squares Regression: A Tutorial. *Analaytica Chim. Acta* **185**, 1–17 (1986).

145. Li, M., Ebel, B., Chauchard, F., Guédon, E. & Marc, A. Parallel comparison of in situ Raman and NIR spectroscopies to simultaneously measure multiple variables toward real-time monitoring of CHO cell bioreactor cultures. *Biochem. Eng. J.* **137**, 205–213 (2018).

146. Andries, J. P. M., Tinnevelt, G. H. & Vander Heyden, Y. Improved modelling for low-correlated multiple responses by common-subset-of-independent-variables partial-least-squares. *Talanta* **239**, 123140 (2022).

147. Tiao, G. C., Draper, N. R. & Smith, H. *Applied Regression Analysis*. *Applied Regression Analysis (3rd Edition)* (WILEY, 1998). doi:10.2307/1401351.

148. Bjoerkstroem, A. Ridge regression and inverse problems. 31 (2001).

149. Chung, J. & Español, M. I. Learning regularization parameters for general-form Tikhonov. *Inverse Probl.* **33**, (2017).

150. Shih, W.-C., Bechtel, K. L. & Feld, M. S. Noninvasive Glucose Sensing with Raman Spectroscopy. *Vivo Glucose Sens.* 391–419 (2009) doi:10.1002/9780470567319.ch14.

151. Kozma, B., Salgó, A. & Gergely, S. Comparison of multivariate data analysis techniques to improve glucose concentration prediction in mammalian cell cultivations by Raman spectroscopy. *J. Pharm. Biomed. Anal.* **158**, 269–279 (2018).

152. Balabin, R. M. & Smirnov, S. V. Variable selection in near-infrared spectroscopy: Benchmarking of feature selection methods on biodiesel data. *Anal. Chim. Acta* **692**, 63–72 (2011).

153. Xiaobo, Z., Jiewen, Z., Povey, M. J. W., Holmes, M. & Hanpin, M. Variables selection methods in near-infrared spectroscopy. *Anal. Chim. Acta* **667**, 14–32 (2010).

154. Santos, R. M., Kessler, J. M., Salou, P., Menezes, J. C. & Peinado, A. Monitoring mAb cultivations with in-situ raman spectroscopy: The influence of spectral selectivity on calibration models and industrial use as reliable PAT tool. *Biotechnol. Prog.* **34**, 659–670 (2018).

155. Mehmood, T., Sæbø, S. & Liland, K. H. Comparison of variable selection methods in partial least squares regression. *J. Chemom.* **34**, 1–14 (2020).

156. Gosselin, R., Rodrigue, D. & Duchesne, C. A Bootstrap-VIP approach for selecting wavelength intervals in spectral imaging applications. *Chemom. Intell. Lab. Syst.* **100**, 12–21 (2010).

157. Yilmaz, D. *et al.* Application of Raman spectroscopy in monoclonal antibody producing continuous systems for downstream process intensification. *Biotechnol. Prog.* (2020) doi:10.1002/btpr.2947.

158. Rowlands, C. J. *et al.* Rapid acquisition of Raman spectral maps through minimal sampling: Applications in tissue imaging. *J. Biophotonics* **5**, 220–229 (2012).

159. Yun, Y. H., Li, H. D., Deng, B. C. & Cao, D. S. An overview of variable selection methods in multivariate analysis of near-infrared spectra. *TrAC - Trends Anal. Chem.* **113**, 102–115 (2019).

160. Afanador, N. L., Tran, T. N. & Buydens, L. M. C. Use of the bootstrap and permutation

methods for a more robust variable importance in the projection metric for partial least squares regression. *Anal. Chim. Acta* **768**, 49–56 (2013).

161. Kim, S., Kano, M., Nakagawa, H. & Hasebe, S. Estimation of active pharmaceutical ingredients content using locally weighted partial least squares and statistical wavelength selection. *Int. J. Pharm.* **421**, 269–274 (2011).

162. Rinnan, Å., Andersson, M., Ridder, C. & Engelsen, S. B. Recursive weighted partial least squares (rPLS): An efficient variable selection method using PLS. *J. Chemom.* **28**, 439–447 (2014).

163. Filzmoser, P., Gschwandtner, M. & Todorov, V. Review of sparse methods in regression and classification with application to chemometrics. *J. Chemom.* **26**, 42–51 (2012).

164. Gruber, N. & Galloway, J. N. An Earth-system perspective of the global nitrogen cycle. *Nature* **451**, 293–296 (2008).

165. Camargo, J. A. & Alonso, Á. Ecological and toxicological effects of inorganic nitrogen pollution in aquatic ecosystems: A global assessment. *Environ. Int.* **32**, 831–849 (2006).

166. Banerjee, P. *et al.* A critical review on the effect of nitrate pollution in aquatic invertebrates and fish. *Water. Air. Soil Pollut.* **234**, 1–14 (2023).

167. Bijay-Singh & Craswell, E. Fertilizers and nitrate pollution of surface and ground water: an increasingly pervasive global problem. *SN Appl. Sci.* **3**, 1–24 (2021).

168. Kocour Kroupová, H., Valentová, O., Svobodová, Z., Šauer, P. & Máchová, J. Toxic effects of nitrite on freshwater organisms: a review. *Rev. Aquac.* **10**, 525–542 (2018).

169. Nolan, B. T. & Hitt, K. J. Vulnerability of shallow groundwater and drinking-water wells to nitrate in the United States. *Environ. Sci. Technol.* **40**, 7834–7840 (2006).

170. Simranjeet Singh a, A. G. A. *et al.* Nitrates in the environment: A critical review of their distribution, sensing techniques, ecological effects and remediation. *Chemosphere* **287**, (2022).

171. Ward, M. H. *et al.* Drinking water nitrate and human health: An updated review. *Int. J. Environ. Res. Public Health* **15**, 1–31 (2018).

172. Rice, K. C. & Herman, J. S. Acidification of Earth: An assessment across mechanisms and scales. *Appl. Geochemistry* **27**, 1–14 (2012).

173. Kicińska, A., Pomykała, R. & Izquierdo-Diaz, M. Changes in soil pH and mobility of heavy metals in contaminated soils. *Eur. J. Soil Sci.* **73**, 1–14 (2022).

174. Lehmann, J., Bossio, D. A., Kögel-Knabner, I. & Rillig, M. C. The concept and future prospects of soil health. *Nat. Rev. Earth Environ.* **1**, 544–553 (2020).

175. Musacchio, A., Re, V., Mas-Pla, J. & Sacchi, E. EU Nitrates Directive, from theory to practice: Environmental effectiveness and influence of regional governance on its

performance. *Ambio* **49**, 504–516 (2020).

176. Byrnes, D. K., Van Meter, K. J. & Basu, N. B. Long-Term Shifts in U.S. Nitrogen Sources and Sinks Revealed by the New TREND-Nitrogen Data Set (1930–2017). *Global Biogeochem. Cycles* **34**, 1–17 (2020).

177. Kanter, D. R., Zhang, X. & Mauzerall, D. L. Reducing Nitrogen Pollution while Decreasing Farmers' Costs and Increasing Fertilizer Industry Profits. *J. Environ. Qual.* **44**, 325–335 (2015).

178. Li, Y. hua *et al.* Fate of nitrogen in subsurface infiltration system for treating secondary effluent. *Water Sci. Eng.* **10**, 217–224 (2017).

179. Samuel, L. & Dines, L. Fertilisers and Manures. in *Lockhart and Wiseman' s Crop Husbandry Including Grassland* 81–114 (2023).

180. University of Georgia - Crop sheets. USA-EC20-7KzN-sOa7USA-EC20-7KzN-sOa7USA-EC20-7KzN-sOa7.

181. EPA Nitrate MCL. https://www.epa.gov/sites/default/files/2021-01/documents/wsg_213_nitrate_wsg_11-30-2020_signed_508-compliantfinal.pdf.

182. Canada Nitrate- Nitrite drinking water limits. https://www.canada.ca/en/health-canada/services/publications/healthy-living/guidelines-canadian-drinking-water-quality-guideline-technical-document-nitrate-nitrite.html.

183. EU Comission Nitrate directive. https://environment.ec.europa.eu/topics/water/nitrates_en#overview.

184. WHO Guidelines for Drinking Water Quality. https://apps.who.int/iris/bitstream/handle/10665/352532/9789240045064-eng.pdf?sequence=1&isAllowed=y#page=107.

185. India Bureau of Standards Nitrate MCL. https://pcb.assam.gov.in/information-services/indian-standard-specifications-for-drinking-water.

186. India Water Monitoring. https://www.in.gov/idem/files/factsheet_owq_pws_nitrate.pdf.

187. Feng, W., Wang, C., Lei, X., Wang, H. & Zhang, X. Distribution of nitrate content in groundwater and evaluation of potential health risks: A case study of rural areas in Northern China. *Int. J. Environ. Res. Public Health* **17**, 1–14 (2020).

188. China Nitrate limits.

189. United States Code,Title 33. https://www.govinfo.gov/app/collection/uscode.

190. John, K. A. *et al.* Lessons Learned from 30 Years of Assessing U.S. Coastal Water. in *Water Quality - Science, Assessments and Policy* (ed. Kevin, S. J.) (IntechOpen, 2020).

191. EPA Summary of the Clean Water Act. https://www.epa.gov/laws-regulations/summary-clean-water-act.

192. EPA NARS. https://www.epa.gov/national-aquatic-resource-surveys/background-national-aquatic-resource-surveys.

193. Musacchio, A., Re, V., Mas-Pla, J. & Sacchi, E. EU Nitrates Directive, from theory to practice: Environmental effectiveness and influence of regional governance on its performance. *Ambio* **49**, 504–516 (2020).

194. Fekete, B. M. *et al.* Time for in situ renaissance. *Science (80-.).* **349**, 685–686 (2015).

195. Steve, P., David, peck V., Philip, K. R. & Alan, H. . Rivers and Streams: Upgrading Monitoring of the Nation's Freshwater Resources - Meeting the Spirit of the Clean Water Act. in *Water Quality - Science, Assessments and Policy* 13 (IntechOpen, 2020).

196. Lal, K., Jaywant, S. A. & Arif, K. M. Electrochemical and Optical Sensors for Real-Time Detection of Nitrate in Water. *Sensors (Basel).* **23**, 1–19 (2023).

197. Singh, P., Singh, M. K., Beg, Y. R. & Nishad, G. R. A review on spectroscopic methods for determination of nitrite and nitrate in environmental samples. *Talanta* **191**, 364–381 (2019).

198. Gan, F., Wu, K., Ma, F., Wei, C. & Du, C. In-situ monitoring of nitrate in industrial wastewater using Fourier transform infrared attenuated total reflectance spectroscopy (FTIR-ATR) coupled with chemometrics methods. *Heliyon* **8**, (2022).

199. Alahi, M. E. E. & Mukhopadhyay, S. C. Detection methods of nitrate in water: A review. *Sensors Actuators, A Phys.* **280**, 210–221 (2018).

200. Matthew J. Moorcroft, Davis, J. & Compton, R. G. Detection and determination of nitrate and nitrite: a review. *Talanta* **54**, 785–803 (2001).

201. Wang, Q., Yu, L. & Lu, Z. Methods for the detection and determination of nitrite and nitrate: A review. *Talanta* **165**, 709–720 (2017).

202. Sah, R. N. Nitrate-nitrogen determination—a critical review. *Commun. Soil Sci. Plant Anal.* **25**, 2841–2869 (1994).

203. Alahi, M. E. E. & Mukhopadhyay, S. C. Detection methods of nitrate in water: A review. *Sensors Actuators, A Phys.* **280**, 210–221 (2018).

204. Singh, P., Singh, M. K., Beg, Y. R. & Nishad, G. R. A review on spectroscopic methods for determination of nitrite and nitrate in environmental samples. *Talanta* **191**, 364–381 (2019).

205. Singh, S. *et al.* Nitrates in the environment: A critical review of their distribution, sensing techniques, ecological effects and remediation. *Chemosphere* **287**, 131996 (2022).

206. Coviello, D. *et al.* Validation of an analytical method for nitrite and nitrate determination in meat foods for infants by ion chromatography with conductivity detection. *Foods* **9**, (2020).

207. Hager, T. J. *et al.* New approach to remote sensing of temperature and salinity in natural

water samples. *Remote Sens.* **11**, 13 (2016).

208. Adjovu, G. E., Stephen, H., James, D. & Ahmad, S. Overview of the Application of Remote Sensing in Effective Monitoring of Water Quality Parameters. *Remote Sens.* **15**, (2023).

209. Gholizadeh, M. H., Melesse, A. M. & Reddi, L. A comprehensive review on water quality parameters estimation using remote sensing techniques. *Sensors (Switzerland)* **16**, (2016).

210. Yang, H. *et al.* A Review of Remote Sensing for Water Quality Retrieval: Progress and Challenges. *Remote Sens.* **14**, (2022).

211. Kay, K. X. E. *et al.* Identification of Illicit Street Drugs with Swept-Source Raman spectroscopy. *J. Raman Spectrosc.* (2022) doi:10.1002/jrs.6357.

212. Fontana, M. D., Mabrouk, K. Ben & Kauffmann, T. H. Raman probe of pollutants in water: Measurement process. *4th IMEKO TC19 Symp. Environ. Instrum. Meas. 2013 Prot. Environ. Clim. Chang. Pollut. Control* 27–29 (2013).

213. Gajaraj, S., Fan, C., Lin, M. & Hu, Z. Quantitative detection of nitrate in water and wastewater by surface-enhanced Raman spectroscopy. *Environ. Monit. Assess.* **185**, 5673–5681 (2013).

214. Hager, T. J. & Sadergaski, L. R. Measuring Hydroxylammonium, Nitrate, and Nitrite Concentration with Raman Spectroscopy for the 238 Pu Supply Program. (2021).

215. Spohn, P. D. & Brill, T. B. Raman spectroscopy of the species in concentrated aqueous solutions of zinc nitrate, calcium nitrate, cadmium nitrate, lithium nitrate and sodium nitrate up to 450.degree.C and 30 MPa. *J. Phys. Chem.* **93**, 6224–6231 (1989).

216. Shahnia, S., Ebendorff-Heidepriem, H., Evans, D. & Afshar, S. A fibre-optic platform for sensing nitrate using conducting polymers. *Sensors (Switzerland)* **21**, 1–11 (2021).

217. Bradley, E. B. & Frenzel, C. A. On the exploitation of laser raman spectroscopy for detection and identification of molecular water pollutants. *Water Res.* **4**, 125–128 (1970).

218. Wu, X., Lu, W., Ou, W., Caumon, M. C. & Dubessy, J. Temperature and salinity effects on the Raman scattering cross section of the water OH-stretching vibration band in NaCl aqueous solutions from 0 to 300 °C. *J. Raman Spectrosc.* **48**, 314–322 (2017).

219. De Beer, T. *et al.* Near infrared and Raman spectroscopy for the in-process monitoring of pharmaceutical production processes. *Int. J. Pharm.* **417**, 32–47 (2011).

220. Ebrahimi, S. B. & Samanta, D. Engineering protein-based therapeutics through structural and chemical design. *Nat. Commun.* **14**, 1–11 (2023).

221. Ebrahimi, S. B. Engineering Protein-Based Therapeutics Through Structural and Chemical Design - supplementary. *Nature* **14**, 1–11 (2023).

222. Lee, H. L. T., Boccazzi, P., Gorret, N., Ram, R. J. & Sinskey, A. J. In situ bioprocess monitoring of Escherichia coli bioreactions using Raman spectroscopy. *Vib. Spectrosc.* **35**,

131–137 (2004).

223. Li, B., Ray, B. H., Leister, K. J. & Ryder, A. G. Performance monitoring of a mammalian cell based bioprocess using Raman spectroscopy. *Anal. Chim. Acta* **796**, 84–91 (2013).

224. Li, B. *et al.* Rapid characterization and quality control of complex cell culture media solutions using Raman spectroscopy and chemometrics. *Biotechnol. Bioeng.* **107**, 290–301 (2010).

225. Holzberg, T. R. *et al.* Sensors for biomanufacturing process development: facilitating the shift from batch to continuous manufacturing. *Curr. Opin. Chem. Eng.* **22**, 115–127 (2018).

226. Zydney, A. L. Perspectives on integrated continuous bioprocessing - opportunities and challenges. *Curr. Opin. Chem. Eng.* **10**, 8–13 (2015).

227. André, S. *et al.* In-line and real-time prediction of recombinant antibody titer by in situ Raman spectroscopy. *Anal. Chim. Acta* **892**, 148–152 (2015).

228. Helgers, H. *et al.* Towards autonomous operation by advanced process control—process analytical technology for continuous biologics antibody manufacturing. *Processes* **9**, 1–31 (2021).

229. Randek, J. & Mandenius, C. F. On-line soft sensing in upstream bioprocessing. *Crit. Rev. Biotechnol.* **38**, 106–121 (2018).

230. Bhatia, H., Mehdizadeh, H., Drapeau, D. & Yoon, S. In-line monitoring of amino acids in mammalian cell cultures using raman spectroscopy and multivariate chemometrics models. *Eng. Life Sci.* **18**, 55–61 (2018).

231. Lee, K. S., Boccazzi, P., Sinskey, A. J. & Ram, R. J. Microscale Controlled Continuous Cell Culture. *Proc. 14th Int. Conf. Miniaturized Syst. Chem. Life Sci.* 1400–1402 (2010).

232. Bower, D. M., Lee, K. S., Ram, R. J. & Prather, K. L. J. Fed-batch microbioreactor platform for scale down and analysis of a plasmid DNA production process. *Biotechnol. Bioeng.* **109**, 1976–1986 (2012).

233. Matthews, T. E. *et al.* Glucose monitoring and adaptive feeding of mammalian cell culture in the presence of strong autofluorescence by near infrared Raman spectroscopy. *Biotechnol. Prog.* **34**, 1574–1580 (2018).

234. Whelan, J., Craven, S. & Glennon, B. In situ Raman spectroscopy for simultaneous monitoring of multiple process parameters in mammalian cell culture bioreactors. *Biotechnol. Prog.* **28**, 1355–1362 (2012).

235. Atkins, C. G., Buckley, K., Blades, M. W. & Turner, R. F. B. Raman Spectroscopy of Blood and Blood Components. *Appl. Spectrosc.* **71**, 767–793 (2017).

236. Craven, S., Whelan, J. & Glennon, B. Glucose concentration control of a fed-batch mammalian cell bioprocess using a nonlinear model predictive controller. *J. Process Control* **24**, 344–357 (2014).

237. Xu, Y. *et al.* Raman measurement of glucose in bioreactor materials. in *SPIE Biomedical Sensing, Imaging, and Tracking Technologies II* vol. 2976 10–19 (1997).

238. Webster, T. A., Hadley, B. C., Hilliard, W., Jaques, C. & Mason, C. Development of generic raman models for a GS-KOTM CHO platform process. *Biotechnol. Prog.* **34**, 730–737 (2018).

239. Mehdizadeh, H. *et al.* Generic Raman-based calibration models enabling real-time monitoring of cell culture bioreactors. *Biotechnol. Prog.* **31**, 1004–1013 (2015).

240. Zhang, W., Guo, C., Jiang, K., Ying, M. & Hu, X. Quantification of lactate from various metabolic pathways and quantification issues of lactate isotopologues and isotopmers. *Sci. Rep.* **7**, 1–12 (2017).

241. Matthews, T. E. *et al.* Closed loop control of lactate concentration in mammalian cell culture by Raman spectroscopy leads to improved cell density, viability, and biopharmaceutical protein production. *Biotechnol. Bioeng.* **113**, 2416–2424 (2016).

242. Trunfio, N. *et al.* Characterization of mammalian cell culture raw materials by combining spectroscopy and chemometrics. *Biotechnol. Prog.* **33**, 1127–1138 (2017).

243. Lim, Z. J. J. Characterisation of Single Photon Avalanche Detectors. 1–43 (2016).

244. Mattson, N. S. & Peters, C. A Recipe for Hydroponic Success. *Insid. Grow.* 16–19 (2014).

245. Son, J. E., Kim, H. J. & Ahn, T. I. *Hydroponic systems. Plant Factory: An Indoor Vertical Farming System for Efficient Quality Food Production: Second Edition* (Elsevier Inc., 2019). doi:10.1016/B978-0-12-816691-8.00020-0.

246. El-Jaoual, T. & Cox, D. Effects of plant age on nitrogen uptake and distribution by greenhouse plantstle. *J. Plant Nutr.* **21**, 1055–1066 (1998).

247. Gupta, S. *et al.* Portable Raman leaf-clip sensor for rapid detection of plant stress. *Sci. Rep.* **10**, 1–10 (2020).

248. Schulz, H., Baranska, M. & Baranski, R. Potential of NIR-FT-Raman spectroscopy in Natural Carotenoid Analysis. *Biopolymers* **77**, 212–221 (2005).

249. Yin, H., Hu, X. & Dias, L. M. Sulfate enrichment in estuaries of the northwestern Gulf of Mexico: The potential effect of sulfide oxidation on carbonate chemistry under a changing climate. *Limnol. Oceanogr. Lett.* **8**, 742–750 (2023).

250. Thorlabs optical fiber specification - attenuation.

251. Thorlabs. Optical Coupler. https://www.thorlabs.com/newgrouppage9.cfm?objectgroup_id=10067.

252. Thorlabs. Optical Isolator. https://www.thorlabs.com/newgrouppage9.cfm?objectgroup_id=6155.

253. Superlum. Booster Superlum. https://www.superlumdiodes.com/booster-oem.htm.

254. Thorlabs. PANDA fibers. https://www.thorlabs.com/newgrouppage9.cfm?objectgroup_id=3125.

255. DiCON. DiCON MEMS Switch. https://www.diconfiberoptics.com/products/Components-1xN-Switches.php.

256. Thorlabs. Splitter SM. TWQ850HFc.

257. Walther, J. *et al.* The business impact of an integrated continuous biomanufacturing platform for recombinant protein production. *J. Biotechnol.* **213**, 3–12 (2015).

258. Herrington, W. F. *et al.* Optical Detection of Degraded Therapeutic Proteins. *Sci. Rep.* **8**, 1–10 (2018).

259. Hou, S., Wang, H., Guo, Y. & Lou, Z. Comparison of the Inhibition Mechanisms of Adalimumab and Infliximab in Treating Tumor Necrosis Factor -Associated Diseases from a Molecular View *. *J. Biol. Chem.* **288**, 27059–27067 (2013).

260. Lippert, J. L., Tyminski, D. & Desmeules, P. J. Determination of the Secondary Structure of Proteins by Laser Raman Spectroscopy. *J. Am. Chem. Soc.* **98**, 7075–7080 (1976).

261. Seki, T. *et al.* The bending mode of water: A powerful probe for hydrogen bond structure of aqueous systems. *J. Phys. Chem. Lett.* **11**, 8459–8469 (2020).

262. Dhamelincourt P & J, R. F. Polarized Micro-Raman and FT-IR Spectra of L-Glutamine. **47**, 446–451 (1993).

263. Pecul, M., Cnr, C. & Moruzzi, V. Vibrational Raman and Raman Optical Activity Spectra of. 11008–11016 (2002).

264. Il-Gyo, C. & Jun, C.-H. Performance of Some variable selection methods when multicollinearity is present. *Chemom. Intell. Lab. Syst.* **78**, 103–112 (2005).

265. Haddock, R. *et al.* Manufacturing Cell Therapies: The Paradigm Shift in Healthcare of this Century. *NAM Perspect.* in press (2017) doi:10.31478/201706c.

266. Sterner, R. C. & Sterner, R. M. CAR-T cell therapy: current limitations and potential strategies. *Blood Cancer J.* **11**, (2021).

267. Li, Y. *et al.* Current status of clinical trials assessing mesenchymal stem cell therapy for graft versus host disease: a systematic review. *Stem Cell Res. Ther.* **13**, 1–22 (2022).

268. Persits, N., Farruggio, C., Vliet, K. Van & Ram, R. J. Metabolite Monitoring of Mesenchymal Stromal Cell Cultures By Spontaneous Raman Spectroscopy. in *AIChE Annual Meeting* 234a (2021).

269. Horiba. Horiba MultiWell. https://www.horiba.com/usa/scientific/products/detail/action/show/Product/multiwell-module-1650/.

270. Lemler, P., Premasiri, W. R., Delmonaco, A. & Ziegler, L. D. NIR Raman spectra of whole

human blood : effects of laser-induced and in vitro hemoglobin denaturation. 193–200 (2014) doi:10.1007/s00216-013-7427-7.

271. Spiro, T. G. & Strekas, T. C. Cytochrome C: Resonance Raman spectra. *Biochim. Biophys. Acta* **278**, 188–192 (1972).

272. Spiro, T. G. & Strekas, T. C. Resonance Raman Spectra of Heme Proteins. Effects of Oxidation and Spin State. *J. Am. Chem. Soc.* **96**, 338–345 (1974).

273. Perry, D. A. *et al.* Responsive monitoring of mitochondrial redox states in heart muscle predicts impending cardiac arrest. *Sci. Transl. Med.* **9**, 1–12 (2017).

274. Sharma, S. K. *et al.* Standoff Raman spectroscopy for future Europa Lander missions. *J. Raman Spectrosc.* **51**, 1782–1793 (2020).

275. Saptari, V. *Fourier-Transform Spectroscopy Instrumentation Engineering*. (SPIE press, 2003).

276. Routley, S. A., Flynn, J., Martin, A. & Palmer, W. High étendue Fourier Transform Spectroscopy by Quadratic Off-axis Path Difference Error Cancellation. *J. Opt. Soc. Am. A* **37**, 1767 (2020).

277. Saptari, V. Interferogram Data Sampling. *Fourier-Transform Spectrosc. Instrum. Eng.* **1**, 65–76 (2009).

278. Li, J., Lu, D. F. & Qi, Z. M. A Modified Equation for the Spectral Resolution of Fourier Transform Spectrometers. *J. Light. Technol.* **33**, 19–24 (2015).

279. Bruker IR spectromtere. https://www.bruker.com/en/products-and-solutions/infrared-and-raman/ft-ir-research-spectrometers/ifs-125hr-high-resolution-ft-ir-spectrometer.html.

280. Fendel, S. & Schrader, B. Investigation of Skin and Skin Lesions by NIR-FT-Raman Spectroscopy. *Fresenius. J. Anal. Chem.* **360**, 609–613 (1998).

281. Rygula, A. *et al.* Raman Spectroscopy of Proteins: A Review. *J. Raman Spectrosc.* **44**, 1061–1076 (2013).

282. Gomer, N. R. *et al.* Raman spectroscopy using a Spatial Heterodyne Spectrometer: Proof of Concept. *Appl. Spectrosc.* **65**, 849–857 (2011).

283. Nathaniel Richard Gomer. The Development of a Spatial Heterodyne Spectrometer for Raman Spectroscopy. (2012).

284. Harlander, J. M., Roesler, F. L. & Chakrabarti, S. Spatial Heterodyne Spectroscopy: a Novel Interferometric Technique for the FUV. *EUV, X-Ray, Gamma-Ray Instrum. Astron.* **1344**, 120 (1990).

285. Harlander, J., R.J., R. & F.L, R. Spatial Heterodyne Spectroscopy for the Exploration of Diffuse Interstellar Emission Lines at Far-Ultraviolet Wavelengths. *Astrophys. J.* **396**, 730–740 (1992).

286. Zettner, A., Gojani, A. B., Schmid, T. & Gornushkin, I. B. Evaluation of a Spatial

Heterodyne Spectrometer for Raman Spectroscopy of Minerals. *Minerals* **10**, 1–16 (2020).

287. Waldron, A., Allen, A., Colón, A., Carter, J. C. & Angel, S. M. A Monolithic Spatial Heterodyne Raman Spectrometer: Initial Tests. *Appl. Spectrosc.* **75**, 57–69 (2021).

288. Allen, A., Waldron, A., Ottaway, J. M., Chance Carter, J. & Michael Angel, S. Hyperspectral Raman Imaging Using a Spatial Heterodyne Raman Spectrometer with a Microlens Array. *Appl. Spectrosc.* **74**, 921–931 (2020).

289. Ottaway, J. M. *et al.* Spatial Heterodyne Raman Spectrometer (SHRS) for In Situ Chemical Sensing Using Sapphire and Silica Optical Fiber Raman Probes. *Appl. Spectrosc.* **73**, 1160–1171 (2019).

290. Conn, G. K. T., Lee, E., Sutherland, G. B. B. M. & Wu, C.-K. Investigations on the Vibration Spectra of Certain Condensed Gases at the Temperature of Liquid Nitrogen. I. Experimental Methods. *Proc. R. Soc. Lond. A. Math. Phys. Sci.* **176.967**, 484–493 (1940).

291. Neumann, W. Detectors for Optical Telescopes. in *Fundamentals of Dispersive Optical Spectroscopy Systems* 143–205 (2014). doi:10.1201/9781420057034.ch18.

292. Buchner, A. *et al.* Analytical Evaluation of Signal-to-Noise Ratios for Avalanche-and Single-Photon Avalanche Diodes. *Sensors* **21**, 1–18 (2021).

293. Kim, Y. S. Y. H., Jeong, Y. C., Sauge, S., Makarov, V. & Kim, Y. S. Y. H. Ultra-low Noise Single-Photon Detector Based on Si Avalanche Photodiode. *Rev. Sci. Instrum.* **82**, 2–7 (2011).

294. Hart, R. J., Pedge, N. I., Steven, A. R. & Sutcliffe, K. In situ monitoring of a heterogeneous etherification reaction using quantitative raman spectroscopy. *Org. Process Res. Dev.* **19**, 196–202 (2015).

295. Cao, K. L. *et al.* A Sparse PLS for Variable Selection when Integrating Omics data. *Stat. Appl. Genet. Mol. Biol.* **7**, 35 (2008).

296. de Jong, S. SIMPLS : an alternative approach to partial least squares regression. *Chemom. I* **18**, 251–263 (1993).

297. Cao, H. *et al.* A Raman Spectroscopic and Microimage Analysis Perspective of the Chang'e-5 Lunar Samples. *Geophys. Res. Lett.* **49**, (2022).